



TECHNISCHE
UNIVERSITÄT
WIEN
Vienna University of Technology

Diese Dissertation haben begutachtet:

Priv. Doz. Dr. Johann Marton

Ass. Prof. Dr. Dennis Schaart

DISSERTATION

Fast single photon detection for scintillation and Cherenkov applications using silicon photomultipliers

Ausgeführt zur Erlangung des akademischen Grades eines Doktors der technischen
Wissenschaften unter der Leitung von

Priv. Doz. Dr. Johann Marton
Stefan-Meyer-Institut für subatomare Physik
der österreichischen Akademie der Wissenschaften
und TU Wien Fakultät für Physik

eingereicht an der technischen Universität Wien Fakultät für Physik von

Dipl.-Ing. Stefan Brunner
Matrikel Nr. 0326022

Antonsplatz 13/22, 1100 Wien

Datum

Unterschrift

Kurzfassung

Hohe Zeitauflösung wird zunehmend wichtig für viele Anwendungen der nuklearmedizinischen Bildgebung und der Hochenergiephysik. Die Einführung der Flugzeitmethode in der Positronen-Emissions-Tomographie (PET) führte zur Verbesserung des Rauschverhaltens von rekonstruierten PET-Bildern. Kommerziell verfügbare Systeme für Flugzeit-PET auf Basis von Photonen-vervielfacherröhren (PMT) erreichen 500-600 ps Halbwertsbreite. Im Labor werden Koinzidenzzeitauflösungen im Bereich von 100 ps Halbwertsbreite erreicht.

Die vorliegende Arbeit zielt auf die Verbesserung der Zeitauflösung von Flugzeit-PET mittels Cherenkov-Effekt als unverzögertem Lumineszenzprozess ab. Der Cherenkov-Effekt tritt in Szintillatoren bzw. Cherenkov-Radiatoren nach der Absorption von Annihilationsphotonen mit der Energie von 511 keV mittels photoelektrischem Effekt auf. Der Zeitpunkt der photoelektrischen Interaktion kann sehr genau bestimmt werden, da die Cherenkov-Photonen durch die Bewegung der durch den photoelektrischen Effekt herausgelösten Elektronen unmittelbar emittiert werden.

Die Untersuchungen wurden für reine Cherenkov-Radiatoren und auch für sogenannte Hybrid-Szintillatoren durchgeführt. Für reine Cherenkov-Strahler kann die Materialzusammensetzung flexibler in Hinblick auf große Cherenkov-Photonenzahl gestaltet werden. In Hybrid-Szintillatoren, die Szintillatoren darstellen in denen auch Cherenkov-Emission stattfindet, kann zusätzlich zur Zeitbestimmung mittels Cherenkov-Strahlung das Szintillationslicht zur Bestimmung der deponierten Energie und somit zur Diskriminierung zwischen echten Koinzidenzen und unerwünschten Koinzidenzen nach Compton-Streuung verwendet werden.

Aufgrund der Vorteile kürzlich entwickelter Lichtdetektoren auf Halbleiterbasis, sogenannter Silizium-Photonenvervielfacher (SiPM) werden große Anstrengungen unternommen diese auch in der PET einzusetzen. Vorteile dieser Technologie sind die Möglichkeit einzelne Photonen zu detektieren, eine gute Zeitauflösung und – im Gegensatz zu traditionellen PMT – Unempfindlichkeit auf Magnetfelder, was sie zu potentiellen Kandidaten im Einsatz von PET Systemen in Kombination mit Kernspinresonanztomographie machen. Die vor kurzem vorgestellte Weiterentwicklung der SiPM zu digitalen SiPM nützt die Vorteile der quasi-digitalen Funktionsweise von SiPM mittels integrierter Elektronik aus und wurde daher für einen Großteil der hier vorgestellten Untersuchungen herangezogen.

In der vorliegenden Arbeit werden zuerst die erreichbaren Zeitauflösungen von analogen und digitalen SiPM mittels Ultrakurzpulslaser bestimmt und verglichen. In einer Machbarkeitsstudie wird die Intensität der zu erwartenden Cherenkov-Strahlung mittels Monte-Carlo-Simulation untersucht und gezeigt, dass in allen untersuchten Materialien Cherenkov-Photonen emittiert werden und auch detektiert werden können.

In einer Messung wird gezeigt, dass für alle untersuchten Materialien Cherenkov-Photonen mittels digitaler SiPM nachgewiesen werden können. So wurden für den inorganischen Kristall LuAG im Mittel 5.7 und im optischen Glas N-LASF31A 3.1 Cherenkov-Photonen nach der photoelektrischen Absorption von Annihilationsphotonen gemessen. In Koinzidenz mit einem LSO:Ce Szintillator wurde für einen 8 mm langen LuAG Kristall eine Koinzidenzzeitauflösung von 145 ± 6.2 ps Halbwertsbreite erreicht, was eine signifikante Verbesserung zu den 192 ± 4.0 ps Halbwertsbreite einer Referenzmessung mit LSO:Ce Szintillatoren darstellt.

Darüber hinaus konnte in einer Messung mit dem Szintillator BGO zusätzlich zum Szintillationslicht auch Cherenkov-Licht nachgewiesen werden. Der Anteil der Koinzidenzen in denen Cherenkov-Photonen detektiert wurden macht 24% aus. Für diese 24% der Koinzidenzen wurde für BGO eine Zeitauflösung von 301 ps FWHM erreicht. Da die vorgestellten Messungen

nur eine Machbarkeitsstudie darstellen ist durch weitere Forschung auf dem Gebiet mit einer signifikanten Verbesserung der Zeitauflösung zu rechnen.

Abstract

High time resolution is becoming increasingly important for many applications in nuclear medicine and high energy physics applications. The introduction of time-of-flight (TOF) into positron emission tomography (PET) has helped to improve noise properties of reconstructed PET images. TOF-PET systems with timing resolution in the order of 500-600 ps FWHM using detectors based on photomultiplier tubes (PMT) are commercially available from major PET vendors. Coincidence time resolutions (CTRs) at the level of 100 ps FWHM are needed to increase the signal-to-noise ratio of the reconstructed images in an extent that patients can benefit from shorter acquisition times and lower radiation exposure. Laboratory measurements already achieve this value by scintillation methods.

This thesis aims at an increase of the time resolution of TOF-PET by investigation of the Cherenkov effect as an almost instantaneous process of luminescence. The Cherenkov effect occurs after the photoelectric absorption of the 511 keV annihilation photons inside the scintillator or Cherenkov radiator and provides very precise time information about the energy deposition.

Furthermore, the development of silicon photomultipliers (SiPM), with properties such as single photon detection, good time resolution and – in contrast to ordinary PMTs – insensitivity to magnetic fields, allows their utilisation in hybrid devices such as PET combined with nuclear magnetic resonance (NMR) imaging. Recently, the digital SiPM was introduced, which exploits the quasi digital nature of SiPM and therefore provides advantages such as integrated readout of the data. To make use of these advantages, SiPM were used in this work for the investigation on the Cherenkov effect.

First, the time resolution of SiPM, both analogue and digital are determined and compared using pulsed lasers in the pico- and femtosecond region. A Monte-Carlo simulation tool was developed for better understanding of the obtained results. Then, factors influencing the time resolution of scintillators and Cherenkov radiators are determined and compared. Using simulations it is shown that Cherenkov emission by electrons at energies below 500 keV can be expected in Cherenkov radiators and scintillators, although, the number of emitted Cherenkov photons is low. A study on the influence several parameters shows that the UV-transmission is the most important factor for increasing the number of detected Cherenkov photons.

Although, the utilisation of pure Cherenkov radiators allows more flexibility on the material parameters, the low yield of Cherenkov photons makes a determination of the deposited energy almost impossible. Energy determination is necessary in PET for discriminating true events from coincidences after Compton scattering. As a consequence, the application of hybrid scintillators could provide both, very precise time resolution due to the Cherenkov emission and additional energy information due to scintillation. Therefore, a case study for LSO:Ce on the impact of additionally detecting Cherenkov photons was done and showed significant improvement of the CTR.

Finally, proof of principle measurements are presented, showing the feasibility of detecting Cherenkov photons after the photoelectric absorption of 511 keV annihilation photons. It is shown that using the Philips digital photon counter (DPC) on average 5.7 Cherenkov photons can be detected for the inorganic crystal LuAG and 3.1 Cherenkov photons can be detected using the optical glass (N-LASF31A). Measuring a 8 mm long LuAG crystal as Cherenkov radiator in coincidence with LSO:Ce, a coincidence time resolution of 145 ± 6.2 ps FWHM could be achieved, which is significantly better than the result of the reference measurement of 192 ± 4.0 ps FWHM achieved for two LSO:Ce crystals with the same dimensions. Furthermore, in a coincidence measurement using two BGO scintillators 24% of the coincidences were found to be triggered by Cherenkov-photons. Utilising the

Cherenkov emission in BGO, a coincidence time resolution of 301 ps FWHM could be achieved for two crystals with 8 mm length. The obtained CTR of the scintillation emission was 2.38 ns FWHM. For this setup an energy resolution of 16.7% was achieved, which proves the feasibility of utilising fast Cherenkov photons for improvement of time resolution in scintillators while preserving the energy information.

Acknowledgements

Zuallererst möchte ich meinem Supervisor Priv. Doz. Johann Marton für die langjährige Unterstützung meiner Arbeit und die vielen kreativen Ideen und Ratschläge zu deren Umsetzung danken. In den vier Jahren seiner Betreuung habe ich viel für mein weiteres berufliches Leben gelernt. Des Weiteren danke ich Ass. Prof. Dennis R. Schaart für seine Bereitschaft die Dissertation trotz der kurzen Zeit, die dafür zur Verfügung stand, zu begutachten und für seine Flexibilität bei der Terminfindung des Rigorosum. Ebenso danke ich Dr. Johann Zmeskal und Prof. Eberhard Widmann für Ihre Auskünfte und Ratschläge zu fachspezifischen, politisch/administrativen und strategischen Fragen. Auch möchte ich meinem ehemaligen Betreuer Paul Lecoq auf diesem Wege danken, der das Potential des Cherenkov Effektes erkannte und mich auf die Idee brachte diesen zu studieren.

Hervorheben möchte ich Dr. Ken Suzuki, dessen Unterstützung der eines Betreuers gleichkam. Seine Vorgehensweise zur Problemlösung, seine uneingeschränkte Bereitschaft zu fachlichen Diskussionen sowie seine Ausdauer bei Erklärungen und Analysen haben mich sehr beeindruckt. Vor allem aber Diskussionen zu späterer Stunde in eines der Wiener Kaffeehäuser zu verlagern haben des öfteren zu interessanten Erkenntnissen geführt. Besonders bedanken möchte ich mich bei Dr. Albert Hirtl, der mir trotz widrigster Umstände mit Rat und Tat zu Seite stand und mich bei meinen Hirngespinnsten unterstützte.

Die fachliche, vor allem aber die moralische Unterstützung all meiner langjährigen Arbeitskollegen und Freunden darf nicht ungedankt bleiben, wobei ich Martin, Lukas, Andi, Dominik, Clemens, Martin S. Oswald und Susanne (in zufälliger Reihenfolge) nennen möchte, die besonders in den zuvor genannten Lokalitäten auch immer wieder notwendige Ablenkung schaffen

konnten. Danken möchte ich auch meinen Freunden Nina, die großen Einfluß auf die Lösung statistischer Probleme hatte, Felix und Johanna, Babsi, Bettina, Oli, Michi, Melina, Dominik, Christoph, Oliver und Michi, Stefan, Karin, Alex und Dani in Vertretung für die gesamte Schladminger-Truppe (zu Schladming zähle ich auch zukünftiger Eingemeindungen).

Hier zum Schluß, aber allen voran möchte ich meiner Familie und meiner Freundin Kathi (eigentlich auch Teil der Familie) danken. Ohne euren Glauben an mich und eure Unterstützung wären weder der Beginn noch die erfolgreiche Umsetzung meiner Arbeit möglich gewesen. Vielen Dank für eure Ausdauer in den letzten vier Jahren.

Contents

1	Introduction	1
1.1	Positron emission tomography	1
1.2	Time-of-flight PET (TOF-PET)	2
1.3	Status of research - state-of-the-art systems	3
1.4	Electron-positron annihilation	4
1.5	The Cherenkov effect	4
1.6	Cherenkov photons for TOF-PET	6
1.7	Motivation	7
2	Materials and theory	9
2.1	Scintillation detector	9
2.2	Scintillators	10
2.3	Silicon photomultipliers (SiPM)	13
2.3.1	Analog SiPM	13
2.3.2	Digital SiPM	14
3	SiPM for fast single photon detection	19
3.1	Development of a multichannel SiPM detector	19
3.2	Time resolution measurements of analog SiPM	21
3.2.1	Setup	21
3.2.2	Data analysis	24
3.2.3	Results	24
3.2.4	Discussion and Conclusion	28
3.3	Oversaturation behaviour at high photon exposure	30
3.4	Time resolution measurements of digital SiPM	32

CONTENTS

3.4.1	Theoretical considerations	32
3.4.2	Setup	37
3.4.3	Results	39
3.4.4	MC simulation of the DPC	43
3.4.5	Measurement of the SPAD time resolution	49
3.4.6	Discussion and conclusion	50
4	Potential of the Cherenkov effect for improved time resolution at low γ-photon energies	53
4.1	Cherenkov photons for TOF-PET	54
4.1.1	MC-simulation environment	55
4.1.2	Cherenkov photon yield	56
4.1.3	Potential Cherenkov radiators	60
4.1.4	Hybrid Cherenkov radiators/scintillators	60
4.1.5	Pure Cherenkov radiators	61
4.1.6	Influence of density and UV-transmission	64
4.2	Factors influencing the time resolution of scintillation and Cherenkov photon detectors	67
4.2.1	Influence of the photon statistics	67
4.2.2	Comparing the time precision of scintillation and the Cherenkov effect	68
4.2.3	Time spread of the Cherenkov emission	71
4.2.4	Time spread due to electron propagation	73
4.2.5	Influence of the DOI on the time resolution	73
4.2.6	Influence of the DOI on the signal rise time of analogue photo detectors	75
4.2.7	Photon propagation and time-walk in a scintillator	77
4.2.8	Tracklength of the photons and photon arrival times	80
4.2.9	Photon arrival times of scintillation and Cherenkov photons	85
4.2.10	Comparing photon arrival rates for various materials	88
4.2.11	Vertex of Cherenkov photon creation and angular emission distribution	92
4.3	Influence of Cherenkov photons on the coincidence time resolution	94

4.4	Summary and Discussion	96
4.5	Experimental evaluation of a multi-timestamp approach for improvement of the timing performance of scintillation detectors	98
4.5.1	Influence of the trigger threshold	98
4.5.2	Multi-timestamp approach	101
5	Cherenkov effect at low energies: proof of principle measurement	105
5.1	Proof of principle using PMTs	105
5.2	Cherenkov photon detection using SiPM	107
5.2.1	Setup	108
5.2.2	Reference measurement using 3 mm cubes of LSO:Ce	109
5.2.3	Reference measurement using a 8 mm long LSO:Ce rod	111
5.2.4	Coincidences with pure Cherenkov radiators	112
5.2.5	CTR with pure Cherenkov radiators	115
5.2.6	Hybrid Cherenkov radiators	119
5.3	Discussion and Conclusion	122
6	Outlook	125
7	Appendix	127
7.1	New approaches for improvement of TOF-PET	128
7.2	Studies on the Cherenkov effect for improved time resolution of TOF-PET	132
7.3	Time resolution below 100ps for the SciTil detector of PANDA employing SiPM	137
7.4	Time resolution below 100ps for the SciTil detector of PANDA employing SiPM	148
7.5	Efficiency and uniformity measurement of a light concentrator in com- bination with an SiPM array	154
7.6	Oversaturation behaviour of SiPM at high photon exposure	158
7.7	Leaflet Philips DPC	166
7.8	Datasheet Saint Gobain optical grease BC-630	169
8	Gloassary	171
	Bibliography	173

CONTENTS

1

Introduction

Positron emission tomography (PET) is a noninvasive medical imaging method that uses radioactive substances injected into patients to obtain quantitative images of the body and its metabolism. PET information complements that from computed tomography (CT) and nuclear magnetic resonance (MR) imaging, both of which provide mainly anatomical information. PET, and the combination of PET and CT as well as PET and MR, help diagnose various oncological diseases and provide a routine option for assessing the response to chemo or radiotherapy. Improvements in PET detector technology allowed the utilisation of time-of-flight (TOF) information, which results in an improvement of the signal-to-noise ratio (SNR) of PET images. Subsequently, the image quality is increased and the quantification of tracer uptake and medical diagnosis can be improved.

1.1 Positron emission tomography

In medical imaging the objective is to obtain an image of a region of the body with, e. g. enhanced metabolism (such as tumour tissue). The basic principle of PET, and nuclear medicine in general, is the tracer principle where a trace amount of a radioactively labeled biomolecule is injected into the body and its metabolic pathways are followed and described quantitatively by measuring the emitted radiation noninvasively. A conventional PET system consists of a ring of s (scintillators mounted to photomultiplier tubes - PMTs) that measures the (two) photons created from the annihilation of a positron and an electron following the β^+ decay of positron emitting nuclei (e.g., ^{18}F

1. INTRODUCTION

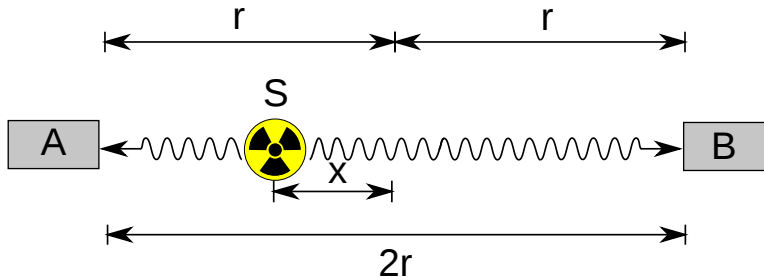


Figure 1.1: Schematic drawing of the TOF-PET principle. A and B are the photo detectors, S the source of the 511 keV annihilation photons, $2r$, the distance between the photo detectors and x the distance of the source to the centre between the photo detectors.

in medical applications, e.g. ^{22}Na for laboratory tests). These photons are emitted almost back-to-back ($\approx 180^\circ$) with an energy of 511 keV each. The detection of two unscattered photons within a fixed time window the coincidence time window (CTW) defines a valid (true) coincidence event. Since the annihilation photons are emitted back-to-back, the origin of each of the photons must be located along a line connecting the two detectors. This connecting line is called the line of response (LOR) and is defining a projection. The final tomographic image is reconstructed after collecting emission data for multiple projections. However, not only true events are detected inside the CTW, also Compton scattered and random coincidences can occur, leading to a decreased signal-to-noise ratio (SNR) and, thus, inferior image quality.

1.2 Time-of-flight PET (TOF-PET)

Under ideal conditions, the emitted positron annihilates with an electron and the resulting two annihilation photons are detected. The source of radioactivity is located somewhere along the LOR. However, the exact location along the LOR is not known. Since the two annihilation photons travel at the speed of light, different lengths of the flight paths will lead to different arrival times at the respective detector. This difference in time of arrival (t) is related to the position of the positron source by $t = \frac{2x}{c}$, where x is the distance of the source from the centre of the scanner and c is the speed of light, see figure 1.1.

The main limiting factor in TOF is the uncertainty in the measurement of the arrival time of the two photons (Δt), leading to an uncertainty of the spatial localisation of the source (Δx) along the LOR, which can be written as $\Delta x = c \frac{\Delta t}{2}$.

1.3 Status of research - state-of-the-art systems

During the reconstruction process, the timing resolution Δt is used for defining a localisation probability function with a width defined by Δx , constraining the location of the source to a small part of the LOR (1). This improves the statistical properties of the data by reducing noise, leading to an increased SNR and, thus, improved image quality. For a subject with 40 cm diameter in a TOF-PET with $\Delta t = 500$ ps timing resolution and, thus, 7.5 cm spatial resolution, the SNR is increased by a factor of approximately 2 (2). The benefit gained by using TOF information has been addressed by many research groups (1; 2; 3; 4; 5). At present, photomultiplier tubes (PMTs) coupled to scintillators are the detector system of choice in TOFPET systems. Since timing resolution is the key parameter for a TOFPET system, improvement in dedicated detector technology is an active field of research.

1.3 Status of research - state-of-the-art systems

In recent years, commercially available PET systems with TOF capabilities were presented by all major manufacturers: Philips (Gemini TF), Siemens (Biograph mCT) and General Electric (Discovery 690), with time resolutions in the range from 500 ps to 600 ps.

A first commercially available PET system based on solid state photo detectors (avalanche photo diodes - APDs) is included in the hybrid PET/MR Biograph mMR developed by Siemens. However, due to the limited timing resolution of APDs (few ns), the mMR does not incorporate TOF capabilities. An overview on the different commercial PET/MR systems (APD and PMT based) can be found in reference (6).

Due to their insensitivity to magnetic fields, several groups are investigating the feasibility of the integration of silicon photomultipliers (SiPMs) into PET. An example is the HYPER Image collaboration, funded by EU-FP7 (7), which developed the PETA chip for SiPM readout (8). Different approaches of using SiPMs for PET are provided by the AX-PET collaboration (9; 10) or the ENDO-TOFPET-US project funded by FP7, aiming at a timing resolution of 200 ps (11). The utilisation of monolithic crystals and arrays of SiPMs with depthofinteraction capabilities is also investigated (12; 13).

The state of research on prototype coincidence detectors is more advanced and coincidence time resolutions (CTR) below 100 ps have been achieved (4; 13; 14; 15; 16). The ultimate goal of many of these research projects is to leverage TOF-PET in new

1. INTRODUCTION

Isotope	Half life [min]	maximum kinetic energy [keV]	positron range FWHM [mm]
^{11}C	20.4	385	0.19
^{13}N	10	491	0.28
^{15}O	2	735	0.5
^{18}F	109.8	242	0.1

Table 1.1: Properties of positron emitting isotopes used for nuclear imaging (17; 18).

PET/MR combinations and/or approach limits where the TOF information could be utilised for direct image reconstruction.

1.4 Electron-positron annihilation

Positron Emission Tomography is based on the property that after electron-positron annihilation the two 511 keV annihilation-photons are emitted in an angle of almost 180° . By this fact the line of response can be drawn if a coincidence of two photon detectors is recorded. Frequently used positron emitting isotopes are ^{11}C , ^{13}N , ^{15}O or ^{18}F . In the laboratory often ^{22}Na or ^{68}Ga as product from the decay of ^{68}Ge are used as positron emitters. Typical values for half lifes and positron ranges are given in table 1.4.

1.5 The Cherenkov effect

A radiation which later became the name Cherenkov radiation was already predicted by Heaviside in the years 1888-1889 (19). First observations dedicated to this kind of luminescence were already done by Marie Curie in 1910. Attempts to study the phenomenon were made by Mallet in the late 1920s. Cherenkov commenced exhaustive studies on the observations in the years 1934-1938. During this time Frank and Tamm proposed a first description of the effect. Shortly after that, Ginsburg developed a quantum theory of the hence called Cherenkov radiation in 1940. By invention of the photomultiplier tube in 1944 the effect was further studied and was used for an increasingly number of radiation detectors. In 1958, Cherenkov shared the Nobel prize with Frank and Tamm for their work on this kind of luminescence. Until today utilisation of Cherenkov radiation is an important method in high energy physics (20).

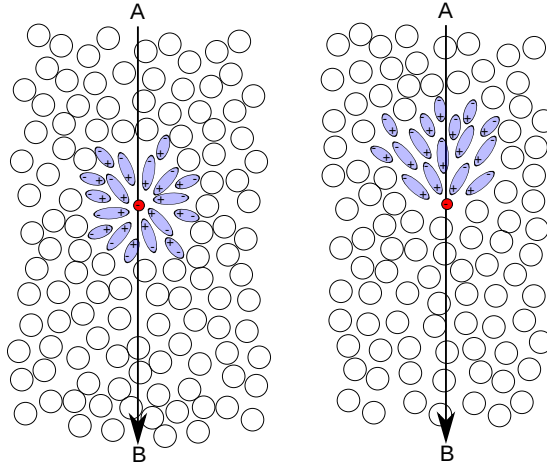


Figure 1.2: Polarisation by an electron in a dielectric material at low velocity at the left hand side and at high velocity at the right hand side (20).

Qualitative description of the effect Supposing a charged particle moving from point A to B (see figure 1.2) in a dielectric medium at relatively low speed. The circles in the figure represent atoms of the medium, e.g., glass. The charged particle, here an electron, is located at point P and the electric field of the particle polarizes the medium around by displacing the electrons of the medium. When the particle moves further, the polarized atoms return to their normal shape. When the atoms are distorted, they behave like elementary dipoles. Thus, as the particle passes the medium, each atom receives a brief electromagnetic pulse. Due to the symmetry of the polarisation field surrounding the electrons, there is no resulting field observable at larger distances and therefore no radiation (20).

If the particle is propagating through the medium at a speed faster than the speed of light in the medium, the polarisation field is no longer symmetric and a resulting dipole field is present along the the particle track. Such a field is momentarily set up by the electron at each element along the track and in turn each element radiates a brief electromagnetic pulse. Usually, these wavelets interfere destructively at a distant point. If the particle velocity is larger than the phase velocity of light in the medium, the wavelets can interfere constructively resulting in a field at a large distance.

The radiation can be observed at the Cherenkov angle θ with

$$\cos \theta = \frac{1}{\beta n} \quad (1.1)$$

1. INTRODUCTION

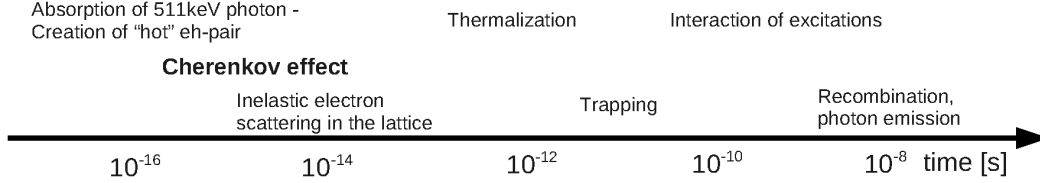


Figure 1.3: Time line of relaxation processes in inorganic scintillators following the interaction of a 511 keV photon by the photoelectric effect.

With c being the speed of light in vacuum βc is the speed of the particle and n is the refractive index of the medium. For a medium with the refractive index n , the threshold velocity for Cherenkov emission is $\beta_{\min} = 1/n$. The radiation mainly occurs in the visible and near UV-spectrum of light for $n > 1$ (20).

The classical description by Frank and Tamm and the quantum theory of the effect by Ginsburg can be found in (20).

1.6 Cherenkov photons for TOF-PET

As discussed, if a charged particle with a velocity v is faster than the speed of light c/n in nonconductive matter (n is the refractive index, c the speed of light in vacuum), Cherenkov radiation can be emitted. In inorganic scintillators, as they are used for PET, scintillation photons are emitted after the interaction of a 511 keV annihilation-photon with the scintillator, leaving an inner shell hole and an energetic primary electron. This is followed by a cascade of energy relaxation processes: radiative (secondary Xrays) and nonradiative decay (Auger processes), inelastic electron-scattering in the lattice, thermalization, electron-phonon interactions, trapping of electrons and holes and energy transfer to luminescent centers. All these processes contribute to an additional time spread of the emission of scintillation photons (21; 22; 23). Since Cherenkov photons are emitted during the phase of electron scattering already, most of these processes are bypassed and hence they are emitted almost instantaneously with a precise time stamp compared to scintillation photons, see figure 1.3 (22). This precise time stamp leads to an improved timing resolution and finally results in a better SNR. The gain of improving time resolutions for TOF-PET in terms of SNR was determined in (1) for the example of a patient of 40 cm in diameter and is shown in table 1.6.

Time resolution Δt [ns]	Δx	TOF SNR gain
2.7	40	1
1.2	18	1.5
0.6	9	2.1
0.3	4.5	3
0.1	1.5	5.2

Table 1.2: SNR gain of the TOF method for PET for various time resolutions for a patient with 40 cm in diameter (1).

1.7 Motivation

PET and TOF-PET are well established medical imaging modalities. Nevertheless, the technology is still part of extensive research and parameters like spatial resolution, energy and time resolution have not reached the limits of physics. Furthermore, the desire to develop multimodal medical imaging devices like PET/MR pushes the research in this field. First of all, the motivation of this thesis is to investigate the potential of the Cherenkov effect for application in TOF-PET and other scintillation applications in terms of timing. Furthermore, silicon photomultipliers (SiPM) are potential candidates for replacing PMTs in TOF-PET as standard photo detectors and for application in PET/MR, due to their good timing characteristics and other features like insensitivity to magnetic fields. Therefore, the major part of the experimental investigations will be based on photon detection with SiPM.

Detection of Cherenkov photons at the energy regime of PET is challenging, as the photon yield of the Cherenkov effect is very small. Nevertheless, successful application of this very fast effect could allow significant improvement not only for TOF-PET but could also have impact on timing detectors in particle physics struggling with low photon yields. One example is the PANDA barrel DIRC which is expecting very low photon yields (24; 25). Within the work on this thesis a 64-channel SiPM detector for investigations on the replacement of MCPs at the PANDA barrel DIRC was developed and characterised (26; 27). Furthermore, the PANDA SciTil detector requires time resolutions below 100 ps (28). Also for this detector studies were done within in PhD work (29). A further example of application in the investigated energy range is the positron annihilation lifetime spectroscopy (PALS) for research on material defects in, e.g, semiconductors. For such applications typical time resolutions lie around 200 ps and

1. INTRODUCTION

improved time resolution would allow to investigate material properties more accurate.

2

Materials and theory

2.1 Scintillation detector

As discussed, in this thesis a focus on fast detection of γ -photons at low energies is put. By low gamma-photon energies, the energy range of photons created by e^+/e^- annihilation is understood which have an energy of 511 keV. A typical scintillation detector for this kind of radiation consists of a scintillator, a photodetector and readout electronics, see figure 2.1. The incoming γ -photons are absorbed in the scintillator and their energy is converted into optical photons. A photodetector is coupled to the scintillator and converts the arriving optical photons into an analog electric signal. This signal is then amplified and digitized by the readout electronics which provides time- and energy information about the initial γ -photon interaction in the scintillator.

Requirements to such kind of detectors are high detection efficiency, high energy resolution and a good time resolution. Dependent on the application, the scintillation detector is usually designed in favour of one of these parameters. For PET, high detection efficiency is desired to decrease the applied dose for the patient and to decrease the measurement time of the investigation. Furthermore, energy resolution is desired to a certain extend for distinguishing true from scattered coincidences and therefore is needed to increase the signal-to-noise ratio (SNR). For TOF-PET additionally, a good timing performance for localisation of the point of annihilation between two responding detectors and thus increase of the SNR is desired.

2. MATERIALS AND THEORY

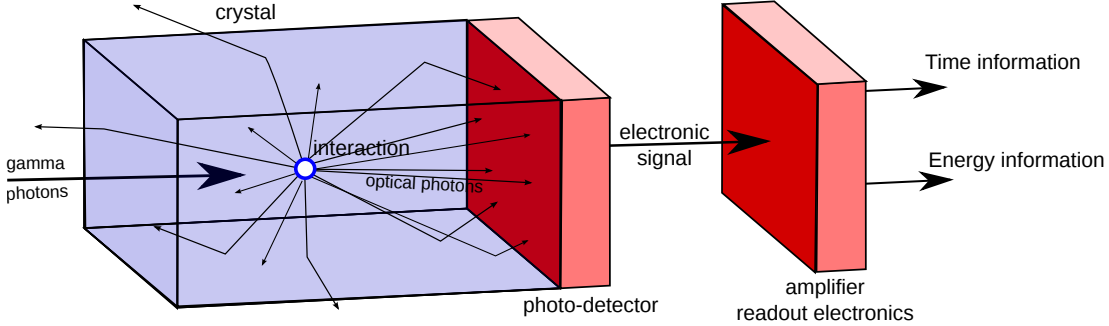


Figure 2.1: Schematic of scintillation detector for gamma detection. A gamma-photon interacts inside a scintillator followed by emission of scintillation photons in the optical wavelength range. The photons propagate through the crystal and some get detected by a photodetector. The induced charge signal is usually amplified and converted to a digital signal in the readout electronics providing the time and energy information of the gamma photon interaction.

2.2 Scintillators

A scintillator can be defined as wavelength-shifter, which converts photons at short wavelengths (high energy) into many photons with longer wavelengths (low energy), i.e. light in the optical region for many cases (30; 31). The interaction of γ -photons in the keV-range with a scintillation material is mainly caused by photoelectric absorption and Compton scattering. Other processes like Rayleigh- and Thompson scattering are dominant at lower energy regions, whereas pair production occurs at energies above 1022 keV with increasing probability dependent on the energy of the γ -photon. Mass absorption coefficients for LSO and BGO are shown in figure 2.2 on the left and on the right hand side, respectively.

The intensity I , of γ -radiation passing a material with the thickness x , can be described by,

$$I(x) = I_0 e^{-\mu x} = I_0 e^{-\frac{\mu}{\rho} \rho x} = I_0 e^{-\frac{x}{\lambda}}, \quad (2.1)$$

with the initial intensity of the γ -radiation I_0 , the attenuation coefficient μ , the mass absorption coefficient $\frac{\mu}{\rho}$, the density of the material ρ and the attenuation length λ . As one can see, the interaction of γ -radiation is dependent on the density of the material, therefore, high density scintillators are preferred for γ -photon for calorimetric measurements.

For the case of photoelectric absorption, an incoming γ -photon is completely ab-

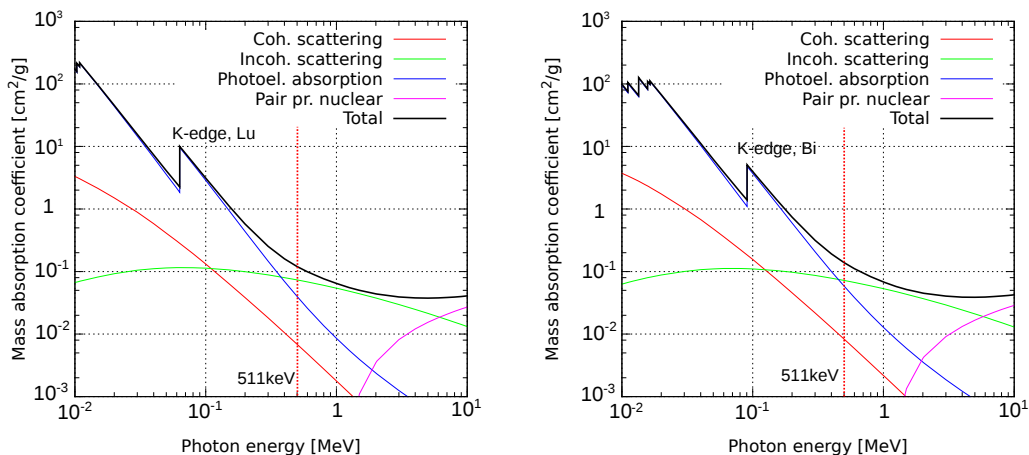


Figure 2.2: Mass absorption coefficients for LSO (left) and BGO (right). Data calculated with (32).

sorbed by an electron which is bound to an atom in the material. Dependent on the energy of the γ -photon, E_γ is usually sufficient to ionize the atom and free the electron having a kinetic energy of $E_{e^-} = E_\gamma - E_b$, with E_b being the binding energy of the electron. The probability for photoelectric interaction in the energy of 511 keV can be approximated by (33),

$$\sigma_{\text{photo}} \cong \text{const.} \cdot Z^5 \left(\frac{m_e c^2}{E_\gamma} \right)^{7/2}, \quad (2.2)$$

with the atomic number of the material Z and the rest mass of the electron $m_e c^2$.

Scintillation is a form of luminescence, which can be described as light emission due to excitation of electron states by radiation (31). It can be separated depending on their emission time into fluorescence (10^{-8} s) and phosphorescence (μs to hours), with scintillation being a form of fluorescence. The scintillation mechanism in inorganic scintillators can be described by five steps (31; 34):

- **Absorption** of a high energy photons and creation of an inner shell hole and an energetic electron (here called hot electron),
- **Carrier multiplication:** electron and hole multiplication due to energy transfer by radiative decay (secondary X-rays), Cherenkov effect, nonradiative decay (Auger processes), inelastic electron-electron scattering (ionisation),

2. MATERIALS AND THEORY

Scintillator	BGO	LSO	LuAG	PWO
Composition	$\text{Bi}_4\text{Ge}_3\text{O}_{12}$	Lu_2SiO_5	$\text{Lu}_3\text{Al}_5\text{O}_{12}$	PbWO_4
Density	7.13	7.4	6.73	8.28
Refractive index	2.15	1.82	1.84	2.2
Z_{eff}	75.2	66	62.9	76
Att. length for photons at 511 keV	1.1	1.1	1.3	0.9
Probability PE	40	32	27	43
X_0	1.12	1.14	1.41	0.89
Light yield	700/7500	3000	3720	210
Decay time [ns]	60/300	40	61/470	5/15

Table 2.1: Properties of inorganic scintillators used in this thesis (4; 17; 30; 32; 36; 37; 38; 39; 40). Z_{eff} is the effective atomic number for the compound, PE is the photoelectric effect and X_0 is the radiation length.

- **Thermalisation:** as the energies of the electrons and holes fall below the energy threshold for ionisation, the carrier multiplication stops and thermalisation of e-h pairs takes places by intra-band-transitions and interactions with photons. These three processes are the major factors influencing the rise time of such scintillators (35),
- **Localisation:** energy transfer to luminescent centres,
- **Luminescence:** recombination of the e-h pairs by emission of scintillation photons.

Main prerequisites to scintillators used in PET are, a high probability for the photoelectric absorption, short time constants (decay time τ_d , rise time τ_r) and a high light yield. A scintillator used for a long time in PET was Bismuth Germanate (BGO), which was replaced by Lutetium Orthosilicate (LSO) in recent years due to its better time and energy resolution (1). The scintillators investigated in this thesis are BGO, LSO doped with Ce, Lutetium Aluminum Garnet (LuAG) undoped and doped with Ce and Lead Tungstate (PWO). In table 2.2 an overview of scintillation parameters is given.

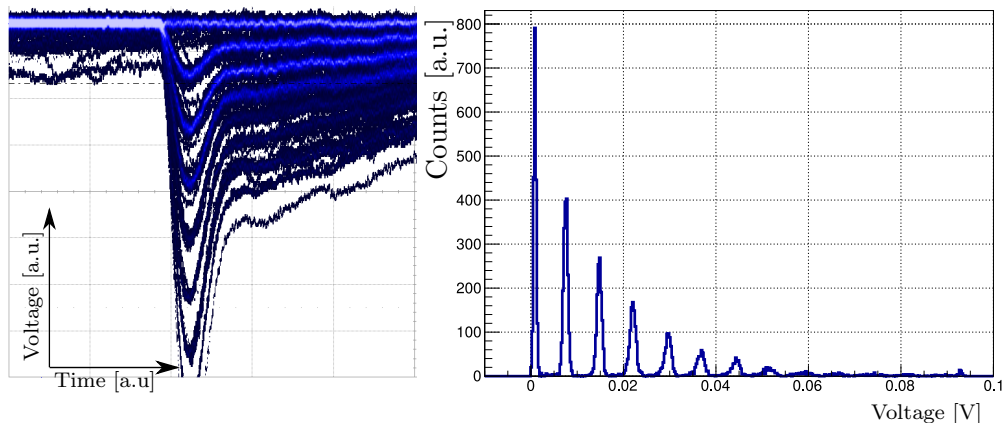


Figure 2.3: On the left hand side: typical signal of a 3×3 mm large SiPM, after amplification, read out via 50Ω . On the right hand side, the resulting amplitude spectrum of the signal is displayed.

2.3 Silicon photomultipliers (SiPM)

In many applications photomultiplier tubes or microchannel plates are used for photon measurements in scintillation detectors. In recent years, in some of these applications these detectors are replaced by silicon photomultipliers, due to some of their advantages, such as, good timing characteristics and insensitivity to magnetic fields SiPM are used in this work for most of the measurements.

2.3.1 Analog SiPM

Silicon photomultipliers or Geiger-mode avalanche photodiodes (GM-APD) are made of p-n junctions operated above breakdown voltage. In this operation mode, the electric field in the depletion zone is so high, that a single charge carrier is capable of triggering a self-sustaining avalanche. SiPMs usually consist of a bulk material made of Silicon with varying dopand concentrations (41; 42). Although, the mechanism was already studied in the 1960s (43; 44), devices making use of this effect were developed in the 1990s (45). The reason for this long lasting development was the nature of the detection process: only a single photon is capable of triggering a self sustaining avalanche, which makes devices working in the Geiger regime insensitive to the number of detected photons. This problem has been overcome by arranging arrays of small photodiodes,

2. MATERIALS AND THEORY

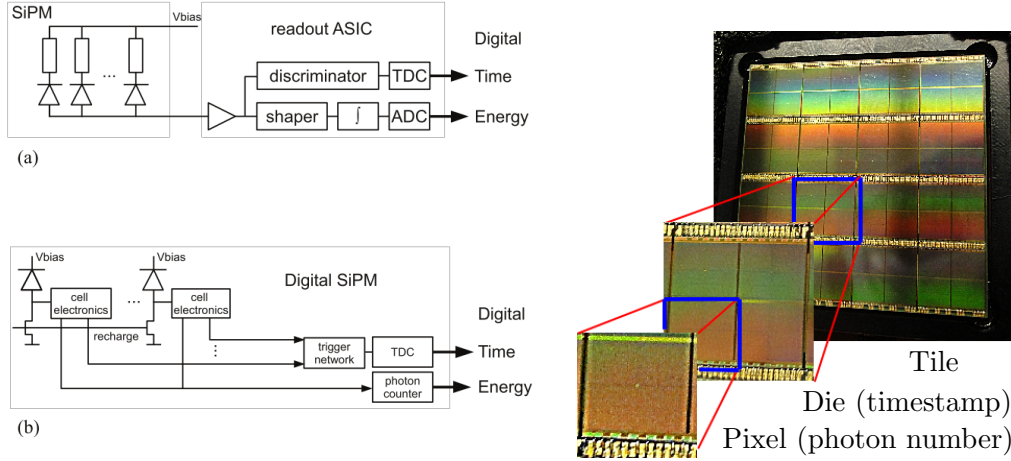


Figure 2.4: On the left: schematic drawings of composition and readout of analog SiPM (a) and the DPC (b) (46). On the right hand side, the structure of the DPC is shown: the whole sensor (tile) is composed of 16 independent dies. Each die again is composed of 4 pixels, which provide the photon numbers per pixel. The 4 pixels share a common trigger network, resulting in one common timestamp per die.

with sizes in the range of $\sim 10 - 100 \mu\text{m}$. These small photodiodes are also called single photon avalanche diodes (SPADs) and are connected in parallel. As the avalanches are self-sustaining, the photodiodes need to be quenched, which is done using a resistor connected in series with each photodiode. The signal itself is read out via a common anode and is usually amplified and readout using modular devices like time-to-digital converters (TDC) and charge-to-digital converters (QDC) or application-specific integrated circuits (ASIC). In recent years many different designs of SiPM were presented and produced by a large variety of manufacturers.

2.3.2 Digital SiPM

SiPMs are analog devices, when looking at the individual SPADs, however, they are working quasi digital: they give a current signal when a photon is triggering an avalanche (1) or they do not (0). As a consequence, research for implementation of the quasi digital behaviour towards the development of digital SiPM is going on (47; 48). So far, the only commercially available digital SiPM is the Digital Photon Counter (DPC) by Philips (46).

In the case of the Philips DPC, each SPAD is connected to individual cell elec-

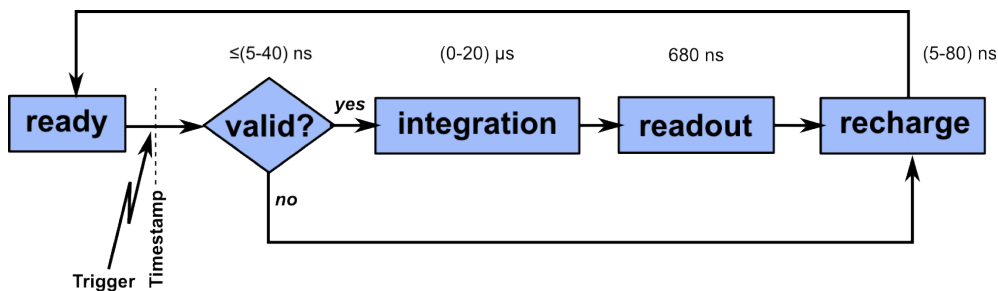


Figure 2.5: Time sequence of the Philips DPC acquisition scheme (49).

tronics before the data is readout, which allows to drive the device without additional preamplifiers. Figure 2.4 shows a schematic comparison of an analog device including amplification and readout electronics and the structure of the DPC including electronics (46).

A DPC-tile has a size of $32.6 \times 32.6 \text{ mm}^2$, and is composed of 16 independent dies with sizes of $7.15 \times 7.875 \text{ mm}^2$. Each of these dies again is composed of four pixels with sizes of $3.2 \times 3.8775 \text{ mm}^2$. The pixels themselves consist of either 6400 or 3200 SPADs. Depending on the model of the DPC, the SPAD size is of $59.4 \times 64 \mu\text{m}^2$ for the DPC3200 and $59.4 \times 32 \mu\text{m}^2$ for DPC6400, see appendix 7.7.

Acquisition scheme The DPC records triggers in frames, which represent temporal loops, similarly to Charge-Coupled Devices (CCD), see figure 2.5. Each die can be seen as independent sensor and provides one timestamp and 4 photon counts (for each pixel) per valid readout cycle. From beginning of a frame, the sensor is waiting for a trigger, i.e., a fired cell. When a cell is fired, the timestamp is generated and a validation scheme is started. The change into the validation mode lasts ~ 2 clock cycles (10 ns) and the validation mode can be set to 5 - 40 ns. In this mode, the sensor records the number of arriving triggers. At the end of the validation window an event gets validated, if a certain validation threshold (1, 2, 4, 8 photons for the DPC3200 and 4, 8, 16, 32 photons for the DPC6400) is exceeded. If this is not the case, all cells are immediately recharged (5 - 80 ns) and a new frame is started. In the case an event is valid the sensor switches into integration mode (0 - 20 μm). After the integration interval a readout sequence is started (680 ns) and subsequently the recharge and a new frame is started.

2. MATERIALS AND THEORY

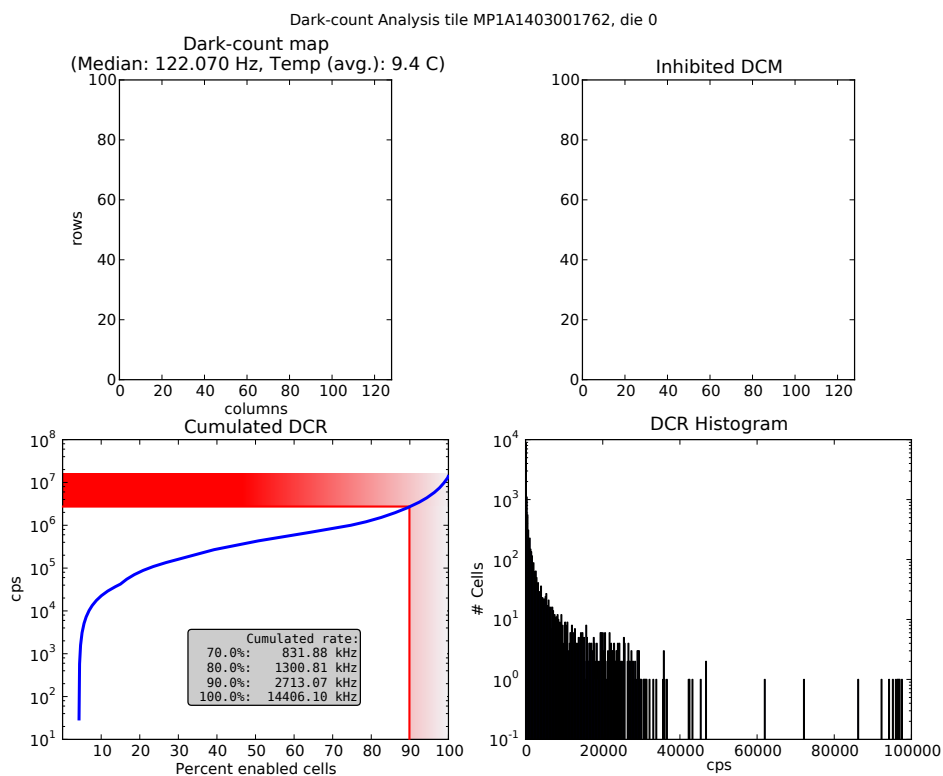


Figure 2.6: On the top left an example of a dark count map of a DPC3200 measured at 9.4°C is shown. Red and green points indicate SPADs with very high dark count rates and can be turned off individually. The top right plot shows the darkcount map after 10% of the most active cells are deactivated (white points). On the bottom left the cumulated darkcount rate (DCR) is plotted as a function of the enabled cells. The red surfaces show the impact on the DCR, when 10% of the cells are turned off. On the bottom right a histogram of the DCR is shown. It can be seen that the majority of the SPADs have a low DCR, whereas a few cells have a extremely high rate of 20 kHz and more.

For generation of the timestamp various trigger schemes can be set (1 - 4). These trigger schemes represent logic settings between sub-pixels and pixels of the sensor. Trigger scheme 1 is a setting where the timestamp is formed by the first photon arriving at the sensor. In the following measurements, this setting was usually used unless otherwise mentioned. The main reason was, that for this scheme the sensor triggers on the first arriving photon, whereas all other trigger schemes need a probable amount of photons until the timestamp is formed due to a logic circuitry and therefore, no definite number of photons for formation of the timestamp can be determined.

The validation mode can be deactivated (validation interval = 0), which was used for the measurements on the time resolution in the regime of lower photon numbers. Furthermore, the integration interval was set to 0 ns to minimise the influence of dark-counts on the resulting photon counts.

Handling of dark-counts Every SPAD of the DPC can be addressed individually and turned off or on. As a high fraction of dark-counts of the whole sensor is often caused just by a few bad SPADs, the feature of activating single cells allows to measure a darkcount map. For this map each single cell is turned on separately, while all others are turned off. This way a map showing the darkcount rate (DCR) for each cell can be measured. Using the resulting darkcount map (DCM) the SPADs with the highest individual darkcount rates can be determined and be deactivated for measurements. A typical DCM is given in figure 2.6 on the top left side. On the top right side of the same figure a dark count map after turning off 10% of the most active cells is shown (inhibited DCM). On the bottom left the cumulated DCR is plotted against the percentage of enabled cells. The red bars show the impact on the overall DCR when 10% of the most active cells are deactivated. In the bottom right plot of the same figure, the number of cells is plotted against the DCR per cell. It can be seen that most of the cells have a DCR of a few counts per second (cps), but a few cells are responsible for a large fraction of the overall DCR.

Due to the different architecture (no preamplifier, larger sensitive area, digital output) of the DPC compared to analog devices, its time resolution was studied using a different setup than for the analog SiPMs.

2. MATERIALS AND THEORY

3

SiPM for fast single photon detection

A comparative timing performance study of analog SiPM and digital SiPM from several vendors was performed. Motivation for this test was on one hand, achieving a time resolution of 100 ps at the PANDA scintillation tile hodoscope, described in (28; 29) and investigations on the potential of replacing microchannel plates (MCP) for photon detection by SiPM for the PANDA barrel DIRC (24; 25), on the other hand. Furthermore, application of the fastest available SiPM for coincidence setups within the research on the Cherenkov effect and TOF-PET was a reason for measurements presented in this chapter.

3.1 Development of a multichannel SiPM detector

Results of this section were part of this PhD work and have been published partly in (26; 27), see also appendix 7.4 and 7.5.

SiPM usually have very small sensitive areas ($\sim 1\text{-}30\text{ mm}^2$) compared to the established PMTs or MCPs with sensitive areas in the range of cm^2 . Therefore, arrays of analog devices with common readout electronics were developed, in recent years. Within the work on this thesis a multichannel SiPM detector with enhanced sensitive area was developed and is presented in the following:

3. SIPM FOR FAST SINGLE PHOTON DETECTION

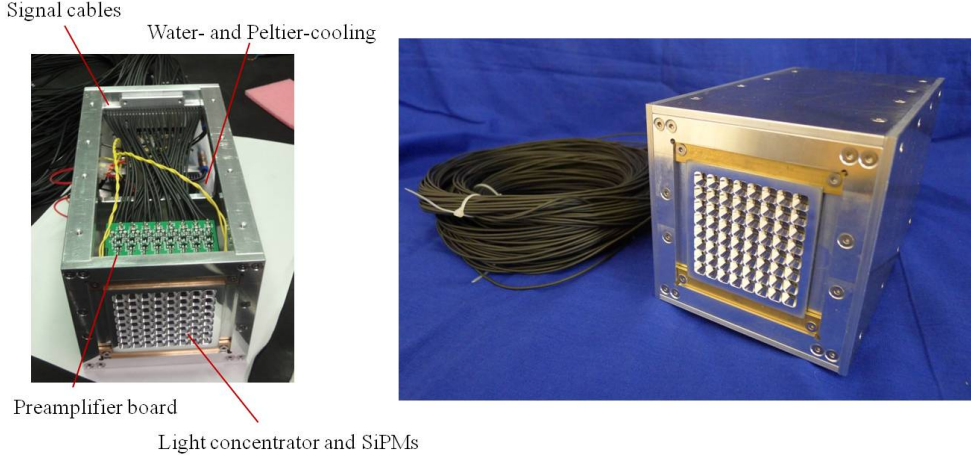


Figure 3.1: Developed multichannel SiPM detector with enhanced sensitive area (26). See appendix 7.4.

Motivation The multichannel SiPM detector has been developed as option for the barrel DIRC detector which will be part of the PANDA detector at the FAIR facility in Darmstadt, Germany (24; 25). Requirements for this detector were sensibility to single photons, good time resolution and operation in magnetic fields. At the time of development of the prototype (2009-2010) MCPs were the proposed detectors, but their lifetimes at the expected photon rates was not sufficient. Therefore, the potential of SiPM for their replacement was studied by development of the multichannel SiPM detector (26; 50).

Design parameters The detector consists of an array of 8×8 SiPMs (Hamamatsu S10931-100P), each with a size of $3 \times 3 \text{ mm}^2$ and a pitch of 7 mm. The area in between the individual SiPM was covered with a light concentrator in order to enhance the sensitive area. The entrance window of each funnel was $7 \times 7 \text{ mm}^2$ and 4.5 mm deep with an exit surface of $3 \times 3 \text{ mm}^2$. The efficiency of the light concentrator was investigated partly within in this PhD work, see (27) and appendix 7.5.

For signal readout 4 amplifier boards, each with 16 channels were developed. Each individual preamplifier channel was based on the Photonique AMP-0611 with some modifications for shorter signal rise times. The whole detector was placed in an Aluminum housing including water- and Peltier-cooling for temperature stabilisation and had a Nitrogen inlet to avoid condensation of water.

The development, design and testing of the multichannel SiPM array was part of this PhD thesis and the results have been published in (26; 27), which can be found in appendix 7.4 and appendix 7.5.

3.2 Time resolution measurements of analog SiPM

Measurements and results of this section have been published partly in (29) and can be found in appendix 7.3. The results presented here were part of the author of this thesis.

3.2.1 Setup

A semi-automatic test-stand for determination of the single photon time resolution (SPTR) of various SiPM was developed and installed. Compared were SiPM from AdvanSiD, Ketek and Hamamatsu. For determination of the SPTR, the setup was equipped with a picosecond laser (PIL040) from Advanced Laser Diode Systems emitting laser pulses of 30 ps FWHM at a wavelength of $\lambda = 404$ nm (for a scheme of the setup, see figure 3.2). The emitted laser pulses were split into two paths using a semi-transparent mirror, with one path directed onto an AdvanSiD-3SP50 SiPM with an active area of 3×3 mm². This SiPM was driven in saturation, which means, at such a high light intensity that all SPADs were firing at every laser pulse. The signal of the SiPM was directly connected to one input of a LeCroy WavePro 735 Zi digital oscilloscope without any amplification. As the sensor was driven in saturation the signal was so large that no amplification was needed and the signal was not further deteriorated by the use of a preamplifier. Using this saturation-mode, a fast reference signal could be provided. In a first measurement, the achievable time resolution of the trigger output provided by the laser driver was compared to the reference signal coming from the fully illuminated SiPM, which resulted in a better time resolution obtained using the SiPM signal.

The second light-path, after the laser-beam was split (figure 3.2), passed a variable optical attenuator before it was coupled into an optical fibre of 1 m length. This fibre was led into a air-tight box which was filled with Nitrogen in order to avoid condensation of water on the electronics and provide thermal conductance. Before the box was flooded with Nitrogen, the humid air inside was evacuated. The Nitrogen filled box contained a smaller, RF-shielded box, in which the tested SiPM and the preamplifier

3. SIPM FOR FAST SINGLE PHOTON DETECTION

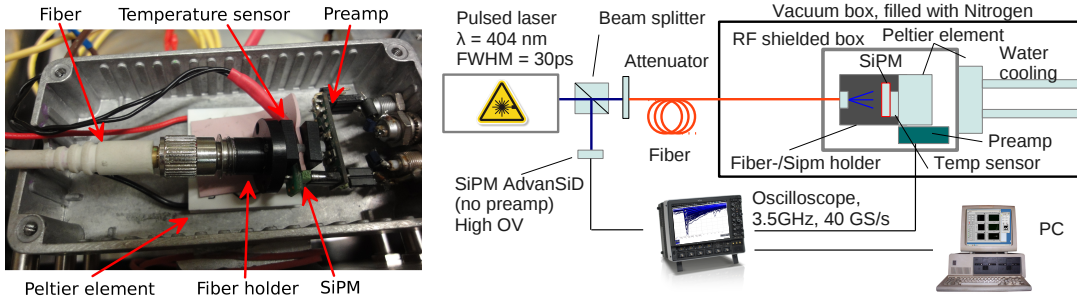


Figure 3.2: On the left hand side, a picture of the installation inside the RF-shielded box can be seen (29). On the right hand side, a schematic of the whole measurement setup is drawn.

Manufacturer	AdvanSiD	Hamamatsu	Ketek		
Type	SiPM3S	S10931	PM3375	PM3360	PM3350
	P-50	-100P	-B72	-A2	-B63
Total size [mm ²]	3×3	3×3	3×3	3×3	3×3
SPAD size [μm]	50	100	75	60	50
Optical trenches	no	no	yes	no	yes
Breakd. vol. [V]	≈ 35	≈ 70	≈ 23	≈ 23	≈ 23
Darkc. rate [MHz]	≤ 45	≤ 12	≤ 4.5	≤ 4.5	≤ 4.5
Gain [×10 ⁶]	2.5	2.4	~ 14	~ 9	~ 6
PDE at peak sens. [%]	22	> 70*	> 62	> 39	> 50
Microcell. cap. [fF]	-	~2800	650	380	270

Table 3.1: List and sensor parameters of the tested devices taken from the data sheets of the manufacturers (29). *PDE is overestimated, because the measurement method includes cross-talk and afterpulses.

were mounted. The optical fibre was coupled to the SiPM using a holder, which kept the fibre at a defined distance for illumination of the whole sensitive area of the sensor. The SiPM electrodes were connected to a preamplifier AMP-0611 from Photonique. For minimization of noise due to the resistance of the connection, the distance between SiPM and preamplifier was kept as short as possible (a few mm). After amplification, the signal was fed into the LeCroy WavePro 735Zi digital oscilloscope, which provided a bandwidth of 3.5 GHz and a sampling rate of 40 GS/s. For control of the SiPM temperature, a temperature sensor (Pt100) was mounted directly beneath the SiPM. The sensor itself was thermally coupled to a Peltier element which again was coupled to a water cooled metal finger. A picture of the setup and a schematic are shown in figure 3.2.

3.2 Time resolution measurements of analog SiPM

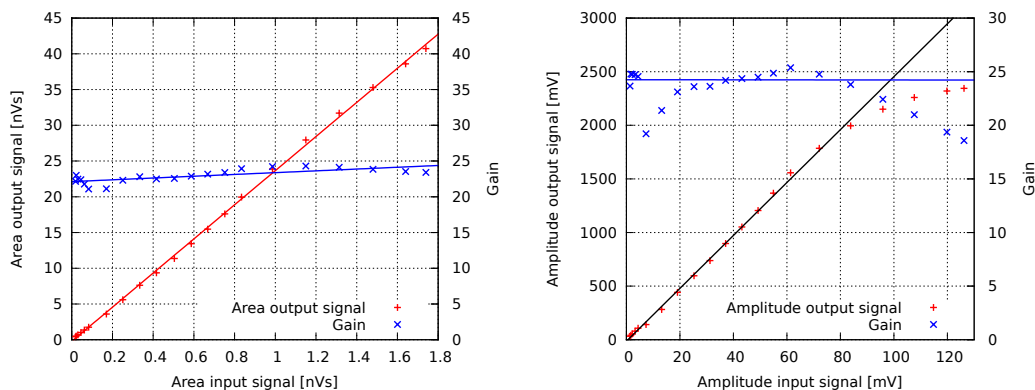


Figure 3.3: Linearity of amplification and gain of the Photonic AMP-0611 preamplifier for measuring the area of the pulse, on the left hand side, and for measuring the amplitude on the right hand side. The lines represent linear regressions of the data points. For the black colored regression only the data in the range of 0-55 mV was considered. Within this range the measurements on the TR were done. The error bars are within the data points.

The measurement was performed by a LabVIEW program which controlled the SiPM bias voltage, the Peltier elements, readout and stored the data of the digital oscilloscope and other parameters. During a measurement, the bias voltage, the provided current, the temperature, the time difference of the trigger signal and the SiPM signal at 50% of the amplitude level (Δ delay), the rise-/fall-time (10-90%), the amplitude and the area of the signal were recorded.

An usual measurement was run at 4 temperatures (-10°C , 0°C , 10°C , 20°C) with an accuracy of $\pm 0.1^\circ\text{C}$. The program ramped the bias voltage from the breakdown voltage in defined steps up (0.1-0.5 V), until a defined current limit (usually 8-10 μA) was reached. At each step several thousand events (triggers) were recorded. After that a new temperature was set and the measurement restarted.

Preamplifier linearity The gain of the AMP-0611 preamplifier from Photonique, used in this setup, was determined using a pulse generator, which provided defined input pulses. The signal was split into two lines with one leading directly to the digital LeCroy WavePro 735Zi oscilloscope and the other to the preamplifier. After amplification the signal was connected to another channel of the oscilloscope and the area and the amplitude of the signals were measured in order to compare the original and the amplified signal. The results and linear fits (parametrisation: $y(x) = kx + d$) of

3. SIPM FOR FAST SINGLE PHOTON DETECTION

	k	d
Area output	23.87 ± 0.14	-0.22 ± 0.12
Area gain	1.25 ± 0.24	22.12 ± 0.2
Amplitude output (input in range 0- 55 mV)	24.68 ± 0.26	-14.7 ± 7.27
Amplitude gain	-0.024 ± 0.01	24.25 ± 0.61

Table 3.2: Fit parameter for the output vs input signal and the gain for the Photonique AMP-0611 preamplifier.

the data are plotted in figure 3.3 and the fit values are given in table 3.2.1. For the gain of the amplitude, the preamplifier shows large deviations from the regression. It seems that the linearity is lost above and input voltage of 60 mV. Therefore, the regression line (black) has been fitted within an input range of 0 up to 55 mV. For the time resolution measurements, the measured amplitudes are well below this range of 0 to 55 mV, which corresponds to a amplified signal of 0 to ~ 1500 mV.

3.2.2 Data analysis

In a first step, the single photon events were separated by fitting the single photon peak of the amplitude-histograms. After that, the time stamps of events with amplitudes within $\pm 2 \sigma$ of the single photon peak were fitted using a normal distribution. The sigma of this fit is the parameter of interest and gives the SPTR at a certain temperature and bias setting. So far, SiPM from AdvanSiD, Hamamatsu and Ketek have been tested. The tested devices and their parameters are listed in table 3.2.1.

3.2.3 Results

Examples for the behaviour of the current, when the bias voltage was increased can be seen for various temperatures in figure 3.4. Each data point is the mean value of 1000 measurements. The plots show the different responses of the current to the applied bias voltage. The reason for the differences are different SiPM architectures and parameters by the manufactures, e.g., it can be seen that the three devices from Ketek respond in a similar way.

Signal rise/falltime In figure 3.5, the measured rise times at -10°C are plotted against the amplitude of the signal. The plots are shown for an OV, where the best

3.2 Time resolution measurements of analog SiPM

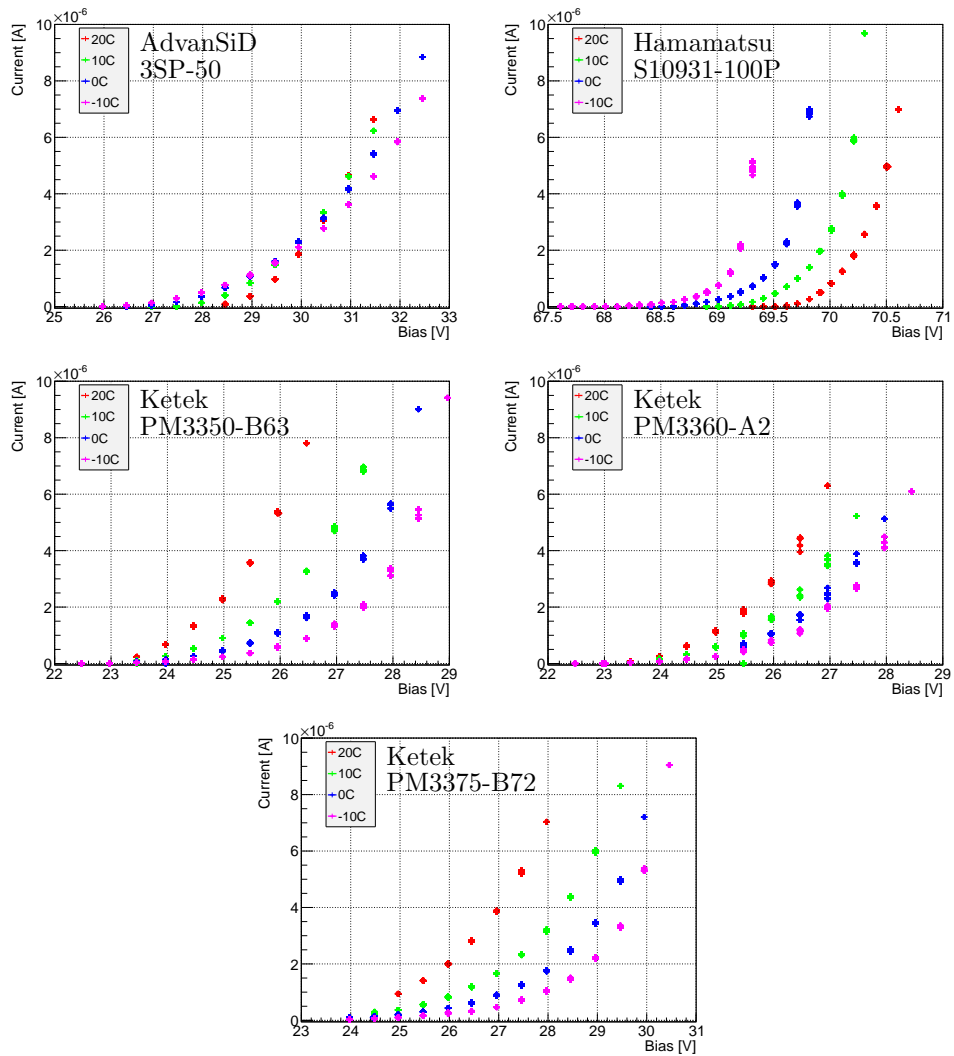


Figure 3.4: Behaviour of the measured current dependent on the applied bias voltage.

3. SIPM FOR FAST SINGLE PHOTON DETECTION

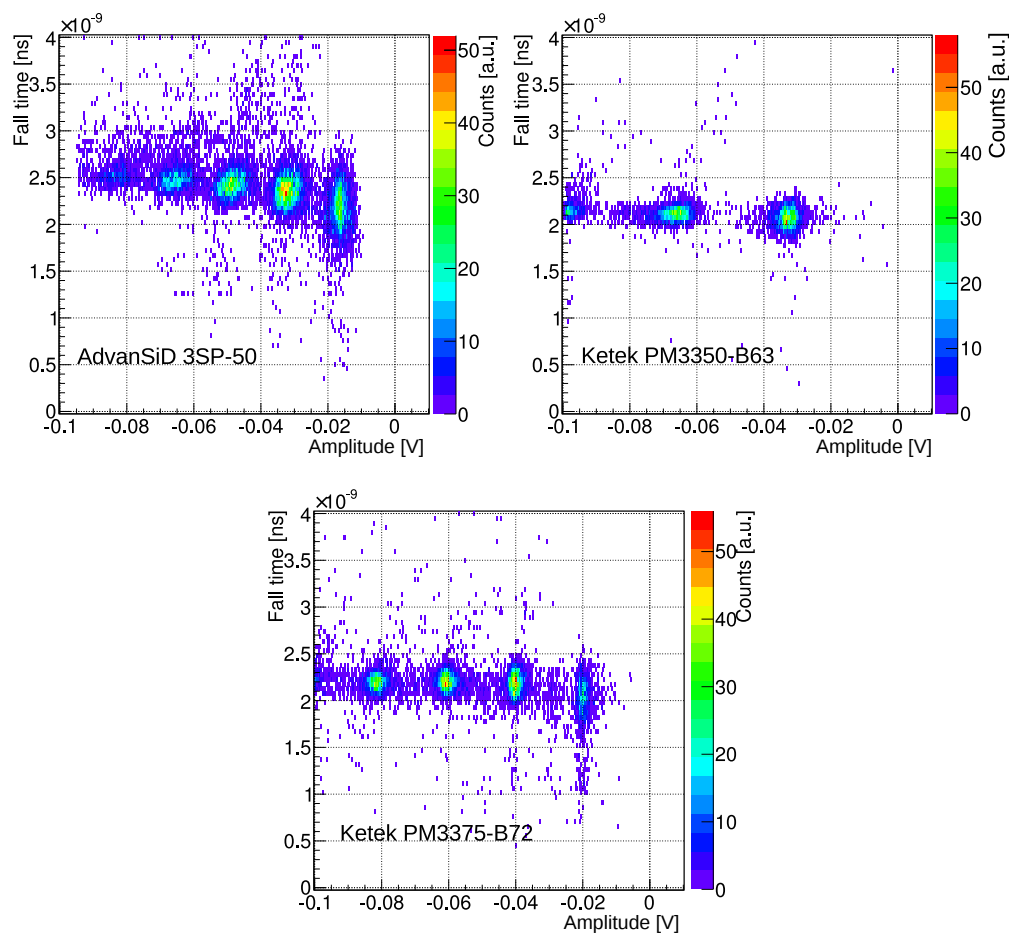


Figure 3.5: Fall time vs. the amplitude of various SiPM at -10°C . The results are shown where the best time resolution for each device has been measured. For the AdvanSiD detector the OV for this plot was at 4.16 V, which is the at the minimum of the measured time resolution, for the Ketek PM3375-B72 the OV was at 5.66 V and for the Ketek PM3350-B63 at 7.14 V.

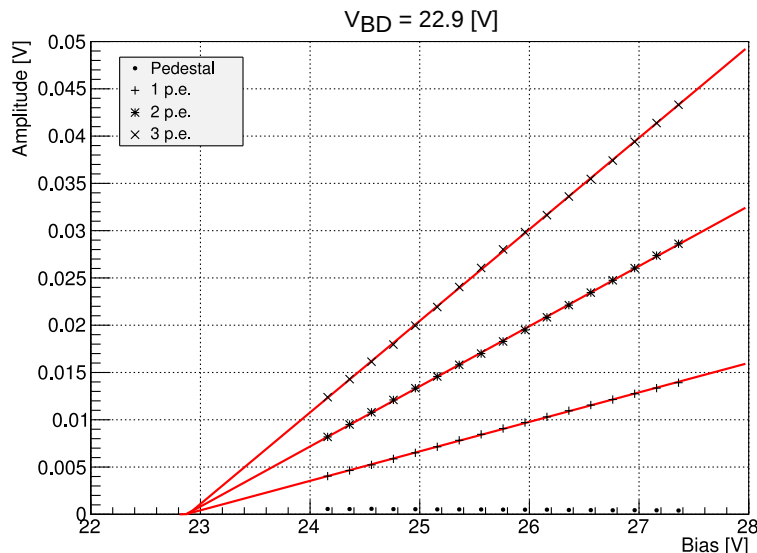


Figure 3.6: Example plot of the automatic determination of the breakdown voltage V_{BD} at a certain temperature. Here, the amplitudes of 1 p.e. up to 3 p.e. are plotted versus the applied bias voltage for the Ketek PM3360-A2 at a temperature of 20°C.

time resolutions have been measured, i.e., an OV of 4.16 V for the AdvanSiD device, 5.66 V and for the Ketek PM3375-B72 and for the Ketek PM3350-B63 7.14 V. It can be seen that the devices from AdvanSiD and Ketek have comparable fall times. But in terms of time resolution, not the shortest fall time, but the steepest slope, dV/dt , of the signal provides the best time pickoff, when the signal-to-noise ratio is at comparable level for the devices, which is case for this measurement. The values for the slopes are 7.49 mV/ns for the Ketek PM3350-B63, 12.96 mV/ns and for the Ketek PM3375-B72 it is 9.7 mV/ns. In figure 3.7 it can be seen that the device with largest slope indeed has the best timing performance.

Determination of the breakdown voltage The determination of the breakdown voltage for each temperature was done using a ROOT script (51). At a certain temperature, the program determined the peaks corresponding to one photo-electron (p.e.) up to several p.e. for each measured bias voltage and fitted the amplitudes using a Gaussian function for each peak. The determined values for the amplitudes with increasing bias voltage were then fitted separately for each p.e. separately, using a linear fit. The mean value of the crossing points of the linear fits with the x -axis (amplitude = 0) was

3. SIPM FOR FAST SINGLE PHOTON DETECTION

defined and used as breakdown voltage for further data analysis. An example plot of the fitted amplitudes for the Ketek PM3360-A2 is plotted in figure 3.6.

The results of the single photon time resolution in dependency on the temperature and the bias voltage is plotted in figure 3.7. Due to the definition of the time resolution in terms of standard deviation (σ) in the proposal for the scintillation tile hodoscope for PANDA (28), the values for the SPTR are also presented in terms of σ . The lines in between the data points, in figure 3.7 are added to guide the eyes and do not represent interpolations.

3.2.4 Discussion and Conclusion

A general trend of improving time resolution with increasing bias voltage and with decreasing temperature can be seen in figure 3.7. At lower temperatures (0°C and -10°C) the improvement tends to saturate below. Moreover, the improvement of the time resolution with increasing bias voltage (which is proportional to the gain) is more significant at higher temperatures. This indicates that increasing dark-count rate, after pulses and cross talk deteriorates the time resolution of the SiPM as they are increasing with the bias voltage and decreasing with the temperature (52). When comparing the Ketek devices, it seems that the SPTR of PM3360-A-2 is not comparable with the other two devices. The reason is that the tested device was a prototype and therefore has slightly different features than the other two devices from Ketek, which are commercially available. Additionally it can be seen that the operational bias range for best time resolution is small compared to the Ketek devices, which suggests that using the Ketek devices an optimum bias setting is much easier to achieve than for the AdvanSiD and the Hamamatsu ones. Overall, the Ketek sensors show the best timing performance for all bias settings and temperatures in this measurement.

Compared to values in the literature (53), the presented values of the SPTR are relatively high. This can be explained by the time resolution of the setup itself, e.g. the optical fibre is adding time spread. The main contribution, however, is related to the measurement method of the digital oscilloscope, which is comparable to a constant fraction discriminator at an relatively high threshold at 50% of the amplitude. Furthermore, the time jitter of the trigger-detector is also included in this value.

When comparing the time resolution at different temperatures in figure 3.7, it can be seen the time resolution seems to saturate above 100 ps. This indicates that the time

3.2 Time resolution measurements of analog SiPM

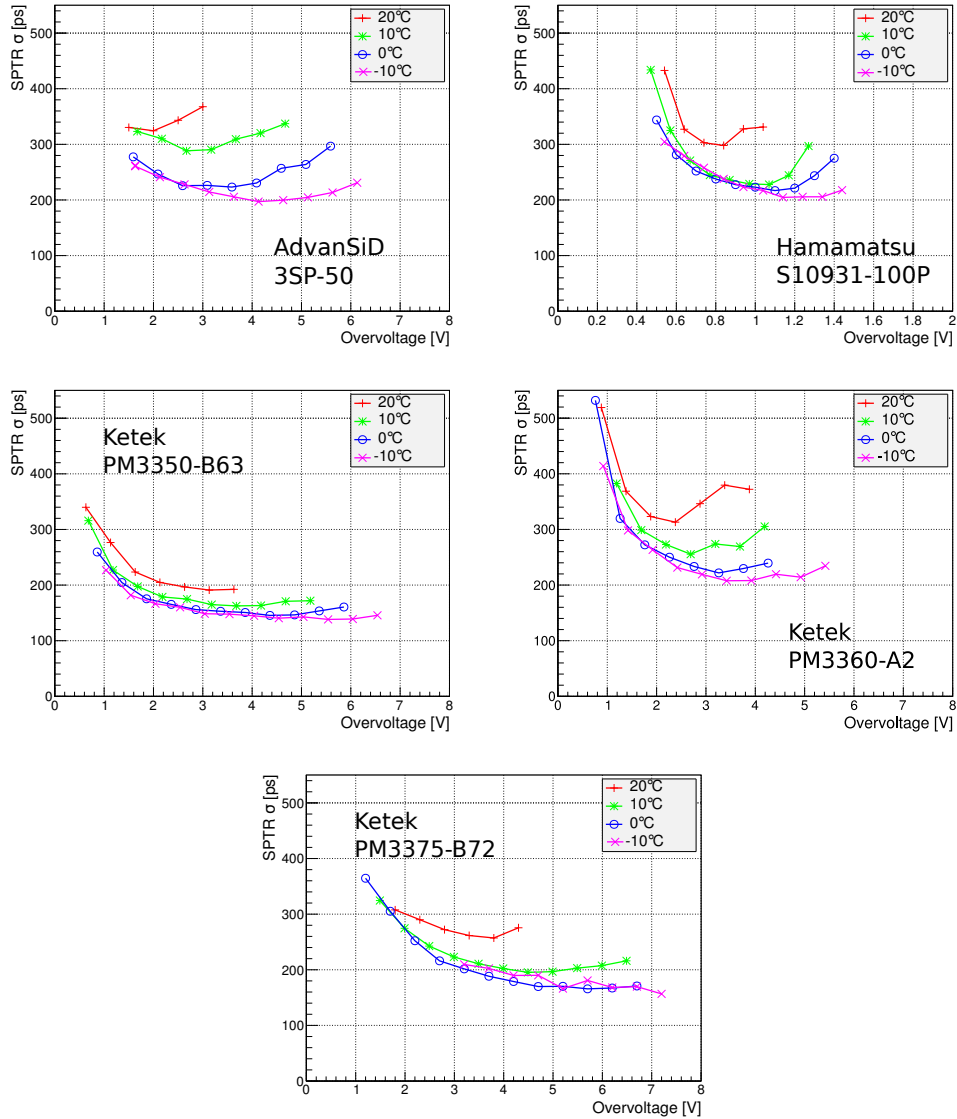


Figure 3.7: Single photon time resolution of the tested SiPMs. The lines are guides for the eyes (no interpolation) (29).

3. SIPM FOR FAST SINGLE PHOTON DETECTION

resolution of the measurement setup is approached with decreasing temperature and starts to dominate the overall time resolution. This effect can be seen especially for the Ketek PM3350-B63 and PM3375-B72 devices. A test, measuring the time resolution of the setup, with increasing number of photons approves this assumption, as the time resolution saturates at about about 110ps at high photon numbers. Therefore, the SPTR of these devices can be expected to be lower than these values. Nevertheless, the results of the measurement reveals the best performing device, which is the Ketek PM3350-B63.

Outlook: setup upgrade As the contribution of the time spread of the setup is large, an upgrade is currently done. For this upgrade several methods will be compared, such as timing by delayed pulses on the same sensor, timing using the laser signal or improving the timing signal of the reference SiPM. Furthermore, the determination of the SiPM-time-stamp will no more be done by the function provided on the oscilloscope, but the SiPM waveforms will be analysed. Approaches for suppressing noise by cutting frequencies after fast Fourier transformation and programming of several software discriminators including multi-threshold approaches have been already done. First tests with these methods already resulted in an significant improvement of the achieved time resolutions. Nevertheless, as the studies are not finished, they will be published in a future work.

3.3 Oversaturation behaviour at high photon exposure

At low photon numbers SiPM respond linear to the incoming number of photons. With increasing number of photons the responding signal saturates until a plateau corresponding to the number of SPADs is reached, which can be described by,

$$N_{\text{fired}} = N_{\text{total}} \times \left[1 - \exp\left(-\frac{N_{\text{seed}}}{N_{\text{total}}}\right) \right]. \quad (3.1)$$

The number of photons arriving at the SiPM that could potentially trigger an avalanche if the cell is not fired is defined as N_{seed} and the total number of SPADs is N_{total} . During characterisation of the SiPM for time resolution measurements an unexpected deviation from this well accepted behaviour occurred, which here is called oversaturation behaviour. The response signal overshoots the theoretical limit of number of fired

3.3 Oversaturation behaviour at high photon exposure

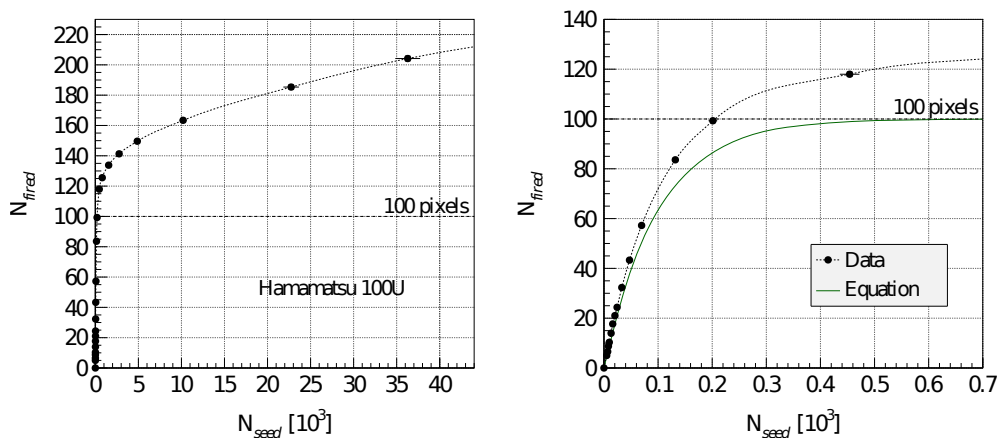


Figure 3.8: Oversaturation behaviour of a Hamamatsu MPPC S10361-11-100U with $1 \times 1 \text{ mm}^2$. Equation 3.1 shows the expected response of the SiPM and saturation at a level of 100 cells, the measured response (Data) overshoots this theoretical plateau (54). This behaviour was also observed for SiPM from other vendors (54).

SPADs times the response of one SPAD. This behaviour is plotted in figure 3.8. On the left hand side of this figure, the response of a Hamamatsu MPPS S10361-11-100U is shown for the whole measurement range up to $N_{seed} > 35 \cdot 10^3$. On the right hand side of the same figure a zoom of the same data and additionally the expected behaviour according to equation 3.1 is shown. The deviation from the equation can be clearly seen.

A detailed description of this phenomenon was published within the work of this PhD and can be found in appendix 7.6 and (54).

3.4 Time resolution measurements of digital SiPM

3.4.1 Theoretical considerations

As discussed, a digital SiPM differs from the analog SiPM in a way that the conversion from analog to digital signal happens directly on the sensor, contrary to the analog case. For the case of the Philips DPC this conversion takes place on a SPAD level. Looking at the signal of an analog sensor the time information of every detected photon is contained in it. Assuming a perfect time pickoff, i.e., the time stamp for every detected photon can be measured, the error of the mean arrival times improve with the number of photons, n , following $\approx 1/\sqrt{n}$, whereas the standard deviation, representing the time resolution of the sensor stays constant.

For a real analog detector with a limited response time, the slope of the signal, contains the temporal distribution of the arriving photons. When measuring, e.g., a voltage signal, V , the slope of the signal can be described by dV/dt , with t being the time. As the arrival rate of the photons is usually much faster than the response time of the SPADs together with the preamplifier, the signal of the individual photons is smeared out and it becomes difficult to determine the arrival times of the individual photons. Therefore, the error of the arrival times deviates from $1/\sqrt{n}$ for the analogue SiPM.

In the case of the perfect digital SiPM, where the analogue signal of every SPAD is converted into a digital time-stamp, the determination of the individual arrival times of the photons would be possible. As this technology is very new and only one type of digital SiPM is commercially available so far, the following considerations are referring to the architecture of this detector which is Philips DPC.

In the case of current version of the Philips DPC it is not possible to receive a time stamp for every fired SPAD, but just for every die. This fact makes it necessary to distinguish the expected behaviour of the TR of this sensor from the analogue device. Furthermore, for the real DPC the variations of the signal path lengths from each single cell to a common TDC, which is giving additional time spread and is called trigger network skew, has to be considered as well. The path length variations (in terms of time) are given in figure 3.9 (55).

Assuming n random variables t_1, t_2, \dots, t_n are independent and identically distributed (i.i.d.) and are following the probability density function (PDF) $f(t)$. The n random

3.4 Time resolution measurements of digital SiPM

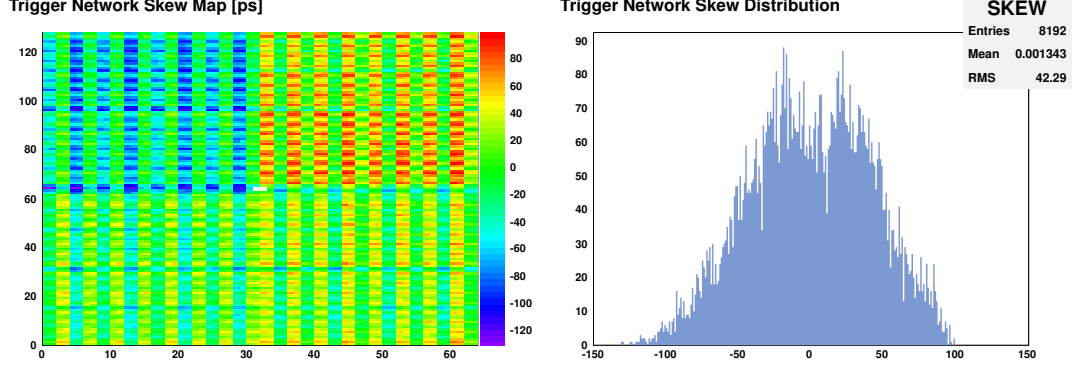


Figure 3.9: Time skew due to the trigger network of the Philips DPC (55). On the left hand side a color plot of the trigger network skew related to each SPAD is shown. On the right hand side the distribution of skews of all SPADs is shown (55).

variables represent the number of detected photons and $f(t)$ the temporal distribution of the photons, e.g, a laser pulse or scintillation. Let us further assume that the time-stamp of the trigger of a DPC-die is created by the first arriving photon, t_{\min} . It should be noted, that the standard deviation of the distribution is independent of the number of photons. Using i.i.d., the cumulated distribution function (CDF) $F_{t_{\min}}(t)$ of the arrival time of the first arriving photon can be rewritten as,

$$F_{t_{\min}}(t) = P(t_{\min} \leq t) = 1 - P(t_{\min} > t) \quad (3.2)$$

$$= 1 - P(t_1 > t, t_2 > t, \dots, t_n > t) \quad (3.3)$$

$$= 1 - P(t_1 > t) \cdot P(t_2 > t) \cdot \dots \cdot P(t_n > t) \quad (3.4)$$

$$= 1 - (P(t_1 > t))^n \quad (3.5)$$

$$= 1 - (1 - P(t_1 \leq t))^n. \quad (3.6)$$

The associated probability density function (PDF) $f_{t_{\min}}(t)$ represents the temporal distribution of the first arriving photon of n total photons. As the PDF is the derivative of $F_{t_{\min}}(t)$ we can write it as

$$f_{t_{\min}}(t) = n \cdot f(t) \cdot (1 - P(t_1 \leq t))^{n-1} \quad (3.7)$$

3. SIPM FOR FAST SINGLE PHOTON DETECTION

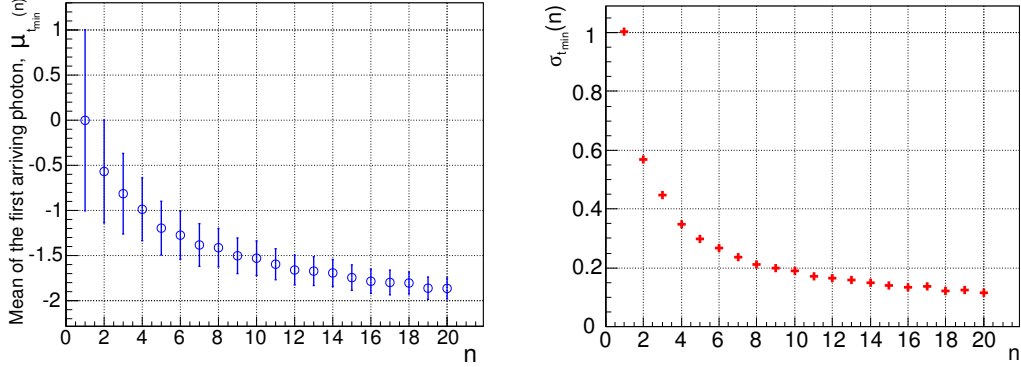


Figure 3.10: Mean $\mu_{t_{\min}}(n)$ (left) and the standard deviation $\sigma_{t_{\min}}(n)$ (right) for the first arriving photon of a normally distributed light pulse with mean $\mu = 0$ and a standard deviation $\sigma = 1$ plotted for n photons.

with

$$P(t_1 \leq t) = \int_{-\infty}^t f(u) du \quad (3.8)$$

So far, the only prerequisites of this derivation are that $f(t)$ is known and the random variables are i.i.d. Therefore, these results can be applied for any known light distribution, e.g., a laser pulse or scintillation.

A MC-simulation was done, to estimate the influence of the order statistics on the time resolution-measurement of the DPC. The temporal distribution of the simulated laser pulse is assumed to be normally distributed with a mean $\mu = 0$ and a standard deviation $\sigma = 1$. Using this distribution, the mean time-stamp of the first arriving photon, $\mu_{t_{\min}}(n)$, and its standard deviation $\sigma_{t_{\min}}(n)$ for increasing number of photons, n , were determined. The results are shown in figure 3.10. It can be seen that due to the order statistics of triggering on the first photon, $\mu_{t_{\min}}(n)$ deviates from the initial mean of the normal distribution for $n > 1$. On the right hand side of this figure the distribution of $\sigma_{t_{\min}}(n)$ is plotted. This curve clearly deviated from a $1/\sqrt{n}$ behaviour, which will be shown and discussed in more detail in the following paragraphs.

So far, an analytic description for $\sigma_{t_{\min}}(n)$, as seen in figure 3.10 on the right hand side, was not derived in this work but will be part of a future work. Nevertheless,

3.4 Time resolution measurements of digital SiPM

$\sigma_{t_{\min}}(n)$, was tried to parameterise with following function,

$$f(x) = \frac{p_1}{x^{p_2}} + p_3. \quad (3.9)$$

The quality of this parameterisation is shown in figure 3.11, on the left hand side. In this plot $\sigma_{t_{\min}}(n)$ is drawn up to 100 photons and fitted with equation 3.9. As the function describes the behaviour of $\sigma_{t_{\min}}(n)$ quite well ($\chi^2/\text{NDF} \ll 1$) this function will be used for data analysis of the DPC-time resolution.

The results of the described simulations can be compared with the CTR measurements of the DPC using the laser. This can be done, assuming all the factors influencing the time resolution are adding a normally distributed time jitter. Therefore, adding the normally distributed SPAD time resolution σ_{SPAD} to the (almost) normally distributed trigger network skew σ_{network} will result in another normal distribution with σ_{tile} . With laser pulse width, σ_{laser} and $\sigma_{\text{tile1}} = \sigma_{\text{tile2}} = \sigma_{\text{tile}}$ one can write,

$$\sigma_{\text{tile}} = \sqrt{\sigma_{\text{SPAD}}^2 + \sigma_{\text{network}}^2} \quad (3.10)$$

$$\sigma_{\text{CTR}} = \sqrt{2 \cdot \sigma_{\text{tile}}^2 + \sigma_{\text{laser}}^2}. \quad (3.11)$$

This shows that the MC-simulation using only a single normal distribution represents the CTR measurement of two DPC-tiles in coincidence. It has to be mentioned that so far influences of dark-counts or optical cross-talk are neglected, which will be discussed later.

Quality of the first photon as time-stamp As discussed, in the case of the DPC, using the first photon as time estimator of an event (i.e. the laser pulse), is the only case where an accurate information of the number of photons which are forming the time estimator, is provided. Therefore, the first arriving photons was used in the measurements presented in the following.

Using the results of the section before, one can estimate the quality of the first arriving photon as time estimator of the event. Here, the laser pulse is forming an event, which can be assumed to be normally distributed. If one wants to use this estimation for scintillators one has to take the photon statistics of the scintillation and other effects into account. This will be shown in section 4.2.1. Nevertheless, following considerations are treating the case of a normally distributed laser pulse, as a pulsed

3. SIPM FOR FAST SINGLE PHOTON DETECTION

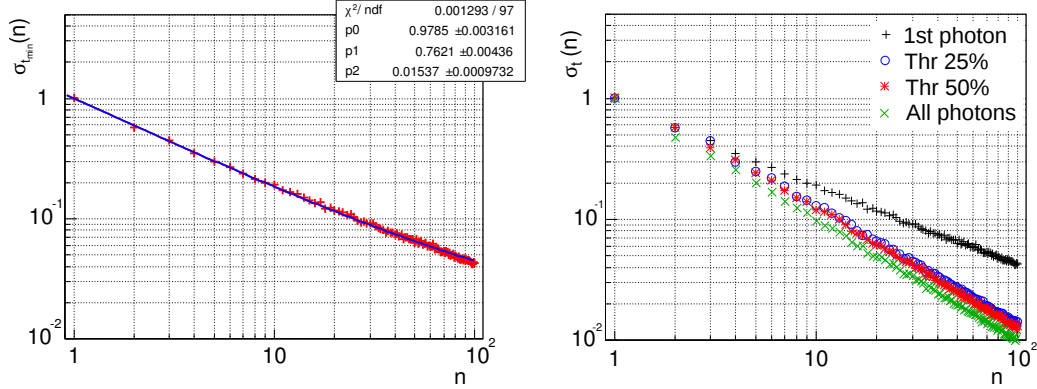


Figure 3.11: Fit of $\sigma_{t_{\min}}(n)$ using equation 3.9, when triggering on the first photon (left). On the right hand side: simulating the distribution of $\sigma_{t_{\min}}(n)$ for a normal distribution, when triggering on various thresholds. The standard deviation is determined for thresholds are set to the first photon, 25% and 50% of the photon number n or by calculating the mean of all n time-stamps.

laser was used for measurements of the DPC-TR which are presented in the following section.

For the estimation of the quality of the first photon as time estimator, four different scenarios are plotted in figure 3.11 on the right hand side: the case of the first photon time estimator, two cases where the time-stamp after 25% and 50% of n photons has arrived, respectively, and for a time estimator which is formed by the mean of all n time-stamps. In this plot it can be seen that for values of $n > 1$ the most accurate time information can be determined when all time-stamps are known and their mean is calculated. The next accurate time estimator is provided when setting the thresholds at 50% followed by 25% of n . The worst time estimator is provided by the first arriving photon. Nevertheless, this estimation has impact on the measurement when, the light pulse and the time resolution of the detector is similar to the width of the light pulse. In the measurements using the femtosecond laser, presented in the next section, the width of the laser pulse is two orders of magnitude smaller than the DPC-time resolution and therefore, the quality of the time-stamp can be neglected in this case. However, also measurements using a picosecond laser will be presented, where the trigger level has impact on the time estimator.

3.4 Time resolution measurements of digital SiPM

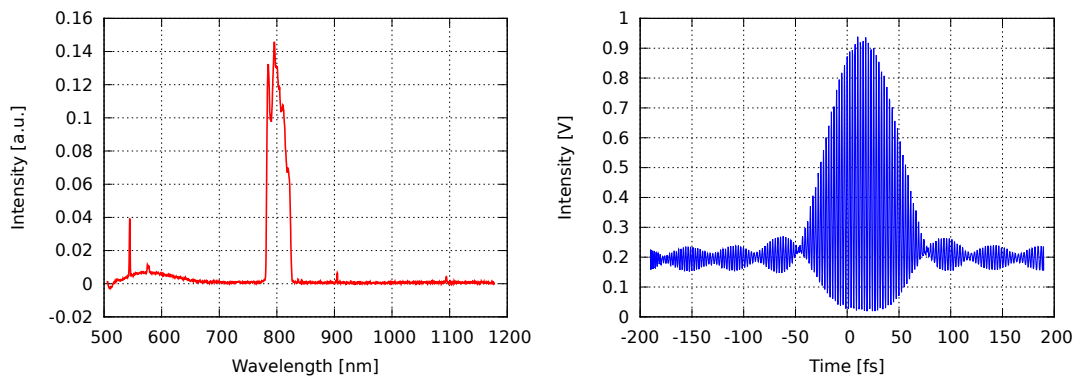


Figure 3.12: Emission spectrum of the Femtosource XL on the left hand side. Pulse width of the same laser on the right hand side. Data provided by Femtolasers GmbH.

3.4.2 Setup

The DPC time resolution measurements were done using a pulsed laser, which was directed onto two dies on the same tile. By measuring the standard deviation of the time differences of the two dies, the time resolution was determined. Several configurations of dies were tested in order to obtain an average value of the sensor time resolution. As the time resolution is dependent on the number of detected photons, a variable attenuator was used in order to adjust the laser intensity. For assignment of the events to a certain number of photons, the photon counts of the individual pixels were used, e.g., for the time resolution at single photon level, the time differences, when each sensor was hit by a single photon, were used for analysis.

Two different lasers were used for the measurements: a diode laser with pulse widths of 30 ps FWHM and a faster laser with pulse widths of ≈ 150 fs located at Femtolasers GmbH, Vienna.

TR using the femtosecond laser The used femtosecond laser was a Femtosource XLTM by Femtolasers GmbH with 650 nJ and 50 fs pulse width at 5 MHz repetition rate. Emission and timing spectra of the laser are given in figure 3.12. As the provided repetition rate of 5 MHz was too high for the acquisition rate of the DPC, the repetition rate of the laser was adjusted to usually 10 kHz using the PulsefinderTM from Femtolasers with a contrast ratio of 30:1. After this stage, the laser wavelength was decreased to 400 nm using a Barium Borate (BBO) crystal for second harmonic gener-

3. SIPM FOR FAST SINGLE PHOTON DETECTION

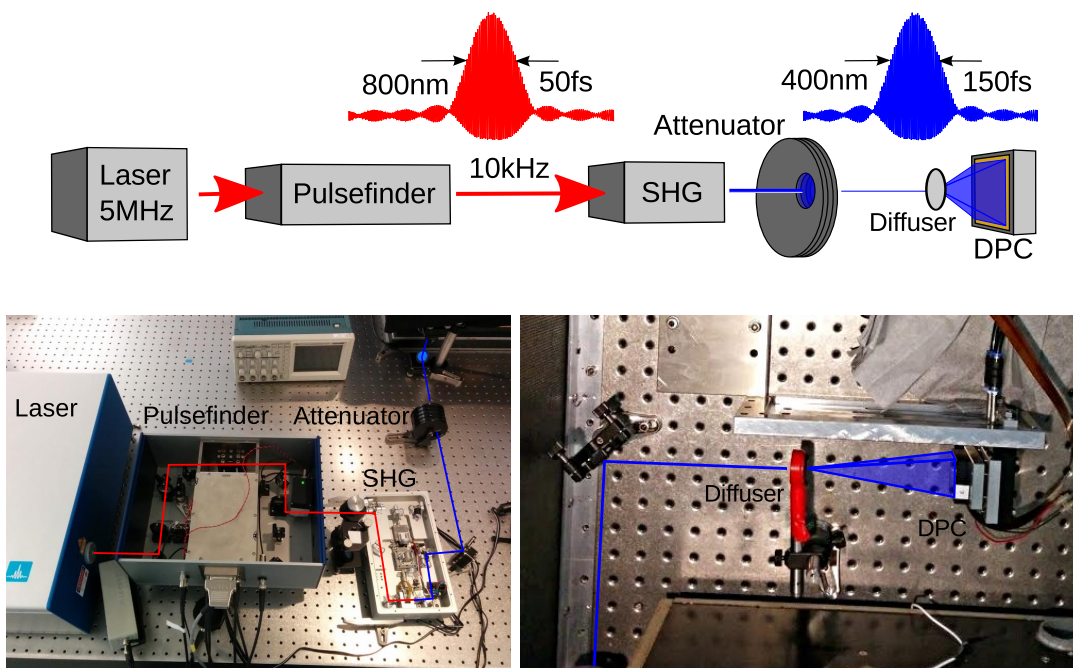


Figure 3.13: Schematic drawing and pictures of the setup for SPTR determination of the DPC. For a detailed description, see the text.

ation (SHG). Additionally, the laser intensity could be tuned roughly by adjusting the alignment of the BBO crystal. After the SHG, the pulse traversed a manual optical attenuator wheel for precise adjustment of the laser intensity and further entered a dark box. Inside the dark box the beam was directed onto the DPC after it passed an optical diffuser to increase the spatial width of the beam. The setup is schematically depicted in figure 3.13.

Due to a compression stage inside the SHG-module, the pulse width behind the SHG is ≈ 50 fs. With temporal diffusion of $\approx 20 \text{ fs}^2 \text{ m}^{-1}$ and a path length from the SHG to the DPC of 2 - 3 m, a pulse width of $\approx 100 - 150$ fs could be expected at the DPC¹.

Figure of merit for the determination of the time resolution is the standard deviation of the time differences of two time-stamps, which are triggered by the same laser pulse. This value is measured in terms of FWHM in this section. For the following measurements, either two dies or two pixels, located on the same sensor (tile) were activated in order to measure the CTR of either two dies or two pixels, respectively.

¹Estimation by staff of Femtolasers GmbH

3.4 Time resolution measurements of digital SiPM

DPC	Active area	Temp. [°C]	Laser rate [kHz]	Inactive cells [%]	SPCTR [ps]	System [ps]
3200	die	0	10	0	265 ± 8.4	67 ± 2.7
3200	die	0	10	20	238 ± 4.3	60 ± 1.2
3200	die	0	10	50	216 ± 3.3	64 ± 0.8
3200	die	10	10	20	361 ± 17.7	66 ± 0.9
3200	pixel	10	10	20	143 ± 3.9	22 ± 3.4
3200	pixel	20	10	20	160 ± 4.9	20 ± 4.4
6400	die	0	10	20	350 ± 4.3	57 ± 0.6

Table 3.3: Extrapolated single photon coincidence time resolution (SPCTR) in terms of FWHM and system time resolution for various measurement settings of the Philips DPC.

The reason for not only measuring the TR of dies but also for pixels was manifold:

- at higher temperatures (e.g., 20 °C), in some cases the dark-count rate was too high, to measure the die time resolution,
- for estimation of the contribution of the trigger network to the time resolution of the sensor
- in chapter 4, measurements of scintillators with base areas of the size of a pixel will be presented. In order to separate the contributions of the DPC and the scintillator to the overall time resolution, also the pixel time resolution of the DPC was measured here.

3.4.3 Results

The results of the determined coincidence time resolution at single photon level (SPCTR) in terms of FWHM are presented in table 3.4.2. The SPCTR was measured for various temperatures, inhibition maps at both die- and pixel-level. It can be seen that the SPCTR improves with decreasing number of active cells and improves with decreasing temperature. Furthermore, the time resolution improves when only pixels are activated instead of whole dies.

The values were determined by fitting the values of the calculated time resolution at a certain photon level. This was done for photon levels typically ranging up to 500 photons. These values were fitted using equation 3.9. Two examples of these fits are given in figure 3.14. On top of this figure the CTR for the DPC3200 at 10 °C and on

3. SIPM FOR FAST SINGLE PHOTON DETECTION

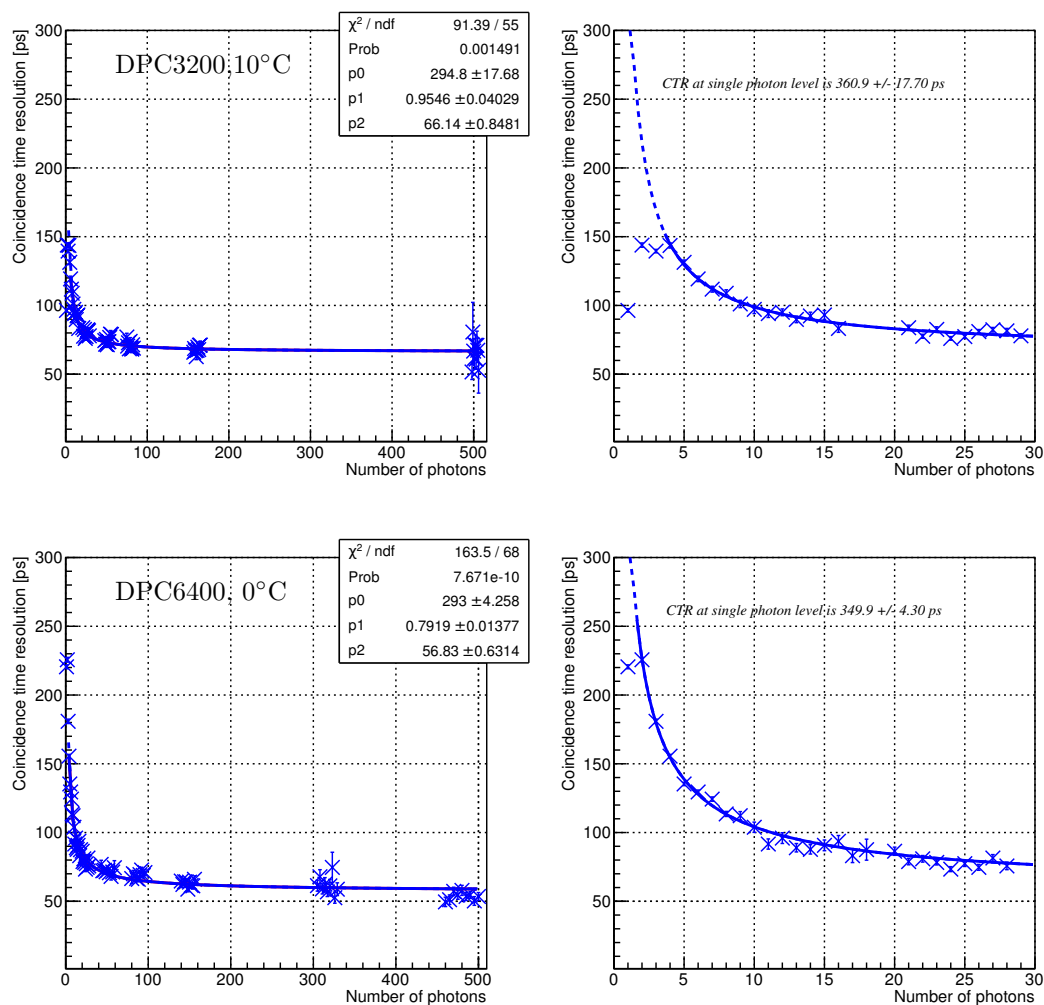


Figure 3.14: Example plots of the DPC time resolution measurements in terms of FWHM. On top for the DPC3200 at 10°C and the DPC6400 at 0°C on the bottom. On the left hand side all data points are shown, whereas on the right hand side a zoom of the data can be seen. The blue line shows a fit using equation 3.9. The dashed lines are the extrapolations to single photon level. For both detectors, 20% of the cells with the highest dark-count rates are inactivated and the repetition rate of the laser was at 10 kHz.

3.4 Time resolution measurements of digital SiPM

the bottom for the DPC6400 at 0° , both measured at die level are given. The left plots in this figure show the whole data, whereas the plots on the right hand side show a zoom of the same data. As one can see, the fit describes the data over a wide range of photon numbers, but at low photon numbers a deviation from this function can be seen. This artefact was mainly caused by cross-talk between the active dies. A detailed description of this effect is given in the following sections. Due to these artefacts, the data ranges for the fits was restricted to values starting at $\sim 2 - 4$ photons and ranges up to the maximum measured values. The value of the SPCTR is then determined by an extrapolation of the fit function down to single photon level. In figure 3.14 the solid lines represent the fits, whereas the dashed lines represent the extrapolation.

Discussion As seen in figure 3.14, the results of the CTR measurements of the DPC showed an unexpected behaviour: at very low photon numbers the time resolution improved. Moreover, when looking at the TOF spectra at low photon numbers, these were not normally distributed any more but showed two additional peaks surrounding a central peak, as one can see in figure 3.15. During the measurements of the background spectra with the laser turned off, the two satellite peaks remained, whereas the central peak vanished. Therefore, the central peak is dedicated to real coincidences. Therefore, the background measurements were subtracted from the data with the laser turned on, the remaining Gaussian shaped peak was fitted and the standard deviation determined. These results are the data are plotted in figure 3.14. As one can see the CTR values at low photon values improve, which is exactly the range where the mentioned double peak structure occurred and therefore a possible connection between the two observations was assumed.

In figure 3.15, the TOF-spectra of two dies of a DPC3200 at 10°C and a laser frequency of 10 kHz are shown. 20% of the most active cells were deactivated. TOF spectra with the laser turned on are shown in the first row, when 1 up to 3 p.e. were detected on each die. It can be seen that the spectra do not follow a normal distribution. The TOF spectra are shown for exactly the same settings but with the laser turned off are plotted. Two peaks around the centre can be seen in these background spectra. The background spectra were subtracted from the measurement with the laser resulting in the last three histograms. These spectra were nicely fit-able using normal distributions.

3. SIPM FOR FAST SINGLE PHOTON DETECTION

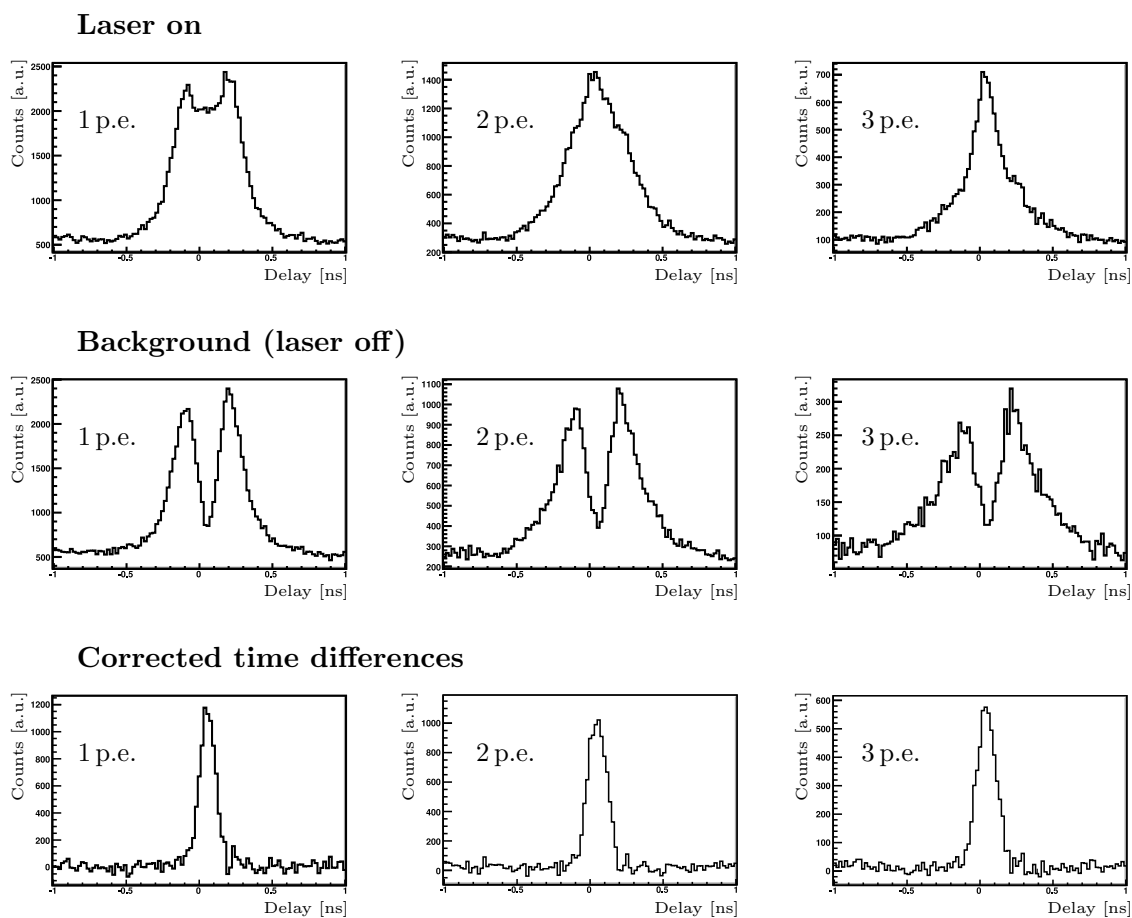


Figure 3.15: TOF spectra of two dies for the Philips DPC3200 in coincidence, measured with a Femtosecond laser (10 °C, 10 kHz and 20 % of the most active cells turned off). On top the time differences (delay) when the laser was turned on is shown, below, results of the same measurement, when the laser is turned off. These background spectra were used to correct the measurement data by subtraction which gave the plots on the bottom. These plots were finally used for fitting.

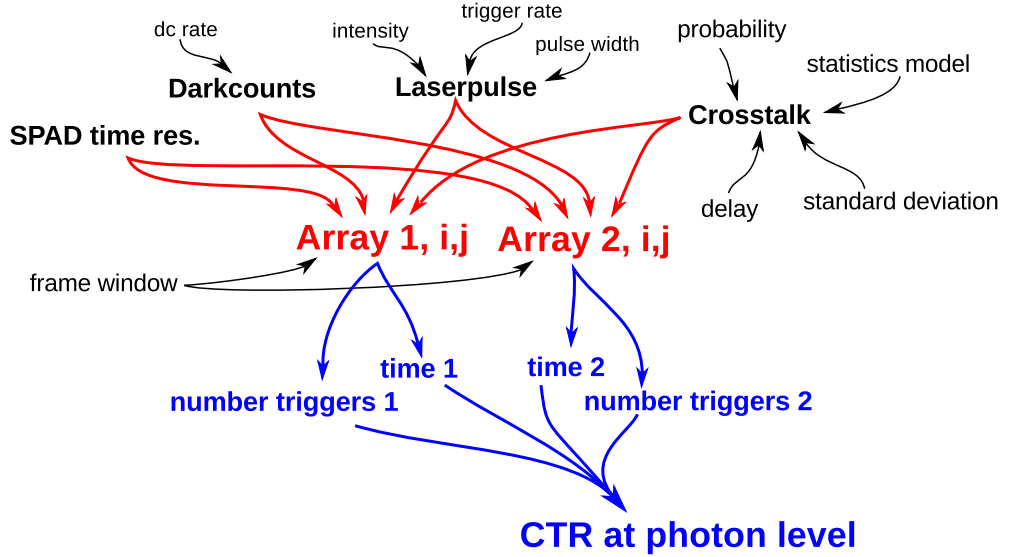


Figure 3.16: Schematic of the MC-simulation of the CTR of the DPC.

3.4.4 MC simulation of the DPC

For a better understanding of the results presented a Monte Carlo simulation of the DPC was done using ROOT. An schematic overview of the simulation structure is shown in figure 3.16. The MC-simulation is based on two boolean arrays with a size of i, j , representing two dies or pixels activated for a coincidence measurement. Each entry in the array represents a SPAD which can either be fired (1) or not fired (0). Additionally to this array, an array storing the reason for firing (dark-count, laser, cross-talk) was used. The laser fires with choose-able frequency and with a defined intensity. The laser intensity was not fixed but represents the mean of a Poissonian distribution. Additionally, the laser pulse width and the SPAD time resolution, both following a Gaussian distribution, can be set. Within the frame, dark-counts are triggering cells according to a choose-able dark-count frequency. It has to be noted that a frame in the simulation does not have exactly the same definition as for the actual DPC. For the simulation no validation scheme was introduced and therefore, the duration of a frame was fixed. For the real measurements, however, the validation scheme was inactivated at low photon number, which is the region of interest. After a frame, the first time stamp of each array represents the trigger time. Calculating their time differences and considering the number of fired cells gives the coincidence time spectrum at a

3. SIPM FOR FAST SINGLE PHOTON DETECTION

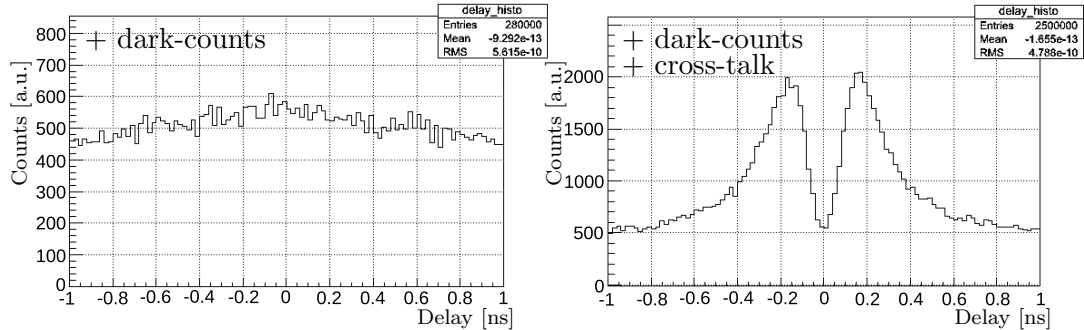


Figure 3.17: Simulated background-spectra. On the left: BG-spectrum with a dark-count-rate of 10 MHz, on the right: cross-talk with a probability of 2% of the events, a mean delay of 170 ps and a width of 60 ps of a Landau distribution.

certain photon level. As for the real DPC the sensor remains partly active until the trigger is formed and therefore additional dark-counts contribute to the determined photon number. So far a validation or integration scheme as for the real DPC was not implemented, as for the measurements at low photon levels these schemes were deactivated anyway.

Two unexpected observations were made at the measurement: improved time resolution at low photon levels and two additional peaks in the timing spectrum also at low photon levels. The peaks in the timing spectrum were not only observed when the laser was on, but also when a background run (laser off) was made. Therefore, the coincidence time distribution of such a background run was simulated as a first step.

Simulating varying dark-count rates showed Gaussian distributed TOF-histograms with standard deviations so large, that the TOF-spectra look equally distributed within a short coincidence time window of several ns, see figure 3.17 on the left hand side. For this simulation no double peak structure could be observed.

In a next step, cross-talk was introduced. In the simulation the cross-talk appears with a certain probability and was realised by either Gaussian or Landau statistics in a way, that after a cell was fired another cell in the other array was fired after a certain time according to the chosen statistics. In figure 3.17, two simulated background spectra are shown: on the left hand side a coincidence spectrum of dark-counts (10 MHz/die) is shown. On the right hand side of the same figure, 2% cross-talk, with a mean delay of 170 ps and a width of 60 ps of a Landau-model was added. Comparing this figure with the measured background spectrum at 1 p.e. level in figure 3.15 a qualitative

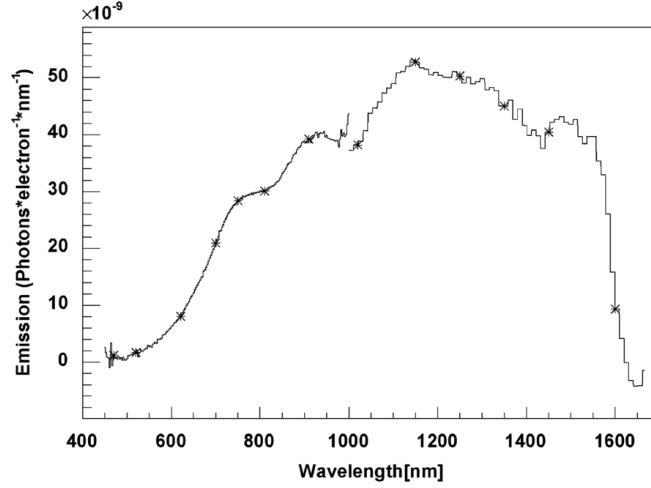


Figure 3.18: Photon emission spectrum by electrons during Silicon-avalanches (56)

similarity can be seen, which indicates, a connection of the double peak structure in the BG-spectrum and cross-talk might be a realistic assumption.

One possibility for cross-talk might be optical cross talk between two dies in a way that the photons are emitted during an avalanche in one die and enter the protective layer on top of the dies. After total reflection at the surface of this layer, the photons might reach the neighbouring dies with a certain delay. An emission spectrum for photons created by avalanches in Silicon (56) is given in figure 3.18.

The figure shows the probability for photon emission per electron and per nm during an Si avalanche. From this figure one can roughly estimate the number of emitted photons per fired cell: (56) measured 1.2×10^{-5} photons per electron in a wavelength region between 500 nm and 1117 nm. Using this number and assuming a gain of 10^6 to 10^7 one can expect 10 to 100 photons per breakdown which can cause optical cross-talk. These photons are more likely to trigger an avalanche in a neighbouring SPAD, but could also trigger avalanches in neighbouring dies.

Verification of the influence of cross-talk If optical cross-talk is the reason for the peaks in the BG-spectra, the strength of the effect is dependent on the distance of the dies. The more the distance is the weaker is the cross-talk effect. The TOF-spectra of such a scan of increasing distance can be seen in figure 3.19. The red squares in the overlaid detector layout in this figure show the active pixels for the measurements,

3. SIPM FOR FAST SINGLE PHOTON DETECTION

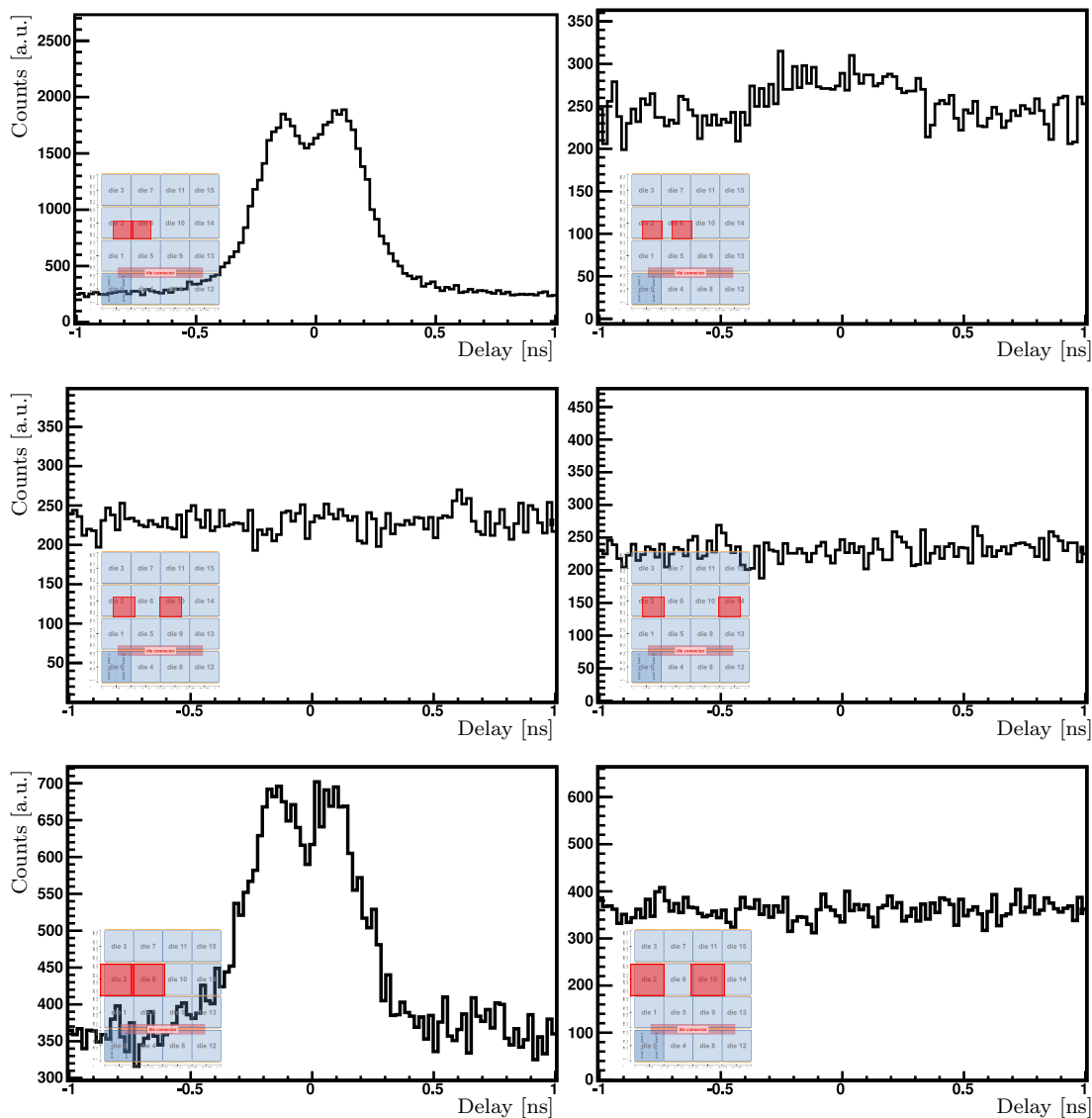


Figure 3.19: TOF spectra of background measurements with increasing distance of the active pixels/dies for investigation of cross-talk (measured data). The red squares indicate the position of the active pixels. It can be seen, that the double peak structure is prominent when the two pixels are next to each other and decrease with increasing distance. The upper four plots show the measured TOF-spectra on a pixel level, whereas the two plots on the bottom show the measurement when whole dies were activated.

3.4 Time resolution measurements of digital SiPM

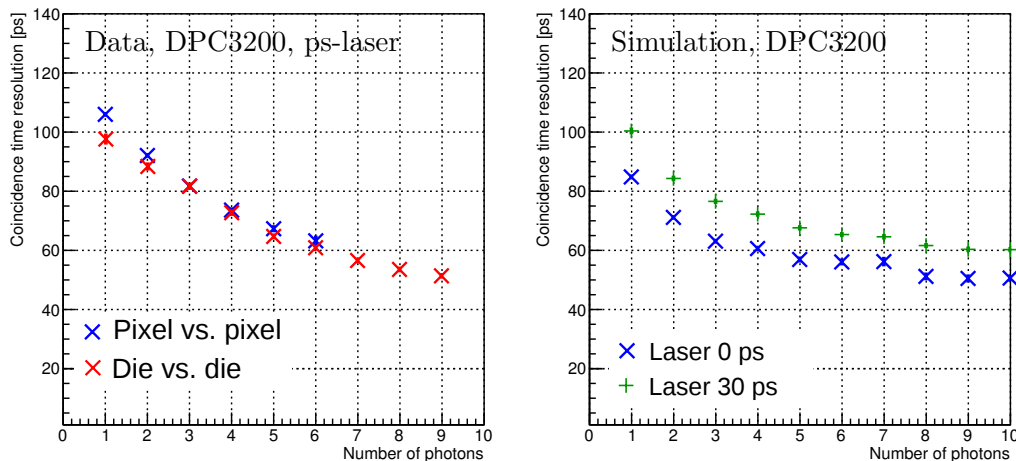


Figure 3.20: On the left: CTR (sigma) of either two pixels or two dies, measured with the picosecond laser. Contrary to the measurement where two neighbouring dies were activated the artificial drop of the TR vanishes and the true distribution of the TR is revealed. On the right: simulated CTR (sigma) for two pixels, once with a simulated laser-pulse width of 0 ps representing the femtosecond laser and once with a width of 30 ps representing the pico second laser. The influence of the laser pulse width on the CTR can be seen clearly.

starting from neighbouring pixels on the top, left and increasing distance until the bottom, right picture. In this figure the cross-talk is clearly visible for the neighbouring cells (top, left) and almost vanished for one pixel farther away (top, right). For the two plots at the bottom only random coincidences due to dark-counts are visible. This measurement was done for a DPC3200 at a temperature of 10°C and 20% of the most active cells deactivated. The validation scheme was deactivated and integration length was set to 0 ns. The coincidence time window was set to 4 ns and 2×10^6 frames were recorded for each setting.

Unfortunately, cross-talk as possible reason for this effect was discussed and simulated after a limited measurement time at Femtolasers GmbH. Therefore this measurement was done using a PIL040 pulsed diode laser from Advanced Laser Diode Systems with an emission wavelength of $\lambda = 404$ nm and a pulse width of 30 ps FWHM which was available at our institute. The setup was similar to the setup at Femtolasers, but without a PulsefinderTM and the SHG. With this setup the whole sensitive area of the DPC tile is illuminated and therefore, the CTR of pixels/dies at maximum distance could be determined.

3. SIPM FOR FAST SINGLE PHOTON DETECTION

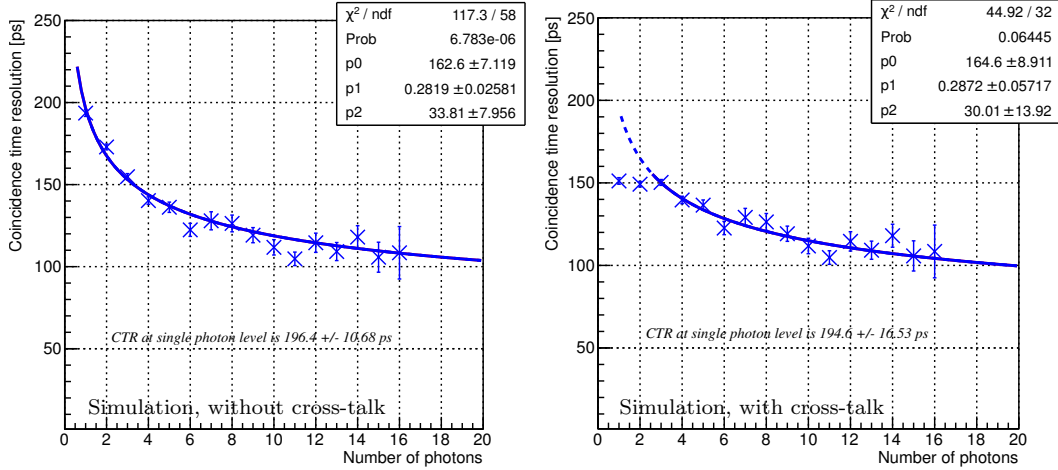


Figure 3.21: Simulated CTR for increasing photon numbers. On the left hand side, only laser triggered events were used for calculation of the CTR. The data was fitted using equation 3.9. For the results on the right hand side, random coincidences of the laser with dark-counts and cross-talk are included and cause an artificial drop in the CTR as it was seen for the experiments data. The data of the simulation on the right hand side was again fitted using equation 3.9 but ignoring the two lowest values. The fit function was then extrapolated to single photon level and results in the same SPCTR as for the true events, plotted on the left hand side.

The results of the time resolution for a DPC3200 using the picosecond laser at a setting of minimized cross-talk are shown in figure 3.20 on the left hand side. It can be seen that the drop in TR at low photon numbers vanished, when compared to figure 3.14. In order to determine the influence of the picosecond laser, two simulations, one with a pulse width of 0 ps and one with a pulse width of 30 ps FWHM were performed. The results are shown on the right hand side of figure 3.20. It shows the simulated CTR of two pixels (two arrays of 64×50 cells as for a DPC3200). For this simulation a SPAD resolution of 60 ps, a dark-count rate of 3 MHz and 1% cross-talk were chosen. The cross-talk was simulated using Landau statistics with a mean of 120 ps and a width of 50 ps. In both plots the error bars are included.

Qualitative validation of data analysis A validation for the extrapolation-method used for the determination of the SPCTR of the DPC was done qualitatively using the presented MC-simulation.

As for the simulation results the origin of firing a cell was stored (laser, dark-count),

3.4 Time resolution measurements of digital SiPM

the events were both triggers were caused by the laser could be separated from all other events. The simulation was done using a SPAD time resolution of 60 ps, 3 MHz dark-count rate for two pixels, cross-talk probability of 1%. The cross-talk was Landau distributed with a mean of 120 ps and a standard deviation of 50 ps. The results are shown in figure 3.21. On the left hand side of the data for events caused only by laser pulses are plotted. For the plot on the right hand side all events were used and from this a simulated background spectrum was subtracted in the same way as it was done for the measurement.

In the same figure on the left hand side it can be seen that the fit using equation 3.9 can be used to describe the CTR down to single photon level, whereas on the right hand side an artifact similar to the measured data appears and therefore the fit range has to be adjusted and the first two values ignored. An extrapolation of the fit (dashed line) down to single photon level can then be used to estimate the SPCTR. One can see that the values for the SPCTR for both plots agree within the given errors and therefore, the analysis method which was applied on the experimental data of the femtolaser measurements should give an quite accurate value of the real SPCTR.

3.4.5 Measurement of the SPAD time resolution

In a further measurement the SPAD time resolution was determined. To determine this value only a single SPAD was activated on each die. Furthermore, the measurement was repeated with increasing number of activated SPADs on each die, see figure 3.22. The determined coincidence time resolution of two SPADs was 42.82 ps FWHM. Dividing this value by $\sqrt{2}$ the SPAD time resolution results in 30.28 ps FWHM for a single SPAD. This value includes also contributions of the readout electronics, but excludes the trigger network skew. In the same figure it can be seen that the CTR stays constant up to activated SPADs larger than 150. This measurement was done using a DPC3200 and showed the best values measured for the CTR of 40.2 ps when 49 SPADs per die were activated. The measurement was done with the whole tiles fully illuminated (≈ 30 photons per SPAD). Doing so the network skew is not only eliminated for two single SPADs in coincidence, but also for increasing the number of active SPADs. The reason for this is that, no matter how many SPADs are active the trigger always comes from a SPAD with the shortest line to the TDC. This way the mean values of the obtain TOF

3. SIPM FOR FAST SINGLE PHOTON DETECTION

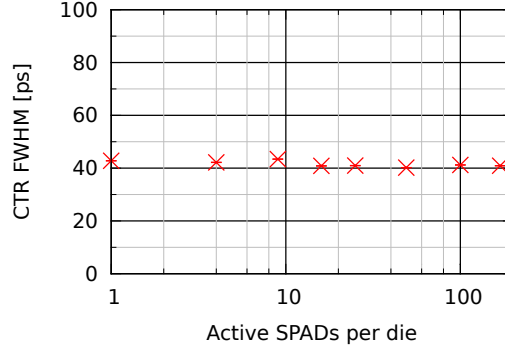


Figure 3.22: Coincidence time resolution of increasing number of SPADs per die. The laser intensity was set to ≈ 30 photons per SPAD. The laser rate was set to 10 kHz.

spectra can change but not its standard deviation (assuming that all SPADs give the same time jitter).

3.4.6 Discussion and conclusion

In this section the results of time resolution measurements of the Philips DPS using a femtosecond-laser have been shown. At low photon numbers (about 1 – 4 photons) the results showed an unexpected improvement in time resolution. The presented extrapolated values of the SPCTR represent an estimation based on the theoretical consideration of order statistics of normal distributions and MC-simulations showing the influence of a cross-talk effect. The physical origin of the cross-talk does not have been identified so far but is likely caused by optical cross-talk. Nevertheless, it has been shown experimentally, that the cross-talk effect vanishes as soon as the distance between the active SPADs is increased. Furthermore, the results show, that at very low photon levels, measurements using the DPC might be contaminated by cross-talk, mimicking an improved time resolution.

The best achieved extrapolated value of the SPCTR was 143 ps FWHM for the DPC3200 at pixel level at 10°C with 20% of the cells turned off, which would lead to a single pixel time resolution of 101 ps at single photon level. At SPAD level a CTR of 42 ps FWHM resulting a time resolution of 30.28 ps FWHM for one SPAD, which includes the contribution of the electronics.

Moreover, the system time resolution of the DPC could be determined and showed coincidence values of about 20 ps FWHM for two pixels in coincidence resulting in

3.4 Time resolution measurements of digital SiPM

12 ps FWHM system time resolution of one pixel. Values determined for whole dies in coincidence ranged from 57 ps to 67 ps FWHM.

Furthermore, the results of the SPCTR show, that the resolution is dependent on the temperature (dark-counts) and on the number of active cells (trigger network skew). An improvement of the trigger network skew has already been proposed by Philips (55) and could bring significant improvement of the time resolution of these devices. The results show that the DPC is a perfect candidate for fast single photon detection and therefore, is very promising for applications for fast Cherenkov and scintillation detectors.

3. SIPM FOR FAST SINGLE PHOTON DETECTION

4

Potential of the Cherenkov effect for improved time resolution at low γ -photon energies

The major motivation for this thesis is the improvement of time resolution of gamma-photon detectors as they are applied in TOF-PET. The idea of the TOF principle for improvement of PET was already object of intensive research in the 1980s (57). In this period time resolutions of 160 ps were already achieved for a single coincidence detector using BaF₂ crystals and system time resolutions reached already down to 470 ps (57). However, problems of hygroscopic crystals, drifting electronics and inferior spatial resolution led the development of the TOF method stop (4). In recent years, however, developments in material science and detectors initiated a renaissance of research on the TOF-method (57).

Best timing performance is not only in TOF-PET, it is also desired in many detectors in high energy physics, e.g. applications of TOF-detectors for particle-identification and Cherenkov detectors for momentum determination. However, at energies close to the Cherenkov threshold the number of emitted photons tends towards zero. Therefore, one problem of Cherenkov detectors is the poor photon yield. Nevertheless, this effect provides outstanding good timing performance as the emission of Cherenkov photons is almost instantaneous. In this chapter the potential of the Cherenkov effect for improvement of TOF-PET, scintillation- and Cherenkov detectors at photon energies of 511 keV for achieving time resolutions below 100 ps is investigated. This will be done by

4. POTENTIAL OF THE CHERENKOV EFFECT FOR IMPROVED TIME RESOLUTION AT LOW γ -PHOTON ENERGIES

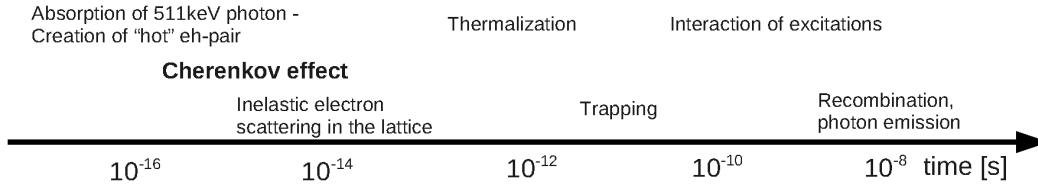


Figure 4.1: Time line of relaxation processes in inorganic scintillators following the interaction of an 511 keV photon by the photoelectric effect.

showing two possible ways: either application of the Cherenkov effect in combination with scintillation or using the Cherenkov effect as only light emitting process. As many of the considerations for the time resolution of scintillation are also valid for Cherenkov detectors, investigations on the timing performance of scintillation detectors are presented, including simulations and experiments showing the potential of the Cherenkov effect for improvement of time resolutions of such detectors.

So far, usually PMTs are used for photon detection in PET-like detectors. As there are some advantages of solid state detectors, such as compactness, robustness, low bias voltage, insensitivity to magnetic fields, photon counting capabilities of SiPM, they tend to replace traditional photo-detectors in an increasing number of applications. On the other hand, SiPM also come with drawbacks such as high temperature sensitivity and high dark-count rates. Especially for single photon detection, the influence of dark-counts is a crucial topic. It will be shown, that these drawbacks can be overcome in a laboratory coincidence setup and prove the feasibility of exploiting Cherenkov emission at photon energies of 511 keV.

4.1 Cherenkov photons for TOF-PET

As discussed in section 1.2, if a charged particle with a velocity v is faster than the speed of light c/n (n is the refractive index, c the speed of light in vacuum) in nonconductive matter, Cherenkov radiation can be emitted. In inorganic scintillators, as they are used for PET, scintillation photons are emitted after the interaction of a 511 keV annihilation photon with the scintillator, leaving an inner shell hole and an energetic primary electron, which is followed by a cascade of energy relaxation processes: radiative (secondary Xrays) and nonradiative decay (Auger processes), inelastic electron-scattering

in the lattice, thermalization, electronphonon interactions, trapping of electrons and holes and energy transfer to luminescent centers. All these processes contribute to an additional time spread of the emission of scintillation photons (21; 22; 23).

The kinetic energy of electrons after photoelectric interaction with 511 keV photons is dependent on their binding energy in the material and ranges from about 450 keV - 510 keV, being sufficiently high for the emission of Cherenkov photons. Since Cherenkov photons are emitted during the phase of electron scattering already, most of the thermalization processes are bypassed and hence they are emitted almost instantaneously with a precise timestamp compared to scintillation photons, see figure 4.1 (22). This precise timestamp leads to improved timing resolution and finally results in better SNR for TOF-PET.

Using the Cherenkov effect for improving the time resolution of TOF-PET has become subject of investigations within the last years (34; 58; 59). The potential for the extent of improvement in coincidence time resolution (CTR) of PET and, thus, in signal-to-noise ratio (SNR) is promising and has been investigated in more detail in references (60; 61).

4.1.1 MC-simulation environment

As a first step the yield of Cherenkov photons in standard scintillators and glasses was determined by simulation. For the simulation Geant4, v9.4.p3 was used employing the Geant4-Livermore libraries for electromagnetic processes. The geometry of the simulation was chosen as simple as possible in order to keep the number of parameters influencing the results low. The input parameters of the investigated materials are shown in table 4.1.

Also the geometry of the simulated setup was kept as simple as possible and can be seen in figure 4.2. It consists of two cubes of $3 \times 3 \times 3 \text{ mm}^3$ of the detector material arranged on a line with a photon source in between. Within this section also different crystal lengths will be investigated, but all of them have a base area of $3 \times 3 \text{ mm}^2$. For all following simulations, perfectly polished faces of the crystals were assumed. The simulated photon source, emits two photons back-to-back with an energy of 511 keV onto the centre of the cubes. Behind the cubes a sensitive detector is placed representing an idealised photo detector, which means a photo detector with a time resolution of zero and a quantum efficiency of one. The refractive index of the detector was assumed

4. POTENTIAL OF THE CHERENKOV EFFECT FOR IMPROVED TIME RESOLUTION AT LOW γ -PHOTON ENERGIES

Material	Density [g/cm ³]	n	λ_1 [nm]	LY [photons/MeV]
LSO:Ce	7.4	1.82	390	27300
LuAG:Ce	6.7	1.84	260*	14000
BGO	7.13	2.15	310	8000
PWO	8.28	2.2	340	210
Pb-glass	5.05	1.79	340**	-

Table 4.1: Input values for calculations and simulations (61) ©2014 IEEE. λ_1 is the lower cutoff wavelength and LY is the light yield due to scintillation. *For transmission the wavelength bands (λ_1 - λ_2) 260 nm - 320 nm, 360 nm - 420 nm and 480 nm - 1000 nm are used (λ_1 is the lower, λ_2 is the upper cutoff wavelength). **Estimated value.

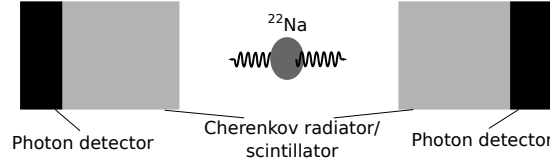


Figure 4.2: Basic coincidence setup used for the Geant4 simulation studies. The Cherenkov radiators/scintillators have a size of 3 mm \times 3 mm \times 3 mm, the photon detector attached has a sensitive surface of 3 mm \times 3 mm (61). ©2014 IEEE.

to be 1.4, which corresponds to the value of a typical optical grease which is used for matching the refractive indexes with the surface coating of photo detectors (e.g. n of BC-630 from Saint-Gobain crystals is 1.465 (62)).

4.1.2 Cherenkov photon yield

Parts of this section were published in (61) and can be found in appendix 7.2. The presented parts are the work of the author of the thesis.

In the following, the expression Cherenkov yield refers to the number photons created by the Cherenkov effect and the scintillation yield refers to the number of photons created by scintillation, their sum is referred to as photon yield. An event is defined as the photoelectric interaction by a 511 keV photon with the detector material.

The number of Cherenkov photons, N , emitted after a charged particle, propagating faster than the speed of light in a dielectric medium, can be determined using

$$\frac{dN^2}{dx d\lambda} = \frac{2\pi z^2 \alpha}{\lambda^2} \cdot \left(1 - \frac{1}{\beta^2 n^2(\lambda)}\right), \quad (4.1)$$

with the range of the electron in the medium x , the charge of the particle (in terms

4.1 Cherenkov photons for TOF-PET

Material	estimation		simulation	
	created photons	created photons	created photons	detected photons
LSO:Ce	18	13.8	13.8	1.1
LuAG:Ce	27	24.3	24.3	7.2
BGO	28	32.8	32.8	4.6
PWO	23	22.6*	22.6*	3.8*
Pb-glass	29	20.9*	20.9*	3.3*

Table 4.2: Estimated and simulated Cherenkov photon yield per photoelectric interaction of a 511 keV photon (61). *Compton scattering is included for these values ©2014 IEEE

of elementary charges) z , the fine structure constant α , the velocity of the particle (in terms of the speed of light, c) β and the refractive index $n(\lambda)$ which is dependent on the wavelength λ (20; 33). This equation was used to estimate the Cherenkov yield in a first step. For this estimation, the electron ranges were determined using the NIST-Estar database (63), which is based on the continuous slowing down approximation. The electron propagates through the material, starting with an energy determined by the initial photon energy (511 keV) subtracted by the binding energy of the electron. For simplicity, the energy of a K-shell electron of the heaviest atom of the compound of the material was used, as this electron has the largest cross-section for photoelectric interaction. The binding energies were taken from (64). As the electron propagates through the medium it loses energy until the Cherenkov threshold $\beta_{\text{thr}} = 1/n$ is reached. The energy of the threshold, E_{thr} can be calculated using equation

$$E_{\text{thr}} = m_e c^2 \cdot \left(\frac{1}{\sqrt{1 - \beta_t^2}} - 1 \right) \quad (4.2)$$

with m_e being the electron mass. By subtracting the electron range at the initial energy by the remaining propagation path at the threshold energy, the path length x , above the Cherenkov threshold was determined. Using this range and the cut-off wavelengths shown in table 4.1 the number of Cherenkov photons can be determined with equation 4.1. It has to be noted that this calculation represents an approximation of the actual Cherenkov yield. The results of this basic calculation are given in table 4.2. The estimation was done to get a rough value of the amount of expected Cherenkov photons in various materials. In a next step, the previously presented MC-simulation was performed, to get a more accurate idea about this value.

4. POTENTIAL OF THE CHERENKOV EFFECT FOR IMPROVED TIME RESOLUTION AT LOW γ -PHOTON ENERGIES

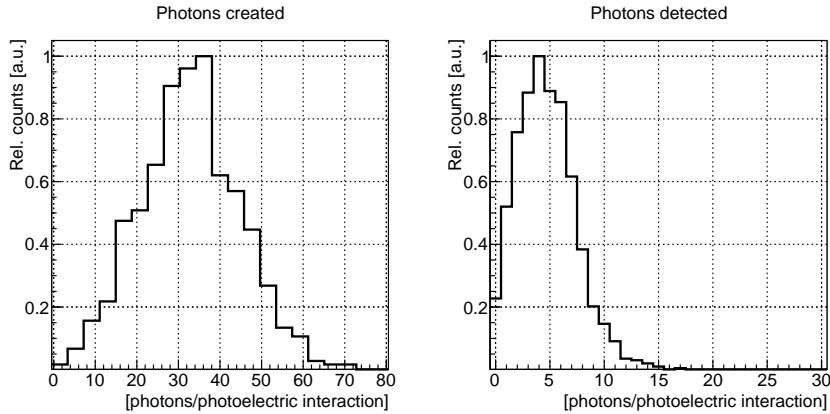


Figure 4.3: Left: number of Cherenkov photons created after photoelectric interaction of 511 keV photons with a cube of BGO with 3 mm edge length. Right: number of detected Cherenkov photons with a photon detector of 3 mm \times 3 mm, attached to the cube (61).
 ©2014 IEEE

For the MC-simulation both the scintillation and Cherenkov photons which were created inside the material and detected by the photo detectors were counted separately. An example plot of the Cherenkov photon yield can be seen in figure 4.3. Only events were the 511 keV photon interacted with the detector material by the photoelectric effect were considered (events where Compton scattering occurred were discarded).

In figure 4.3 an example Cherenkov yield spectrum of BGO can be seen. When comparing the left and the right plot one can see that many Cherenkov photons are lost during propagation through the material. The numbers of calculated, created and detected Cherenkov photons are given in table 4.2.

Discussion When looking at the numbers of table 4.2 the discrepancy of calculated and created number of Cherenkov photons is obvious. This difference is caused by the fact that the calculation was just an estimation using some simplifications and thus giving just the order of magnitude of the Cherenkov yield. Furthermore, the high losses of Cherenkov photons in this simulation, when comparing the created and the detected number of photons, is result of two effects: photons leaving the crystal and absorption inside the crystal. Losses due to propagation outside of the material could be reduced by wrapping of the detector with, e.g. Teflon[®] tape. Absorption inside the detector material is a major problem. This is caused by the fact, the intensity of Cherenkov emission is $\propto 1/\lambda^2$, which means most of the Cherenkov photons are emitted in the blue

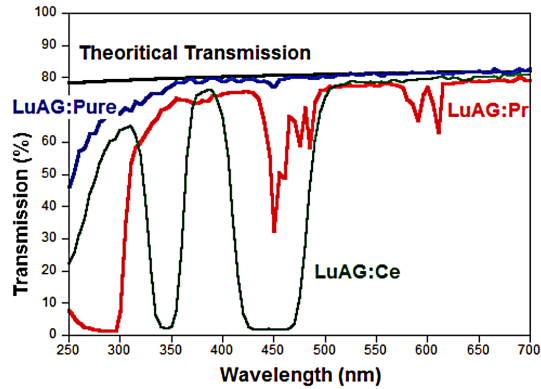


Figure 4.4: Transmission spectrum of LuAG with Ce, Pr and without doping. The influence of the dopands on the transmission becomes obvious, when comparing the spectra (37).

and UV-region of the optical light spectrum. Many scintillators are not transparent in these regions and therefore many Cherenkov photons cannot arrive at the detector.

In all investigated materials Cherenkov photons were created, with the lowest value for LSO:Ce and the highest Cherenkov yield for BGO. Furthermore, the most Cherenkov photons reached the detector for LuAG:Ce. However, it has to be noted that most of the photons which arrived at the photo detector have a wavelength of 260-330 nm. A solid state detector usually has the highest detection efficiency around 420 nm with a fast drop towards lower wavelengths. Looking at figure 4.4 it can be seen that for a real detector much less photons can be expected, due to the absorption bands of LuAG:Ce. Contrary to that, BGO shows a moderate Cherenkov detection yield in the simulation, however, it probably would be more suitable for hybrid Cherenkov photon and scintillation detection than LuAG:Ce due to its good transmission properties down to wavelengths of ~ 310 nm.

The transmission spectra of, e.g., LSO:Ce or LuAG:Ce, have major absorption bands in the main wavelength region of Cherenkov emission, which can be seen for the case of LuAG in figure 4.4 (37). In this figure it can be seen that pure LuAG has a high transmission over the whole displayed wavelength region. By doping the material absorption bands are appearing for both, the Pr doped and especially for the Ce doped crystals. Cherenkov photons (and also scintillation photons) at these wavelengths are absorbed and re-emitted at higher wavelengths by scintillation. This effect is called

4. POTENTIAL OF THE CHERENKOV EFFECT FOR IMPROVED TIME RESOLUTION AT LOW γ -PHOTON ENERGIES

self-absorption (65). Thus, when this effect occurs, the good intrinsic time resolution of the Cherenkov emission cannot be used any more.

4.1.3 Potential Cherenkov radiators

Cherenkov emission after the photoelectric effect of a 511 keV annihilation-photons should occur for almost all transparent dielectric materials. As the Cherenkov photon yield at these low energies is very small the yield of Cherenkov photons needs to be high. With respect to equation 4.1, materials should also offer a high refractive index, transmission at short wavelengths and a long radiation length. In first order the long radiation length can be realized by a low electron density Z_{eff} of the material, but at the same time this would lead to an decreased probability for photoelectric absorption of the 511 keV annihilation-photons. Due to this trade-off, materials with a short radiation length were investigated in order to provide a high interaction probability for the 511 keV photons. Additionally, a detector with a high density material could be build more compact and therefore the time spread due to photon propagation could be decreased.

4.1.4 Hybrid Cherenkov radiators/scintillators

In this work hybrid Cherenkov radiators/scintillators are scintillators with a detectable Cherenkov photon emission for 511 keV photons. In the previous section materials, such as LSO:Ce, LuAG:Ce, BGO and PWO were investigated and compared in terms of their Cherenkov emission. Using MC-simulations it was shown that all of them should show detectable Cherenkov photon emission. On the left hand side of figure 4.5, the transmission spectra for the investigated hybrid Cherenkov radiators/scintillators are plotted for comparison (37; 66). LuAG:Ce shows two absorption bands due to the Ce doping, with one of them between ~ 400 -490 nm, which is the most sensitive region for many photo detectors, as discussed before. Therefore, just a few Cherenkov photons are expected for this material. More Cherenkov photons are expected for LSO:Ce and especially BGO. The transmission of the pure Cherenkov radiator LuAG is included for comparison.

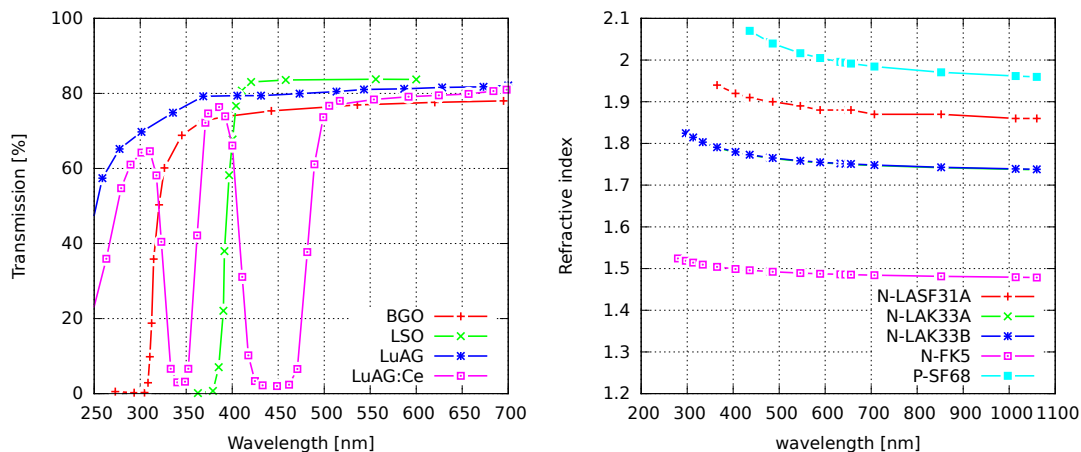


Figure 4.5: Transmission of the investigated hybrid Cherenkov radiators for samples with lengths of 1.5 times the radiation length, except for the data of LuAG which is for a sample length of 10 mm (37; 66). The wavelength dependent distribution of the refractive index is drawn for several pure Cherenkov radiators on the right hand side. The refractive index for LuAG is 1.84 at 436 nm (37; 67).

4.1.5 Pure Cherenkov radiators

Pure Cherenkov radiators are defined here as crystals or glasses which show good properties for Cherenkov photon emission but do not show scintillation at the same time. In this section some of these materials which show promising characteristics like high density, high refractive index and transparency in the blue and UV range are investigated. An important parameter influencing the Cherenkov photon yield is the refractive index as the number of emitted Cherenkov photons is $\propto 1 - \frac{1}{n^2}$. Therefore, the refractive index of the material should be as large as possible. The refractive indexes for the materials are plotted in figure 4.5 on the right hand side. Unfortunately no measurement for the refractive index of LuAG over the whole transmission region could be found but only two values. One at 193 nm which is 2.14 (68) and another one at 436 nm, which is 1.84 (37). These values were used for the following MC-simulations of LuAG.

A comparison of the transmission spectra for optical photons is plotted in figure 4.6. It can be seen, that all materials reach a transmittance of ~ 1 at some point except for the transmittance of LuAG, which saturates at a value of ~ 0.8 . Nevertheless, this material shows the lowest cut-off wavelength and highest density of the investigated materials. For comparison the normalised PDE of the Philips DPC3200 was plotted as filled curve in the background, the maximum of this curve has a PDE of $\sim 37\%$ (55).

4. POTENTIAL OF THE CHERENKOV EFFECT FOR IMPROVED TIME RESOLUTION AT LOW γ -PHOTON ENERGIES

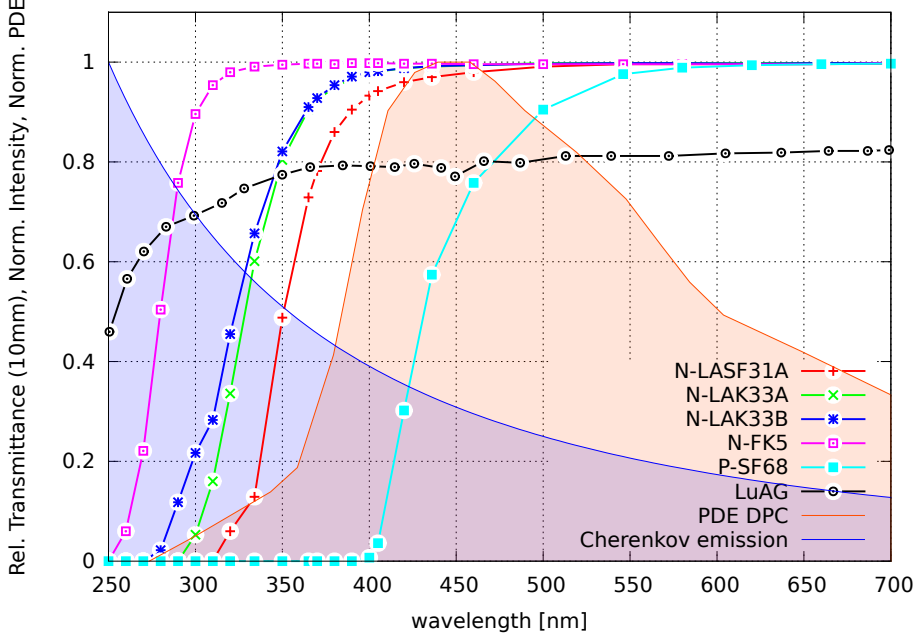


Figure 4.6: Transmittance of several potential Cherenkov radiators. The transmittance is measured after 10 mm of the material. In the background the normalised PDE of the Philips DPC3200 is drawn, the value of the PDE at the maximum is $\sim 37\%$ (37; 55; 67). Additionally, the distribution of the wavelength dependent relative Cherenkov photon emission proportional to $\frac{1}{\lambda^2}$ is drawn in the background.

This curve was added to the figure as this detector will be used for measurement in the following chapter. It can be seen that most of the materials have cut-off wavelengths lower than the most sensitive region of the DPC3200. Its sensitivity reaches below 300 nm, which is important as the wavelengths of Cherenkov emission is increasing with decreasing wavelength. The intensity of the Cherenkov emission is $\propto \frac{1}{\lambda^2}$ and is plotted additionally in figure 4.6 (20).

These data were applied in a MC-simulation on the Cherenkov photon yields using the MC-simulation environment presented in section 4.1.1. The base of the simulated materials was $3 \times 3 \text{ mm}^2$ and the lengths were 3 mm and 10 mm, respectively. For the simulation some assumptions needed to be made: first, the compositions of the glasses were not known. Therefore, the material was assumed to be SiO_2 , but the densities given in table 4.3 were used for the simulations. As a consequence, the detection efficiency of the materials could not be determined. Furthermore, this assumption influences the determined Cherenkov photon yield in way that the electron ranges are

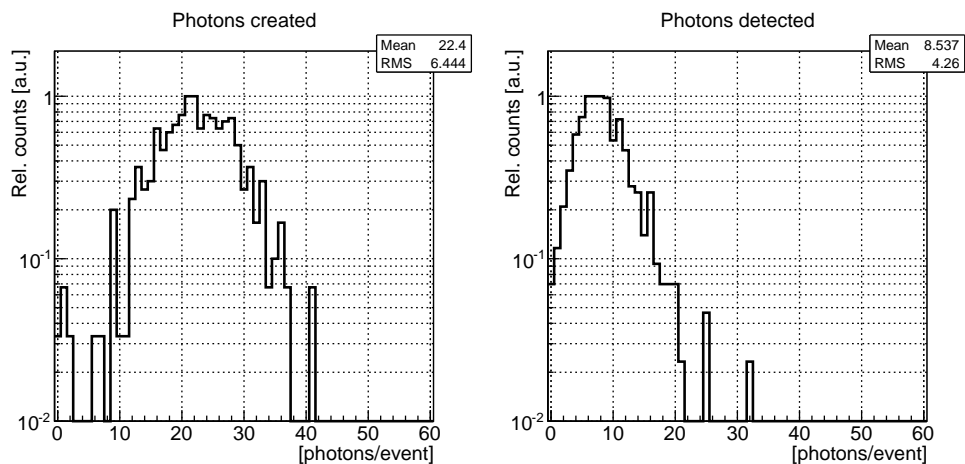


Figure 4.7: Example of the number of created (left) and detected (right) number of photons for a pixel of N-LAK33A with the size of $3 \times 3 \times 10 \text{ mm}^3$.

dependent on the effective electron density Z_{eff} . Nevertheless, the photon yields can be compared and give an idea of the influence of the UV-transmission and densities on the number of detected Cherenkov photons.

Figure 4.7 shows an example of the created and detected number of Cherenkov photons for a 10 mm long sample of N-LAK33A. A summary of the resulting mean values of created and detected Cherenkov photons are given in table 4.3. Among the compared materials, the crystal length shows a large influence on the photon yields of LuAG. A reason might be that LuAG was the only material whose composition known exactly. As discussed, all other materials were assumed to be SiO_2 . Furthermore, the refractive index for LuAG was set to be 1.84 at 436 nm and 2.14 at 193 nm (37; 68). The transmission at a wavelength of 193 nm was assumed to approach zero, as adequate data on the transmission at this wavelength was missing. Besides these assumptions for LuAG, the low numbers of detected photons are mainly caused by the bad transmission of this material which is at maximum ~ 0.8 for 10 mm long crystals. All other materials approach transmission values of about 1. One has to note that the value for the created Cherenkov photons of undoped LuAG deviates from the simulated value for LuAG:Ce, presented previously in table 4.2. That is simply caused by the lower cut-off frequency for undoped LuAG compared to LuAG:Ce.

Considering the characteristics of the materials, P-SF68 would be a good candidate for a Cherenkov radiator due to its high density and high refractive index, but has

4. POTENTIAL OF THE CHERENKOV EFFECT FOR IMPROVED TIME RESOLUTION AT LOW γ -PHOTON ENERGIES

Material	density [gcm ⁻³]	n (@436nm)	lower cutoff wavel. [nm]	creat. photons	detected photons	
					3 mm	10 mm
N-LAK33A	4.22	1.77	300	22.4	13.7	8.5
N-LAK33B	4.22	1.77	280	24.9	14.5	8.5
N-FK5	2.45	1.5	260	26.1	14.6	13.2
N-LASF31A	5.51	1.91	310	19.6	12.1	5.5
P-SF68	6.19	2.07	400	12.8	8.4	3.0
LuAG pure	6.73	1.84	180	32	10.6	4.8

Table 4.3: List of promising Cherenkov radiators and their characteristics (37; 67; 68). Using these data the number of created Cherenkov photons (creat. photons) and the number of Cherenkov photons reaching the photo detector for 3 mm and 10 mm long radiators, both with a base of $3 \times 3 \text{ mm}^2$ were simulated. The optimal photo detector was attached to the face at the far side in respect to the incoming 511 keV photons and had a size of $3 \times 3 \text{ mm}^2$.

unfortunately a cut-off wavelength at $\sim 400 \text{ nm}$ which leads to a low number of detected Cherenkov photons. On the contrary, N-FK5 would have a very low cut-off wavelength but on the other hand it has a low density, resulting in a low detection efficiency of the 511 keV annihilation photons. Therefore, a material with the best trade-off of the parameters need to be found.

4.1.6 Influence of density and UV-transmission

In the following the trade-off relation of density, refractive index and UV-transmission of the Cherenkov radiator is studied in the multi parameter space using the detectable number of photons as a figure of merit. This was again done using the previously presented simulation environment. For the parameter scan the glass N-LAK33A as one example of a pure Cherenkov radiator was chosen. The parameters shown in table 4.3 and figure 4.6 were used and the UV transmission shifted from the real value by $\pm 40 \text{ nm}$. Furthermore, the refractive index was varied in the range from 1.4 to 2.3 in steps of 0.1. The results on the influence of these parameter scans on the number of detected Cherenkov photons is shown in figure 4.8. It can be seen that the number of Cherenkov photons increases with increasing refractive index and with decreasing cut-off wavelength (wavelength-shift) and behaves as expected. It can be seen, that the shift of the cut-off becomes more influencing at high refractive indexes.

Additionally, the density of the material was varied. The results for the real density

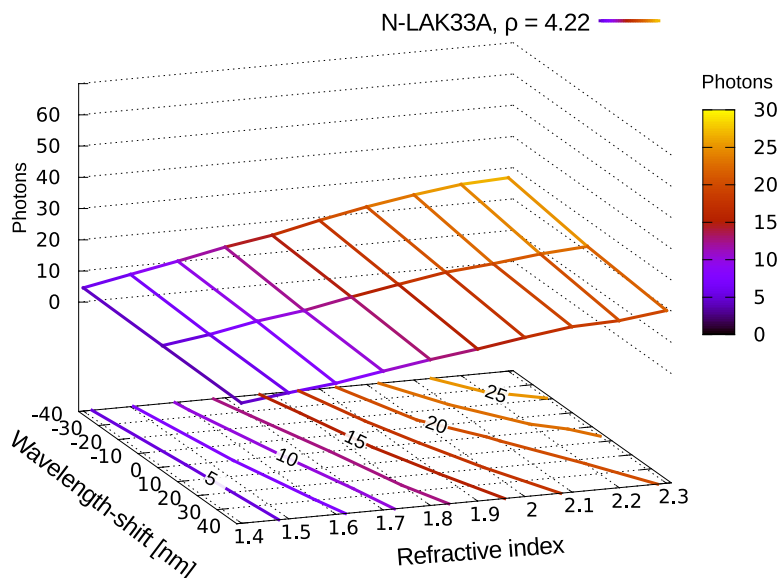


Figure 4.8: Simulated number of detected photons using $3 \times 3 \times 3 \text{ mm}^3$ long pixel of N-LAK33A with a density of 4.22 g cm^{-3} and a refractive index of 1.77 at 436 nm. The parameters refractive index and the cutoff wavelength were varied for studying their influence on the Cherenkov photon yield. A wavelength shift of 0 nm refers to the real cut-off frequency. The grid on top of the figure represents the determined photon numbers, whereas the isolines below represent interpolated data from the data above.

of the material was already shown in figure 4.8, additionally the parameter scans for densities of $\rho = 4.22 \pm 1 \text{ g/cm}^3$ are drawn in figure 4.9. It can be seen that the density has big influence on the number of detected photons as the radiation length increases for lower densities. Again the determined values behave as expected.

As one can see from figures 4.8 and 4.9, the highest Cherenkov photon yields were achieved at a low density of the material. This, however, would result in a low detection efficiency for the 511 keV photons and thus, is no favourable solution as detector material. This trade-off could be compensated to a certain extent by decreasing the UV-transmission of the material. Furthermore, a detector with high QE in the UV region would be needed to maximise the Cherenkov yield. Detectors like the Philips DPC offer sensitivity down to $\sim 300 \text{ nm}$ and therefore detection of a sufficient number of Cherenkov photons could be expected.

4. POTENTIAL OF THE CHERENKOV EFFECT FOR IMPROVED TIME RESOLUTION AT LOW γ -PHOTON ENERGIES

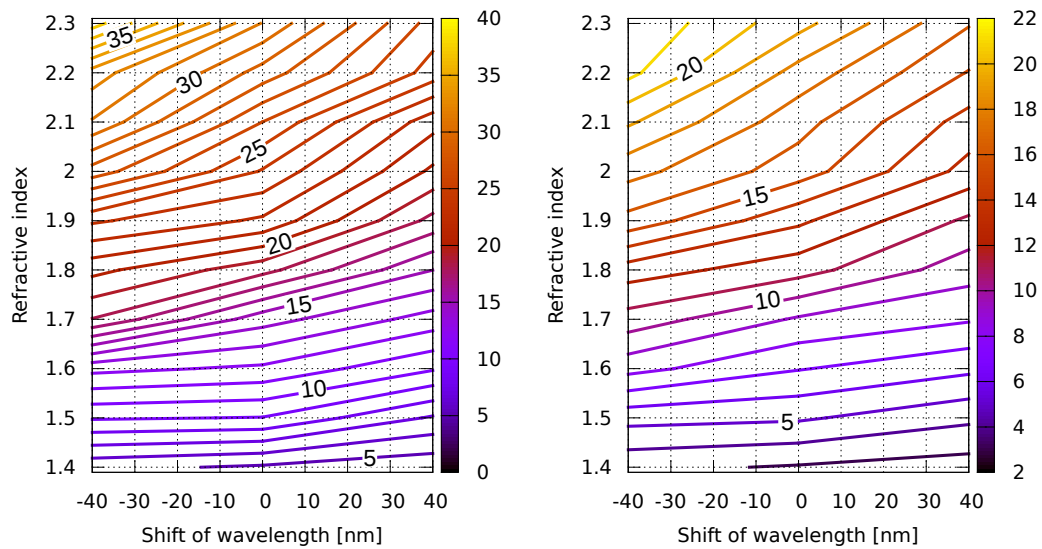


Figure 4.9: Parameter scans of the $3 \times 3 \times 3 \text{ mm}^3$ large pixel of N-LAK33A at various densities. On the left hand side the parameter scan for a density of 3.22 g/cm^3 is drawn on the left hand side and for a density of 5.22 g/cm^3 on the right hand side. The Cherenkov yield for the real density of the material of 4.22 g/cm^3 is shown in figure 4.8.

4.2 Factors influencing the time resolution of scintillation and Cherenkov photon detectors

As discussed, a scintillation/Cherenkov detector can be grouped into three major parts: scintillator/radiator, photo detector and electronics. As the timing performance of the photo-detector part and the influence of the material parameters were already investigated, the following sections will focus on the time resolution of the scintillator/Cherenkov-radiator part.

4.2.1 Influence of the photon statistics

The photon statistics describes the distribution of creation times of luminescent processes such as scintillation or Cherenkov radiation. Depending on the nature of luminescence various statistical models can be used to describe the photon emission. The main parameters describing the photon statistics are the overall light yield and the rise and decay times of the luminescence process.

In previous works the importance of including the rise time into the photon statistics has been shown (16; 34; 59) which are based by investigations of (69; 70; 71; 72). The lower bound of the time resolution of scintillation detectors was already determined in (16). In this section an approach of using order statistics will be presented. This approach is motivated by the use the information of several timestamps of the Philips DPC but is applicable also for other detectors.

Assuming N random variables x_1, x_2, \dots, x_i describing the arrival times of N photons belonging to the same scintillation (luminescence) event started at a time θ . Let's further assume that the random variables are independent and identically distributed (i.i.d.) and are described by the probability density function (PDF) $f(x|\theta)$. For many scintillation processes it is sufficient to describe the energy transfer and the radiative decay by two exponential functions (16; 73). The PDF $f(x|\theta)$ can be written then as

$$f(x|\theta) = \begin{cases} \sum_i \frac{P_i}{\tau_{d,i} - \tau_{r,i}} \left[e^{-\frac{x-\theta}{\tau_{d,i}}} - e^{-\frac{x-\theta}{\tau_{r,i}}} \right], & \text{for } x \geq \theta \\ 0, & \text{else} \end{cases} \quad (4.3)$$

when only looking at one possible scintillation mechanism $i=1$. The rise time and the

4. POTENTIAL OF THE CHERENKOV EFFECT FOR IMPROVED TIME RESOLUTION AT LOW γ -PHOTON ENERGIES

decay time are τ_r and τ_d respectively. The CDF $F(x|\theta)$ can be written as (16)

$$F(x|\theta) = \sum_i \frac{P_i}{\tau_{d,i} - \tau_{r,i}} \left(\tau_{d,i} - \tau_{r,i} - \tau_{d,i} e^{-\frac{x-\theta}{\tau_{d,i}}} + \tau_{r,i} e^{-\frac{x-\theta}{\tau_{r,i}}} \right). \quad (4.4)$$

Let $x_{[n_1]}, x_{[n_2]}, \dots, x_{[n_k]}, x_{[n]}$ be the ordered set of random variables describing the arrival time of the first up to the n^{th} photon. The joint PDF of $X_{(n_1)}, \dots, X_{(n_k)}$ ($1 \leq n_1 < \dots < n_k \leq n$) for $x_1 \leq \dots \leq x_k$ and $x_0 = -\infty, x_{k+1} = +\infty, n_0 = 0, n_{k+1} = n + 1$ can be written as

$$L(\theta) = g_{(n_1)\dots(n_k)} = n! \cdot \left[\prod_{j=1}^k f(x_j) \right] \cdot \prod_{j=0}^k \left\{ \frac{[F(x_{j+1}) - F(x_j)]^{n_{j+1} - n_j - 1}}{(n_{j+1} - n_j - 1)!} \right\}, \quad (4.5)$$

which represents the maximum likelihood function $L(\theta)$. The best estimator $\hat{\theta}$ for the interaction time θ can then be determined by

$$\hat{\theta} = \arg \max L(\theta) \quad (4.6)$$

Approaches for solutions of this equation have been presented in (13; 16).

Applying $f(x|\theta)$ to a simulation, which was presented in section 3.4.1, the influence of the scintillator parameters and trigger levels can be determined. For the probability density function $f(t)$ equation 4.3 was used. The influence of the light yield and the trigger threshold on the CTR is shown in figure 4.10. The plot shows the simulated CTR with increasing number of photons and for various thresholds, when only the photon statistics is taken into account. For this simulation a rise time τ_r of 0.1 ns and a decay time τ_d of 40 ns were used. It can be seen, that the CTR improves with the number of detected photons and worsens with increasing threshold. It has to be noted that no influence of photon propagation or the photo detector is included.

4.2.2 Comparing the time precision of scintillation and the Cherenkov effect

By simulation of the creation and arrival time distribution of the Cherenkov effect and knowing the Cherenkov photon yield, the expected time precision of the Cherenkov effect can be determined. To do so, another analytic approach for determination the time precision is presented in the following.

4.2 Factors influencing the time resolution of scintillation and Cherenkov photon detectors

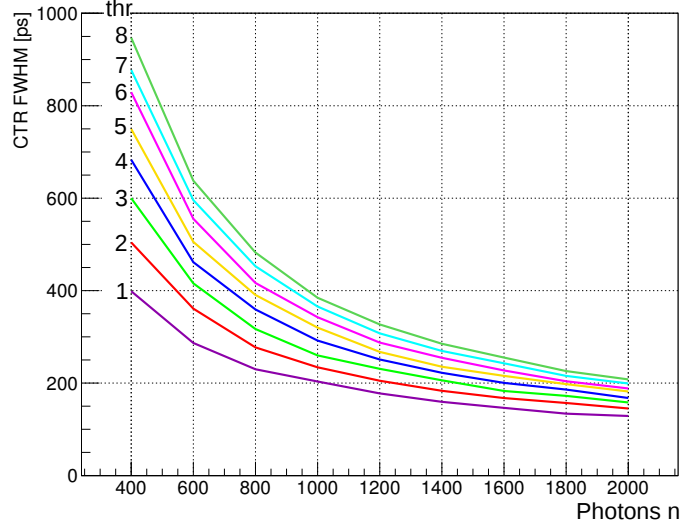


Figure 4.10: Simulated CTR for thresholds (thr) ranging from 1 to 8 and increasing photon numbers n . The simulation is only based on photon statistics. As scintillation constants $\tau_r = 0.1$ ns, $\tau_d = 40$ ns were used.

In (34) a model for estimation of the time precision of scintillators based on the works by (35; 70; 71; 74) was presented. Variable parameters are rise- and decay times of the scintillator and the light yield. The probability density function $f(t)$ and the cumulative distribution function $F(t)$ for a scintillation pulse were already determined and are given in equation 4.3 and 4.4. Same as before only the contribution of the photon statistics is determined. All other effects, namely, photon transport or transit time spread of the photon detector are ignored and will be discussed later. For the model, a photon detector with perfect detection efficiency and the possibility of single photon detection is assumed. Furthermore, a discriminator with a threshold level Q , measured in number of photons is assumed. The expected number of photons follows the PDF $f(t)$ within $t = 0$ and t . The total photon yield for $\lim_{t \rightarrow \infty}$ is R .

With these assumptions the probability that Q photons are detected within $t = 0$ and t is given by the Poisson distribution

$$P(Q, t) = \frac{f(t)^Q e^{-f(t)}}{Q!}. \quad (4.7)$$

Furthermore, the probability density $W(Q, t)$, that the Q^{th} photon is detected within t

4. POTENTIAL OF THE CHERENKOV EFFECT FOR IMPROVED TIME RESOLUTION AT LOW γ -PHOTON ENERGIES

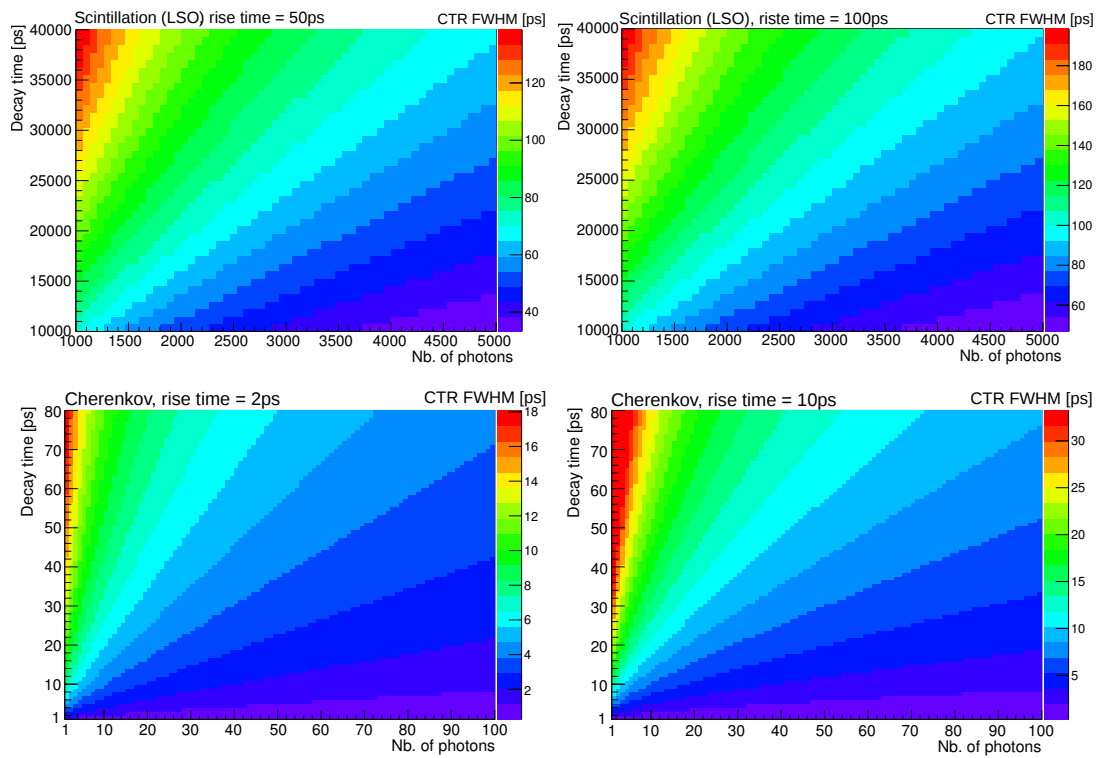


Figure 4.11: Calculated CTR due to photonstatistics according to the presented model in terms of FWHM. On top parameters are chosen to cover the range of LSO, on the left hand side with a rise time of 50ps and on the right hand side with a rise time of 100 ps. The parameters for the two plots on the bottom are chosen to cover the parameter range for Cherenkov emission. On the left hand side the CTRs are calculated for a rise time of 2ps, on the right hand side for a rise time of 10 ps.

4.2 Factors influencing the time resolution of scintillation and Cherenkov photon detectors

and $t+dt$ depends on the probability that $(Q - 1)$ photons arrive until t (34; 35). The probability density can then be written as

$$W(Q, t) \cdot dt = P_{Q-1}(t) \cdot \frac{df}{dt} dt. \quad (4.8)$$

According to (69) and (72) the time precision t_Q of the Q^{th} photon is $arg\ max_t W(Q, t)$.

The expected CTRs in terms of FWHM is dependent on the decay time τ_d and rise time τ_r and is plotted in figure 4.11. On top of this figure, a scenario similar to the parameters of LSO is shown. The light yield of LSO is typically ≈ 30000 photons/MeV, $\tau_r \approx 50$ -100 ps and $\tau_d \approx 40$ ns. It has to be noted that the number of photons represent the number of detected photons after interaction of 511 keV annihilation-photons with an additional loss due to the quantum efficiency of the photo detector, therefore about 3000 photons are expected to be detected for LSO. According to simulations which are presented in section 4.2.10, values for the rise time of $\tau_r \approx 2$ -10 ps and the decay time $\tau_d \approx 10$ -20 ps can be expected. The CTRs for this scenario is shown in figure 4.11 on the bottom. For this case a light yield in the range of 1-10 photons can be expected.

It can be seen in these plots that the CTR improves with increasing number of detected photons and improves for decreasing rise and decay times, which is expected. Comparing the top and the bottom plots it can be seen, that although the photon yield for Cherenkov emission is expected to be within 1–10 photons the calculated CTR is significantly better than for the case of the typical scintillator which can be seen on top of figure 4.11. These results reveal the potential of the Cherenkov emission although a low number of photons is expected.

4.2.3 Time spread of the Cherenkov emission

In a non-dispersive medium the wavefront of the Cherenkov photons can be considered as infinitely thin (20). For dispersive media the Cherenkov angle θ is dependent on the wavelength of emission. As a consequence, the wave trains spread out from each other. According to (20) the duration Δt of the light pulse along a line at a distance ρ (see figure 4.12 on the left hand side) parallel to the axis of the moving charged particle is

$$\Delta t = \frac{\rho}{\beta c} \left(\sqrt{\beta^2 n^2(\lambda_2)} - \sqrt{\beta^2 n^2(\lambda_1)} \right) = \frac{\rho}{\beta c} (\tan \theta_2 - \tan \theta_1) \quad (4.9)$$

4. POTENTIAL OF THE CHERENKOV EFFECT FOR IMPROVED TIME RESOLUTION AT LOW γ -PHOTON ENERGIES

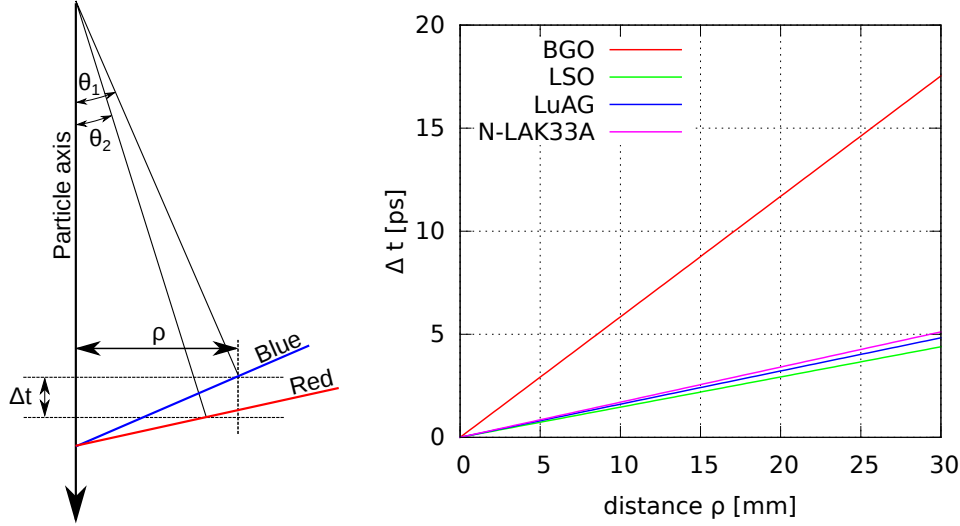


Figure 4.12: Estimation for the duration of a Cherenkov light pulse in a dispersive medium (20). On the left hand side the geometrical considerations and on the right hand side the results of these estimations for 500 keV electrons in several materials in the wavelength region of 400-800 nm.

	BGO	LSO	LuAG	N-LAK33A
$n(\lambda_1)$	2.2186	1.849	1.8686	1.7785
$n(\lambda_2)$	2.0712	1.815	1.831	1.74

Table 4.4: Values for the refractive indexes at $\lambda_1 = 400$ nm and $\lambda_2 = 800$ nm used for estimating the time spread of the Cherenkov emission due to dispersion at a distance ρ (20; 40; 75; 76).

Using this equation, the value of Δt was calculated for electrons with kinetic energies of 500 keV in a wavelength range of $\lambda_1 = 400$ nm to $\lambda_2 = 800$ nm for some materials. The used values for $n(\lambda)$ are given in table 4.4 and the results are shown in figure 4.12, on the right hand side. Values for the refractive indexes are taken from (40; 75; 76).

It can be seen that the values for Δt reach up to 5 ps at a distance ρ of 30 mm except for BGO which shows a much larger influence due to this effect. For short crystals the typical values for ρ are usually below $\rho = 30$ mm (compare with figure 4.20) and therefore the calculated time spread represents an upper boundary for such crystals. But it has to be noted that λ_1 was 400 nm. If decreasing λ_1 , the time spread of the Cherenkov photon detection increases.

4.2 Factors influencing the time resolution of scintillation and Cherenkov photon detectors

4.2.4 Time spread due to electron propagation

The Cherenkov photons are emitted, while the first energetic electrons are propagating to the material. Estimated ranges of the electrons are 200-300 μm (34) Assuming, that the electron is propagating with an velocity higher than the velocity of the Cherenkov threshold velocity $\beta_t = \frac{1}{n}$ one can estimate an upper boundary of the influence of the electron propagation path, by dividing the electron range by the electron velocity at the Cherenkov threshold which results in an additional time spread of $\sim 1-2$ ps.

4.2.5 Influence of the DOI on the time resolution

In a first, step the direct influence of the DOI on the time resolution of scintillation detectors is shown, in a second step the indirect influence due to photon losses during photon propagation is discussed. The results can be applied for both Cherenkov and scintillation detectors.

The DOI is dependent on the absorption coefficient, μ , following the Lambert-Beer-law,

$$I(x) = I_0 e^{-\mu x} \quad (4.10)$$

with I , being the intensity at a location x in the material and I_0 the initial photon intensity. The absorption coefficients for several scintillators for 511 keV annihilation-photons are given in table 4.2.5.

Using this law, the expectation value $E(x)$, which represents the DOI and its variance $Var(x)$ can be calculated. The expectation value in is defined as

$$E(x) = \int_{-\infty}^{\infty} x f(x) dx. \quad (4.11)$$

Interpreting equation 4.10 as the probability density for interaction of a 511 keV photon in a material and adding a normalisation factor $N(x)$, the PDF $f(x)$ is

$$f(x) = N(x) e^{-\mu x}. \quad (4.12)$$

As the expectation value should be calculated for a crystal length, the normalization

4. POTENTIAL OF THE CHERENKOV EFFECT FOR IMPROVED TIME RESOLUTION AT LOW γ -PHOTON ENERGIES

Table 4.5: Absorption coefficients for the photoelectric effect at 511 keV for several scintillation materials (30).

Material	ρ [g/cm ³]	n	μ_{PE} at 511 keV [cm ⁻¹]
LSO:Ce	7.4	1.82	0.28
LuAG:Ce	6.7	1.84	0.205
BGO	7.13	2.15	0.336
PWO	8.28	2.2	0.485

factor becomes

$$N(l) = \frac{1}{\int_0^l f(x)dx} = \frac{1}{1 - e^{-\mu l}} \quad (4.13)$$

Using this equation and $f(x) = 0$ for $x \in (-\infty, 0)$, one obtains

$$E(l) = \frac{N(l)}{\mu} \left(1 - e^{-\mu l} (1 + \mu l) \right). \quad (4.14)$$

Furthermore, the variance of the DOI can be calculated using the definition

$$\text{Var}(x) = \int_{-\infty}^{\infty} x^2 f(x)dx - E(x)^2. \quad (4.15)$$

With this one gets

$$\text{Var}(l) = N(l) \int_0^l x^2 f(x)dx - E(l)^2 = \quad (4.16)$$

$$= \frac{1}{\mu} \left(2E(l) - l^2 e^{-\mu l} \right) - E(l)^2. \quad (4.17)$$

The resulting standard deviation $\sigma(x) = \sqrt{\text{Var}(x)}$ is plotted in figure 4.13 on the left hand side. As the influence of the DOI on the time resolution of scintillators should be determined, the standard deviation can be expressed in terms of a time by dividing by the speed of light in the material, $\sigma(t = \frac{xn}{c})$, with n being the refractive index of the material. For example, a photon emitted at a point $E(x) + \frac{1}{2}\sigma(x)$ needs $\sigma(t = \frac{xn}{c})$ times longer to arrive at the photon detector at $x = 0$ than a photon emitted at $E(x) - \frac{1}{2}\sigma(x)$, when both propagate the shortest possible path to the detector. The values for the standard deviations $\sigma(t)$ are plotted in figure 4.13 on the right hand side for several materials in dependency on the crystal length l . The small plot inside represent a zoom of the same plot for crystal lengths up to 3 cm.

4.2 Factors influencing the time resolution of scintillation and Cherenkov photon detectors

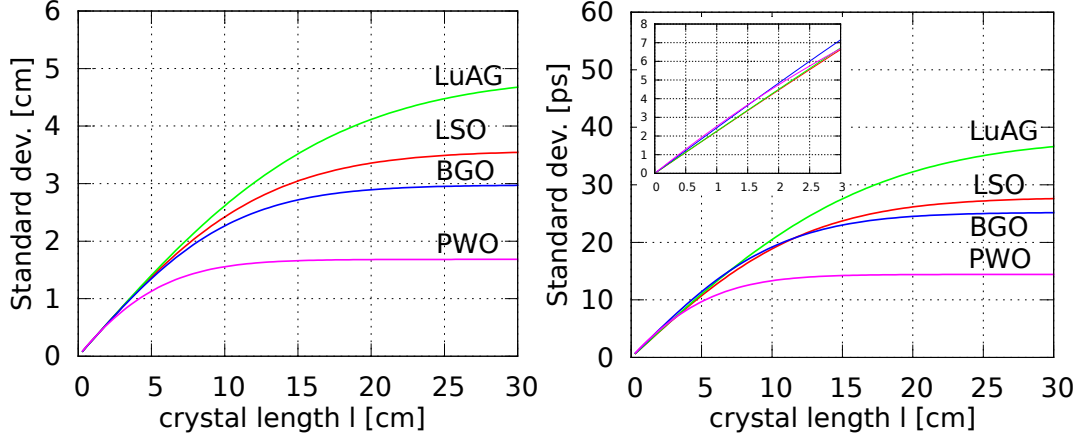


Figure 4.13: Standard deviation due to DOI uncertainty in dependency of the crystal length for several scintillators. On the left hand side, the standard deviation is plotted in terms of cm. On the right hand side the consequence of this standard deviation is plotted in terms of time. In this plot the speed of light in the scintillator $\frac{c}{n}$ is taken into account. The small insert in this plot shows a zoom for the standard deviation in the range of $l = 0-3$ cm.

In figure 4.13 the influence of the DOI on the overall standard deviation of a scintillation detector was determined using an analytical approach. It can be seen that the standard deviation exceeds values of 10 ps for crystals longer than 5 cm. As for photons of 511 keV shorter crystals are sufficient for stopping them, this value is negligible for overall CTRs above 100 ps. When one tries to push the time resolutions towards 10 ps this effect should also be considered.

4.2.6 Influence of the DOI on the signal rise time of analogue photo detectors

A short rise time is one key-parameter for a good time resolution of scintillators and is subject of investigations for improvement of TOF-PET (21; 59; 71; 77).

To investigate the influence of the DOI on the observable rise time an experiment, following the method presented in (77) was performed. Simulations following this approach are shown in section 4.2.9. A picture of the coincidence setup is shown in figure 4.14 on the left hand side. The setup consisted of two R1450 (H3167) PMTs from Hamamatsu with a typical gain of 1.7×10^6 a rise time of 1.8 ns and a transit time spread of 360 ps sigma. The left one was fixed and a LSO:Ce crystal from EPIC crystal (78) with a size of $3 \times 3 \times 16$ mm³ and a polished surface was attached to the

4. POTENTIAL OF THE CHERENKOV EFFECT FOR IMPROVED TIME RESOLUTION AT LOW γ -PHOTON ENERGIES

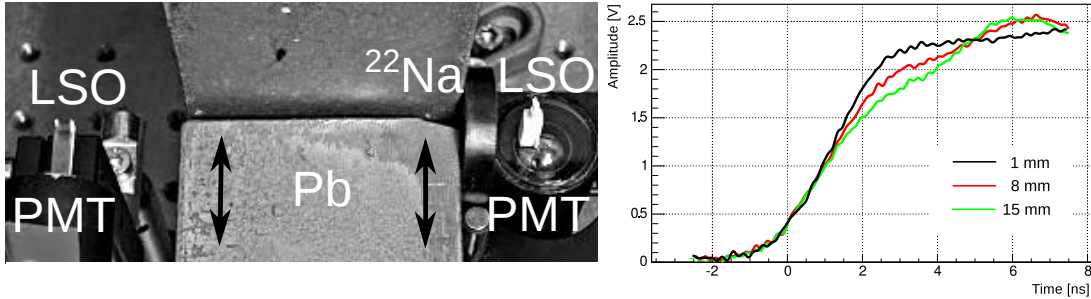


Figure 4.14: Signal distributions for several DOIs in a 16 mm long LSO:Ce crystal. On the left hand side the setup used for the measurement can be seen. The bricks of lead, the ^{22}Na and the right PMT with an $3 \times 3 \times 8 \text{ mm}^3$ LSO:Ce crystal were movable using a stepping motor. Although the intrinsic rise time of the PMTs is rather long, the influence of the photon arrival time distribution is visible in the plot on the right hand side. Here, the rise times for three different distances are plotted. The distances are measured along the arrows in the left picture relative to the entrance window of the left PMT.

PMT using optical grease. The other PMT (right PMT in the picture), the ^{22}Na source, and a slit-collimator made of two bricks of lead were mounted on a rail and could be moved along the rail using a stepping motor. On the right PMT a crystal with a size of $3 \times 3 \times 8 \text{ mm}^3$ with all faces polished and wrapped in Teflon tape was mounted. This crystal was arranged in a way that the longer crystal axis was perpendicular to the axis of the other crystal in order to minimize the effects of photon propagation in this crystal and provide an accurate timestamp. The rise times were measured for three different positions representing the DOI, relative to the entrance window of the left PMT along the arrows in figure 4.14. The signal waveforms were digitised and recorded using a LeCroy WavePro 735Zi digital oscilloscope (bandwidth 3.5 GHz, 40 Gs/s) and the validation thresholds were set above the Compton edges in the area spectrum of the signals of the 511 keV photons. A few thousand coincidences were recorded and the resulting average signal is plotted in the right panel of figure 4.14.

Although, the rise time of the PMTs is large compared to the scintillation rise time of $\leq 100 \text{ ps}$, the averaged signals reveal the influence of the distance on the rise times. When setting the threshold e.g. on a level of one p.e., at the time when the signal reaches the threshold it is already influenced by the contribution of many photons and not just by one. This is the reason why the CTR is hardly improved by the Cherenkov effect when using analogue photo detectors. Contrary to that, it will be shown that using digital photo detectors the CTR can be improved significantly by the Cherenkov

4.2 Factors influencing the time resolution of scintillation and Cherenkov photon detectors

effect. Furthermore, a difference of the signal slopes above 1 V can be seen. This is caused by the influences of photon propagation as it is presented in section 4.2.7. The overall obtained CTRs were of the order of 500 ps FWHM for the setup, which was mainly caused by the large TTS of the PMTs. Due to the bad rise times of the photo detectors and bad CTRs, the influence of the DOI on the rise time is shown here on ly qualitatively.

Nevertheless, the presented qualitative dependency of the rise time and the DOI could be used for determination of the DOI, by measuring the waveform of the signal. This approach is not applicable for standard single threshold techniques but could be feasible with the use of waveform-samplers. By determining the DOI by the rise time, parallax errors in PET could be reduced on the one hand, furthermore, the overall CTR could be improved by applying time-walk corrections as they will be presented in section 4.2.7. Nevertheless, this would need further quantitative investigations. A similar approach was studied in (79) and (80).

4.2.7 Photon propagation and time-walk in a scintillator

Parts of this section have been published in (60) and can be found also in appendix 7.1. The parts used in this section are the work of the author of the thesis.

For investigations on the time resolution of a scintillator, MC-simulations according the environment presented in section 4.1.1 were performed. A crystal of LSO:Ce with $3 \times 3 \times 30 \text{ mm}^3$ with a perfect photo-detector attached to one of the small faces was simulated. The 511 keV photons were shot centrally from the opposite side of the photo detector parallel to the long crystal axis. The used geometry is drawn in figure 4.15. The axis conventions and dimensions are also plotted in this figure, with the z-axis parallel to the beam axis of the 511 keV photons, ranging from -15 mm where the photons enter the crystal to 15 mm where the photo-detector is located. Additionally, the interaction rate of the 511 keV annihilation-photons inside the crystal is drawn. The size of the boxes in the figure is proportional to the interaction rates of the annihilation photons inside the crystal.

The resulting photon arrival times can be seen in figure 4.16 (a). Figure 4.16 (b) shows a scatter plot of the number of optical photons per 511 keV annihilation-photon and the time when the first photon is arriving at the detector. Compton scattered events are discriminated with a discriminator threshold of 1600 photons per event.

4. POTENTIAL OF THE CHERENKOV EFFECT FOR IMPROVED TIME RESOLUTION AT LOW γ -PHOTON ENERGIES

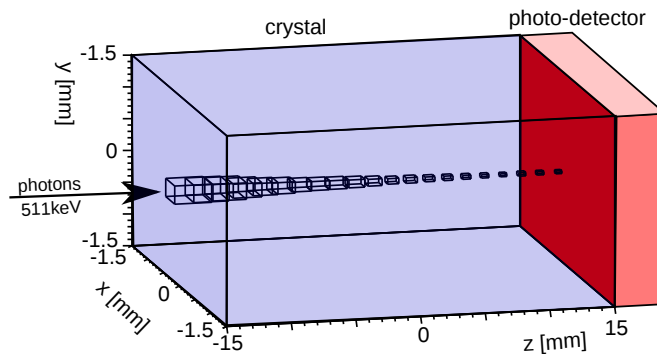


Figure 4.15: Geometry for the simulations of a $3 \times 3 \times 30$ mm. The 511 keV photons are shot from the left side ($z = -15$ mm) and the photo detector is located at the opposite side ($z = 15$ mm). The size of the cubes inside the crystal are proportional to the interactions of the 511 keV photons inside the crystal at the position of the cubes.

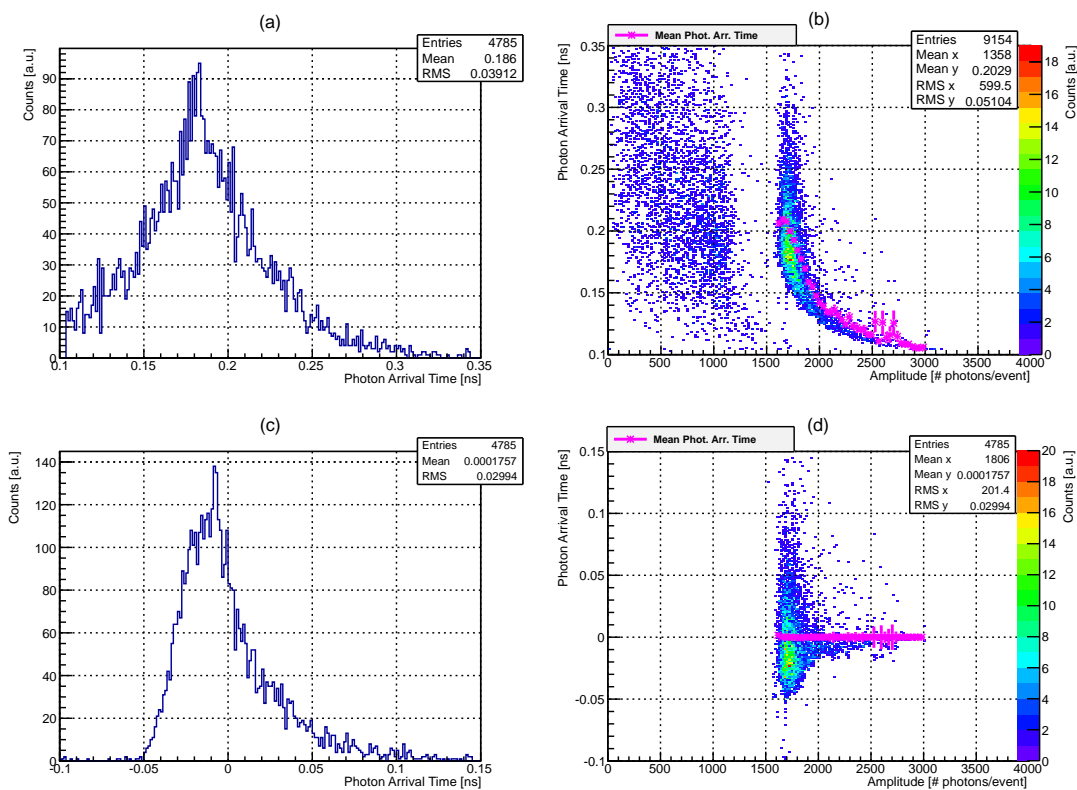


Figure 4.16: Photon arrival times for the determination of the time resolution of a scintillator. (a) shows the photon arrival time, (b) the dependency of photon arrival time on the number of arriving photons. In (b) also the Compton events are visible in the range below 1600 photons per event: the mean photon arrival times were calculated for different amplitudes and used to perform a time walk correction. Figures (c) and (d) show the time walk corrected photon arrival times and the corrected scatter plot, respectively (60).

4.2 Factors influencing the time resolution of scintillation and Cherenkov photon detectors

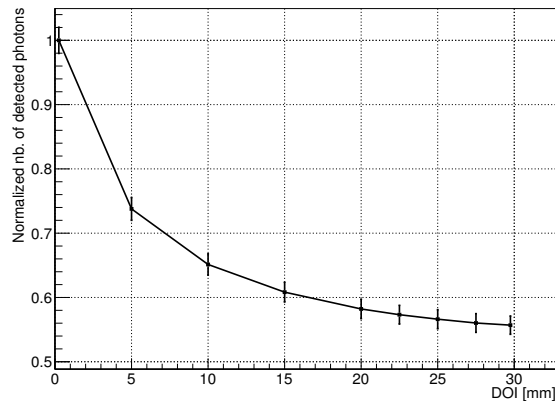


Figure 4.17: Number of detected photons as a function of the DOI. This dependency can be used for time walk correction in PET-like detector configurations (60).

92 % of the 511 keV photons were detected, and 48 % of them were Compton events. In figure 4.16 (b) the time walk is visible. By calculating the mean photon arrival times for increasing amplitudes, time walk correction was applied. The corrected arrival time spectra can be seen in figure 4.16 (c) and (d).

The total time resolution σ_{total} of the scintillator is $\cong 92$ ps FWHM. The corrected data of figure 4.16 (c) gives a TR of $\cong 71$ ps FWHM. Using

$$\sigma_{\text{total}}^2 = \sigma_{\text{time-walk}}^2 + \sigma_{\text{corrected}}^2$$

results in $\sigma_{\text{time-walk}} \cong 25$ ps.

The corrected time resolution $\sigma_{\text{corrected}}$ still includes the standard deviation of the scintillation process, the contribution of the Cherenkov process and a contribution of photon propagation. Note, that the name of the variables σ do not imply normal distributions, but are measures for the standard variation.

Photon losses Another phenomenon could be investigated by the presented simulation and the result is plotted in figure 4.17. In this figure the amount of photon losses due to absorption and losses at the surfaces are can be seen. The data is normalised to the maximum detected number of photons and is plotted against the DOI. It can be seen that the number of detected photons decreases rapidly with increasing DOI. Although, the photon losses result in a decrease of the total time resolution this fact

4. POTENTIAL OF THE CHERENKOV EFFECT FOR IMPROVED TIME RESOLUTION AT LOW γ -PHOTON ENERGIES

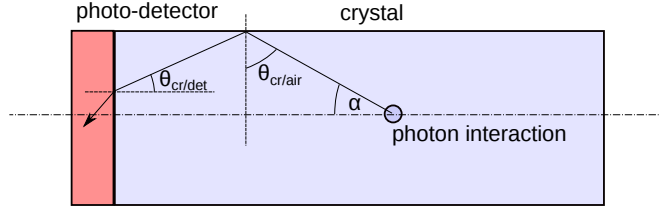


Figure 4.18: Schematic drawing for the geometrical estimation of the time spread due to photon-propagation.

might be used for DOI correction by calibration following the data plotted in figure 4.17.

Information about the DOI allows to reduce parallax errors for PET and might be used for determination of the accurate timestamps of photon interactions, which would result in improvement of TOF for PET. This could be done either by measuring the pulse amplitude of a scintillation pulse, or by the signal rise time as seen in before in section 4.2.6 or both. As the development of readout electronics proceeds quickly, extracting amplitude and rise-time information by waveform analysis would be realistic also for full TOF-PET systems (80).

4.2.8 Tracklength of the photons and photon arrival times

Adapting and reinterpretation of the geometrical considerations determined in (34), the spread of the photon arrival times can be estimated by calculating the critical angle of total reflection according to Snellius' law. The derivation is valid under the assumption that a longitudinal crystal is used with its length larger than the edge length of its quadratic base. These considerations are based on the difference of the propagation times for a minimum possible tracklength of the emitted photons t_{\min} and the time of the maximum possible tracklength t_{\max} . The time for the minimum propagation time is $t_{\min} = DOI \cdot \frac{c}{n}$, with c the speed of light in vacuum and n the refractive index of the medium, when a photon is propagating directly to the photo detector. A drawing of this geometrical consideration is shown in figure 4.18.

The maximum possible propagation time is determined by the critical angle of total reflection, $\theta_{\text{cr/air}} = \sin\left(\frac{n_{\text{air}}}{n_{\text{cr}}}\right)$ and the critical angle $\theta_{\text{cr/det}} = \sin\left(\frac{n_{\text{det}}}{n_{\text{cr}}}\right)$ at the border from crystal to the photo detector. In order to fulfil the requirements of total reflection,

4.2 Factors influencing the time resolution of scintillation and Cherenkov photon detectors

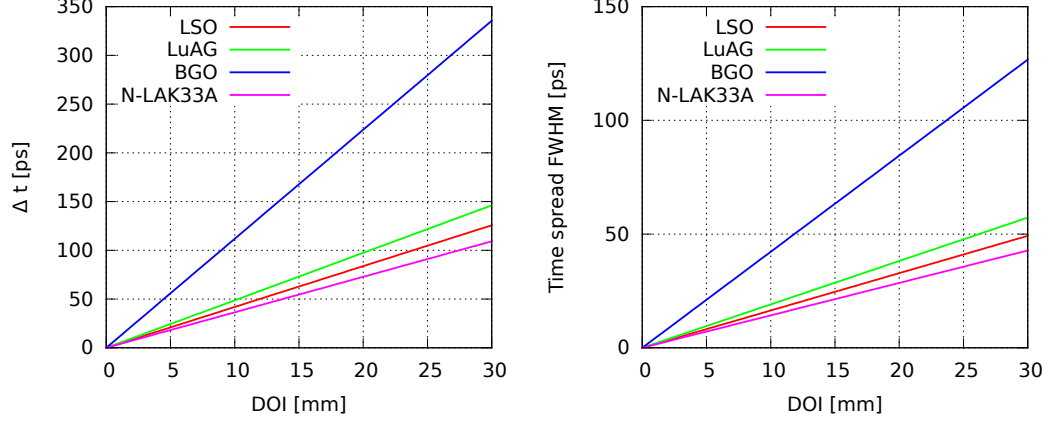


Figure 4.19: Maximum possible time spread for several materials on the left hand side. On the right hand side an estimation of the time spread in terms of FWHM has been made under the assumption of a normal distribution and that Δt represents a width of $\pm 3\sigma$, i.e., $> 99\%$ of the events.

two constraints concerning a maximum possible angle for photon propagation α_{\max} can be made:

- $\alpha_{\max} < 90 - \theta_{\text{cr/air}}$ and
- $\alpha_{\max} < \theta_{\text{cr/det}}$.

Assuming $n_{\text{air}} < n_{\text{det}} < n_{\text{cr}}$ and $45^\circ \leq \theta_{\text{cr/air}} < \theta_{\text{cr/det}}$ results in the constraint $\alpha_{\max} < \theta_{\text{cr/det}}$. This gives,

$$t_{\max} = \frac{DOI}{c} \cdot \frac{n_{\text{cr}}}{\cos(\alpha_{t_{\max}})} \quad (4.18)$$

This is valid for a two-dimensional consideration, expansion into three dimensions gives,

$$t_{\max} = \frac{DOI}{c} \cdot \frac{n_{\text{cr}}}{\cos(\alpha_{t_{\max}})^2} = \frac{DOI}{c} \cdot \frac{n_{\text{cr}}^3}{n_{\text{det}}^2}. \quad (4.19)$$

Calculating the time differences for the photon propagation along the two tracks gives,

$$\Delta t = t_{\max} - t_{\min} = DOI \cdot \frac{n_{\text{cr}}}{c} \left(\frac{n_{\text{cr}}^2}{n_{\text{det}}^2} - 1 \right). \quad (4.20)$$

Values of this estimation are plotted for various materials in figure 4.19, on the left hand side. This estimation gives an estimation on the maximum possible time

4. POTENTIAL OF THE CHERENKOV EFFECT FOR IMPROVED TIME RESOLUTION AT LOW γ -PHOTON ENERGIES

spread, but do not include any statistics inside these borders. The distributions within these borders are similar to a Landau distribution. Nevertheless, by assuming a normal distribution and that the width Δt represents $\pm 3\sigma$ ($> 99.9\%$) of the events one can estimate a time spread due to the photon propagation by $\text{TR} = \Delta t/6$. By multiplication with a factor of 2.35 one obtains a rough estimation of the time spread due to the photon propagation inside the crystal in terms of FWHM. This resulting distribution is drawn for several materials in figure 4.19, on the right hand side.

One has to be aware that some assumptions were made to obtain this result. It represents an estimation for the spread of all photons reaching the photon detector. If one would trigger on the first arriving photons at the photo detector and the light yield would be high, the estimated time spread would shrink, as more and more photons are likely to be emitted under a small angle $\alpha' < \alpha_{\text{max}}$. If the photon yield is low, as for Cherenkov emission, the estimated value of the time spread due to photon propagation should approximate the real value.

The simulated path lengths of photons travelling through the crystal (here called *tracklength*) dependent on the DOI is shown in figure 4.20. This figure was obtained by a MC-simulation with the same framework and parameters used in section 4.1.1, for a LSO:Ce crystal with the dimensions $3 \times 3 \times 30 \text{ mm}^3$. A schematic drawing of the setup and the axis conventions can be seen in figure 4.18.

The data of figure 4.20 is separated by their creation mechanism, i.e. scintillation on the left hand side and Cherenkov emission on the right hand side. It can be seen that the tracklengths form bands with a width dependent on the DOI. The bands start at a DOI of 15 mm, which is the DOI of the photo detector. The lower boundary of the bands follows the minimum propagation times of photons in the crystal. The upper boundary follows the value of the maximum possible propagation paths according and can be compared with t_{min} and t_{max} from the discussion before.

In the plots at the bottom of figure 4.20, the arrival times of the photons are plotted for scintillation on left hand side and for Cherenkov emission on the right hand side. The red dashed lines show the borders of t_{min} and t_{max} , which were determined by equation 4.20 and can be compared with the results for LSO in figure 4.19, on the left hand side. In the plot on the right hand side it can be seen the calculated width of the lines describe the distribution of the photon arrival times quite well for the case of Cherenkov emission. Whereas, for scintillation this is not so obvious.

4.2 Factors influencing the time resolution of scintillation and Cherenkov photon detectors

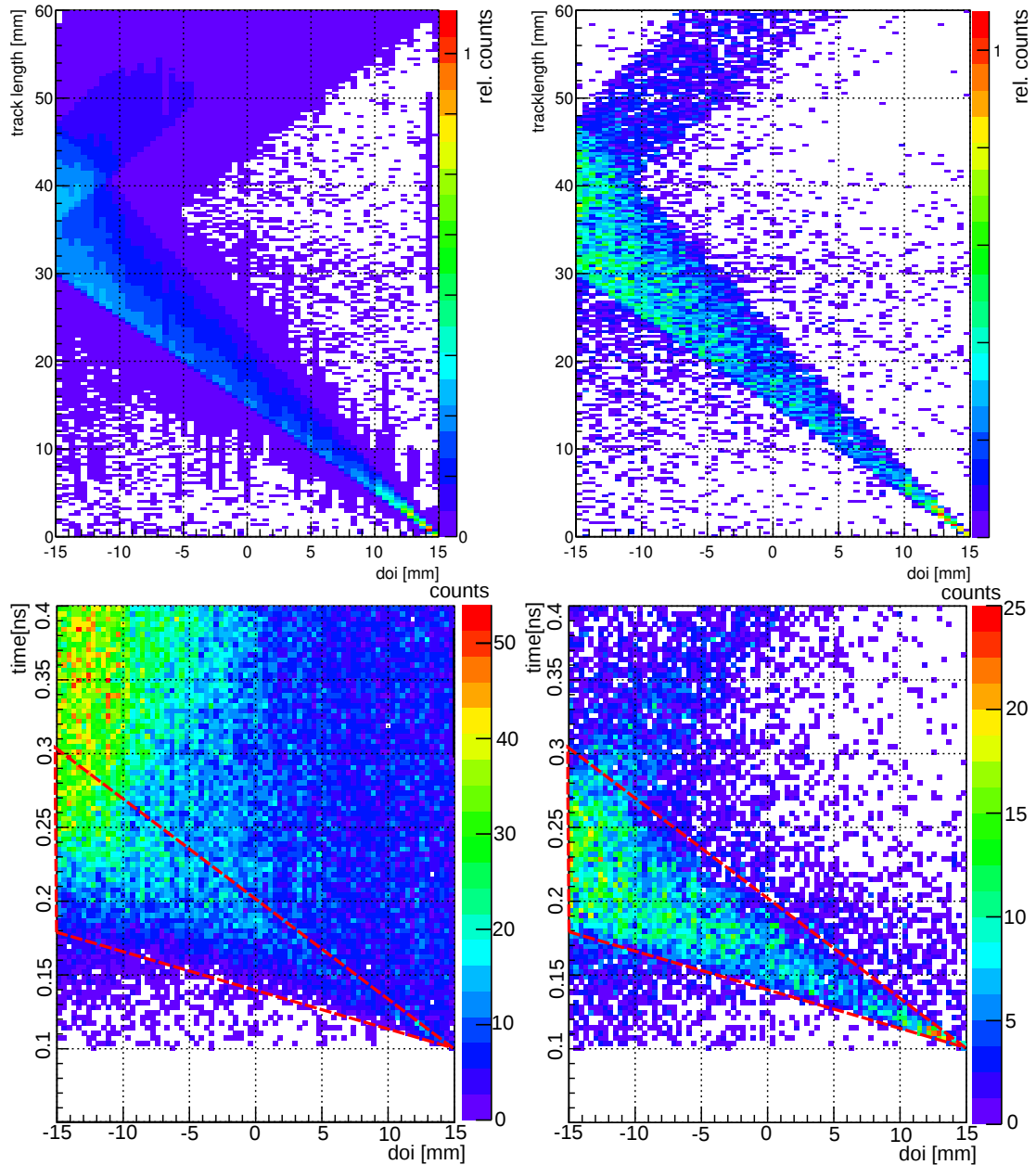


Figure 4.20: Simulated tracklength of photons (top) for scintillation (left) and Cherenkov photons (right) in a $3 \times 3 \times 30$ mm long LSO:Ce crystal and the simulated arrival times of these photons at the photo detector (bottom) plotted versus the depth of interaction of the 511 keV annihilation-photons inside the crystal. The DOI of -15 mm is at the far side of the crystal whereas a DOI of 15 mm is at the side of the photon detector.

4. POTENTIAL OF THE CHERENKOV EFFECT FOR IMPROVED TIME RESOLUTION AT LOW γ -PHOTON ENERGIES

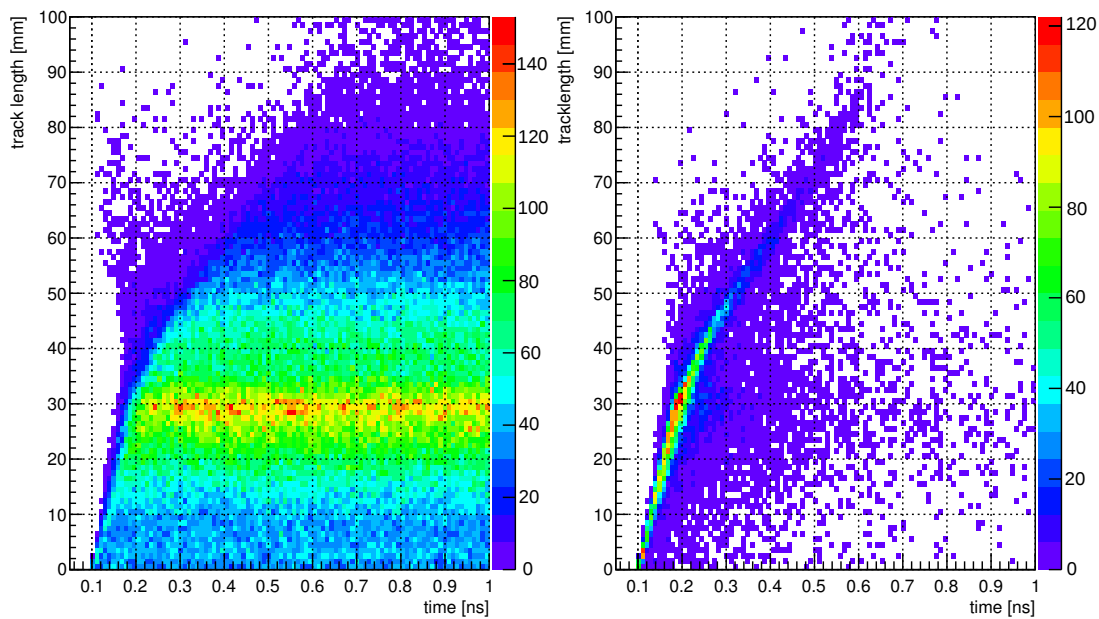


Figure 4.21: Simulated tracklength for scintillation (left) and Cherenkov photons (right) in a $3 \times 3 \times 30$ mm long LSO:Ce crystal plotted versus the arrival times of the photons at the detector. The DOI of -15 mm is at the far side of the crystal whereas a DOI of 15 mm is at the side of the photon detector. The influence of the time constants of scintillation and Cherenkov emission can be seen nicely, when comparing the arrival times of scintillation photons on the left hand side with the relatively sharp arrival times of the Cherenkov photons.

4.2 Factors influencing the time resolution of scintillation and Cherenkov photon detectors

When comparing the upper with the bottom plots of the same figure it can be seen that in the case of tracklengths relatively sharp bands of the photon propagation are formed, whereas this is not so obvious for the photon arrival times. The reason is that the photon statistics blurs the distributions in the bottom plots of arrival times for both, scintillation and Cherenkov emission. As the time constants are significantly smaller for Cherenkov emission (range of ps, see following chapters) the band is still visible in this case, whereas for scintillation ($\tau_{\text{rise}} = 100$ ps, $\tau_{\text{decay}} = 40$ ns), it is not visible any more.

In order to demonstrate the tracklength a photon had to propagate until it arrives at the photo detector, the tracklength of the photons was plotted dependent on their arrival time which can be seen in figure 4.21. On the left hand side the distribution is plotted for scintillation and on the right hand side for Cherenkov emission. The arrival times of scintillation photons is distributed starting from 100 ps all over the histogram. This is not the case for Cherenkov photons which form a narrow band in the histogram. In this plot the influence of the photon statistics on the time distributions becomes more obvious.

4.2.9 Photon arrival times of scintillation and Cherenkov photons

Parts of this section already has been published in (60) and can be found also in appendix 7.1. The parts presented in this section are the work of the author of this thesis.

The influence of both the Cherenkov photons in combination with the DOI were investigated following an experiment done by (77), who measured the photon arrival times of LSO:Ce with a size $3 \times 3 \times 30$ mm³. A schematic drawing of the setup is drawn in figure 4.22 on the left hand side. The results on the photon arrival times obtained by (77) are shown in the same figure on the right hand side.

For this simulation following the experiment of (77) again the simulation environment presented in 4.1.1 was used but the geometrical setup was changed. For the simulation a LSO:Ce crystal with the size of $3 \times 3 \times 30$ mm³ was used, which can be seen see figure 4.22, on the left hand side. The crystal was attached to a photo detector with its base, which has a size of 3×3 mm. In this simulation study, the 511 keV annihilation-photons were shot into the crystal from the side at a defined distance relative to the photo detector. This distance was varied and again the photon arrival rates

4. POTENTIAL OF THE CHERENKOV EFFECT FOR IMPROVED TIME RESOLUTION AT LOW γ -PHOTON ENERGIES

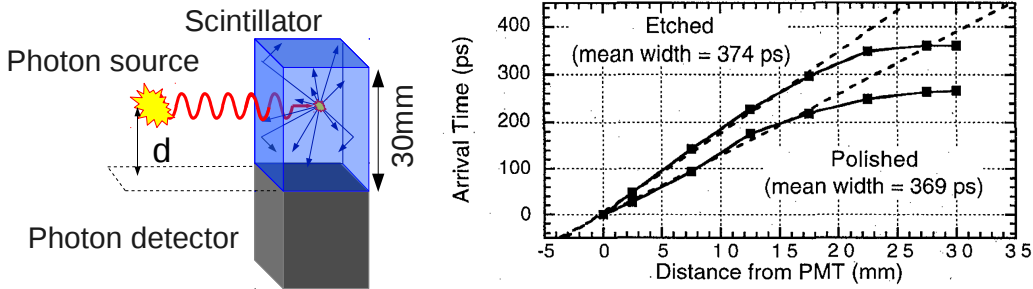


Figure 4.22: On the left hand side setup for the simulation of the photon arrival rates in LSO:Ce in dependency on the DOI. The 511 keV photons are penetrating the crystal from the side parallel to the detector face and at a defined distance relative to it. On the right hand side, experimental data obtained with a similar setup, using PMTs as photodetectors, can be seen, which was measured by (77). For the measurement ^{68}Ge was used as positron source, which was arranged in a coincidence setup with a small pixel of LSO:Ce.

at the detector were recorded. The creation of the 511 keV photons was defined as the starting time $t = 0$ for the photon detector.

In figure 4.23 the mean of the trigger times of the first arriving photon for two different cases are plotted: the red squares give the mean trigger times when only scintillation photons are used for analysis. It can be seen that the mean trigger times increase with increasing DOI. When adding the Cherenkov photons to data analysis, it can be seen, that the mean trigger times of the first photons are improving and approach the theoretical minimum which was calculated in a previous section. For the goal of improving the overall time resolution of the detectors, the influence due to photon propagation of the first photon is decreased which has an improving influence on the TR of the whole detector system. This influence will be shown later for the case of a coincidence setup. This result can be compared with the experimental result of (77), shown in figure 4.22 on the right hand side. However, contrary to the measurement, the QE in the simulation is set to 1. In the experiment of (77), only a fraction of the photons were detected and therefore, the arrival times were degraded additionally.

In the following, the photon arrival distributions of scintillation and Cherenkov photons is analysed in more detail. To do so, three different DOIs were chosen for plotting the photon arrival times: a DOI far from the detector at 29.75 mm, one at the centre 15 mm and one close to the photodetector at 0.25 mm. The results are plotted in figure 4.24. In these plots, the photon arrival rates in terms of number of photons per

4.2 Factors influencing the time resolution of scintillation and Cherenkov photon detectors

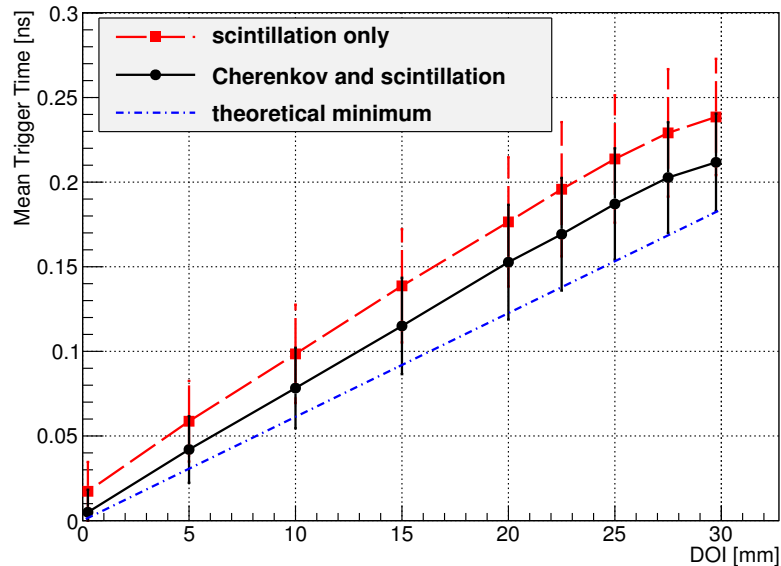


Figure 4.23: Photon arrival time at the photon detector (60).

511 keV-photon is drawn dependent on the photon arrival times at the photon detector. A bin size of 5 ps was chosen. At a DOI of 29.75 mm it can be seen, that the rate of scintillation photons forms a rise of ~ 100 ps followed by a plateau. Contrary to that, the rate of Cherenkov photons forms a small peak with a similar width. Comparing the scintillation rates for decreasing DOIs, it can be seen that the rise of the scintillation photon rate becomes shorter and therefore steeper. The rise of the Cherenkov photon rate becomes even steeper and the width of the curve becomes smaller. At a DOI of 15 mm a second, smaller peak for the rates of Cherenkov photons can be seen ~ 200 - 350 ps later, which corresponds to a propagation path of roughly 33-57 mm. At the same time a second rise of the scintillation rate is visible. The peak for Cherenkov photons and the rise of the scintillation rate is caused by photons which are emitted in a direction away from the photon detector, but get reflected at the end of the crystal and arrive at the photon detector with a delay proportional to their tracklength. Looking at a DOI of 0.25 mm, which is very close at the photodetector, it can be seen, that both, the scintillation and Cherenkov photon rates form a very steep rise in the order of 30 ps. Moreover, the peak for the arriving Cherenkov photons is very narrow with a FWHM < 20 ps. As for a DOI of 15 mm a second rise of the scintillation rate and a second peak in the Cherenkov photon rate can be seen at a delay of ~ 500 ps.

4. POTENTIAL OF THE CHERENKOV EFFECT FOR IMPROVED TIME RESOLUTION AT LOW γ -PHOTON ENERGIES

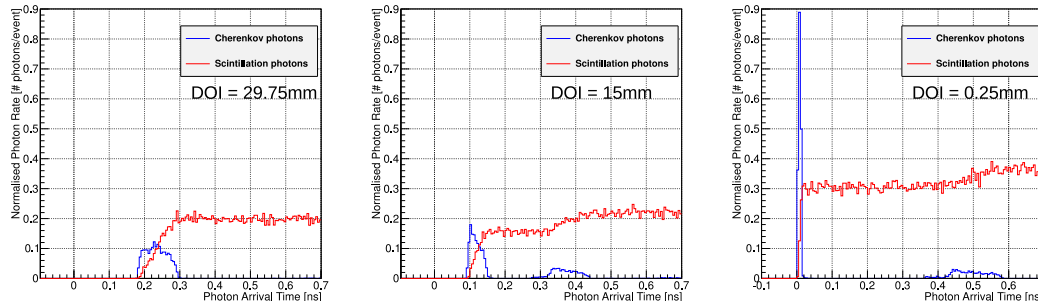


Figure 4.24: Photon arrival rates per 511 keV photon (event) with a bin size of 10 ps. The rates are normalised by the average number of detected photons per event. The rates are separated by the creation process of the photons, which is scintillation and Cherenkov emission and plotted for three different DOIs (60).

These plots clearly show the influence of the DOI on the photon arrival rates at the photon detector. Furthermore, comparing the overall rates it can be seen, that for large DOIs the rates are almost half of the rates as for DOIs very close at the detector, which is a result of photon losses via the surfaces and by absorption in the crystal. This absorption is one of the major factors reducing the Cherenkov photon detection rates, as Cherenkov photons are emitted mostly in the UV range of the light spectrum, where, e.g. LSO:Ce has a high absorption.

Furthermore, the narrow peaks for the arrival rates of the Cherenkov photons could potentially improve the TR of the detector system. According to the simulations Cherenkov photons are present after the absorption of 511 keV annihilation-photons in the considered scintillators and can also be detected. In the case of the investigated material LSO:Ce their yield is so small, that their influence is hardly affecting the mean photon arrival times and therefore the time resolution. If, crystal parameters are chosen that a high Cherenkov emission can be expected on the one hand and photon detectors are used with fast single photon detection capabilities, the influence of the Cherenkov effect on the time resolution is expected to be measurable in experiment.

4.2.10 Comparing photon arrival rates for various materials

Parts of this section already has been published in (61) and can be found also in appendix 7.2©2014 IEEE. The parts presented in this section are the work of the author of this thesis.

4.2 Factors influencing the time resolution of scintillation and Cherenkov photon detectors

The overall photon arrival times are the origin of the observed rise time of scintillators, which is a major parameter influencing the time resolution of scintillation detectors (21; 59; 77) and therefore has impact on the CTR (71). As shown by the simulations before, scintillation and Cherenkov photons are emitted after the photoelectric interaction of a 511 keV annihilation-photon in the scintillator material. Therefore, both emissions are shaping the overall rise time of scintillators already at these low energies. In this section the photon arrival rates will be compared for various materials. This should be done with a realistic setup and simultaneously with minimum influence of absorption and photon propagation in the crystals. Therefore, for the MC-simulation the crystal size was reduced to small cubic pixels with sizes of $3 \times 3 \times 3 \text{ mm}^3$.

In this investigation, the arrival rates are not separated by their DOI any more and the creation times of both, scintillation and Cherenkov emission are compared without this information. Additionally, the arrival times of the photons at the detector are investigated. The results are plotted in figure 4.25 for two example scintillator materials: LSO:Ce on the top and PWO on the bottom. On the left hand side of this figure, the creation times of scintillation (red, dashed lines) and Cherenkov photons (blue lines) are plotted. On the right hand side, the arrival times of the photons at the photo detector are shown. The data is normalized to the maximum Cherenkov creation rate (blue lines on the left) in order to be able to compare the relative photon rates and losses due to absorption and photon propagation.

The width of the creation times of Cherenkov photons, on the left hand side of figure 4.25, is mainly determined by the time the 511 keV annihilation-photon needs to propagate through the 3 mm thick crystal at the speed of light c , i.e. 10 ps. This is the main contribution to the time spread of Cherenkov photon creation and is independent of the material. Although the size of the cubes is small, photon propagation and absorption have a significant influence on the photon arrival time distribution of both, the Cherenkov and the scintillation photons.

In total, the simulations were done for four different scintillators: LSO:Ce, LuAG:Ce, BGO and PWO. For quantitative comparison of the influence of the Cherenkov photons on the photon rates, the yield ratio YR is introduced which is defined as,

$$YR = \frac{n_{\text{Cherenkov}}}{n_{\text{scintillation}}} \quad (4.21)$$

4. POTENTIAL OF THE CHERENKOV EFFECT FOR IMPROVED TIME RESOLUTION AT LOW γ -PHOTON ENERGIES

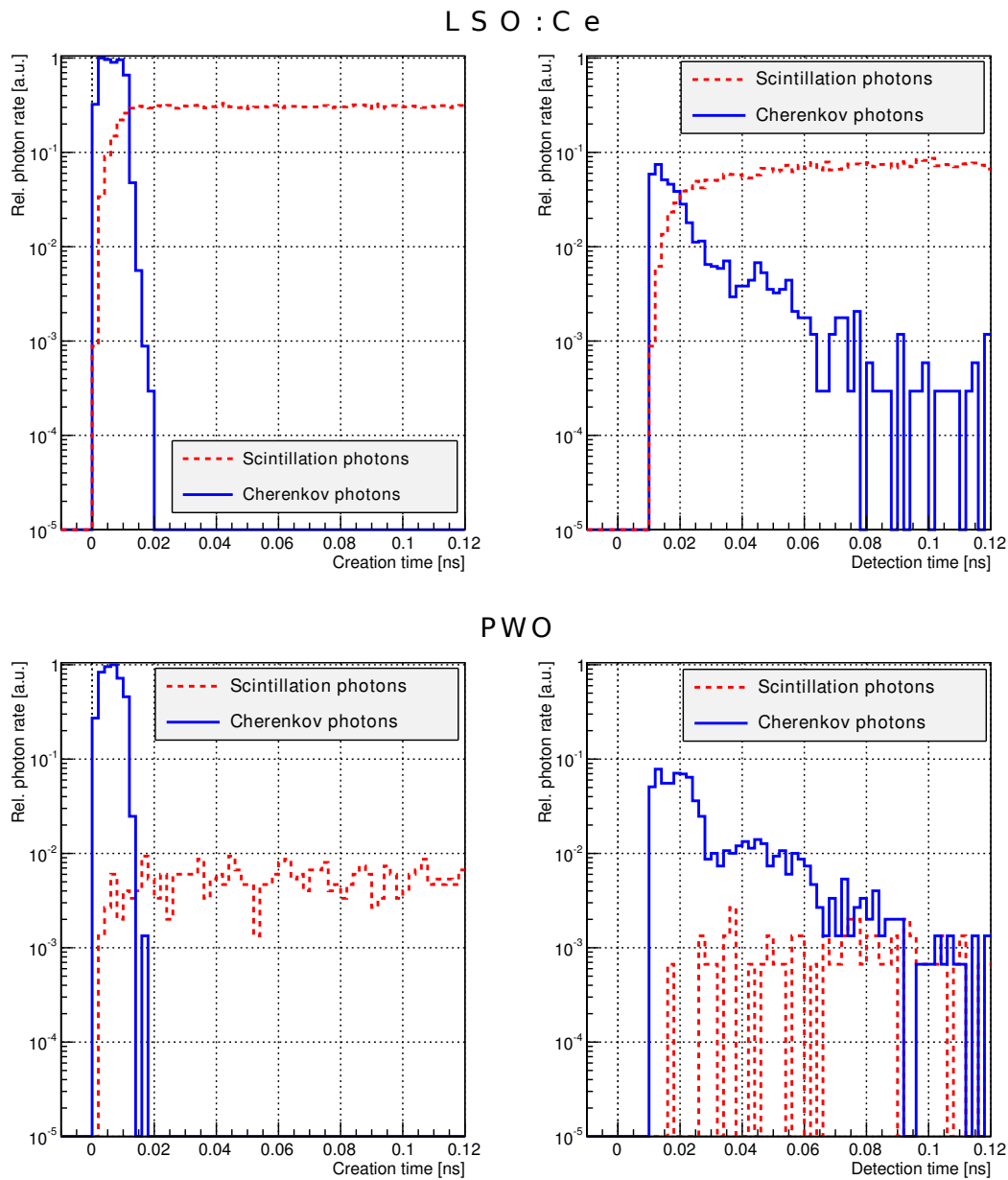


Figure 4.25: Photon creation (left) and arrival times (right) of photons in LSO:Ce (top) and PWO (bottom) separated by their creation process, blue line for Cherenkov emission and red, dashed line for scintillation (61). The bin width of the histograms is set to 2 ps and the data is normalized to the maximum Cherenkov creation rate (blue lines on the left) in order to better compare the photon rates and losses. ©2014 IEEE

4.2 Factors influencing the time resolution of scintillation and Cherenkov photon detectors

Material	Yield ratio			
	created		detected	
	< 25 ps	< 100 ps	< 25 ps	< 100 ps
LSO:Ce	1.77	0.34	1.78	0.16
LuAG:Ce	11.5	2.1	41.5	3.4
BGO	122	24.2	364	28
PWO	86	16.6	134	21

Table 4.6: Simulated yield ratio for the rates of Cherenkov and scintillation creation and detection within 25 ps and 100 ps after the photoelectric absorption of 511 keV annihilation-photons (61).©2014 IEEE

with $n_{\text{Cherenkov}}$ the number of Cherenkov photons and $n_{\text{scintillation}}$ the number of scintillation photons.

Although the number of Cherenkov photons produced in scintillators is low, their creation and detection rates can exceed the ones of scintillation photons, since they are created in a very narrow time span. This effect can be seen from the values in table 4.6, where a quantitative overview of the yield ratio within time windows of 25 ps and 100 ps is given. The time windows were measured from the time of creation or detection of the first photon, respectively. Considering a time window of 25 ps only, the Cherenkov rates are exceeding those of the scintillation yields for all materials. These numbers suggest, that Cherenkov photons are an important factor influencing the rise times of scintillators and therefore are improving the time resolution of scintillation detectors. Depending on other scintillation parameters, e. g. the scintillation yields and transmission spectra, the influence of the Cherenkov photons on the rise times is significant. Knowing this fact, scintillators can be chosen in favour of higher Cherenkov photon emission to further improve the time resolution and still provide energy information about the initial interaction.

Triggering really on the first arriving photon is hardly possible for the case of an usual analogue photo detector. As an example for the case of, e.g., LSO:Ce and a PMT with a rise time of 500 ps already many photons are influencing the signal until a threshold of, e.g., one p.e. is reached. This behaviour was also discussed in (14) and is simply due to the fact that the rise time of LSO:Ce is shorter than the rise time of the PMT. It is possible to trigger on the first arriving photon with the Philips DPC. The DPC will be therefore able to exploit the fast Cherenkov photons more efficiently.

4. POTENTIAL OF THE CHERENKOV EFFECT FOR IMPROVED TIME RESOLUTION AT LOW γ -PHOTON ENERGIES

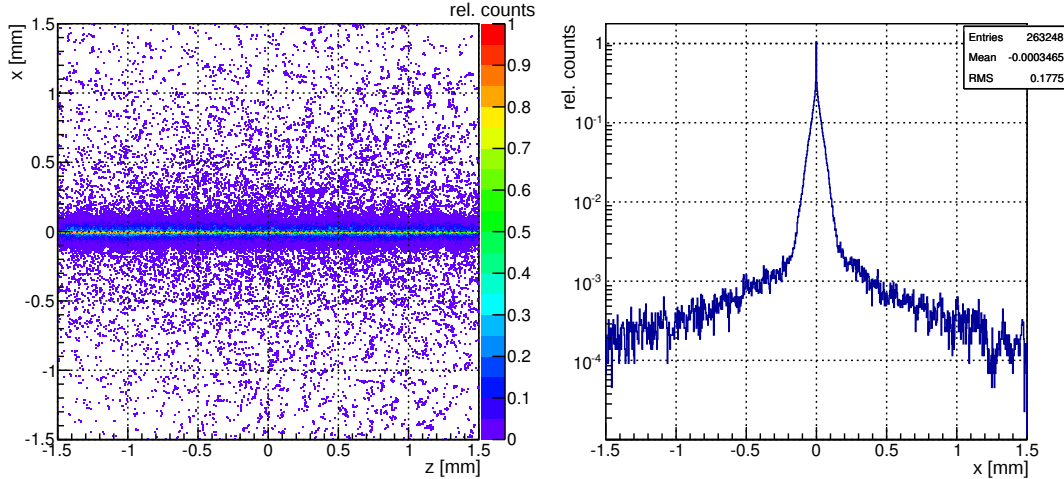


Figure 4.26: Projections of the origin of the Cherenkov photons emitted in a cube of LSO:Ce with edge lengths of 3 mm. On the left hand side a 2-dimensional plot is shown, whereas on the right hand side a 1-dimensional projection of the same data is drawn. It can be seen that the emission of the Cherenkov photons is closely located (FWHM $< 5 \mu\text{m}$) of the axis incident 511 keV photons at $x = 0 \text{ mm}$

Another behaviour can be seen from these numbers in table 4.6: the yield ratio is significantly larger for the case of detected photons than for the created photons. This is caused by the preferred direction of the Cherenkov emission in the direction of the incoming 511 keV annihilation-photon and thus towards the photo detector. Contrary to Cherenkov emission, scintillation photons do not have a preferred direction and therefore, the yield ratio increases when comparing created and detected photons. The angular distribution is studied in more detail in the following section.

4.2.11 Vertex of Cherenkov photon creation and angular emission distribution

For studying the origin and the direction of the Cherenkov emission the simulation data of section 4.2.10 was further analysed. This was done for investigating the reason for increasing yield ratios for detected photons, in comparison with the one of created photons. On the left hand side of figure 4.26, a colour plot of the origin vertex of Cherenkov photons is shown. The 511 keV annihilation-photons are entering the crystal at $z = -1.5 \text{ mm}$ and $x = 0 \text{ mm}$ (from the left side in the plot) and the photo detector

4.2 Factors influencing the time resolution of scintillation and Cherenkov photon detectors

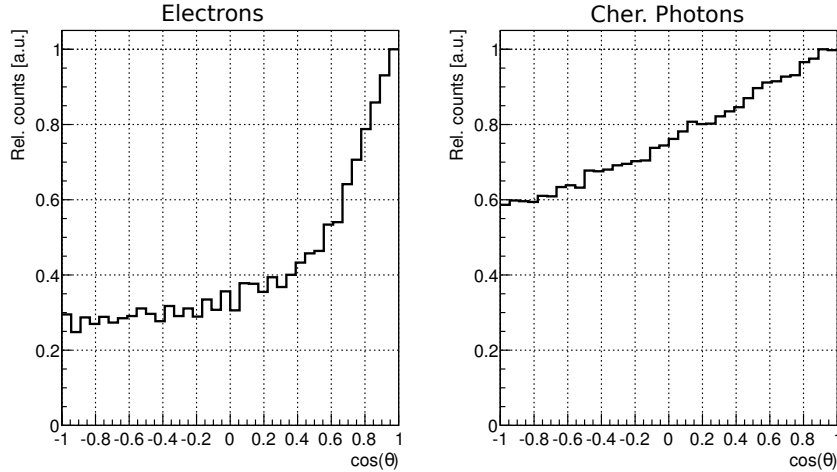


Figure 4.27: Angular distribution of recoil electrons due to 511 keV annihilation photons (left) and the subsequently emitted Cherenkov photons (right) (61). ©2014 IEEE. A projection parallel to the axis of the incoming 511 keV photons are drawn.

is placed along $z = 1.5$ mm. It can be seen that the origin of the Cherenkov photons forms a narrow band along the beam axis. The rate along the beam axis quickly increases to a maximum close to the entrance of the beam into the crystal then decreases exponentially. A projection perpendicular to the beam axis for $z = y = 0$ is plotted in figure 4.26, on the right hand side. It can be seen that the width of the Cherenkov photon emission is very narrow ($\text{FWHM} < 5 \mu\text{m}$) along the beam axis.

Additionally, the initial direction of the electrons propagating through the crystal after photoelectric interaction was investigated. The initial direction of Cherenkov emission is plotted in figure 4.27. For $\cos \theta$ relative to the beam axis ranging from -1 to 1 (relative to the direction of the initial 511 keV photons), a distribution increasing towards the direction $\cos \theta = 1$ can be seen. This is prominent for the electrons but can be seen also for the Cherenkov photons which are emitted in the Cherenkov angle relative to these electrons. Therefore, the spread of the initial direction is larger for the Cherenkov photons. One has to note that Cherenkov photons are also emitted in opposite direction of the initial 511 keV annihilation-photon.

As the total number of emitted Cherenkov photons is very small, this result could be used to optimise detector geometry for increasing the detection of Cherenkov photons, by placing the photo detectors at a position with a high Cherenkov arrival rate. On

4. POTENTIAL OF THE CHERENKOV EFFECT FOR IMPROVED TIME RESOLUTION AT LOW γ -PHOTON ENERGIES

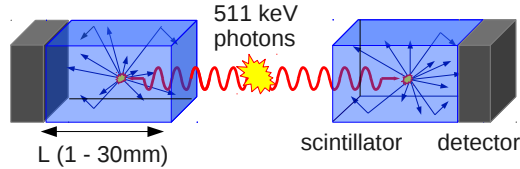


Figure 4.28: Setup used for the MC-simulations on the coincidence time resolution, where the length of the LSO crystal L was varied for both crystals from 1 mm to 30 mm. The source of the 511 keV photons was placed in between the crystals.

the other hand, these results explain the result of section 4.2.10 where the determined yield ratios increase significantly when comparing the values for created and detected photons.

4.3 Influence of Cherenkov photons on the coincidence time resolution

Parts of this section have been published in (60) and can be found in appendix 7.1. The parts used in this section are the work of the author of this thesis.

For evaluation of the influence of Cherenkov emission on the coincidence time resolution, a basic coincidence setup with two finger-like scintillators, each connected to one photon detector, was simulated, see figure 4.28. This was done using the same MC-simulation environment presented in section 4.1.1. The simulated material was LSO and the crystal sizes were $3 \times 3 \times L \text{ mm}^3$ with L ranging from 1 mm to 30 mm.

In figure 4.29, the simulated CTR is shown for various crystal lengths and was analysed first only for scintillation. The results are drawn as red squares in the plot. The lines between the points are no fits or interpolations but should guide the eyes. In a next step Cherenkov-photons were included in the data analysis. The results are shown in the same figure and are represented by the blue circles. For both results the dependency on the crystal lengths is clearly visible. This is mainly a result of photon propagation and is a known behaviour. For crystal lengths from 1 mm to 30 mm the CTR ranges from 32 ps to 144 ps FWHM for scintillation. By adding the Cherenkov photons to data analysis the obtained CTRs improved and ranges from 12 ps to 125 ps FWHM, respectively. The impact of the Cherenkov effect on the CTR is clearly visible in figure 4.29.

4.3 Influence of Cherenkov photons on the coincidence time resolution

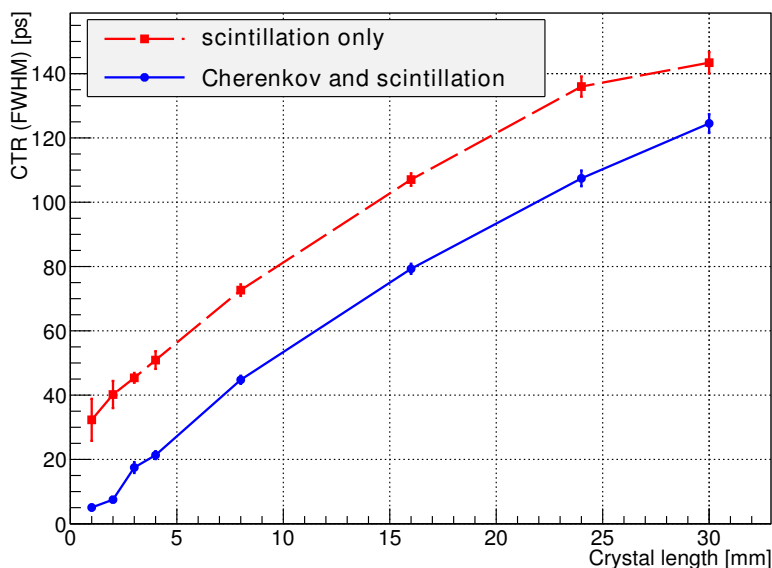


Figure 4.29: Simulated CTR for various crystal lengths. The red dashed curve represents the CTR when only scintillation photons are detected. The blue solid line shows the CTR if Cherenkov photons are included in the simulation (60). The lines are added to guide the eyes and do not represent a fit.

Although, the time resolution improves with decreasing crystal lengths, longer crystals are providing reasonable sensitivity to the 511 keV photons and therefore, are used for real PET systems. The simulated detection efficiency of coincidences ranges from 2%, for $L = 1$ mm to above 50% for $L = 30$ mm. For real TOF-PET scanners a trade-off between time resolution and sensitivity has to be made.

Already a small amount of detected Cherenkov photons (~ 1 photon per 511 keV photon in LSO:Ce, see section 4.1.2) improves the CTR significantly. These Cherenkov photons could be detected already in existing detectors and hence benefiting to a better CTR. However, as shown before, the Cherenkov photon yield for the case of LSO:Ce is very small. By knowing that Cherenkov photons could be detected also at low energies of annihilation-photons, scintillators could be optimized for simultaneous scintillation/Cherenkov photon detection, by optimizing crystal parameters for high Cherenkov emission and transmission and the photo detector for high efficiency of Cherenkov-photon detection. Furthermore, the photo detector need to be suitable for fast single photon detection and be capable of extracting the time stamps of the first arriving photons at the detector.

4. POTENTIAL OF THE CHERENKOV EFFECT FOR IMPROVED TIME RESOLUTION AT LOW γ -PHOTON ENERGIES

4.4 Summary and Discussion

In this chapter analytic studies and MC-simulations on the Cherenkov photon yield after the photoelectric absorption of annihilation photons at energies at 511 keV were presented. This was done for several scintillators and Cherenkov radiators. For an improved estimation and respecting the effects of photon transmission in the materials, the simulations showed the amount Cherenkov photons absorption for the presented materials. Nevertheless, the simulations also revealed that Cherenkov photons arrive at the photo detector and can be detected.

Two different approaches have shown the influence of the photo statistics on the overall time resolution. It has been shown how the CTR depends on the following key parameters: photon yield, rise and decay times and the trigger level of an attached detector. Using one of the approaches, significantly better CTRs can be expected for Cherenkov emission when considering the photon statistics. This can be expected despite the low Cherenkov photon yield when compared to scintillation.

In a next step, factors besides photon statistics which are influencing the time resolution of scintillation and Cherenkov detectors were presented and investigated. It has been shown that the time spread of the Cherenkov emission due to dispersive Cherenkov emission angle has an influence < 10 ps for photon propagation paths in the range of 10 mm, which is a minor effect for state-of-the-art detectors with CTRs above 100 ps but would become non-negligible when the system TR approaches 10 ps. Also the direct effect of the time spread due to the DOI was found to be in the range of a few ps for crystal lengths of about 10 mm.

In further investigations the indirect influence of the DOI, the time-walk, was determined and the influence of photon propagation and photon losses was discussed. It was shown that information of both, photon number and rise time could be used to determine the DOI of the photoelectric absorption and therefore, provides a method to correct for this effect. The influence of the time-walk was determined to be in the range of $\sigma \approx 25$ ps in a 30 mm long piece of LSO:Ce.

In the following, the phenomenon of photon propagation was investigated in more detail. An analytic approach for estimating the maximum boundaries for the time spread due to photon propagation was presented and resulted in an equation for estimating the magnitude of photon propagation on the time resolution. Assuming the

influence of the photon propagation follows a Gaussian statistics, a time spread well below 50 ps, for most of the materials even below 25 ps FWHM for 10 mm long crystals could be determined. This estimation holds when all emitted photons are included in the analysis. Depending on the trigger method and the light yield in a real setup this estimation becomes inaccurate but still represents an estimation for an upper boundary of this effect.

Furthermore, it has been shown that the detection of Cherenkov photons among scintillation can improve the mean trigger times, for the first arriving photon at the photon detector. Consequently, the overall time resolution of PET-like scintillation detectors can be improved by detection of Cherenkov photons.

The influence of parameters, refractive index, density and photon transmission have been investigated in another section. By increasing refractive index, radiation length and decreasing the cut-off wavelength the number of detected Cherenkov photons could be improved significantly. This investigation was done on the example of a pure Cherenkov radiator. As energy information is needed for PET-like detectors, scintillator engineering towards increased Cherenkov emission and transmission in scintillators could lead to improved overall CTR of such detectors while still preserving energy determination and therefore, discrimination of photoelectric interaction and Compton scattering. Would it be possible to improve the Cherenkov photon yield by an order of magnitude, this could also be provided only by Cherenkov emission.

It has to be noted, that the presented simulation studies showed that, Cherenkov photons should already be present and be detected in state-of-the-art detector systems. However, most of these systems are using LSO:Ce where the Cherenkov yield is very low. As photon detectors often analogue PMTs or in recent years also analogue SiPMs are used. Therefore, no obvious profit of the fast nature of Cherenkov emission can be seen in these systems at the moment. This is due to the fact that they are not designed for Cherenkov detection. By knowing that Cherenkov emission can improve the time resolution for such detectors and by knowing the parameters for increasing the number Cherenkov photon yield, systems benefiting from the fast nature of Cherenkov emission can be developed and built.

4. POTENTIAL OF THE CHERENKOV EFFECT FOR IMPROVED TIME RESOLUTION AT LOW γ -PHOTON ENERGIES

4.5 Experimental evaluation of a multi-timestamp approach for improvement of the timing performance of scintillation detectors

4.5.1 Influence of the trigger threshold

The influence of photo statistics and the trigger threshold was discussed before. For experimental validation of the influence of the trigger threshold on the CTR, a measurement using the Philips DPC3200 was done. As scintillators two crystals of LSO:Ce from EPIC crystal (78) were used. Each crystal had a size of $4 \times 4 \times 4 \text{ mm}^3$ and all faces were polished. Only one pixel has been activated on each DPC and 10% of the cells with the highest dark-count rates were inactivated. The temperature was stabilised at 15°C using Peltier- and water-cooling. The validation threshold was set to 8 photons with a validation interval of 10 ns, which was followed by an integration interval of 85 ns. In between the two crystals, ^{22}Na was placed and the two annihilation photons with energies of 511 keV following the β^+ -decay in ^{22}Na , were used to measure the CTR of the detector system.

A photon number spectrum is shown in figure 4.30, on the left hand side. Up to ~ 1000 photons, the Compton plateau followed by the Compton edge can be seen. A peak dedicated to the 511 keV photons can be seen around 1500 photons. The peak for the 1275 keV photon emission of ^{22}Na is missing due to the fact that the data was recorded in coincidence mode, i.e., only events within a defined coincidence time window of 5 ns are recorded by the DPCs, all other events were discarded.

For the 511 keV photons, on average 927 scintillation photons were detected without wrapping and a energy resolution $\Delta E/E$ (FWHM) of 15.5% was determined. With Teflon wrapping 1427 photons could be detected giving an energy resolution of 10.9%. One reason for the relatively low number of detected photons is photon loss due to an active area of $3.2 \times 3.8775 \text{ mm}^2$ compared to the scintillator surface of $4 \times 4 \text{ mm}^2$, resulting in an active detector surface of 78%.

On the right hand side of figure 4.30, an example plot for a TOF spectrum, i.e., the time difference of the two trigger-timestamps, can be seen. To obtain the TOF spectrum, the photon number spectrum, on the left hand side of the same figure, was fitted using a Gaussian for the 511 keV peak and an exponential function for the Compton edge. Cuts on the photon numbers were made with $-1 + 1.5$ sigma of the

4.5 Experimental evaluation of a multi-timestamp approach for improvement of the timing performance of scintillation detectors

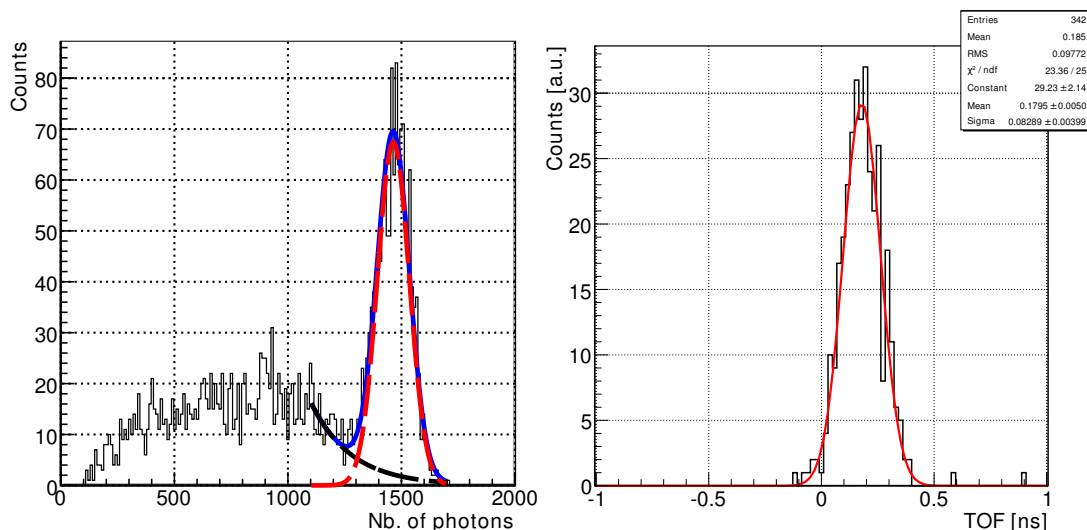


Figure 4.30: Photon number spectrum of ^{22}Na detected with LSO:Ce with $4 \times 4 \times 4 \text{ mm}^3$, wrapped in Teflon, on the left hand side. On the right hand side, the TOF spectrum of two of these crystals coupled with optical grease to a DPC3200 photon detector. 10% of the cells with the highest dark-count rates were inactivated, the trigger level set to 1 photon, validation to 8 photons with validation length of 10 ns and the length of the subsequent integration interval was set to 85 ns.

mean of the Gaussian fit. With the timestamps of these events, the TOF-spectra were obtained. These TOF-spectra (see figure 4.30, right hand side) were then fitted with a normal distribution and the standard deviation multiplied by a factor of 2.35 gave the CTR in terms of FWHM.

For the measurement, all available trigger schemes of the DPC (1-4) were scanned, once without and once with Teflon wrapping around the crystals. According to the DPC user manual (49), the four trigger schemes equal thresholds of 1, 2.333, 3 and 8.333 photons, where all values besides a threshold of one photons are average values (already two photons could trigger the detector, when the threshold is set to 3). This is due to the trigger network scheme which is based on logic circuits.

Results of the threshold scan are shown in figure 4.31 (data points). It can be seen, that the best CTRs can be achieved, when the threshold is set to one agreeing with the results of the theoretical considerations of section 4.2.1. Furthermore, the Teflon wrapping improves the CTR for all thresholds. Additionally, the contribution of the photon statistics to the observed CTR is plotted by the red and blue bands. The basic simulation presented in section 4.2.1 was used at with the determined mean number of

4. POTENTIAL OF THE CHERENKOV EFFECT FOR IMPROVED TIME RESOLUTION AT LOW γ -PHOTON ENERGIES

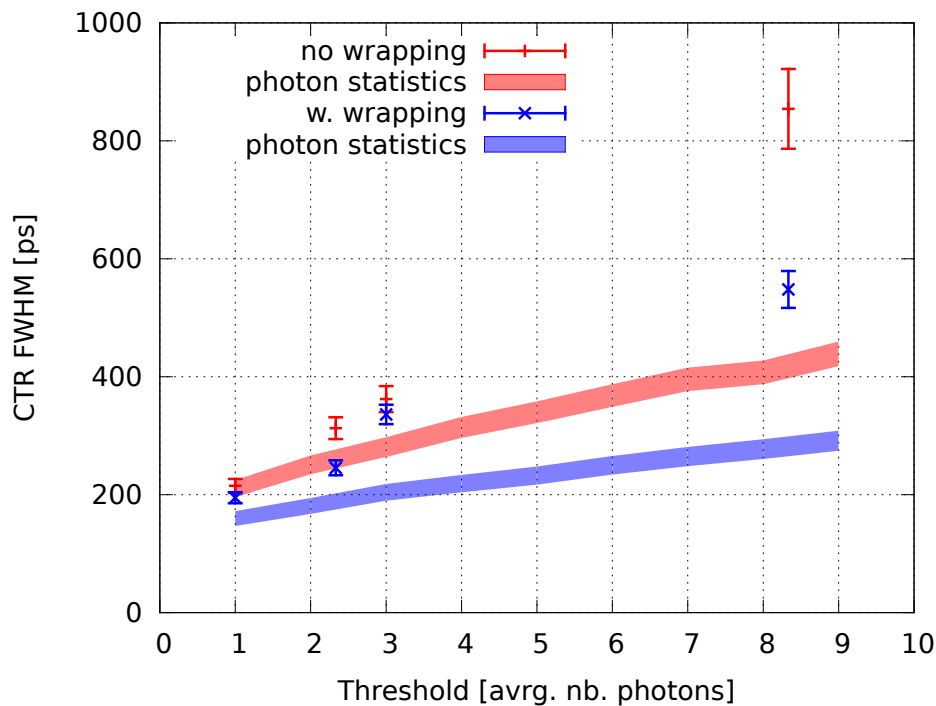


Figure 4.31: Threshold scan for the CTR of LSO:Ce 4x4x4 mm³, once unwrapped (red lines) and once wrapped with Teflon (blue crosses). The crystals were connected to the DPC with optical grease and 10% of the cells with the highest dark-count rates were inactivated. Validation was set to 8 photons with validation interval of 10 ns and integration interval of 85 ns. The trigger scheme was scanned from 1 to 4 representing a threshold level of 1 photon, 2.333, 3 and 8.333 photons according to (49). The coloured bands represent the part of the photon statistics contributing to the overall CTR determined by MC-simulation using a rise time of 100 ps and a decay time of 40 ns. As photon numbers the determined mean 927 photons were used for simulation of the unwrapped crystal and the mean 1427 photons were used for the simulation.

4.5 Experimental evaluation of a multi-timestamp approach for improvement of the timing performance of scintillation detectors

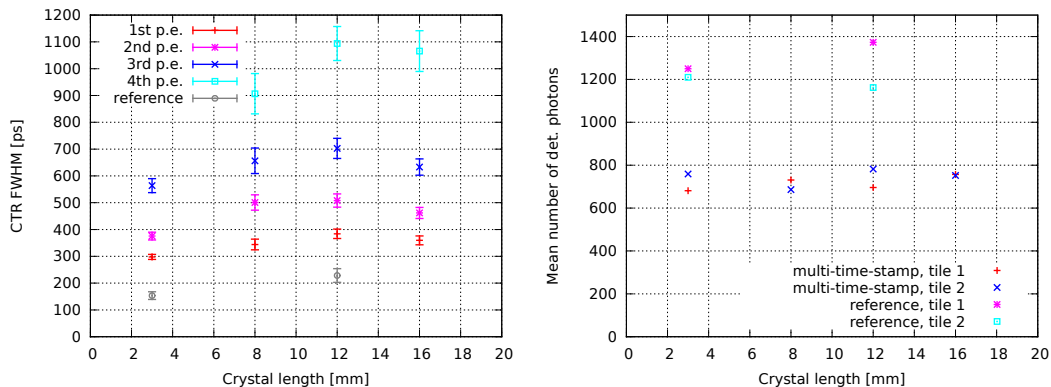


Figure 4.32: Measured coincidence time resolutions using LSO:Ce wrapped in Teflon on the left hand side. The results are plotted for the reference measurement (the crystal is covering a whole pixel) and for utilisation of only the first up to the fourth detected photoelectron, respectively. On the right hand side the mean number of detected photons per die is plotted.

927 photons without wrapping and 1427 photons with wrapping. A rise time of 100 ps and a decay time of 40 ns were applied, which are estimated values. The bands represent the simulated value for the CTR_{sim} including an error of $\pm\sqrt{CTR_{sim}}$. The simulated CTR bands underestimate the real measured values especially at high thresholds. A reason is that contributions of photon detector and photon propagation to the overall CTR are not included here, which additionally increase the CTR especially at higher thresholds. Nevertheless, the results agree with the predicted tendency of obtaining the best time resolution by detecting the time of the first arriving photon.

4.5.2 Multi-timestamp approach

A multi-timestamp approach (MTA) according to the previous theoretical considerations in section 4.2.1 and (13; 16) was performed using the Philips DPC. This was done to investigate to potential of recording more than one timestamp per scintillator-pixel. Contrary to the analog SiPM where the analog sum of all SPADs is recorded, only one timestamp per die can be detected with the digital SiPM. This, however, with a high time precision.

The crystals for the experiment had sizes of $3 \times 3 \times l$, with l being, 3, 8, 12 and 16 mm and were made of LSO:Ce by EPIC crystals. The crystals were wrapped with Teflon tape and the temperature was stabilized at 10°C. 20% of the most active cells

4. POTENTIAL OF THE CHERENKOV EFFECT FOR IMPROVED TIME RESOLUTION AT LOW γ -PHOTON ENERGIES

were deactivated, the trigger thresholds were set to 1, the validation was set to 4 with a validation interval of 5 ns followed by an integration interval of 85 ns. Two of such detectors (1 crystal, 1 DPC) were mounted in a coincidence setup with a ^{22}Na source in between. The 511 keV back-to-back emitted annihilation photons were used for determination of the CTR. The crystals were arranged in a way that their smaller faces were attached to 4 pixels on 4 separate dies, in order to be able to obtain 4 timestamps per scintillation. Reference measurements of crystals covering only one pixel and therefore provide only one timestamp were done, for comparing the obtained CTRs.

The recorded timestamps were sorted for data analysis, in order to make use of the order statistics. The obtained results are shown in figure 4.32. On the left hand side of this figure, the obtained CTR in dependency on the crystal length is plotted when using the only the 1st photon up to the 4th photon in order to calculate the CTR. The reference measurements (*single die*) were done for the crystal lengths 3 mm and 12 mm and are plotted in the same figure.

As expected, the CTR worsens with increasing order of the timestamp. Furthermore, it can be seen the reference measurement (CTR = 153 ps FWHM for 3 mm and 228 ps FWHM for 12 mm) defeats the results when utilising the first photon for the MTA significantly. The main reason for this is the much lower photon detection yield, for the MTA measurements, which can be simply explained by the low fill factor when the crystals are covering 4 neighbouring dies, see figure 4.32, on the right hand side. The fill factor for the MTA is 0.77, when comparing with the reference measurement and therefore, 23% of the photons are lost simply due to this geometrical effect. It seems that even more than 23% of the photons were lost for the MTA measurements which might be a result of the difficult alignment of the crystals on the dies. As a consequence the intrinsic time resolution for the MTA approach is bad compared to the reference measurement.

Nevertheless, the obtained data were used for comparing three different ways of obtaining a time estimator for the electron-positron annihilation in the ^{22}Na source:

- single timestamps (1st to 4th) were used for calculation of the CTR separately (*single*),
- the average timestamp was calculated (*average*),

4.5 Experimental evaluation of a multi-timestamp approach for improvement of the timing performance of scintillation detectors

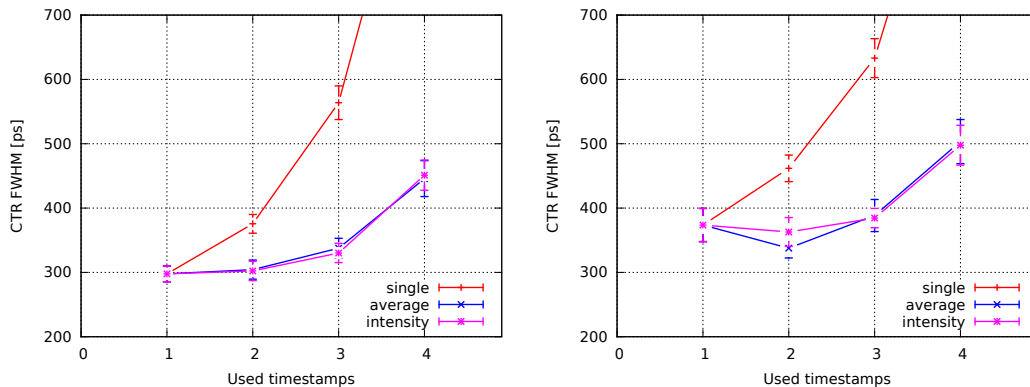


Figure 4.33: Comparing the results of three methods for determination of the CTR using a multi-timestamp approach for a crystal with a length of 3 mm, on the left hand side and a crystal of 16 mm length on the right hand side. The lines are including as eye-guides and do not represent fits.

- and a intensity weighted timestamp (*intensity*) was determined.

In figure 4.33, the results of this analysis are plotted and show, that the *single* timestamp gives the worst results for more than one timestamp. Nevertheless, the other methods do not improve the CTR. Although, the decrease in time resolution is not so significant as for the *single* timestamps.

Discussion Using the MTA, worse CTRs were obtained when compared to the reference measurement. This can be explained by the bad fill factor due to the bonding gaps in between the dies of the DPC. Therefore, many photons were lost for the MTA measurements resulting in a worse CTR. Nevertheless, this approach should evaluate the potential of utilising more than one timestamp for determination of a photo-interactions time estimator. In (13; 16) it has been shown that information of additional timestamps can be used for improvement of the overall CTR of monolithic scintillators. Due to the large volume of the scintillators an estimation of the point of photon-interaction can be performed using the measured photon intensities. With this information the timestamps can be corrected for the delay due to photon propagation.

Using crystal rods, as it was done for this measurement, this cannot be done in a similar way. Due to the fact, that the photons which are arriving later at the sensor, have a significantly larger time spread due to photon propagation. In that case, the intensities give not a precise information about the location in the plane parallel to the

4. POTENTIAL OF THE CHERENKOV EFFECT FOR IMPROVED TIME RESOLUTION AT LOW γ -PHOTON ENERGIES

detector surface and therefore this approach did not result in a relative improvement of the CTR.

The results were very sensitive on the crystal-position on the tiles and small deviations already had a large impact on the detected photon numbers and therefore the CTR. An intensity weighing was done, which seems to correct partly for the errors due to inaccurate mounting of the crystals on the tiles. Conclusively, the simple methods of calculating average or a intensity weighted time estimator do not improve the CTR for this measurement, nevertheless, an improved setup and advanced analysis methods might have the potential to exploit the additional information.

An additional effect can be seen in figure 4.32: a decreasing CTR with increasing crystal length showing the influence of DOI and photon propagation. Furthermore, it should be noted that the CTR for the 16 mm long crystals are not following the overall trend of increasing CTRs. A reason for the unexpected improvement of the CTR is probably linked to the fact, that this crystal was not coming from the same production batch of crystals and may have slightly better properties than the other crystals. This needs to be verified and will be part of future research.

Summarising, studies on the influence of photon statistics were done and tried to be applied in experiment using LSO:Ce scintillators with a multi-timestamp approach. Although, the results did not show an improvement in time resolution, this approach is promising for future investigations, as the major factor worsening the results was the low fill factor for this setup. At an comparable photon detection efficiency, this approach has potential to improve the overall CTRs. A new generation of the Philips DPC with increased fill factor is under development which should solve this handicap and allow more accurate investigations¹.

¹Private communication with Philips

5

Cherenkov effect at low energies: proof of principle measurement

Parts of this chapter have been published in (61) and can be found also in appendix 7.2 ©2014 IEEE. The parts presented in this section are the work of the author of this thesis.

In this section, proof of principle measurements of detecting Cherenkov photons following the photoelectric absorption of 511 keV annihilation-photons will be shown. First of all, this will be done in a basic measurement using PMTs and lead glass. In a next step, the investigations are extended to Cherenkov photon detection using the Philips DPC as photon detectors. Finally, several pure and hybrid Cherenkov radiators will be investigated in terms of their Cherenkov photon yield and coincidence time resolution.

5.1 Proof of principle using PMTs

Coincidence measurements have been performed to proof the principle of detecting Cherenkov photons due to the recoil electrons generated by the 511 keV annihilation photons.

Two Hamamatsu R1450 PMTs with a transit time spread of 360 ps (sigma) were used for the measurement. The PMTs were arranged in a coincidence setup with a ^{22}Na source in the centre, see figure 5.1. For optimizing the alignment, the source could be moved in vertical direction by a stepping motor. Artefacts due to 511 keV photons

5. CHERENKOV EFFECT AT LOW ENERGIES: PROOF OF PRINCIPLE MEASUREMENT

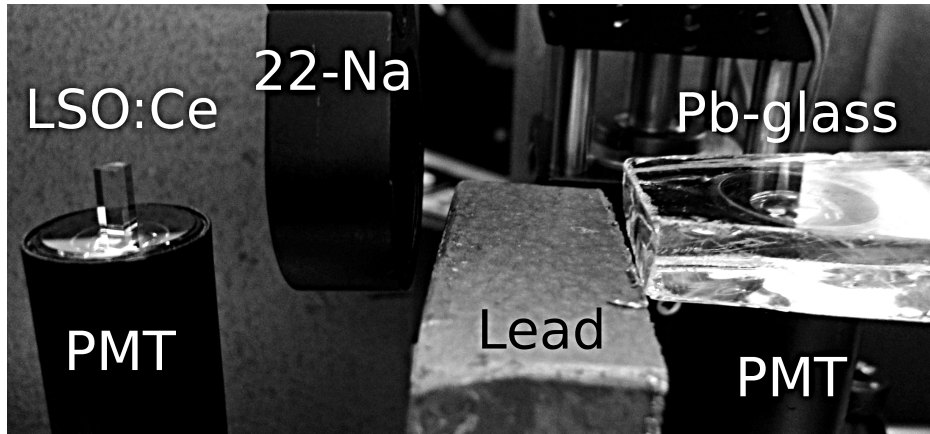


Figure 5.1: Setup for the proof of principle of Cherenkov photon detection (61). ©2014 IEEE

entering the PMT and the PMT-window were avoided by placing a brick of lead in between the source and the PMT attached to the Cherenkov radiator. As Cherenkov radiator, a shard of lead glass RD50 from Schott, with a high fraction of lead-oxide ($> 65\%$), with a size of $\sim 4 \text{ cm} \times 5 \text{ cm} \times 0.8 \text{ cm}$ and two faces polished was used. On the opposite side LSO:Ce, with a size of $3 \text{ mm} \times 3 \text{ mm} \times 8 \text{ mm}$ was coupled to the second PMT as reference detector. The output signals of both PMTs were split, with one part connected directly to a 4 channel digital WavePro 735Zi oscilloscope from LeCroy and the other part to a constant fraction discriminator (CFD, model 103, developed at PSI) before connected to the oscilloscope.

For an accurate threshold setting, the output of the PMT with the lead glass on top was amplified using a NIM amplifier module 778 from Philips. The CFD thresholds were set to a level of 0.5 photons for the PMT attached to the lead glass and for the reference detector to a level between the Compton edge and the 511 keV photo peak. The coincidence was done by triggering on the two CFD outputs and coincidence time resolution of 832 ps FWHM was obtained, see figure 5.2, on the left hand side.

To ensure not to trigger on photons created in the PMT window, the measurement was repeated after removing the lead glass from the PMT. The obtained background spectrum is plotted in figure 5.2, on the right-hand side. Comparison of the two plots proves that Cherenkov photons have been detected with this setup.

The relatively poor CTR is a result of the equipment and setup configuration, which

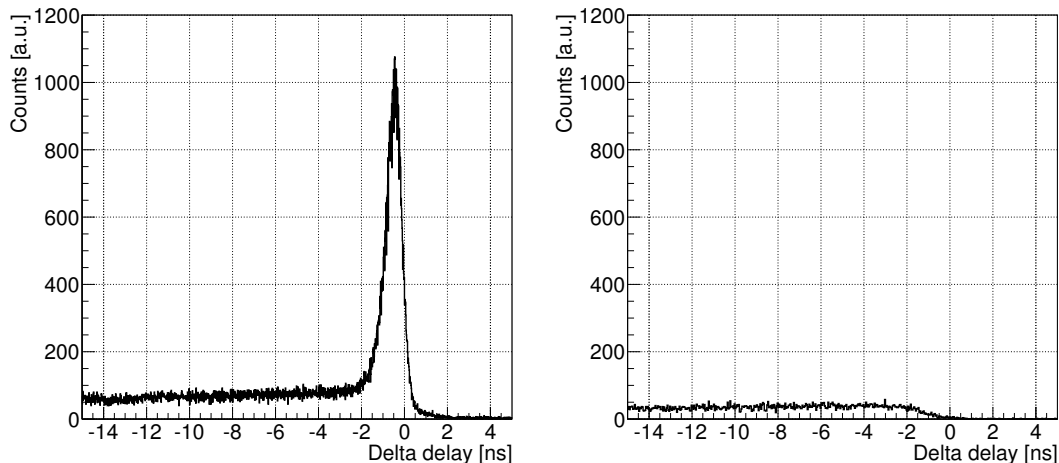


Figure 5.2: Time difference of the two PMT signals from the coincidence measurement of lead glass vs LSO:Ce on the left. On the right, the measured background spectrum is shown, when the lead glass is removed from the PMT (61). ©2014 IEEE

was chosen for a proof of principle of Cherenkov photon detection and not for achieving the best time resolution. Furthermore, the large size of the lead glass leads also to an additional time spread. By optimizing the setup, including the geometry of the lead glass, an improved CTR can be expected.

Nevertheless, the detection of Cherenkov photons following photoelectric absorption of 511 keV annihilation-photons in lead glass was proven, however, with a relatively poor Cherenkov detection yield of ~ 1 -2 photons on average.

5.2 Cherenkov photon detection using SiPM

The setup presented before was only suitable for proving the principle of detecting Cherenkov photons at energies of the annihilation photons of 511 keV. As PMTs are more and more replaced by solid state photo detectors due to their advantages, the Philips DPC were used for further investigations. These detectors combine insensitivity to magnetic fields, with fast triggering on the first arriving photon and offers additional photon counting capabilities. Although, the advantages of the DPC are good for precise time determination especially for the low photon yields of Cherenkov emission, the high dark-count rates of such semi-conductor devices makes the detection of the number of photo electrons difficult. This is because the validation threshold has

5. CHERENKOV EFFECT AT LOW ENERGIES: PROOF OF PRINCIPLE MEASUREMENT

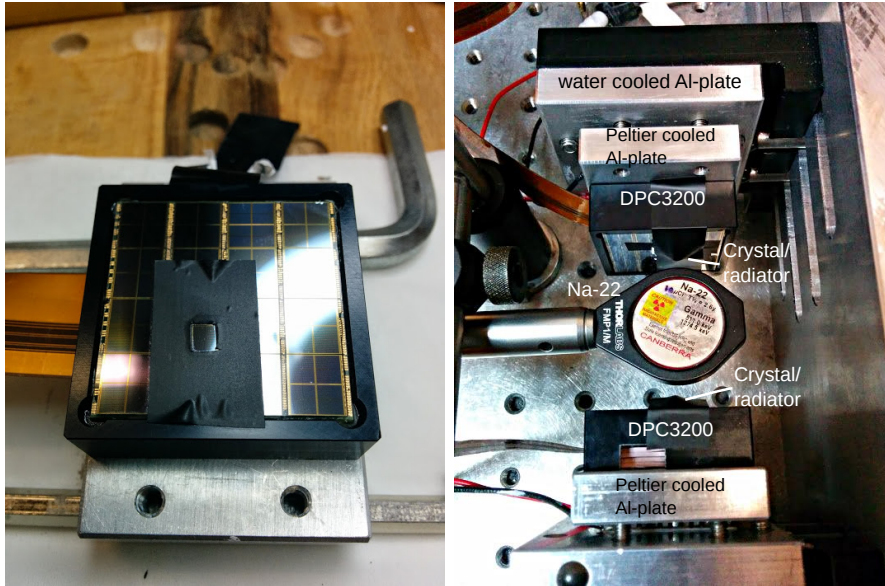


Figure 5.3: Setup for the coincidence measurements using pure and hybrid Cherenkov radiators. The Teflon wrapped crystals are fixed below black tape. ^{22}Na was used as positron source and mounted in between the crystals, emitting back-to-back annihilation-photons at 511 keV. Below the DPCs the Peltier and water cooling can be seen.

to be set to the level of dark-counts and consequently dark-counts can trigger unwanted events. Nevertheless, proving Cherenkov photon detection at these low energies using silicon photon detectors could have big impact on the time resolution of TOF-PET-like detectors.

5.2.1 Setup

Two DPCs (type 3200) were mounted on aluminium plates which were cooled by Peltier elements and water. For fixation of the crystals the sensitive area of the DPC was surrounded by black tape. The scintillators or Cherenkov radiators, respectively, were attached to the sensors using BC-430 optical grease from Saint-Gobain, with a refractive index of 1.465 and a flat transmission of 95% for wavelengths between 280 and 700 nm, see 7.8. Furthermore, the crystals were fixed using black tape. A picture of the setup can be seen in figure 5.3.

For the reference measurement, two cubes of LSO:Ce from EPIC crystal (78) with edge lengths of 3 mm and wrapped in Teflon tape were mounted on top of a DPC. Each crystal was positioned in the center of a pixel, which was the only pixel activated for

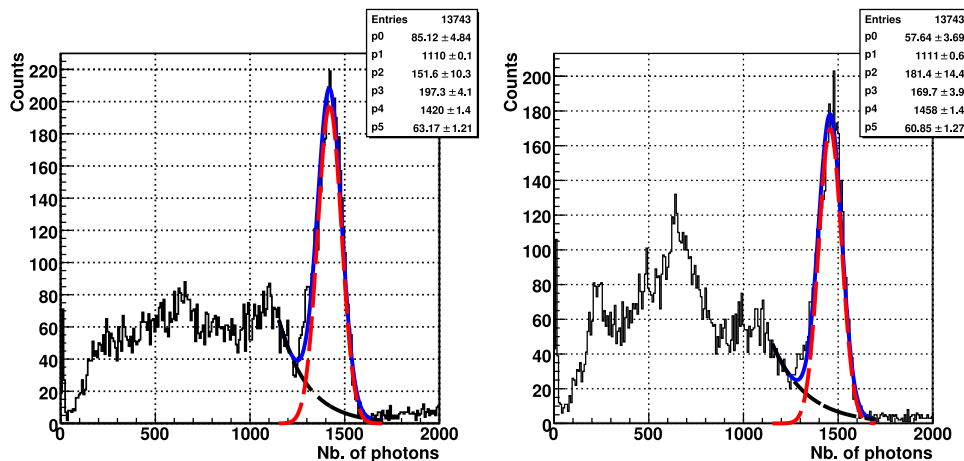


Figure 5.4: Obtained photon number spectra with two cubes of LSO:Ce with edge sizes of 3 mm and Teflon wrapping. The fits of the peaks dedicated to the photoelectric interaction of the 511 keV annihilation photons (red, dashed curves) are included.

the measurement. The DPCs with the crystals were arranged face-to-face and a ^{22}Na source was mounted in between them. The temperature was stabilized at 10°C , and 10% of the cells with the highest dark-count rate were switched off. Trigger levels were set to 1 and validation to 4, with validation intervals of 5 ns and integration intervals of 85 ns.

With these settings, an energy resolution of 10.4% and 9.8% in terms of FWHM was obtained, respectively. The 511 keV peak was fitted using an exponential and a Gaussian function:

$$p0 \cdot e^{-\frac{x-p1}{p2}} + p3 \cdot e^{-\frac{1}{2} \left(\frac{x-p4}{p5} \right)^2} \quad (5.1)$$

with the parameter $p4$ representing the mean and parameter $p5$ the standard deviation of the Gaussian contribution of the fit. The photon number spectra are shown in figure 5.4 for both scintillators.

5.2.2 Reference measurement using 3 mm cubes of LSO:Ce

For determination of the CTR cuts on the photon number spectra were set in order to exclude Compton-scattered events. This was done using the mean and the standard deviation of the Gaussian fit of the peak dedicated to the 511 keV photons. The lower cut was set to the mean-value of the Gaussian fit of the photon number spectrum,

5. CHERENKOV EFFECT AT LOW ENERGIES: PROOF OF PRINCIPLE MEASUREMENT

Temp. [°C]	Cells deact. [%]	OV [V]	l_{crystal} [mm]		Energy resolution [%]		CTR
			left	right	left	right	FWHM [ps]
12	20	2.5	3	3	10 ± 0.15	8.2 ± 0.16	149.2 ± 6.86
12	20	3	3	3	8.6 ± 0.18	8.6 ± 0.18	153.5 ± 5.88
12	20	3.3	3	3	8.3 ± 0.15	8.2 ± 0.16	168.3 ± 5.64
-18	10	2.5	3	3	11 ± 0.19	11.7 ± 0.21	156 ± 3.67
-18	10	2.75	3	3	10.8 ± 0.17	9.1 ± 0.21	154.7 ± 4.84
-18	10	3	3	3	10.6 ± 0.18	10.3 ± 0.18	149.3 ± 4.44
-18	10	3.3	3	3	9.7 ± 0.18	10.2 ± 0.2	159.9 ± 4.7
-18	10	3	3	8	9.1 ± 0.11	7.6 ± 0.08	191.8 ± 3.95

Table 5.1: Energy resolution and coincidence time resolution for cubes of LSO:Ce with edge lengths of 3 mm. Both, energy resolution and CTR are presented in terms of FWHM. Temp. is the tile temperature, OV is the overvoltage, l_{crystal} is the length of the crystal, which is given for the left and the right detector, as it is for the energy resolution. The last line of the table shows the results for the reference used for following investigations on Cherenkov radiators. This measurement was done with one LSO:Ce cube with edge sizes of 3 mm in coincidence with an 8 mm long rod of LSO:Ce.

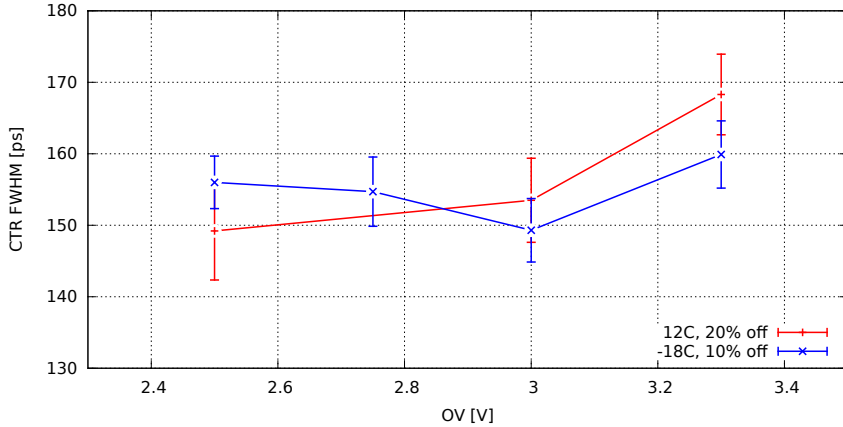


Figure 5.5: Coincidence time resolutions of the reference measurements using LSO:Ce with edge sizes of 3 mm and Teflon wrapping at an energy of 511 keV for various overvoltages at two different temperatures and different fractions of inactivated cells. The lines are included in the plot to guide the eyes.

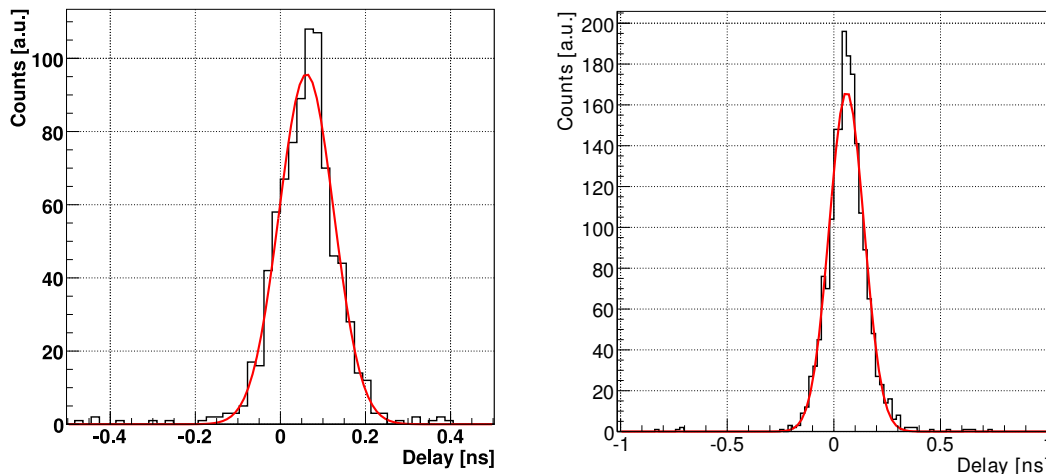


Figure 5.6: Obtained coincidence time resolution using two cubes of LSO:Ce with edge sizes of 3 mm and Teflon wrapping at an energy of 511 keV, on the left hand side and for one cube replaced by a $3 \times 3 \times 8 \text{ mm}^3$ crystal of LSO:Ce, on the right hand side.

subtracted by one sigma of the fit. The upper cut was set to the mean of the fit with two times sigma added. The lower cut was chosen to be closer to the mean value in order to reduce the influence of Compton scattered events in the TOF spectrum. Using these cuts and fitting the time differences with a Gaussian function a coincidence time resolution of 151 ps FWHM was obtained, see figure 5.6. The FWHM was calculated by multiplying the sigma with a factor of 2.35.

During further measurements, the temperature, the fraction of the most active cells and the over voltage was varied. The results of the measurements are summarized in table 5.2.1. Depending on the settings, the CTR varies from 149.2 ps to 168.3 ps.

5.2.3 Reference measurement using a 8 mm long LSO:Ce rod

As the dimensions of the available Cherenkov radiators had dimensions of $3 \times 3 \times 8 \text{ mm}^3$, the reference measurement was done using crystals with the same dimensions. Therefore, one cube of LSO:Ce was replaced by LSO:Ce with a size of $3 \times 3 \times 8 \text{ mm}^3$. The overvoltage was set to 3 V, which gave the best results in the measurements before, the temperature was set to -18° and 10% of the cells with the highest dark-count rates were deactivated. All other settings remained untouched. At 12°C a CTR of $201.8 \pm 4 \text{ ps}$ FWHM was obtained. Decreasing the temperature to -18°C a CTR of

5. CHERENKOV EFFECT AT LOW ENERGIES: PROOF OF PRINCIPLE MEASUREMENT

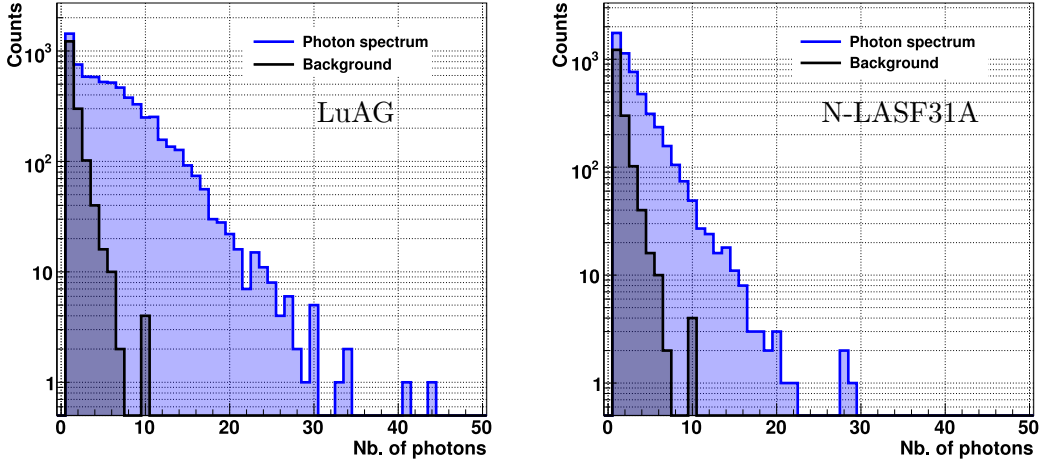


Figure 5.7: Photon number spectrum, when triggering on 511 keV photons on LSO:Ce. Compared to figure 5.9 all settings are the same except for using cut on the LSO:Ce photon number spectrum (Gaussian fit $-1\sigma + 2\sigma$), which was also used for the background spectrum. The mean number of photons is 5.7 for LuAG (rms = 4.7) and 3.1 (rms = 2.7) for N-LASF31A.

191.2 ± 4 ps FWHM was obtained, which is significantly worse than the 149.3 ps for two cubes with 3 mm edge lengths but comes as expected due to the influence of photon propagation.

The decrease in temperature resulted in a 10 ps better CTR and is therefore, preferred as reference. Furthermore, the main reason of decreasing the temperature is to decrease the dark-count rate of the DPC and therefore, decrease the probability of random coincidences triggered by dark-counts.

5.2.4 Coincidences with pure Cherenkov radiators

For the measurements of the coincidence time resolution using Cherenkov radiators, the LSO:Ce bar with 8 mm length of the reference measurement was replaced by a Cherenkov radiator. In this case the Cherenkov radiators were undoped LuAG and the optical glass N-LASF31A. Both were wrapped in Teflon. The properties of these materials have been shown in table 4.3. Both pixels had a size of $3 \times 3 \times 8$ mm³ and were mounted with their small face onto a pixel of a DPC3200. As for the reference measurement before, the DPCs were cooled to -18 °C to decrease dark-counts. Trigger level and validation threshold were set to 1 photon, furthermore, the validation interval

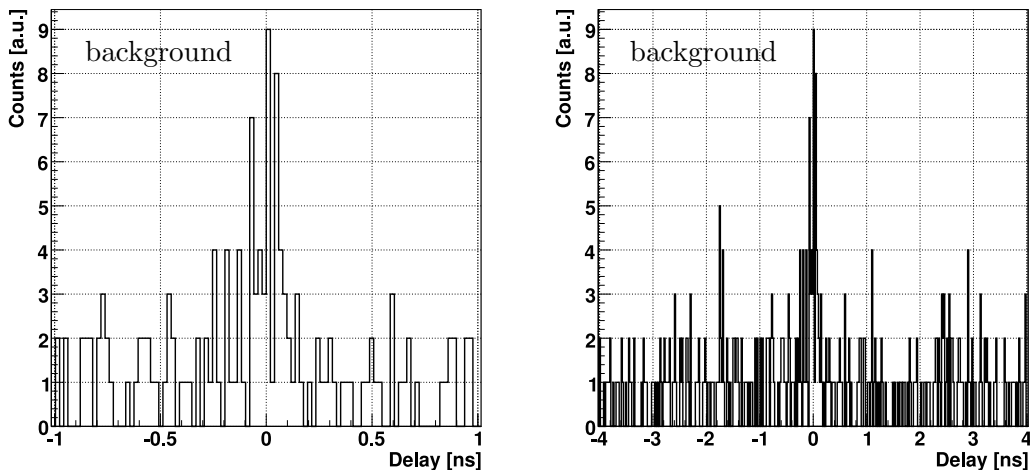


Figure 5.8: TOF spectra of the background measurement with the Cherenkov radiators removed in coincidence with the reference LSO:Ce crystal. It can be seen that almost no random coincidences with dark-counts could be detected within the 5×10^6 recorded frames.

was set to 5 ns and the integration interval was set to 0 ns. These values were used for the sensor equipped with the Cherenkov radiators. For the reference crystal, the parameters remained untouched. The trigger level was set to 1, validation interval to 5 ns with a validation threshold of 4 and an integration interval of 85 ns. In total 1×10^7 frames were recorded for the measurement.

Histograms of the number of detected Cherenkov photons are shown in figure 5.7, on the left for LuAG and on the right hand side for N-LASF31A. The data of the cube of LSO:Ce was used to select events of photoelectric absorption in this crystal. The mean number of detected photons for 5.7 for LuAG and 3.1 for N-LASF31A. It can be seen that up to 30 photons can be detected for LuAG and up to 20 photons for N-LASF31A.

Additionally, a background spectrum was taken for 5×10^6 frames and was multiplied by a factor of two to be comparable with the 1×10^7 measured frames of the measurement with the crystals. The background spectrum is overlaid to the histograms in figure 5.7. For the background measurement, the whole setup and parameters were left untouched but only the Cherenkov radiator was removed. The LSO:Ce crystal remained on the reference DPC. For this configuration up to 10 photon-counts, which are

5. CHERENKOV EFFECT AT LOW ENERGIES: PROOF OF PRINCIPLE MEASUREMENT

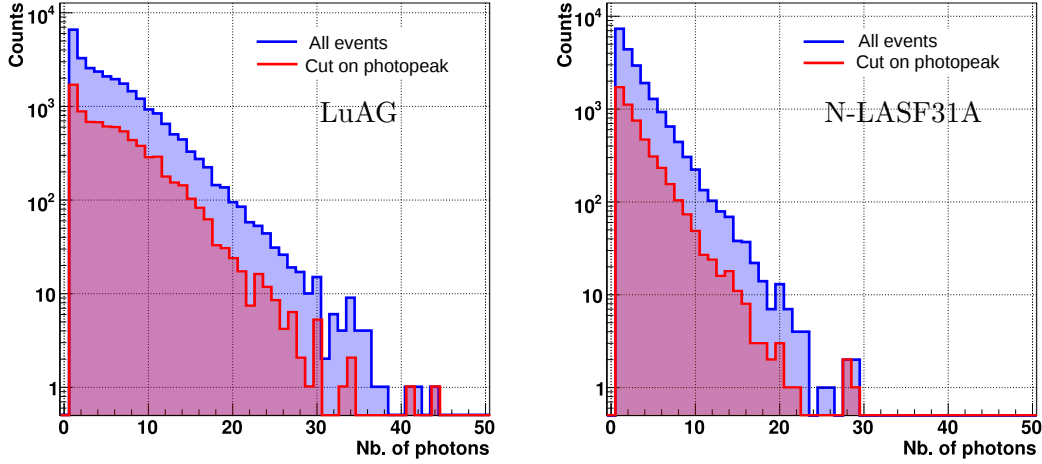


Figure 5.9: Influence of cuts in the reference data on the photon spectra of Cherenkov radiators. The number of detected Cherenkov photons in LuAG for 511 keV annihilation-photons. By triggering on the photopeak with the reference detector, the obtained mean Cherenkov photon yield increases from 5.51 to 5.7 for LuAG and remains at 3.1 photons for N-LASF31A.

attributed to dark-counts, could be detected on the DPC without a crystal attached. Compared to the number of photon-counts, in the case the Cherenkov radiators are attached, a significant difference can be seen for both N-LASF31A and even for LuAG, which proves that Cherenkov photons are emitted in the materials and can be detected with the DPCs. A comparison of Cherenkov emission and background is shown in figure 5.7.

For excluding artefacts due to random coincidences with dark-counts, also the TOF spectra of the background measurement were analysed and are plotted in figure 5.8, in time window of 2 ns on the left hand side and the same data within a time window of 8 ns on the right hand side. It can be seen, that almost no random coincidences with dark-counts were detected within the 5×10^6 frames and therefore, the influence of dark-counts on the results presented in the next section is small.

In figure 5.9, the data with when the Cherenkov radiators, is compared, once when no cuts were set for the reference detector (blue line) and second, when cuts on the photopeak were applied at the reference crystal (red). It can be seen that the mean number of detected photons hardly varies but there is a large change in the count rate of the events.

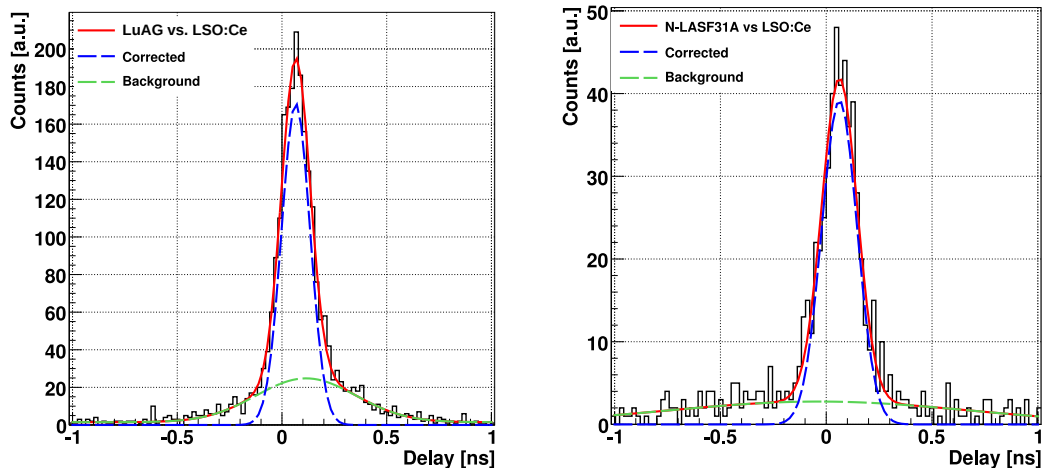


Figure 5.10: CTR of LSO:Ce (3x3x3mm) and LuAG (3x3x8mm) on the left hand side. The window for valid LSO:Ce events was set to the mean of the 511 keV $-1\sigma + 2\sigma$. The threshold for the Cherenkov detectors is set to 6 photons, which resulted in a CTR 146 ± 16 ps FWHM for LuAG and a CTR of 178 ± 16 ps for N-LASF31A. The bin width of the histograms corresponds to the TDC bin width of $10 \text{ ns}/512 \cong 19.5$ ps.

5.2.5 CTR with pure Cherenkov radiators

In figure 5.10, two example TOF-histograms are shown, on the left for LuAG and on the right hand side for N-LASF31A. On the data of the LSO:Ce reference crystal cuts on the photopeak were applied as discussed before. For the plots, the thresholds on the photon numbers were set to 6 photons. Thus, in the plots the data of all events with 6 or more detected photons of the Cherenkov radiators are plotted. The bin width of the histogram was chosen according to the bin width of the DPC-TDC. A TDC bin is determined by $10 \text{ ns}/512$ TDC bins, which is ~ 19.5 ps. It can be seen, that the histogram is not a perfect Gaussian but has a tail. Therefore, the fit function for determination of the CTR consists of 2 Gaussian functions. The green dashed line represents the background, whereas the blue dashed line represents the coincidences with Cherenkov photons.

What is understood as background is probably dedicated to two effects: first of all random coincidences with dark-counts add artificial events, but this effect should be small as seen for the background measurement before and should not make a structure as it is. Probably more important is the influence of the low Cherenkov photon yield.

5. CHERENKOV EFFECT AT LOW ENERGIES: PROOF OF PRINCIPLE MEASUREMENT

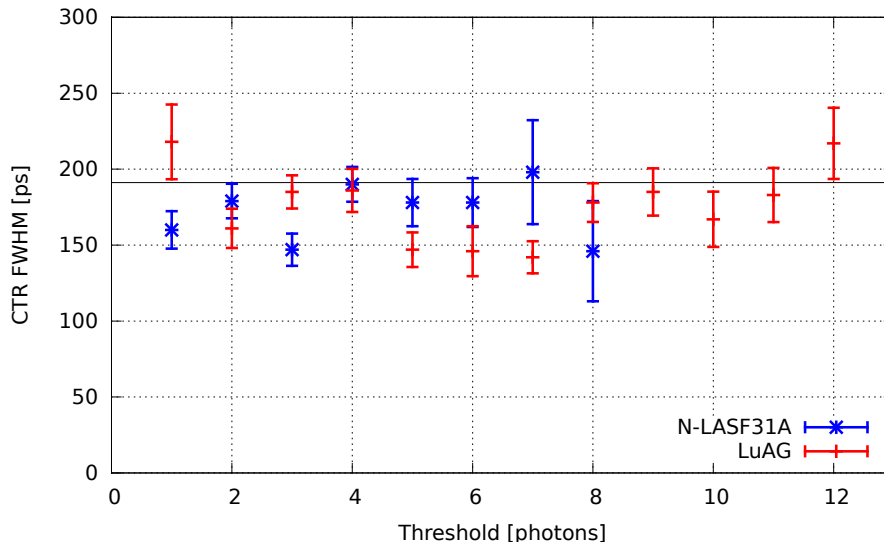


Figure 5.11: CTR of LSO:Ce ($3 \times 3 \times 3 \text{ mm}^3$) vs. LuAG ($3 \times 3 \times 8 \text{ mm}^3$) and LSO:Ce ($3 \times 3 \times 3 \text{ mm}^3$) vs. N-LASF31A ($3 \times 3 \times 8 \text{ mm}^3$). The results for N-LASF31A are represented by the blue stars. The results for LuAG are represented by the red crosses. Additionally, the CTR of the reference measurement with LSO:Ce ($3 \times 3 \times 3 \text{ mm}^3$) vs. LSO:Ce ($3 \times 3 \times 8 \text{ mm}^3$) is drawn as black line. Comparing the obtained CTRs with the value of the reference measurement it can be seen that especially for LuAG the CTRs are better for all thresholds between 2 and 11.

As the number of Cherenkov photons is small, the probability that one Cherenkov photon arrives at the photo detector without being reflected is small. This results in photons which arrive with a delay due to photon propagation inside the crystal. As discussed in the previous chapter this degrades the overall CTR.

A threshold scan of the number of detected photons was done and the time resolution was determined using the presented analysis method with a double Gaussian function. The results are plotted in figure 5.11. The blue stars represent the results for N-LASF31A and the red crosses represent the results with LuAG. Comparing the obtained CTRs with the value of the reference measurement with LSO:Ce which was 191 ps and is represented by the black line in the figure, it can be seen that especially for LuAG the CTRs are better for all thresholds between 2 and 11 photons. The obtained results show the potential of the Cherenkov effect due to its prompt photon emission compared to scintillation.

Besides the analysis method with the two Gaussian fits, two other analysis methods were investigated for determination of the CTRs. One is simply to determine FWHM

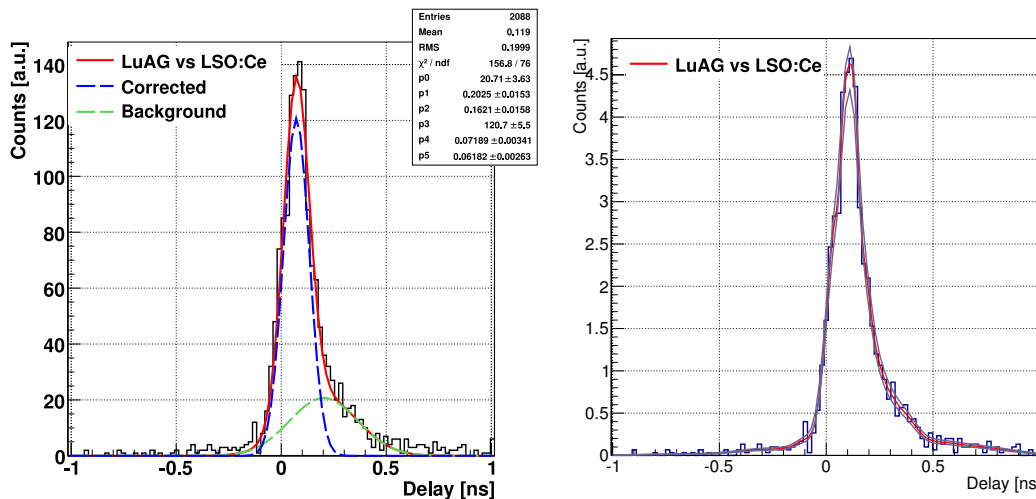


Figure 5.12: Example plots of two analysis methods for determination of the CTR for LuAG in coincidence with LSO:Ce. The plot on the left hand side shows the fit using two Gaussians, in order to deal with the contamination due to reflected photons. The Gaussian fit referring to the not reflected Cherenkov photons gives $\sigma = 61.82$ ps or 145.3 ± 6.2 ps FWHM. The CTR of the KDE is 159 ± 9.1 ps FWHM. These values represent the best obtained CTRs for the presented setup and are significantly better than the CTR of the reference measurement of 191.8 ± 4 ps.

of data in the histogram. This method is very sensitive on varieties of the maximum of the histogram, which can be large. In order to minimize this effect, an approach for smoothing the histogram using kernel density estimation (KDE) based on normal distributions was done. Using the function obtained by KDE the FWHM was determined. In figure 5.12 an example plot for the analysis using two Gaussian function is shown on the left hand side and an example for smoothing the histogram using the KDE approach is shown in the same figure on the right hand side.

In figure 5.12, on the left hand side, the histogram of the measurement with LuAG is shown with two thresholds applied: a lower one at ≥ 4 photons and the upper one at ≤ 8 photons. Analysing the data with the two Gaussian functions results in a CTR of 145.3 ± 6.2 ps FWHM, which is the best result for this configuration and is even better than the reference measurement of two LSO:Ce cubes, both with 3 mm edge sizes. Using the KDE method, which is plotted in the right hand side of the figure a CTR of 159 ps \pm 9 ps FWHM was obtained, which is also significantly better than the reference measurement with the 8 mm long LSO:Ce bar. Measuring simply the FWHM

5. CHERENKOV EFFECT AT LOW ENERGIES: PROOF OF PRINCIPLE MEASUREMENT

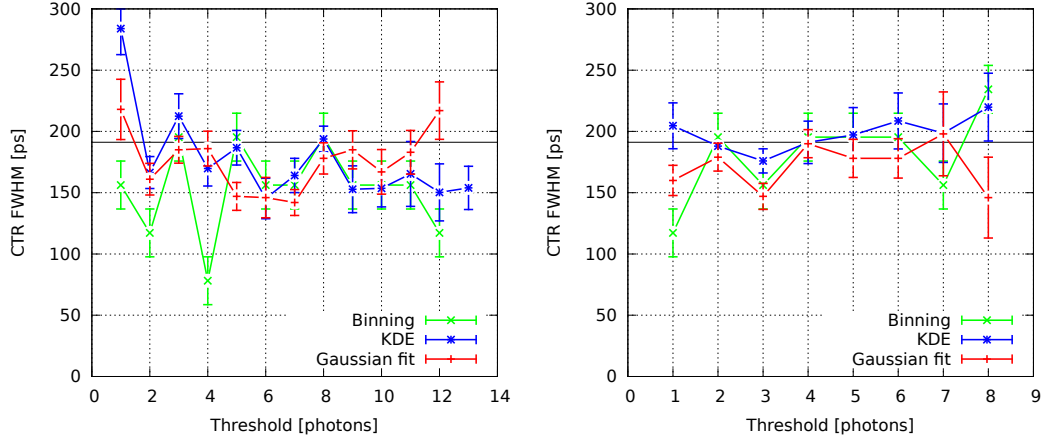


Figure 5.13: CTR of LSO:Ce (3x3x3mm) and LuAG (3x3x8mm) at certain photon numbers. The lines are guides for the eyes and don not represent a fit. For evaluation of the CTR from the histogram a binning of two TDC bins were chosen. The horizontal line at 191.18 ps represents the CTR of the reference measurements using two LSO:Ce crystals with the same dimensions as for this measurement. The threshold in here represents precise trigger levels, i. e., a trigger on a certain amount of photons.

of the histogram results in a width of 8 bins or 156 ps.

The three methods were also compared in a threshold scan. The comparison of the results obtained by the different analysis methods are shown in figure 5.13 for LuAG on the left hand side and for N-LASF31A on the right hand side. In this figure large variations when determining the FWHM of the histograms can be seen. As discussed before, this is mainly caused by large variations of the maximum of the histogram. The analysis using the KDE shows less fluctuations for the variation of the threshold. Nevertheless, it can be seen that the results for all analysis methods show in general better results for the CTR compared to the reference measurement over a wide range of thresholds, especially for LuAG.

One major problem for all of these methods is the limited amount of recorded events, which was mainly caused by an experimental problem due to condensation of water on the detectors. This lack of events mainly causes the large fluctuations for all of the CTRs. This problem will be solved by mounting the setup in an air tight box filled with dry air or nitrogen, which will be part of future research. Nevertheless, when comparing the results with the reference measurement, the obtained CTRs of all three methods tend to give better results than the reference measurement with LSO:Ce over

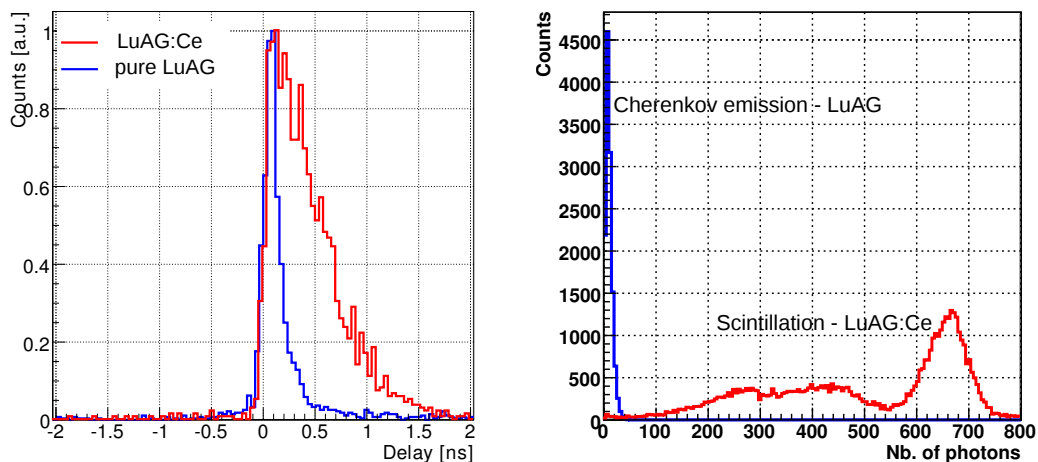


Figure 5.14: On the left hand side, the TOF-spectrum for LuAG:Ce vs. LSO:Ce drawn in red, the TOF-spectrum of undoped LuAG vs. LSO:Ce is drawn in blue. The difference of the two plots is the Ce doping and therefore, the main mechanism for photon emission, which is scintillation for Ce doped LuAG and Cherenkov emission for the undoped LuAG crystal. On the right hand side, the photon number spectra of both LuAG (blue) and LuAG:Ce (red) are plotted. The number of detected photons is for scintillation much higher than for the Cherenkov emission.

a wide range of thresholds, which shows the potential of using the Cherenkov effect for improving the time resolution.

5.2.6 Hybrid Cherenkov radiators

In this thesis hybrid Cherenkov radiators are understood as Cherenkov radiators, which additionally are a scintillator. In principle all of the scintillators can act as Cherenkov radiators. However, in scintillators such as LSO:Ce or LuAG:Ce most of the Cherenkov photons are absorbed, depending on the transmission spectra of the crystals, see figure 5.15. In the previous section the CTR of undoped LuAG was determined. For comparison of Cherenkov emission and scintillation two measurements were done, one with undoped LuAG and one with LuAG:Ce.

Results of the measurement comparing pure LuAG with LuAG:Ce are plotted in figure 5.14. On the left hand side of the figure, the obtained TOF spectra are compared. The blue line shows the TOF spectrum of pure LuAG which was obtained within the measurements presented in the previous section. For LuAG only Cherenkov emission

5. CHERENKOV EFFECT AT LOW ENERGIES: PROOF OF PRINCIPLE MEASUREMENT

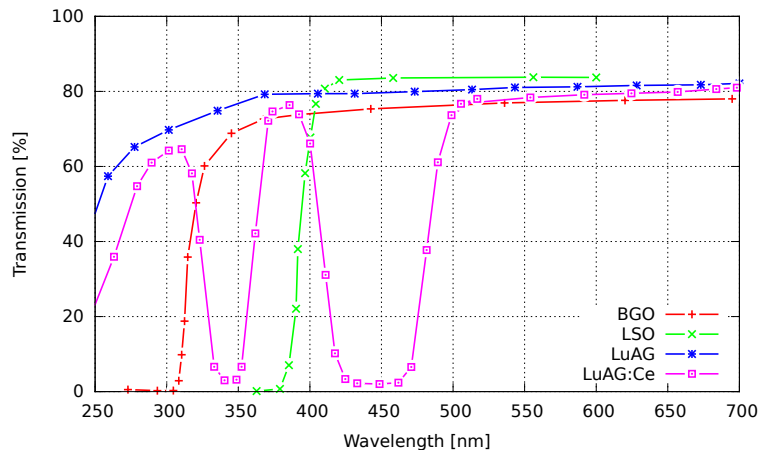


Figure 5.15: Transmission spectra for the investigated hybrid Cherenkov radiators (37; 66).

the main process of luminescence, accompanied, by relatively slow photon emission in the region of ns to μ s (38). However, the slow emission is hardly influencing the results due to the long time constants. The red line in figure 5.14, shows the obtained TOF spectrum of LuAG:Ce in coincidence with the LSO:Ce reference crystal.

According to the previously presented simulations scintillation accompanied by Cherenkov emission was expected. But it seems that hardly any of the fast Cherenkov photons reach the photo detector, as the obtained CTR is bad. Probably most of the Cherenkov photons are absorbed in the crystal and re-emitted by scintillation, which was also discussed before. The two absorption bands of LuAG:Ce, which can be seen in figure 5.15, are probably the reason that hardly any Cherenkov photons could be detected.

Another promising hybrid Cherenkov radiator is BGO not only due to its transmission characteristics but also due to its density and high refractive index. In last decades BGO was commonly used for PET, but recently it is more and more substituted by the faster LSO:Ce (4; 57). Calculations and simulation done in the previous chapter showed this material to be very promising. A transmission spectrum of BGO compared to LSO:Ce, LuAG:Ce and undoped LuAG can be seen in figure 5.15. It can be seen that BGO does not have the absorption bands of LuAG:Ce and has a low cutoff wavelength close to 300 nm and moreover, a high refractive index of 2.15, both of which are beneficial for Cherenkov emission. With the MC-simulation presented in chapter 4.1.2,

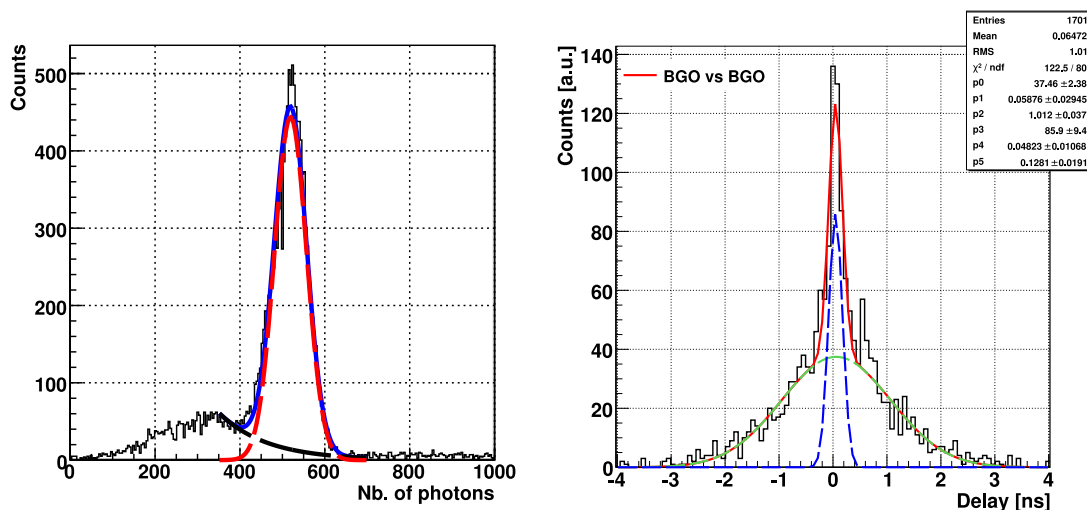


Figure 5.16: Energy spectrum of ^{22}Na measured with two BGO crystals in coincidence. The crystal were wrapped in Teflon.

4.2 Cherenkov photons for a short crystal of 3 mm length were obtained with a perfect photon detector.

Due to the promising characteristics, a coincidence measurement with BGO was done. Contrary to the measurements before, both BGO crystals had a size of $3 \times 3 \times 8 \text{ mm}^3$. Again the manufacturer of the crystals was EPIC crystal (78). All faces were polished and the crystals were wrapped in Teflon tape. 20% of the SPADs with the highest dark-count rates were turned off for this measurement because the measurement was performed not at -18°C but -8°C due to technical difficulties with condensation. The trigger level of the DPC3200 was set to one photon. The validation length was 10 ns with a validation threshold of 4, followed by an integration interval of 645 ns. The obtained photon number spectrum and TOF spectrum are shown in figure 5.16. On the left hand side the photon number spectrum is drawn with on average 517 photons detected within the peak dedicated to the photoelectric absorption of the 511 keV annihilation-photons. The obtained energy resolution in terms of FWHM is 16.7%. On the right hand side of the figure, the obtained TOF spectrum is plotted and fitted by two normal distributions. The green dashed curve is dedicated to scintillation photons of BGO and shows a CTR of 2.38 ns FWHM. The blue dashed curve which is assumed to come from Cherenkov photons shows a CTR of 301 ps FWHM. The ratio of coincidences, potentially triggered by Cherenkov photons is 24% of the total

5. CHERENKOV EFFECT AT LOW ENERGIES: PROOF OF PRINCIPLE MEASUREMENT

coincidences. Together, these are the best measured CTRs for BGO according to the values in (4). For comparison, the determined CTR for LSO:Ce with the same crystal sizes (both 8 mm long) and the same setup is in the range of 240 ps FWHM.

5.3 Discussion and Conclusion

Proof of Cherenkov photon detection has been given, first, by using PMTs and lead glass in coincidence with LSO:Ce. The bad time resolution due to the transit time spread of the PMT was overcome by application of digital SiPM, the Philips DPC. Measurements of both, pure Cherenkov radiators and hybrid Cherenkov radiators has been performed and showed the possibility to detect Cherenkov photons after photoelectric absorption of 511 keV annihilation-photons. The measurements of the pure inorganic crystal material LuAG and the optical glass N-LASF31A showed Cherenkov emission. On average 5.7 Cherenkov photons were detected for LuAG and 3.1 photons were detected with N-LASF31A.

BGO was used for PET for a long time due to its high stopping power and good achievable spatial resolution. The observed narrow peak in the TOF spectrum of BGO, is assumed to be the result of fast Cherenkov emission. It indicates that the good timing properties of Cherenkov photons could be exploited in hybrid Cherenkov radiators, by applying the digital SiPM for photon detection. Using two BGO crystals of $3 \times 3 \times 8 \text{ mm}^3$, a CTR of 2.38 ns FWHM was obtained for the slow component and 301 ps FWHM for the fast component. To the best knowledge of the author, the obtained CTRs represent the best measured values for BGO so far (4). Although the CTR of BGO does not represent a breakthrough, it demonstrates the feasibility of adopting hybrid Cherenkov radiators and scintillators for TOF-PET. Further research on adequate materials and further development of the photo detector, would allow this approach to combine good timing performances with the determination of the deposited energy. Nevertheless, the low fraction of detected coincidences due to Cherenkov emission of 24% needs to be increased by research on the hybrid Cherenkov radiators in order to use such materials for TOF applications.

Contrary to the readout with analogue photo detectors, such as PMTs or analogue SiPMs, the use of the digital SiPM allows to really trigger on the first arriving photon and therefore to exploit the fast Cherenkov emission. In the case of the analogue

SiPM, the Cherenkov photons would be detected as well, but the Cherenkov photons might just slightly change the slope of the overall scintillation signal. Due to the slow rise time of preamplifiers and the use of time pick-off methods like constant fraction discrimination, the information of the Cherenkov photons would therefore, be lost. In other words the information of the Cherenkov photons would drown in the signal induced by scintillation due to the slow rise time of the electronics. Consequently, applying such analogue systems a benefit from the Cherenkov emission can be seen, as maybe a slight change in the initial slope of the analogue signal. This is especially the case in hybrid Cherenkov radiators with high light yield. The situation becomes more clear, when comparing the simulated photon arrival rates shown in section 4.2.9, with typical signal rise times of analogue photo detectors which are in the range of ~ 1 ns. The yield ratios given in table 4.6 show that Cherenkov emission is much higher in the first instants of a few hundred pico seconds compared scintillation itself. As a consequence, the digital SiPM seems to be the best suitable detector for exploiting the fast nature Cherenkov photon emission, especially in hybrid Cherenkov radiators.

Eventually, Cherenkov photon emission after photoelectric absorption of 511 keV annihilation-photons was proven in both, pure and hybrid Cherenkov radiators and showed, that the overall coincidence time resolutions of PET-like detectors can be improved by using this effect. On top of that, by the approach of applying hybrid Cherenkov radiators, energy determination of the annihilation-photon interaction can be provided.

5. CHERENKOV EFFECT AT LOW ENERGIES: PROOF OF PRINCIPLE MEASUREMENT

6

Outlook

In this thesis the time resolution of scintillation and Cherenkov emission for application to TOF-PET was investigated. The investigations were mainly based on silicon photomultipliers as photo detectors, due to advantages such as insensitivity to magnetic fields. Analytic and numerical simulation approaches showed that the major factors influencing the time resolution of the investigated detectors are photon statistics and photon propagation. The influence of photon statistics can be improved by utilisation of the Cherenkov effect and maximising its photon yield as proposed in this work. The contribution of photon propagation could be reduced by development and application of multi-timestamp-approaches, as they allow to determine the point of the annihilation-photon absorption and hence allow to correct for photon propagation. Such approach could be realised at best for large monolithic scintillators.

Theoretical approaches for better understanding of formation of the time resolution have been done already. Yet, further development of accurate theory especially on the influence of photon propagation could help to find the best time estimator for photoelectric interaction and consequently would help to determine a better estimator for time and place of the electron-positron annihilation of a PET-like system. Besides, theoretical investigations on implementation of the Cherenkov effect into established theory would additionally help to improve the benefits of this approach.

The potential of applying the Cherenkov effect to TOF-PET has been shown using a coincidence setup with one Cherenkov radiator in coincidence with a scintillator. As a next step coincidences of two 511 keV annihilation-photons using two Cherenkov radiators should be proven. First tests have been already done at our institute and

6. OUTLOOK

show promising results. However, further systematic measurements should validate these first results. For construction of a PET system, the number of channels need to be further increased, which can only be done when a separation of true events and dark-counts is possible. One way is the use of hybrid Cherenkov radiators.

A first approach to allow this separation was the use of BGO. With this scintillator not only a separation of true events and dark-counts could be done but also the deposited energy of the annihilation-photons could be determined and by this, Compton scattered events could be distinguished. Nevertheless, also pure Cherenkov radiators could emit a sufficiently high amount of photons to discriminate true events from dark-counts. First tests with increasing the validation threshold of the DPCs have been done already, and showed encouraging results. However, energy determination would still not be possible with a pure Cherenkov radiator at these low energies.

A promising candidate for a hybrid Cherenkov radiator/scintillator would be the inorganic crystal LuAG:Pr. This material would allow fast Cherenkov photon emission due to its high transmission, which is almost similar to pure LuAG. It would provide a scintillation yield which is 1.7 times lower than for LuAG:Ce (37), but sufficiently enough for energy determination. Another good candidate for a hybrid Cherenkov radiator would be PWO due to its characteristics like a high density of 8.28 gcm^{-3} , high refractive index of 2.2 and a low cut-off wavelength at $\sim 340 \text{ nm}$. Investigations on PWO have already been performed by (58; 81) and showed promising results on the emission of Cherenkov photons for 511 keV annihilation photons. However, the measurements were done using MCPs. Therefore, it would be interesting to investigate the potential of this material in combination with the digital SiPM. Samples of this material already arrived at our institute and will be investigated soon. Other more creative, approaches for increasing the Cherenkov photon yield could also help to improve the performance of this method. One of them would be increasing of the electron range, by, e.g., channeling effects of electrons inside the crystal lattice.

7

Appendix

7. APPENDIX

7.1 New approaches for improvement of TOF-PET

Reprinted, with permission, from L. Gruber, J. Marton, K. Suzuki, A. Hirtl. Reference: (60).

Author's personal copy

Nuclear Instruments and Methods in Physics Research A 732 (2013) 560–563



Contents lists available at ScienceDirect
Nuclear Instruments and Methods in
Physics Research A

journal homepage: www.elsevier.com/locate/nima



New approaches for improvement of TOF-PET



S.E. Brunner^{a,*}, L. Gruber^a, J. Marton^a, K. Suzuki^a, A. Hirtl^b

^a Stefan Meyer Institute for Subatomic Physics, Austrian Academy of Sciences, Vienna, Austria
^b Department of Radiology and Nuclear Medicine, Medical University of Vienna, Vienna, Austria

ARTICLE INFO

Available online 15 May 2013

Keywords:
Positron emission tomography (PET)
Time-of-flight (TOF)
Time resolution
Cherenkov effect
Depth of interaction (DOI)
Time walk

ABSTRACT

We present results of simulations on the influence of photon propagation and the Cherenkov effect on the time resolution of LSO:Ce scintillators. The influence of the scintillator length on the coincidence time resolution is shown. Furthermore, the impact of the depth of interaction on the time resolution, the light output and the arrival time distribution at the photon detector is simulated and it is shown how these information can be used for time walk correction.

© 2013 Elsevier B.V. All rights reserved.

1. Introduction

Advances in detector technology led to the construction of time-of-flight (TOF) positron emission tomography (PET) scanners, resulting in enhanced signal-to-noise ratio. Goal of this work is the improvement of time resolution of scintillation detectors for PET, by a better understanding of photon propagation inside scintillators and the influence of the Cherenkov effect.

The time resolution of scintillation detectors depends on several factors. It can be distinguished between the time resolution of the scintillator, the photon detector and the readout electronics. The magnitude of time resolution of the scintillator itself has two major origins: statistical processes of the scintillation ($\sigma_{\text{statistics}}$) and the photon propagation from the point of interaction to the photon detector ($\sigma_{\text{propagation}}$). The statistical processes are in principle influenced by scintillation rise- and decay-times and the light yield. The photon propagation process is influenced by factors, such as refractive index, scintillator geometry and surface finishing.

Cherenkov photons in scintillators are emitted by electrons, ionised by incident 511 keV photons and propagate faster than the speed of light c/n in the scintillator, with c and n being the speed of light in vacuum and the refractive index, respectively. Making use of the Cherenkov effect is very promising for TOF-PET detectors, as the time spread of this process is smaller than for scintillation in inorganic materials [1,2]. The direction of the Cherenkov photons can be described as a cone relative to the electron motion. The opening angle is determined by electron velocity and the refractive index of the crystal. Since the electron can be scattered to any direction, the direction of the photons is quasi-random. The

number of emitted Cherenkov photons for LSO:Ce is about 15 per 511 keV photon [2].

Monte Carlo simulations were performed to investigate the impact of photon propagation and the Cherenkov effect inside scintillators on the time resolution. These simulations will be described in the following sections.

2. Simulation setup

For the simulations Geant 4 [3] was used. LSO:Ce was chosen as scintillator material, since this is a common scintillating material for PET. The optical properties such as refractive index and transmission spectrum were taken from Ref. [4]. For the light yield, decay and rise time, typical values of 3×10^4 photons/MeV, 40 ns and 100 ps were chosen, respectively. In order to evaluate only the effect of photon production and photon propagation, the detection efficiency of the photon detectors was set to 100% over all wavelengths. Instead of simulating a positron source, photons with energies of 511 keV were generated in a point source and emitted into a defined direction, see Fig.1. The photon detectors recorded arrival time, wavelength and creation process of the photons. Compton scattered events were discriminated.

3. Coincidence time resolution

Besides photon statistics, the coincidence time resolution (CTR) of PET-like detector systems is influenced by variations of the depth of interaction (DOI) in the opposing scintillators, resulting in differences of the photon propagation lengths to the photon detectors. This effect can be reduced by shortening the crystals, however, leading to decreasing detection efficiency for 511 keV photons.

* Corresponding author. Tel.: +43 1427729735.
E-mail address: stefan.enrico.brunner@oeaw.ac.at (S.E. Brunner).

7.1 New approaches for improvement of TOF-PET

Author's personal copy

S.E. Brunner et al. / Nuclear Instruments and Methods in Physics Research A 732 (2013) 560–563

561

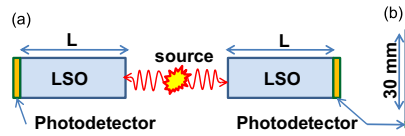


Fig. 1. Setup for the Geant 4 simulations. The setup (a) was used for the simulations on the coincidence time resolution, where the length of the LSO crystal L was varied from 1 mm to 30 mm. The source of the 511 keV photons was placed in between the crystals. Configuration (b) shows the setup for the simulations on the influence of the DOI on the time spread of photons at the detector due to photon propagation and the photon output of a scintillator. In this case the crystal is 30 mm long and D is the distance of the 511 keV photon source, which varies from 0.25 to 29.75 mm.

To evaluate the coincidence time resolution, a basic coincidence setup with two finger-like scintillators, each connected to one photon detector, was simulated, see Fig. 2(a). The crystal sizes were $3 \times 3 \times L$ mm³ with L ranging from 1 mm to 30 mm.

In Fig. 1, the simulated CTR is shown for various crystal lengths. Two curves are plotted, one representing the detection of scintillation photons only, the other one showing the improvement of time resolution if the detection of Cherenkov photons is included. For both lines the dependency on the crystal lengths is clearly visible. For crystal lengths from 1 mm to 30 mm the CTR ranges from 32 ps to 144 ps FWHM for scintillation and from 12 ps to 125 ps FWHM for including the Cherenkov effect, respectively. The reason for this behaviour is the decrease in localisation of the 511 keV photon interaction inside both of the crystals, simply due to the increasing size of the crystals. This uncertainty of localisation causes increasing time spread as a function of the crystal length. The impact of the Cherenkov effect on the CTR is clearly visible in Fig. 1.

Although time resolution improves with decreasing crystal lengths, longer crystals, providing reasonable sensitivity to the 511 keV photons, are used for real PET systems. The simulated detection efficiency of coincidences ranges from 2%, for $L=1$ mm to above 50% for $L=30$ mm. For real TOF-PET scanners a trade-off between time resolution and sensitivity has to be made.

4. DOI and time resolution

In the following, the impact of the DOI on the photon arrival rates and the photon output of the scintillator at the photon detector will be discussed. For the simulations, the setup of Fig. 2 (b) was used. The size of the simulated crystal was $3 \times 3 \times 30$ mm³ and was connected to a photon detector. A source of 511 keV photons was placed at the side of the scintillator and the distance D of the source relative to the photon detector was varied over the whole crystal length from 0 mm to 30 mm. By knowing the distance D , the DOI is determined.

The simulated photon arrival rates for three distances D at the photon detector are shown in Fig. 3. For the photon arrival rates coming from the scintillation process, a fast rise can be seen at early times, followed by an intermediate plateau until a second, smaller and slower increase of the photon rate is visible. The width of the plateau is directly related to the DOI of the penetrating 511 keV photons and vanishes for DOIs reaching the length of the scintillator.

The reason is originated in the isotropic emission of scintillation photons. The photons emitted towards the photon detector form the first rise of the number of scintillation photons and the consecutive plateau. The second rise is caused by photons emitted away from the photon detector, getting reflected at the end of the

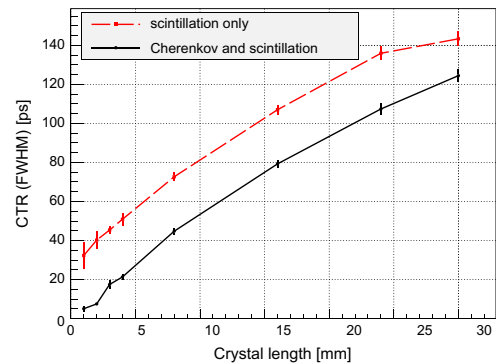


Fig. 2. CTR for various crystal lengths. The dashed curve indicates the CTR when only scintillation photons are detected. The solid line shows the CTR if Cherenkov photons are included in the detection.

scintillator and reaching the photon detector with a delay, depending on their travel path.

For the Cherenkov photons this effect is more obvious, since the duration of the Cherenkov process is shorter, compared to the scintillation process. The Cherenkov photons form two subsequent peaks with a distance and width proportional to the effective travel path inside the scintillator. Compared to the scintillation photons, the rates of Cherenkov photons form sharp peaks, providing accurate time information of the interactions of the 511 keV photons.

From the simulations, the mean trigger times at single photon level were determined for various DOIs, see Fig. 4. Until large DOIs, the trigger times are depending linearly on the DOI, but deviate at DOIs > 25 mm. The reason is that for low DOIs, photons emitted towards the photon detector are triggering the detector, the photons emitted into the opposite direction arrive at the detector with a significant delay. With increasing DOI, the time delay of these two consecutive peaks decreases until they merge at high DOIs, resulting in a higher photon rate at the photon detector and, therefore, in earlier trigger probability [6]. Furthermore, the number of detected photons is dependent on the DOI, see Fig. 5. It is clearly visible that the light output of the crystal decreases with increasing DOI.

Since Cherenkov photons provide very fast response to the photon interaction, for good time resolution it is beneficial to detect as many Cherenkov photons as possible. Unfortunately, many of them are lost in real detector systems due to low quantum efficiencies of photon detectors in the blue and UV-range and the cut-off frequencies of photon transmission in scintillators. Analyzing scintillation pulse shapes and detection of the first and second rise of photon arrivals, can provide information about DOI, and help reducing parallax errors of PET systems.

Due to limited time resolution of state-of-the-art photon detectors it is difficult to discriminate the first rise, the width of the plateau, and the second rise of the photon arrival rate. Nevertheless, this effect should be observable as variation of the rise time of scintillation pulses. Therefore, measuring the rise time or the number of detected photons not only parallax errors can be reduced by estimation of the DOI but also improved time resolution by determination of a corrected time stamp of interactions of the 511 keV photons inside the scintillator can be achieved. A dependency of scintillation rise times and the number of detected photons on the DOI has been measured by Refs. [5,6].

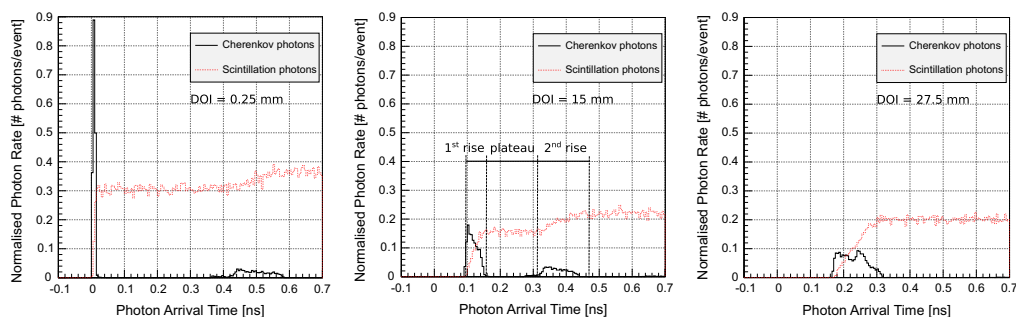


Fig. 3. Normalised photon arrival rates at the photon detector for various DOIs. The photon rates are discriminated by their creation process, which is either the scintillation or the Cherenkov effect. Normalisation was done using the number of detected 511 keV photons within the photopeak in the energy spectrum (i.e. an event). As bin size 10 ps was chosen. In the plot for a DOI of 15 mm the 1st rise, the intermediate plateau and the 2nd rise are marked for the arrival rate of scintillation photons.

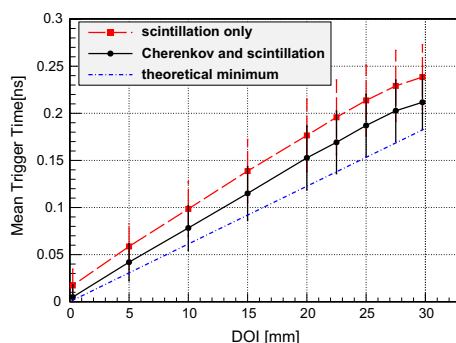


Fig. 4. Mean trigger time of the first photon vs. DOI for detection of only scintillation photons or detection of both. The blue dashed-dotted line indicates the theoretical minimum trigger time in LSO, when the photons undergo no reflections while propagating to the detector. (For interpretation of the references to color in this figure caption, the reader is referred to the web version of this article.)

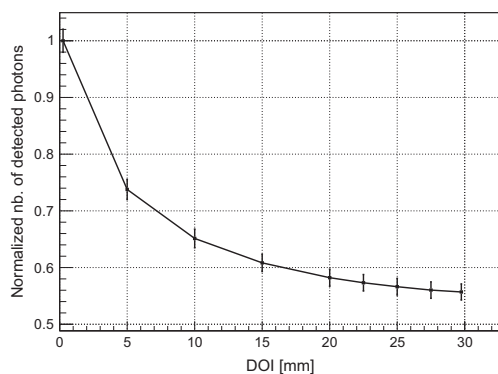


Fig. 5. Number of detected photons as a function of the DOI. This dependency can be used for time walk correction in PET-like detector configurations.

5. Time resolution of a scintillator

For investigations on the time resolution of a scintillator, a setup similar to that in Fig. 2(b) was used, but with the only

difference, that the photons were emitted from top, towards the photon detector. The time stamps were determined triggering on the first arriving photon (scintillation and Cherenkov effect). Contrary to the simulation in Section 4, the DOI is unknown.

The resulting photon arrival times can be seen in Fig. 6(a). Fig. 6(b) shows a scatter plot of the number of optical photons per 511 keV photon and the time when the first photon is arriving at the detector. Compton scattered events are discriminated with a discriminator threshold of 1600 photons per event. 92% of the 511 keV photons were detected, and 48% of them were Compton events. In Fig. 6(b) the time walk is visible. By calculating the mean photon arrival times for increasing amplitudes, time walk correction was applied. The corrected arrival time spectra can be seen in Fig. 6(c) and (d).

The total time resolution σ_{total} of the scintillator is ≈ 39 ps. The corrected data of Fig. 6(c) gives $\sigma_{\text{corrected}} \approx 30$ ps. Using

$$\sigma_{\text{total}}^2 = \sigma_{\text{time-walk}}^2 + \sigma_{\text{corrected}}^2$$

results in $\sigma_{\text{time-walk}} \approx 25$ ps.

The corrected time resolution, $\sigma_{\text{corrected}}$, still includes the standard deviation of the scintillation process, the contribution of the Cherenkov process and a contribution of photon propagation. Note, that the name of the variables σ do not imply normal distributions but are measures for the standard variation.

6. Discussion and conclusion

Simulations for determination of the time resolution of LSO:Ce crystals were performed. The influence of crystal sizes on the CTR for PET-like detector systems was shown and ranged from 32 ps to 144 ps FWHM for crystal lengths from 1 mm to 30 mm. Including the detection of Cherenkov photons showed a significant improvement of the CTR (12–125 ps FWHM). It was shown that the light output and the photon rate distribution at the photon detector are dependent on the DOI and that applying time walk correction significantly improves the time resolution from $\sigma_{\text{total}} \approx 39$ ps to $\sigma_{\text{corrected}} \approx 30$ ps. The contribution of the time walk was $\sigma_{\text{time-walk}} \approx 25$ ps.

By measuring the pulse amplitude or the rise time of a scintillation pulse, the DOI can be estimated. Information on the DOI allows to reduce parallax errors for PET and determination of the accurate time stamps of photon interactions results in improvement of TOF for PET. As the development of readout electronics proceeds quickly, extracting amplitude and rise-time information is realistic also for full TOF-PET systems [7].

7.1 New approaches for improvement of TOF-PET

Author's personal copy

S.E. Brunner et al. / Nuclear Instruments and Methods in Physics Research A 732 (2013) 560–563

563

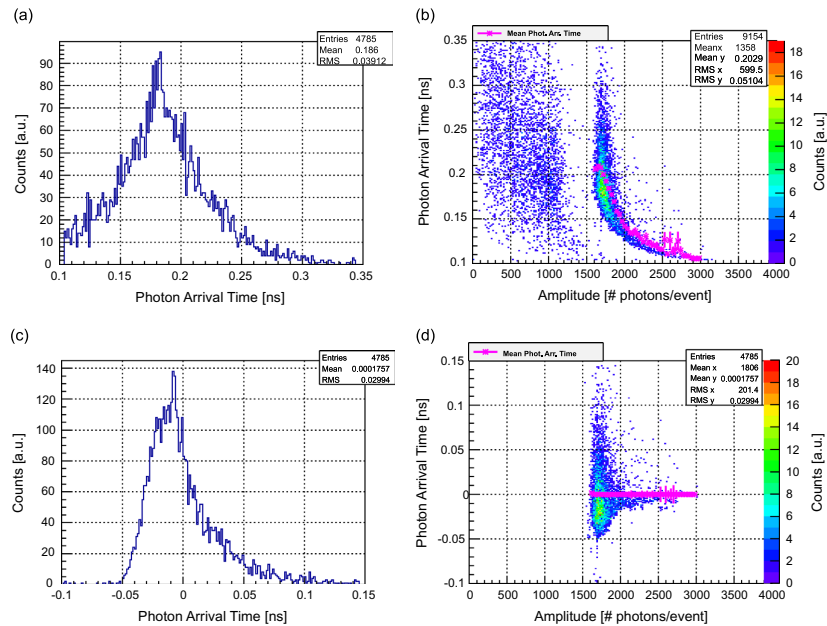


Fig. 6. Photon arrival times for the determination of the time resolution of a scintillator. (a) shows the photon arrival time, (b) the dependency of photon arrival time on number of arriving photons. In (b) also the Compton events are visible in the range below 1600 photons per event: the mean photon arrival times were calculated for different amplitudes and used to perform a time walk correction. Figures (c) and (d) show the time walk corrected photon arrival times and the corrected scatter plot, respectively.

For real PET-systems, photon detectors with high quantum efficiency in the blue- and UV-range and scintillators with increased transmission in these wavelength-bands would help to improve TOF for PET by making use of the Cherenkov effect. However, for time resolutions of state-of-the-art photon detectors the benefit from the Cherenkov effect is small, but becomes increasingly important if the time resolution of photon detectors approximates the time resolution of the scintillators.

Acknowledgments

This work was partly funded by EU-project HadronPhysics3 (project 283286).

References

- [1] R. Dolenc, et al., in: IEEE Nuclear Science Symposium Conference Record, 2010, p. 280.
- [2] P. Lecoq, et al., IEEE Transactions on Nuclear Science NS-57 (5) (2010) 2411.
- [3] S. Agnostoni, et al., Nuclear Instruments and Methods in Physics Research Section A 506 (2003) 250.
- [4] R. Mao, et al., in: IEEE Nuclear Science Symposium Conference Record, vol. 3, 2007, p. 2285.
- [5] R.L. Wiener, et al., in: IEEE Nuclear Science Symposium Conference Record 1991, 2010.
- [6] W.W. Moses, et al., IEEE Transactions on Nuclear Science NS-46 (3) (1999) 474.
- [7] W.J. Ashmanskas, et al., IEEE Nuclear Science Symposium Conference Record, 2011, p. 3347.

7.2 Studies on the Cherenkov effect for improved time resolution of TOF-PET

©2014 IEEE. Reprinted, with permission from L. Gruber, J. Marton, K. Suzuki, A. Hirtl, Studies on the Cherenkov effect for improved time resolution of TOF-PET, IEEE Transactions on Nuclear Science, 2014. This version is the accepted but not the published version, reference: (61).

IEEE TRANSACTION ON NUCLEAR SCIENCE

1

Studies on the Cherenkov Effect for Improved Time Resolution of TOF-PET

S. E. Brunner, L. Gruber, J. Marton, K. Suzuki, and A. Hirtl

Abstract—With the newly gained interest in the time of flight method for positron emission tomography (TOF-PET), many options for pushing the time resolution to its borders have been investigated. As one of these options the exploitation of the Cherenkov effect has been proposed, since it allows to bypass the scintillation process and therefore provides almost instantaneous response to incident 511 keV annihilation photons. Our simulation studies on the yield of Cherenkov photons, their arrival rate at the photon detector and their angular distribution reveal a significant influence by Cherenkov photons on the rise time of inorganic scintillators - a key-parameter for TOF in PET. A measurement shows the feasibility to detect Cherenkov photons in this low energy range.

I. INTRODUCTION

IN recent years, the Cherenkov effect for electrons at energies below 511 keV has become issue of investigations for improving the time resolution of time of flight positron emission tomography (TOF-PET) [1], [2]. The use of this effect promises an improvement of the coincidence time resolution (CTR) and therefore improvement of the signal to noise ratio in PET. The impact of the Cherenkov effect on the CTR was investigated in ref. [3].

In inorganic scintillators, as they are used for PET, scintillation photons are emitted after interaction of 511 keV annihilation photons with the scintillator, leaving an inner shell hole and an energetic primary electron, followed by a cascade of energy relaxation processes: radiative (secondary X-rays) and non-radiative decay (Auger processes), inelastic electron-scattering in the lattice, thermalization, electron-phonon interactions, trapping of electrons and holes and energy transfer to luminescent centers. All of them are introducing additional time spread to the emission of scintillation photons [4], [5]. For the emission of Cherenkov photons, most of these processes are bypassed, since Cherenkov photons are emitted during the phase of electron scattering. This is the reason why Cherenkov photons are emitted almost instantaneously, with a precise time stamp compared to scintillation photons.

The kinetic energy of electrons after photoelectric interaction with 511 keV photons is dependent on their binding energy in the material and ranges from about 450 keV - 510 keV. This energy is in the range of the lower boundary for the emission of Cherenkov photons, which is, e. g., about 100 keV for LSO. Nevertheless, it is sufficiently above the threshold for

Manuscript received May 24, 2013. This work was supported in part by EU-project HadronPhysics3 (project 283286).

S. E. Brunner (email: stefan.enrico.brunner@oeaw.ac.at), L. Gruber, J. Marton and K. Suzuki are with the Stefan-Meyer-Institute for Subatomic Physics of the Austrian Academy of Sciences, Vienna, Austria. A. Hirtl is with the Department of Radiology and Nuclear Medicine of the Medical University of Vienna, Austria.

TABLE I
INPUT VALUES FOR CALCULATIONS AND SIMULATIONS.

Material	Density [g/cm ³]	n	λ_1 [nm]	LY [photons/MeV]
LSO:Ce	7.4	1.82	390	27300
LuAG:Ce	6.7	1.84	see ¹	14000
BGO	7.13	2.15	310	8000
PWO	8.28	2.2	340	210
Pb-glass	5.05	1.79	340 ²	-

their emission. Calculations and simulations in this work will estimate the yield of the Cherenkov photons in the scintillator and after propagation to photon detectors.

A short rise time is known as one key-parameter for good time resolution of scintillators and is issue of investigations in TOF-PET [1], [4], [6], [7]. Therefore, this work focuses on the time distribution of both, scintillation and Cherenkov photons, when they are created inside the crystal and when they arrive at the photon detector. These arrival time distributions contain the information about the observable rise time of scintillators.

In the following, results of calculations and Geant4 [8] simulations on the yield of Cherenkov photons, their angular distribution, their influence on the observable rise time and their loss and absorption in scintillators will be shown. Finally, results of measurements of a basic coincidence setup using lead glass as Cherenkov radiator will be presented.

II. SIMULATION



Fig. 1. Basic coincidence setup used for the Geant4 simulation studies. The Cherenkov radiators/scintillators have a size of 3 mm × 3 mm × 3 mm, the photon detector attached has a sensitive surface of 3 mm × 3 mm.

For investigations of the influence of the Cherenkov effect on the time resolution in Cherenkov radiators and scintillating materials, Geant4 simulations were performed (Geant4, v9.4. p3), using the Geant4-Livermore libraries for electromagnetic processes. The simulations were done for cubic crystals of cerium doped lutetium-oxorthosilicate (LSO:Ce), cerium doped lutetium-aluminum-garnet (LuAG:Ce), lead-tungstate (PWO), bismuth-germanate (BGO) and lead glass with edge

¹The wavelength bands ($\lambda_1 - \lambda_2$) used are 260 nm - 320 nm, 360 nm - 420 nm and 480 nm - 1000 nm.

²Estimated value.

7.2 Studies on the Cherenkov effect for improved time resolution of TOF-PET

lengths of 3 mm. Their surfaces were polished and surrounded by air. For optical photon detection, a photon detector with a size of $3\text{ mm} \times 3\text{ mm}$ was attached to one of the faces of the crystals. Using these geometries, simple coincidence setups were simulated with a ^{22}Na source in between and the photon detectors located at the outer sides of the setup, see figure 1. The photon detectors were assumed to be ideal, i. e., infinite time resolution and a photon detection efficiency of 1. The creation time of the back-to-back photons with 511 keV represents time $t = 0$ for the simulation. For the rise times of all scintillators 100 ps were assumed. This assumption was done due to ambiguous numbers in the literature, which resulted from different measurement methods and influences of the rise times of photon detectors, electronics and photon propagation in the scintillator [9], [10]. The input values for the refractive index, n , the lower cutoff wavelength of the transmission spectrum, λ_1 , and the light yield, LY, are given in table I [11]–[15].

In the following, the scintillation yield is the number of optical photons emitted by scintillation and Cherenkov yield is the number of optical photons emitted due to the Cherenkov effect.

A. Yield of Cherenkov Photons

The number of Cherenkov photons emitted by an electron traveling faster than the speed of light in a dielectric medium can be calculated using

$$\frac{dN^2}{dx d\lambda} = \frac{2\pi\alpha}{\lambda^2} \cdot \left(1 - \frac{1}{\beta^2 n^2(\lambda)}\right), \quad (1)$$

with α being the fine structure constant, β , the electron velocity over the speed of light v/c and n , the refractive index, which was assumed to be constant for all wavelengths [16]. The Cherenkov yield was calculated and simulated for several scintillators and Cherenkov radiators, see table II. The upper boundary, λ_2 , was 1000 nm, the lower boundary, λ_1 , was chosen according to ref. [11] for LSO:Ce, BGO and PWO and in the case of LuAG:Ce according to ref. [12].

The numbers in table II give the expected yield of Cherenkov photons as response to 511 keV photons. For the values which are found under photoel. effect, only events, where the 511 keV annihilation photons interacted with the material by the photoelectric effect were considered. In the case of simulation, this was done by setting a threshold between Compton edge and 511 keV-peak in the total photon emission spectrum.

An example of the distribution of created Cherenkov photons in a cube of BGO, emitted after interaction of a 511 keV annihilation photon with the crystal, can be seen in figure 2, on the left-hand side. On the right-hand side of figure 2, the number of detected Cherenkov photons per event at the photon detector, attached to the cube, can be seen.

Comparing the numbers of created and detected Cherenkov photons in table II and figure 2, reveals a high loss of Cherenkov photons while their propagation through the crystal to the photon detector. One part comes from losses on the surfaces, when photons leave the crystal, the major part,

TABLE II
CALCULATED AND SIMULATED CHERENKOV PHOTON YIELD PER 511 KEV PHOTON INTERACTION.

Material	photoel. effect		all events		photoel. effect	
	calculated	created	created	detected	created	detected
LSO:Ce	18	7.6	0.7	13.8	1.1	
LuAG:Ce	27	11.5	3.2	24.3	7.2	
BGO	28	20.8	3.1	32.8	4.6	
PWO	23	22.6	3.8		see ³	
Pb-glass	29	20.9	3.3		see ⁴	

however, comes from absorption inside the crystal. This can be understood, as the number of emitted Cherenkov photons is increasing at shorter wavelengths proportional to $1/\lambda^2$ [17], i. e., mainly in the blue and ultra violet (UV) range, where the crystals are often not transparent, depending on λ_1 . Especially for LuAG:Ce a high Cherenkov yield of detected photons can be seen, due to the transmission spectra used in the simulation.

In the case of, e.g., LSO:Ce and LuAG:Ce, many Cherenkov photons are absorbed in the range of the excitation bands due to the cerium doping. Excitation and emission bands overlap and therefore, absorption not only of Cherenkov photons but also of scintillation photons is an issue (self absorption) [18], [19]. This overlap and the influence of the cerium doping on the transmission spectrum for LuAG:Ce is illustrated in ref. [12]. Absorption of Cherenkov photons could be decreased by adjusting (lowering) the amount of cerium doping. Increasing the Cherenkov yield with this method would lead to a decrease of the scintillation yield at the same time. Nevertheless, the total time resolution of the material might be improved, which will be shown in the following section.

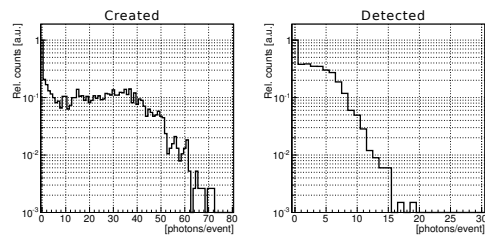


Fig. 2. Left: number of Cherenkov photons created in a cube of BGO with 3 mm edge length. Right: number of detected Cherenkov photons with a photon detector of $3\text{ mm} \times 3\text{ mm}$, attached to the cube. No thresholds were set (both, Compton scattered and events due to the photoelectric effect were respected).

B. Influence of Cherenkov photons on the Rise Time

A good rise time of scintillators is understood to be important for good time resolution in TOF-PET [1], [4], [6] and can influence the CTR significantly [7]. As discussed above, the total yield of photons created in scintillators is composed

³Discrimination not possible due to poor energy resolution.

⁴Discrimination not possible due to no scintillation.

7. APPENDIX

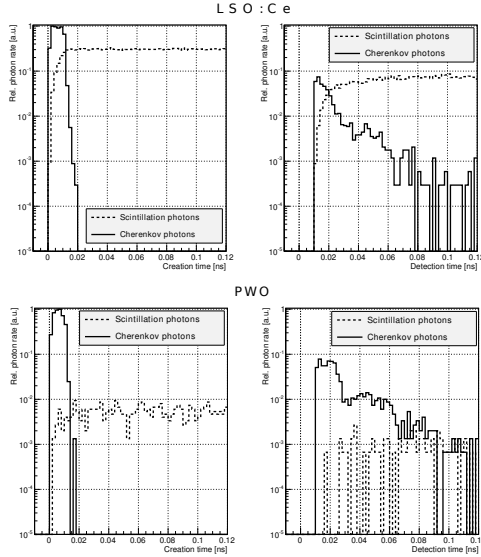


Fig. 3. Accumulated photon creation (left) and detection (right) rates at the photon detector for Cherenkov and scintillation photons for LSO:Ce (top) and PWO (bottom). The normalization for created and detected photons was done using the maximum of the creation rate of Cherenkov photons. A bin width of 2 ps was chosen.

of both, Cherenkov and scintillation photons. To understand the influence of Cherenkov photons on the total rise time of scintillators, the photon creation rates for both, Cherenkov and scintillation photons have been simulated. These rates are plotted in figure 3 for LSO:Ce and PWO, on the left side.

The time distribution of photons arriving at the photon detector after propagating through the crystal can be seen on the right-hand side of figure 3. Although the size of the simulated scintillators is small, photon propagation inside the scintillators introduce a significant spread to the arrival times of the photons at the photon detector. These spreads can be seen when comparing the left and the right side of figure 3. These accumulated photon creation and detection rates can be understood as probability density distributions and moreover contain information about the rise times of photon creation and the observable rise times at photon detectors.

The very short time span for creation of Cherenkov photons explains, that their creation and detection rate can exceed the rate of scintillation photons, although the Cherenkov yield is low compared to the scintillation yield. In table III, this effect becomes more explicit: it gives a quantitative overview of the ratio of the number of Cherenkov photons and the number of scintillation photons within time windows of 25 ps and 100 ps. The time windows were measured from the time of creation or detection of the first photon, respectively. When looking at a time window of 25 ps the Cherenkov yields of all materials are exceeding the scintillation yields. These

TABLE III
SIMULATED RATIO OF CHERENKOV AND SCINTILLATION YIELD.

Material	Yield ratio			
	created		detected	
	< 25 ps	< 100 ps	< 25 ps	< 100 ps
LSO:Ce	1.77	0.34	1.78	0.16
LuAG:Ce	11.5	2.1	41.5	3.4
BGO	122	24.2	364	28
PWO	86	16.6	134	21

numbers suggest, that Cherenkov photons are an important factor of forming the rise times of scintillators. Depending on other scintillation parameters, e.g. the scintillation yields and transmission spectra, the influence of the Cherenkov photons on the rise times becomes more or less significant.

As mentioned in the previous section, the ratio of Cherenkov and scintillation yield might be optimized by adjusting the amount of doping in some scintillators. Therefore, the time resolution of scintillators might be improved, simply due to a higher photon density at the beginning of the light pulse, although the total light yield might be decreased.

C. Angular Distribution

Table II shows, that the yield of Cherenkov photons at PET energies is low. In order to detect as many Cherenkov photons as possible, an optimized position for attaching photon detectors to Cherenkov radiators is important. Therefore, simulations on the angular distribution of Cherenkov photons have been performed. This was done for an LSO:Ce cube with 3 mm edge length. For the axis of the spherical coordinate system, the flight direction of the incident 511 keV photon was chosen to be the direction $\cos \theta = 1$, which, in the following, is also called forward direction.

In θ -direction, for both, the electrons and the Cherenkov photons an anisotropic distribution with a maximum at $\cos \theta = 1$ was observed, see figure 4. This θ -dependency is stronger for the electrons than for the Cherenkov photons. This anisotropy could be used for optimizing the scintillator geometry and the positioning of the photon detectors on the crystals in order to maximize the detection yield of Cherenkov photons.

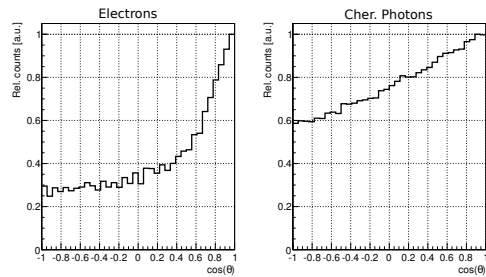


Fig. 4. Angular distribution of recoil electrons due to 511 keV annihilation photons (left) and the subsequently emitted Cherenkov photons (right).

7.2 Studies on the Cherenkov effect for improved time resolution of TOF-PET

III. MEASUREMENT

Coincidence measurements have been performed to proof the principle of detecting Cherenkov photons due to the recoil electrons of 511 keV annihilation photons.

For this, two Hamamatsu R1450 PMTs with a transit time spread of 360 ps (σ) were used. The PMTs were arranged in a coincidence setup with a ^{22}Na source in the center, see figure 5. For optimizing the alignment, the source could be moved in vertical direction by a stepping motor. Artifacts due to 511 keV photons entering the PMT and the PMT-window were avoided by placing a brick of lead in between the source and the PMT attached to the Cherenkov radiator. As Cherenkov radiator, lead glass RD50 from Schott, with a high fraction of lead-oxide ($> 65\%$), a size of $\sim 4\text{ cm} \times 5\text{ cm} \times 0.8\text{ cm}$ and two faces polished was used. On the opposite side LSO:Ce, with a size of $3\text{ mm} \times 3\text{ mm} \times 8\text{ mm}$ was coupled to the second PMT as reference detector. The output signals of both PMTs were split, with one part connected directly to a 4 channel digital WavePro 735Zi oscilloscope from LeCroy and the other part to a constant fraction discriminator (CFD, model 103, developed at PSI) before connected to the oscilloscope.



Fig. 5. Setup for the proof of principle of Cherenkov photon detection.

For accurate threshold setting, the output of the PMT with the lead glass on top was amplified using a NIM amplifier module 778 from Philips. The CFD thresholds were set to a level of 0.5 photons for the PMT attached to the lead glass and for the reference detector to a level between the Compton edge and the 511 keV photo peak. The coincidence was done by triggering on the two CFD outputs. By measuring the time differences of the two CFD outputs a coincidence time resolution of 832 ps FWHM was obtained, see figure 6 on the left side.

To ensure not to trigger on photons, created in the PMT window, the measurement was repeated after removing the lead glass from the PMT. The obtained background spectrum is plotted in figure 6, on the right-hand side. Comparison of the two plots proves that Cherenkov photons have been detected with this setup.

The relatively poor CTR is due to the equipment, which was chosen for a proof of principle and not for achieving the best time resolution. By optimizing the setup, including the geometry of the lead glass, an improved CTR can be expected.

IV. DISCUSSION AND CONCLUSION

The results of section II show that both, Cherenkov photons and scintillation photons, are emitted by recoil electrons due

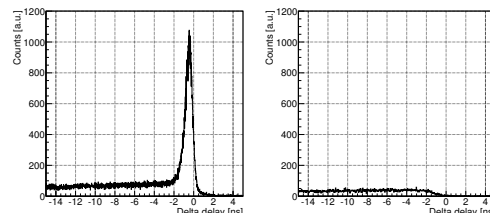


Fig. 6. Time difference of the two PMT signals from the coincidence measurement of lead glass vs LSO:Ce on the left. On the right, the measured background spectrum is shown, when the lead glass is removed from the PMT.

to 511 keV annihilation photons, in commonly used scintillators for PET. For improvement of the rise time, the Cherenkov yield should be increased. One factor influencing the Cherenkov yield is the refractive index, as seen in equation 1. Therefore, choosing a material with higher refractive index is one way to increase the Cherenkov yield. A low creation threshold and a high kinetic energy of the recoil electron would additionally increase the Cherenkov yield. The initial kinetic energy depends on its binding energy in the material and ranges from 0.5 keV for oxygen to 90 keV for bismuth (K1s state) [20].

More important is the influence of photon absorption inside the scintillators. Since the emission rate of Cherenkov photons is increasing at shorter wavelengths, materials with high transmission in the blue and UV-range, accompanied with photon detectors which are sensitive in this region are beneficial. Although it would be easier to detect photons at longer wavelengths, due to higher sensitivities of photon detectors, the low yield of Cherenkov photons in this region would not lead to a significant increase of the Cherenkov detection yield.

Comparing the numbers of the calculated Cherenkov yield in table II with ref. [1], one notices a slight difference, which can be explained by the different wavelengths used for the calculations. Furthermore, the numbers for the detected photons in the same table show a large deviation from ref. [2]. This, however, can be explained mainly by the quantum efficiency used for the simulations and additionally by the dimensions of the crystals which is much larger in [2], than in our case. Nevertheless, the interaction efficiency of the 511 keV annihilation photons is proportional to the crystal lengths, which shows one trade-off in PET: a high interaction efficiency of the annihilation photon with the scintillator versus a high detection efficiency of optical photons.

In all investigated scintillators, both, Cherenkov and scintillation photons are emitted after the interaction of a 511 keV annihilation photon with the scintillator, the Cherenkov yield, however, is low compared to the scintillation yield. Nevertheless, during the first few ten picoseconds the emission rates of Cherenkov photons exceed the rates of scintillation photons for all investigated materials. This is even more obvious for scintillators like BGO and PWO due to their lower scintillation and higher Cherenkov yield, respectively. As the investigated

time windows of 25 ps and 100 ps for the calculated ratios of the Cherenkov yield are in the range of scintillation rise times for the simulated scintillators, the Cherenkov effect seems to be an important factor influencing the total rise time of scintillators. One has to note, that a decreased scintillation yield itself might lead to a shorter rise time but not to an improved time resolution. The crucial point is the temporal photon density at the beginning of the light pulse, which can be increased by increasing the Cherenkov yield, although a decrease of the scintillation yield at the same time is expected.

A proof of principle measurement of detecting Cherenkov photons due to 511 keV annihilation photons was done. Lead glass, usually used for radio-protection, was used for the measurement, as it is a cheap and easy to get Cherenkov radiator which is free of scintillation. The equipment for the setup was chosen to detect Cherenkov photons with a basic setup, which explains the relatively poor coincidence time resolution of 832 ps FWHM. Nevertheless, the detection of Cherenkov photons is proven.

A crucial issue for TOF-PET is the not existing energy resolution when using the Cherenkov effect only, simply due to the low Cherenkov yield in this energy range. This would lead to problems in PET as energy information is needed for discrimination between scattered events and events due to the photoelectric effect. But the Cherenkov effect can be exploited in combination with scintillation. This might be done in two ways: either subsequent detection of Cherenkov and scintillation photons, or the improvement of the rise time of scintillating materials by increasing the Cherenkov-yield of the material. The first point would require very slow rise times of the scintillation process and very fast photon detectors with excellent time resolution and very low dark count rates. An advantage of this method would be the possibility to measure two time stamps (Cherenkov and scintillation) per event, which might improve the time resolution additionally. The second point of improving the rise time by increasing the ratio of the Cherenkov yield, seems to be easier. Especially, the high emission rate of Cherenkov photons during the beginning of scintillation emission, would make this option promising. As a consequence, maximizing the Cherenkov-yield by optimizing the geometrical detector layout, refractive index, the kinetic energy available for the recoil electron and especially enhancing the transmission spectrum could lead to an improved total rise time of scintillators and therefore to improved time resolution of TOF-PET.

V. OUTLOOK

The results of this work show, that both, Cherenkov photons and scintillation photons are emitted after interactions of 511 keV photons. The good timing properties of the Cherenkov photon emission could be exploited using materials with high Cherenkov-yield, which might be achieved by optimizing refractive index and transmission wavelengths. Furthermore, the method of subsequent photon detection seems to be promising in terms of timing. Nevertheless, photon detectors should be optimized for the emission wavelengths of Cherenkov photons, which are mainly in the blue and UV-range. Measurements

on the rise times of scintillators would be very interesting, e.g., for LSO:Ce or LuAG:Ce with varying Ce doping, as a dependency of the rise time on the doping would strengthen the conclusions of this work.

REFERENCES

- [1] P. Lecoq, E. Auffray, S. Brunner, H. Hillemanns, P. Jarron, A. Knapitsch, T. Meyer, and F. Powolny, "Factors Influencing Time Resolution of Scintillators and Ways to Improve Them," *IEEE Trans. Nucl. Sci.*, vol. 57, no. 5, pp. 2411–2416, 2010.
- [2] R. Dolenc, S. Korpar, P. Krizan, R. Pestotnik, A. Stanovnik, and R. Verheyden, "Time-of-flight measurements with Cherenkov photons produced by 511 keV photons in lead crystals," *IEEE Nuclear Science Symp. Conf. Rec.*, pp. 280–284, 2010.
- [3] S. E. Brunner, L. Gruber, J. Marton, K. Suzuki, and A. Hirtl, "New Approaches for Improvement of TOF-PET," *Nucl. Instrum. Methods Phys. Res. A*, In press, Accepted Manuscript, <http://dx.doi.org/10.1016/j.nima.2013.05.028>.
- [4] S. E. Derenzo, M. J. Weber, E. Bourret-Courchesne, and M. K. Klittenberg, "The quest for the ideal inorganic scintillator," *Nucl. Instrum. Methods Phys. Res. A*, vol. 505, pp. 111–117, 2003.
- [5] R. T. Williams, K. B. Ucer, and J. L. Lopresti, "In the first instants ... ultrafast views of radiation effects," *Radiation Measurements*, vol. 33, no. 5, pp. 497–502, 2001.
- [6] W. W. Moses and S. E. Derenzo, "Prospects for Time-of-Flight PET using LSO Scintillator," *IEEE Trans. Nucl. Sci.*, vol. 46, no. 3, pp. 474–478, 1999.
- [7] Y. Shao, "A new timing model for calculating the intrinsic timing resolution of a scintillator detector," *Phys. Med. Biol.*, vol. 52, no. 4, pp. 1103–1117, Feb. 2007.
- [8] Agostinelli et al., "GEANT4 - A simulation toolkit," *Nucl. Instrum. Methods Phys. Res. A*, vol. 506, pp. 250–303, 2003.
- [9] S. E. Derenzo, M. J. Weber, W. W. Moses, and C. Dujardin, "Measurements of the Intrinsic Rise Times of Common Inorganic Scintillators," *IEEE Trans. Nucl. Sci.*, vol. 47, no. 3, pp. 860–864, 2000.
- [10] S. Seifert, J. H. L. Steenbergen, H. T. Van Dam, and D. R. Schaart, "Accurate measurement of the rise and decay times of fast scintillators with solid state photon counters," *Jour. Instr.*, vol. 7, P09004, 2012.
- [11] R. Mao, L. Zhang, and R. Zhu, "Optical and Scintillation Properties of Inorganic Scintillators in High Energy Physics," *IEEE Nuclear Science Symp. Conf. Rec.*, vol. 3, pp. 2285–2291, 2007.
- [12] E. Auffray, D. Abler, S. E. Brunner, B. Frisch, A. Knapitsch, P. Lecoq, G. Mavromanolakis, O. Poppe, and A. Petrosyan, "LuAG material for dual readout calorimetry at future high energy physics accelerators," *IEEE Nuclear Science Symp. Conf. Rec.*, pp. 2245–2249, 2009.
- [13] I. Dafinei, E. Auffray, M. Schneegans, V. Missevitch, V. B. Pavlenko, A. A. Fedorov, A. N. Annenkov, V. L. Kostylev, and V. D. Ligun, "Lead tungstate (PbWO₄) scintillators for LHC EM calorimetry," *Nucl. Instrum. Methods Phys. Res. A*, vol. 365, no. 23, pp. 291–298, 1995.
- [14] J. S. Salacka and M. K. Bacrania, "A Comprehensive Technique for Determining the Intrinsic Light Yield of Scintillators," *IEEE Trans. Nucl. Sci.*, vol. 57, pp. 901–909, 2010.
- [15] C.L. Melcher and J.S. Schweitzer, "A promising new scintillator: cerium-doped lutetium oxyorthosilicate," *Nucl. Instrum. Methods Phys. Res. A*, vol. 314, pp. 212–214, 1992.
- [16] W. R. Leo, *Techniques for Nuclear and Particle Physics Experiments*, Berlin: Springer, 1994.
- [17] J. V. Jelley, "Cherenkov radiation and its applications," *Brit. Jour. Appl. Phys.*, vol. 6, pp. 227–232, 1955.
- [18] G. Ren, L. Qin, S. Lu, and H. Li, "Scintillation characteristics of lutetium oxyorthosilicate (Lu₂SiO₅:Ce) crystals doped with cerium ions," *Nucl. Instrum. Methods Phys. Res. A*, vol. 531, no. 3, pp. 560–565, Oct. 2004.
- [19] J. D. Naud, T. A. Tombrello, C. L. Melcher, J. S. Schweitzer, and O. Q. Road, "The Role of Cerium Sites in the Scintillation Mechanism of LSO," *IEEE Nuclear Science Symp. Conf. Rec.*, vol. 1, pp. 367–371, 1995.
- [20] A. Thompson et al., *X-ray data booklet*, Lawrence Berkeley National Laboratory, University of California, 2009.

7.3 Time resolution below 100ps for the SciTil detector of PANDA employing SiPM

7.3 Time resolution below 100ps for the SciTil detector of PANDA employing SiPM

Reference: (29), abstract: <http://iopscience.iop.org/1748-0221/9/03/C03010>. Reprinted, with permission, from L. Gruber, J. Marton, H. Orth, K. Suzuki.

Preprint typeset in JINST style - HYPER VERSION

Time resolution below 100 ps for the SciTil detector of PANDA employing SiPM

S. E. Brunner^{a*}, L. Gruber^a, J. Marton^a, H. Orth^b and K. Suzuki^a

*^aStefan Meyer Institute for Subatomic Physics, Austrian Academy of Sciences,
Boltzmannngasse 3, 1090 Vienna, Austria*

*^bGSI Helmholtzinstitut für Schwerionenforschung,
Planckstraße 1, 64291 Darmstadt, Germany*

E-mail: stefan.enrico.brunner@oeaw.ac.at

ABSTRACT: The barrel time-of-flight (TOF) detector for the PANDA experiment at FAIR in Darmstadt is planned as a scintillator tile hodoscope (SciTil) using 8000 small scintillator tiles. It will provide fast event timing for a software trigger in the otherwise trigger-less data acquisition scheme of PANDA, relative timing in a multiple track event topology as well as additional particle identification in the low momentum region. The goal is to achieve a time resolution of $\sigma \simeq 100$ ps. We have conducted measurements using organic scintillators coupled to Silicon Photomultipliers (SiPM). The results are encouraging such that we are confident to reach the required system time resolution.

KEYWORDS: Scintillation detector; timing detector; fast timing; time resolution; Silicon Photomultiplier (SiPM); PANDA.

*Corresponding author.

Contents

1. Introduction	1
2. Scintillator time resolution	2
2.1 Method	2
2.2 Results	3
3. SiPM time resolution	6
3.1 Method	6
3.2 Results	7
4. Conclusion and outlook	8

1. Introduction

The Scintillator Tile Hodoscope (SciTil) is a proposed sub-detector of the planned \bar{P} ANDA experiment [1] situated at FAIR [2]. The tasks of the SciTil detector are particle identification for slow particles (below 700 MeV/c) in combination with a central tracker [3], relative time-of-flight information, event timing, conversion detection and charge discrimination in front of the electromagnetic calorimeter. Furthermore, it would increase the detection probability for $\bar{\Xi}$ by monitoring slow Kaon decay products and help to deconvolute particle tracks. The space for the barrel SciTil is limited to 2 cm in radial direction including the support structure. Requirements for the detector are minimum use of material and a time resolution of $\sigma \simeq 100$ ps.

A basic layout of the detector has been proposed in Ref. [4]. It suggests tiles made out of small organic scintillators with sizes of $\sim 30 \times 30 \times 5$ mm³, attached to Silicon Photomultipliers (SiPM) with a sensitive area of 3×3 mm², see Fig. 1, left hand side. The main reasons for choosing organic scintillators are their fast response (short rise- and decay-times) and their high light yield. SiPM provide advantageous properties such as good timing, compactness, high photon detection efficiency (PDE) and operation in magnetic fields which will be 2 T in the \bar{P} ANDA target spectrometer.

In order to achieve the required time resolution of $\sigma \simeq 100$ ps, research on the detector design was divided into two major parts, the scintillator and the photodetector. The first part includes the choice of the optimally suited scintillator material, the size and shape of the scintillator, as well as finding the optimal position to attach the photodetectors onto the scintillator. The second part contains the identification of the SiPM with the best time resolution among a variety of manufacturers and the determination of optimal operating conditions for the expected photon pulse shapes emitted by the scintillators.

7.3 Time resolution below 100ps for the SciTil detector of PANDA employing SiPM

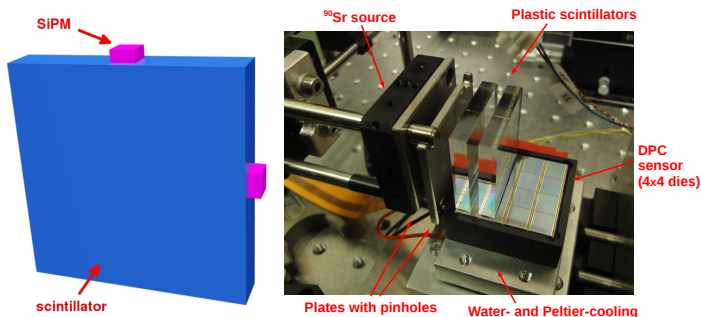


Figure 1. Left: conceptual design for the layout of one scintillation tile for SciTil with a size of $\sim 30 \times 30 \times 5 \text{ mm}^3$. Right: setup used to evaluate the time resolution of plastic scintillator tiles. The scintillators are read out using the Philips DPC, which consists of 16 individual die sensors arranged in a 4×4 matrix.

2. Scintillator time resolution

2.1 Method

There are several parts contributing to the time resolution of a scintillation detector, e.g. the scintillator type, the photodetector and the electronics. Regarding the scintillator itself, the material properties, e.g. rise- and decay-times and light output, are directly influencing the time resolution. The coupling between scintillator and photodetector is important such that no photons are lost at the transition. Furthermore, the matching between the emission spectrum of the scintillator and the spectral sensitivity of the SiPM is a critical point.

The geometry of the scintillator influences the time resolution in a way that light path variations from the point of photon creation to the photodetector add time spread to the signal. For SciTil a square tile size of 20 mm to 30 mm is proposed [4], in order to achieve a time resolution of about 100 ps on the one hand and to keep the number of channels low on the other hand. A thickness in the order of 5 mm is sufficient to create $\sim 10 \text{ k}$ photons in the proposed plastic scintillators for minimum ionizing particles (MIP). Simulations have shown that a time resolution below 100 ps is feasible when detecting more than 100 photons [4]. This can be reached when attaching two SiPM, with a sensitive area of $3 \times 3 \text{ mm}^2$ each, to the rim of a tile. To increase the number of detected photons and improve time resolution, the ideal position of the photodetector on the tile has to be found.

In order to study the scintillator time resolution and the individual parameters described above, a simple setup was used, see Fig. 1, on the right hand side. A ^{90}Sr source provides electrons up to an energy of 2.28 MeV. The electrons were collimated using two steel plates with 3 mm thickness and centered holes of 2 mm diameter. These pinholes and the source could be moved with μm -resolution in two dimensions in order to define the beam position. As photodetector, the Digital Photon Counter (DPC) from Philips [5] was used. Being a fast photodetector with large active area and position sensitivity, the DPC is suited for such comparative studies and for testing position dependency of the time resolution by simply placing the plastic scintillator tiles on top of

7. APPENDIX

Table 1. Scintillation properties taken from data sheets [7, 8].

Scintillator	BC-408	EJ-228
Light yield [photons/MeV]	10,000	10,200
Rise time [ns]	0.9	0.5
Decay time [ns]	2.1	1.4
Pulse width (FWHM) [ns]	2.5	1.2
Wavelength of max. emission [nm]	425	391

the DPC using optical grease in between. Like the analog device, the DPC consists of an array of Single Avalanche Photo Diodes (SPADs). In contrast to the conventional SiPM, where the output signal corresponds to the analog sum of individual SPAD pulses, the DPC output is the digital sum of trigger bins with additional digital time stamps from the TDCs. The DPC has an active area of $32.6 \times 32.6 \text{ mm}^2$ and consists of 16 independent die sensors, arranged in a 4×4 matrix (see Fig. 1 on the right hand side). A die is sub-divided into a 2×2 pixel matrix. One pixel has a sensitive area of $3.2 \times 3.9 \text{ mm}^2$, which comes close to the size of a conventional SiPM. Depending on the sensor type (DPC-6400 or DPC-3200), each pixel consists of 6400 or 3200 SPADs, respectively. The user can define how many dies, pixels or individual SPADs to activate for data acquisition. After occurrence of an event, the number of breakdowns (photon count) and a single time stamp per die corresponding to the trigger time is saved.

The DPC was operated at 3 V above the breakdown voltage for all measurements and the trigger level was set to 1 photon, in order to use the time stamp of the first detected photon. In case of analog SiPM the optimum threshold would be higher due to statistical effects [6]. The setup was mounted inside a dark box and the temperature was stabilized at 20°C using water- and Peltier-cooling. In this experimental study we used the following plastic scintillators: 1 piece of BC-408 with size of $30 \times 30 \times 4 \text{ mm}^3$, 2 pieces of BC-408 with size of $25 \times 25 \times 5 \text{ mm}^3$, both from Saint-Gobain Crystals and 2 pieces of EJ-228 ($30 \times 30 \times 5 \text{ mm}^3$) from Eljen Technology. EJ-228 has similar physical properties as BC-418. The main parameters of the scintillators are summarized in Table 1.

2.2 Results

First we measured the number of detected photons and evaluated the photon distribution along the rim of the scintillator. Therefore, a BC-408 scintillator tile ($30 \times 30 \times 4 \text{ mm}^3$) was coupled to the DPC-6400 and read out by 4 dies. Since only half of a die's active area was covered by the thin scintillator, only 2 out of 4 pixels per die were activated during data acquisition. The measurement was performed by moving the ^{90}Sr -source position two-dimensionally in steps of 5 mm across the entire scintillator surface, counting the number of detected photons at each position. Fig. 2 shows the photon number spectrum for electrons directed onto the center of the square scintillator surface for two pixels activated. The photon counts of individual die sensors are shown in Fig. 3 (left hand side). The plot shows a mean photon count of all 25 positions. Die number 1 and 4 are located at the edge of the scintillator tile, die number 2 and 3 at the center. Evidently, the photons are rather equally shared among the different dies, demonstrating scintillation light to be equally distributed over the rim of the scintillator. Since each die gives a time stamp at the instant of trigger generation

7.3 Time resolution below 100ps for the SciTil detector of PANDA employing SiPM

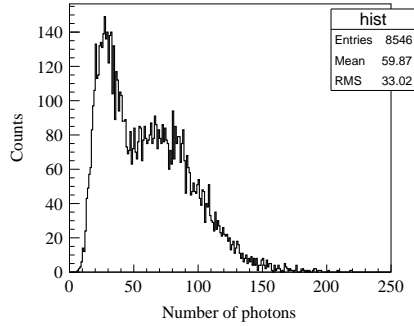


Figure 2. ^{90}Sr spectrum measured with a BC-408 scintillator ($30 \times 30 \times 4 \text{ mm}^3$) and a DPC-6400. The histogram shows the photon number detected on one die (2 pixels activated).

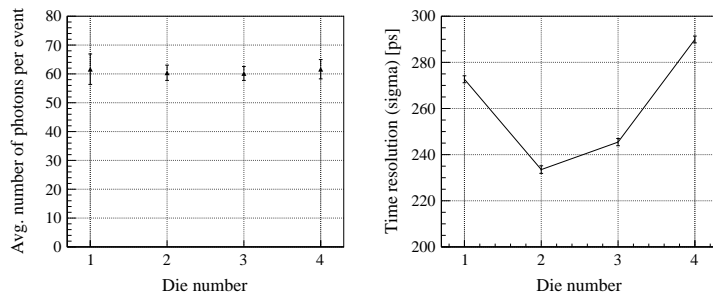


Figure 3. The plot on the left shows the photon distribution measured at the rim of the scintillator (BC-408, $30 \times 30 \times 4 \text{ mm}^3$). Die number 1 and 4 correspond to the dies located at the edge of the scintillator tile, die number 2 and 3 to the central dies. On the right, one can see the corresponding time resolution. The values are mean numbers of 25 different beam positions.

(detection of the first arriving photon), one can disentangle the time resolution of each die using all possible die combinations. On the right hand side of Fig. 3 one can see that the time resolution improves for dies positioned in the center. Again, the values are mean numbers for 25 source positions. The asymmetry of the graph can be explained by an instrumental asymmetry, caused by the positioning of the scintillator on the active area of the DPC. In the analysis, all events were considered without energy cuts on the photon spectra. The results show that there is a position dependence of the time resolution, indicating that the best timing can be achieved by placing the photodetector at the center of the scintillator rim. For equally distributed source positions, the light path variations inside the scintillator from the point of photon creation to the photodetector are on average smaller when the detector is placed in the center and thus, the arrival time jitter of the detected photons is smaller.

In order to increase the detected number of photons, we exchanged the DPC model and used the DPC-3200 for further measurements. This model consists of 3200 SPADs per pixel and pro-

7. APPENDIX

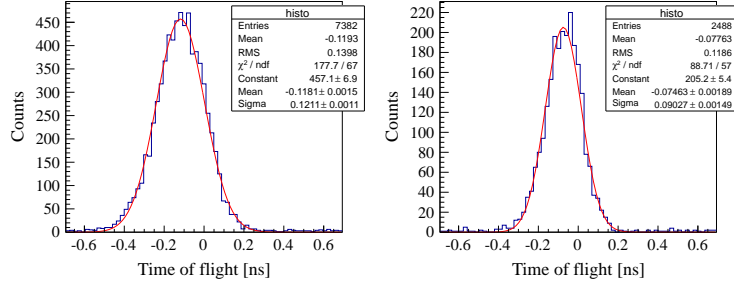


Figure 4. Time-of-flight spectrum between two tiles of BC-408 with size of $25 \times 25 \times 5 \text{ mm}^3$ (left) or EJ-228 with size of $30 \times 30 \times 5 \text{ mm}^3$ (right). The spectra were fit using a Gaussian distribution.

vides a higher PDE compared to the DPC-6400 due to a higher fill factor. Two plastic scintillator tiles were placed on the sensitive area of the DPC, covering two rows of dies (see Fig. 1). In each row only the central two dies (two pixels each) were activated and used for read out. The source position was directed onto the center of the scintillator surface. By putting the two scintillator tiles in coincidence (in total 4 dies), only high energy events ($\Delta E > 0.8 \text{ MeV}$ in the first tile) were selected. For each die, the arrival time of the first photon was saved. The start and stop signals were created by taking the mean of the two time stamps for the first and second tile, respectively. Fig. 4 shows the time-of-flight spectra using two tiles of BC-408 with a size of $25 \times 25 \times 5 \text{ mm}^3$ and EJ-228 with a size of $30 \times 30 \times 5 \text{ mm}^3$, respectively. With the latter, a time-of-flight resolution of 90 ps (sigma) was achieved, much better than with the BC-408 tile. The EJ-228 scintillator has a larger surface. Hence, travel path variations inside the scintillator are larger and the number of detected photons is a factor 1.3 to 1.4 smaller at comparable light yield, compared to the BC-408 scintillator. However, the timing properties are superior because of shorter rise- and decay-times (see Table 1).

Since it is planned to finally read out the scintillator tiles with conventional SiPM, we decreased the detection area on the DPC by switching on only individual pixels, which have similar sensitive surface compared to analog sensors. One pixel of the DPC has an active area of about 12 mm^2 . The measurement was performed using 2 tiles of BC-408 with a size of $25 \times 25 \times 5 \text{ mm}^3$. The first scintillator tile is again read out using two dies (two pixels per die), for the second tile only single pixels are used. Fig. 5 (left) shows the time resolution of the second scintillator tile, read out by individual pixels. Pixel number 1 and 4 correspond to pixels located at the edge of the scintillator tile, pixel number 2 and 3 to pixels in the center. Using both center pixels for read out instead of one, the time resolution was improved to 115 ps (sigma).

The sensitive area of the DPC was further decreased to $3 \times 3 \text{ mm}^2$ by switching off individual SPADs. On the right hand side of Fig. 5, one can see the time resolution of the EJ-228 tile in dependence of the activated sensitive area used for read out. The time resolution improves with increasing sensitive area S , since the number of detected photons N_{ph} is dependent on the sensitive area. From statistics, one could expect that the time resolution improves with $1/\sqrt{N_{\text{ph}}}$, as indicated by the dashed line in Fig. 5 (right). For increasing sensitive area the skew of the trigger network

7.3 Time resolution below 100ps for the SciTil detector of PANDA employing SiPM

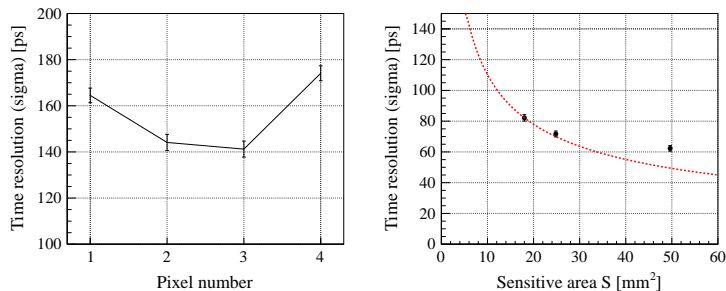


Figure 5. Time resolution of BC-408 ($25 \times 25 \times 5 \text{ mm}^3$) read out with single pixels (left). Pixel number 1 and 4 correspond to pixels located at the edge of the scintillator tile, pixel number 2 and 3 to pixels in the center. On the right hand side, the time resolution of one scintillator tile (EJ-228, $30 \times 30 \times 5 \text{ mm}^3$) as a function of the sensitive sensor surface (S) is plotted. The black dots are the data points, the dashed curve indicates the time resolution expected when scaling with $1/\sqrt{S}$, normalized to the point $S = 18 \text{ mm}^2$. The deviation at large sensitive area could be explained by the skew of the trigger network scheme of the DPC.

scheme seems to become a prominent factor influencing the time resolution [9]. This is visible for the deviation of the data point from the dashed curve at $S = 50 \text{ mm}^2$.

3. SiPM time resolution

3.1 Method

In order to obtain the best detector time resolution for SciTil, the SiPM with the smallest intrinsic time spread needs to be found. Therefore, we performed a comparative timing performance study of SiPM from several vendors: AdvanSiD, Hamamatsu and Ketek. The figure of merit is the single photon time resolution (SPTR) of the devices. In order to obtain this value a semi-automatic setup was developed.

Setup This setup is equipped with a picosecond laser from Advanced Laser Diode Systems (PIL040) with an emission wavelength of $\lambda = 404 \text{ nm}$ and a pulse width of $\approx 30 \text{ ps}$ FWHM. The setup is shown in Fig. 6. The laser beam is split into two paths. One path is used for providing a trigger signal and is led directly onto a 3SP50 SiPM from AdvanSiD. The SiPM is fully saturated for every laser pulse and its signal is read out directly without further amplification in order to obtain low time jitter. This trigger method was chosen, since better values of the SPTR were obtained as compared to using the trigger output of the laser itself.

The other path of the laser beam is directed onto the device to be measured. It passes a variable attenuator before it is coupled into a fiber, which is entering a vacuum box. The box was evacuated and filled with Nitrogen in order to avoid condensation of water on the electronic circuits. Inside the vacuum box, a single mode fiber was used to reduce the transit time spread of the light pulses. The fiber enters an RF-shielded box and is directed onto the SiPM. In order to obtain homogeneous illumination of the sensitive area, the fiber and the SiPM were mechanically coupled using a small plastic holder (see Fig. 6). The SiPM were biased using a Keithley 6517A electrometer which was

7. APPENDIX

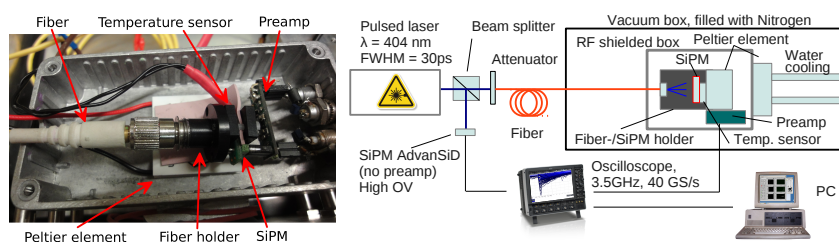


Figure 6. Picture of the RF-shielded box containing the tested SiPM and the preamplifier (left hand side). A schematic drawing of the whole setup (right hand side).

also used to measure the current in the SiPM. Additionally, a Keithley 617 electrometer was used to measure the bias voltage applied. Temperature stabilization was achieved by two Peltier elements which were coupled to a water chilled metal finger. The temperature was measured using a Pt100 temperature sensor, which was attached directly to the SiPM and was read out with a LakeShore 211 temperature monitor. An AMP-0611 preamplifier from Photonique was used to amplify the signal before it was fed into a LeCroy WavePro 735 Zi digital oscilloscope with a bandwidth of 3.5 GHz and 40 GS/s. A LabView program managed the measurements and controlled the oscilloscope for recording the data, the two electrometers, the Peltier elements and recorded the temperature.

Data taking A measurement run was done at constant temperatures (-10°C , 0°C , 10°C , 20°C with an accuracy of $\pm 0.1^{\circ}\text{C}$) varying the bias in small voltage steps. Starting from a bias voltage, slightly above the breakdown voltage, the program ramped the bias in steps of 0.1 V or 0.2 V respectively, dependent on the ratio of gain to bias voltage (e.g., for a small ratio, steps of 0.2 V were applied). Several thousand events were recorded at each voltage step until a current limit (usually $8\ \mu\text{A}$) was reached. Using the oscilloscope, the time difference relative to the trigger signal taken at 50% of the amplitude, the amplitude, the area and the rise-/fall-time (10% - 90%) of the waveform were recorded for each trigger. Additionally, the bias voltage, current and temperature for offline data analysis were measured and stored.

Data analysis Automatic fitting of the pedestal and the single photon peak in the histograms of the signal amplitude was performed for all bias steps using a double Gaussian distribution. With this method, the single photon events are identified. Using the time stamps which correspond to single photon events (within a window of $\pm 2\sigma$ of the single photon amplitude) the time delay spectrum of the signal relative to the trigger can be plotted. The resulting time stamp distribution was fitted with a Gaussian, giving a standard deviation which represents the SPTR.

Tested SiPM SiPM of three different vendors, AdvanSiD, Hamamatsu and Ketek have been tested. A list of the devices and their parameters can be found in Table 2.

3.2 Results

The results of the SPTR measurements can be seen in Fig. 7, which shows the SPTR in dependency of the bias voltage and the temperature. The general trend is an improving time resolution

7.3 Time resolution below 100ps for the SciTil detector of PANDA employing SiPM

Table 2. List and detector parameters of the tested devices taken from the data sheets of the manufacturers. The PDE value indicated by * includes cross talk and after pulses.

Manufacturer	AdvanSiD	Hamamatsu	Ketek		
	SiPM3S	S10931	PM3375	PM3360	PM3350
Type	P-50	-100P	-B72	-A2	-B63
Total size [mm ²]	3×3	3×3	3×3	3×3	3×3
SPAD size [μm]	50	100	75	60	50
Optical trenches	no	no	yes	yes	yes
Breakdown voltage [V]	≈ 35	≈ 70	≈ 23	≈ 23	≈ 23
Darkcount rate [MHz]	≤ 45	≤ 12	≤ 4.5	≤ 4.5	≤ 4.5
Gain [× 10 ⁶]	2.5	2.4	14	9	6
PDE at peak sensitivity [%]	22	> 70*	> 62	> 39	> 50
Microcell capacitance [fF]	-	~2800	650	380	270

with increasing bias voltage and with decreasing temperature, however, the improvement tends to saturate below 10 °C. The dependency on the bias voltage (which is proportional to the gain) is more prominent at higher temperatures, especially for the sensors from AdvanSiD and Hamamatsu and the Ketek PM3360. It indicates that the dark count rate, afterpulses and cross talk are factors influencing the time resolution of the SiPM as they are increasing with the bias voltage and decreasing with the temperature [10].

It has to be noticed that the presented values of the SPTR do not represent absolute values but coincidence values of an asymmetric system corrupted by many factors in the intrinsic time resolution of the setup (e. g. trigger sensor operated at high temperature, the laser jitter, the preamplifier, the time precision of the first photon within a laser pulse is dependent on the laser pulse intensity, pick up noise) which becomes obvious when comparing the results with Ref. [11]. As the bias voltage range for the best SPTR at 20 °C is very small for the Hamamatsu sensors (~0.3 V) compared to the Ketek sensors, the Ketek sensors would allow easier bias adjustment to obtain a good time resolution. This becomes important when considering the system time resolution of the several thousand channels planned for SciTil. Moreover, the Ketek sensors show the best timing performance over all bias settings and temperatures in this measurement. All three companies recently published new versions of their sensors, which will be tested in further measurements.

The SPTR is the parameter of interest when comparing the SiPM in terms of time resolution. Nevertheless, when using the SiPM in combination with the scintillator tiles, not only one but 100 photons per MIP are expected. Due to statistics the time resolution improves by a factor $1/\sqrt{N_{\text{ph}}}$ with increasing number of detected photons N_{ph} . Therefore, time resolutions well below 100 ps should be achievable for all tested SiPM when detecting 100 photons.

4. Conclusion and outlook

The time resolution of two square scintillators with different areas was measured using the Philips DPC. Best results were obtained when detecting photons centrally on the scintillator rims. For BC-408 a TOF resolution of 121 ps (sigma) and for the EJ-228 a TOF resolution of 90 ps (sigma)

7. APPENDIX

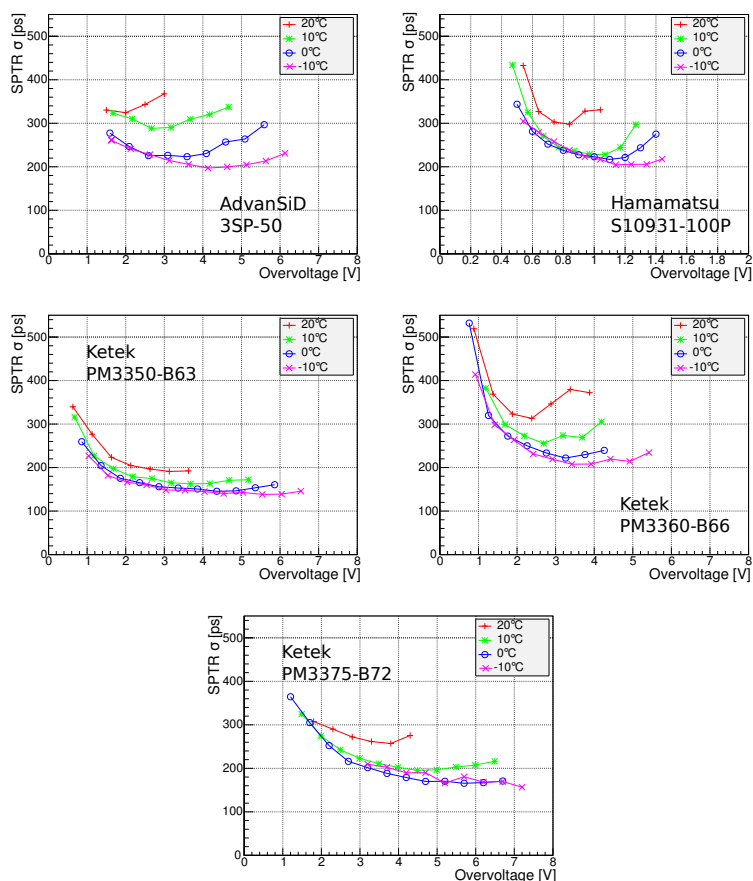


Figure 7. Single photon time resolution of the tested SiPM. The lines are included to guide the eyes.

was obtained. Although the ratio of the sensitive area to the surface was smaller for EJ-228, a better TOF resolution was achieved. This indicates that the shorter rise- and decay-times of EJ-228 are significantly improving the time resolution of the scintillator. The time resolution of a single tile can be expected to be better than the measured TOF resolution. Further scintillator materials (EJ-200, EJ-204, EJ-232, BC-420) and geometries will be tested with our setup.

The time resolution of several SiPM was measured. Among the tested sensors the PM3350-B63 with optical trenches showed the best SPTR over a wide voltage range. Nevertheless, we will continue our tests with an improved setup and a broader variety of SiPM from more vendors.

As a next step, measurements with two analog SiPM attached to one scintillator tile will be

7.3 Time resolution below 100ps for the SciTil detector of PANDA employing SiPM

performed. Furthermore, these systematic studies for optimizing the scintillator time resolution will be continued and finally, be tested at a particle accelerator facility.

Acknowledgments

Many thanks go to Lars Schmitt for his seminal work on the SciTil detector design and to Carsten Schwarz for his continuing support of our work. Furthermore, we thank the Philips Technologie GmbH - Innovative Technologies acting through the team of Philips Digital Photon Counting for their support and interested participation in this research work. This work was partly supported by the EU Project HadronPhysics3 (project 283286).

References

- [1] D. Bettoni, *The PANDA Experiment at FAIR*, arXiv:0710.5664 (2007).
- [2] I. Augustin et al., *New Physics at the International Facility for Antiproton and Ion Research (FAIR) next to GSI, Fourth International Conference on Fission and Properties of Neutron-Rich nuclei*, doi:10.1142/9789812833433_0016, (2008).
- [3] A. Gillitzer et al., *Motivation of the Barrel Time-of-Flight Detector for PANDA*, PANDA Note, (2011), <http://panda-wiki.gsi.de/cgi-bin/view/ToF/TimingBarrel>, last visited Jan. 2014..
- [4] K. Goetzen et al., *Proposal for a Scintillator Tile Hodoscope for PANDA*, (private communication), <http://panda-wiki.gsi.de/pub/ToF/SciTil/scitil.pdf>, last visited Jan. 2014.
- [5] T. Frach, et al., *The Digital Silicon Photomultiplier - Principle of Operation and Intrinsic Detector Performance*, IEEE Nucl. Sci. Symp. Conf. Rec., (2009).
- [6] S. Gundacker et al., *Time of flight positron emission tomography towards 100ps resolution with L(Y)SO: an experimental and theoretical analysis*. JINST **8-07** (2013) P07014.
- [7] Saint-Gobain Crystals, <http://www.detectors.saint-gobain.com/Plastic-Scintillator.aspx>, last visited Jan. 2014..
- [8] Eljen Technology, <http://www.eljentechnology.com/index.php/products/plastic-scintillators>, last visited Jan. 2014..
- [9] T. Frach et al., *The digital silicon photomultiplier - System architecture and performance evaluation*, IEEE Nucl. Sci. Symp. Conf. Rec., (Oct. 2010), pp. 1722-1727.
- [10] N. Dinu et al., *Temperature and bias voltage dependence of the MPPC detectors*, IEEE Nucl. Sci. Symp. Med. Imaging Conf., (Oct. 2010) pp. 215-219.
- [11] G. Collazuol et al., *Single photon timing resolution and detection efficiency of the IRST silicon photo-multipliers*, Nucl. Instr. Meth. A, **581**, (2007) 461-464.

7.4 Time resolution below 100ps for the SciTil detector of PANDA employing SiPM

Reference: (26), abstract: <http://iopscience.iop.org/1748-0221/6/11/C11024>. Reprinted, with permission, from L. Gruber, J. Marton, H. Orth, K. Suzuki.



PUBLISHED BY IOP PUBLISHING FOR SISSA

RECEIVED: August 12, 2011

ACCEPTED: November 14, 2011

PUBLISHED: November 28, 2011

WORKSHOP ON FAST CHERENKOV DETECTORS - PHOTON DETECTION,
DIRC DESIGN AND DAQ
APRIL 4–6, 2011, GIESSEN, GERMANY

Position sensitive SiPM detector for Cherenkov applications

L. Gruber,^{a,b,1} G.S.M. Ahmed,^a S.E. Brunner,^{a,b} P. Bühler,^a J. Marton^a and K. Suzuki^a

^aStefan Meyer Institute for Subatomic Physics, Austrian Academy of Sciences,
Boltzmannngasse 3, 1090 Vienna, Austria

^bVienna University of Technology, Faculty of Physics,
Karlsplatz 13, 1040 Vienna, Austria

E-mail: lukas.gruber@oeaw.ac.at

ABSTRACT: A prototype of a position sensitive photo-detector with $5.6 \times 5.6 \text{ cm}^2$ detection area readout with 64 Hamamatsu MPPCs (S10931-100P) with $3 \times 3 \text{ mm}^2$ active area each has been built and tested. The photo-sensors are arranged in a 8×8 array with a quadratic mirror light guide on top. The module is currently readout by in-house developed preamplifier boards but employing existing ASIC chips optimized for SiPM readout is also planned. Such a device is one of the candidates to be used for photon detection in the PANDA DIRC detectors.

KEYWORDS: Cherenkov detectors; Photon detectors for UV, visible and IR photons (solid-state)

¹Corresponding author.

7.4 Time resolution below 100ps for the SciTil detector of PANDA employing SiPM

Contents

1	Introduction	1
2	Position sensitive Cherenkov detector	1
2.1	Light concentrator	1
2.2	Prototype detector	2
3	Efficiency measurements and simulations	2
3.1	Measurements of the light concentrator efficiency	2
3.2	Simulations of the light concentrator efficiency	3
4	Conclusions and outlook	4

1 Introduction

Silicon Photomultipliers (SiPMs) are extremely versatile photo-sensors and can be used in many fields ranging from astrophysics, particle and nuclear physics to medical imaging.

Recently, we have built a position sensitive photo-detector based on an array of SiPMs which could be used for photon detection in the PANDA experiment at the FAIR facility in Darmstadt, Germany. For charged particle identification in the momentum range of 0.5 GeV/c to 4.5 GeV/c, two DIRC detectors are foreseen. The barrel DIRC detector [1] has a total detection area of a few m² which will be covered by about 10 000 photo-sensors. The DIRC detector must be able to detect Cherenkov light at very low intensities with an angular resolution of 2 - 2.5 mrad. Microchannel plate PMTs (MCP-PMTs) are considered as an option for photon detection in the PANDA DIRCs. However, the lifetime is still not sufficient for the expected photon rates [2] and therefore we are studying SiPMs as an alternative to MCP-PMTs.

2 Position sensitive Cherenkov detector

2.1 Light concentrator

In order to increase the number of incident photons on the active area of the sensor, the idea of using an array of suitable light guides on top of the photo-sensor has been studied. Such a light concentrator leads to increased geometric acceptance and increased signal to noise ratio, since the dark count rate is not affected by the light guides. The light concentrator consists of 64 regularly arranged pyramid-shaped funnels with quadratic (round edges) entrance windows of 7×7 mm² and exit apertures of 3×3 mm², respectively, and thus increases the geometric detection area by a factor of $(7/3)^2 \times \epsilon_{\text{geo}} \approx 5.1$, where $\epsilon_{\text{geo}} = 0.93$ is the geometric fill factor of the light concentrator. The funnel height is 4.5 mm. The light guide array is made out of brass and the funnels were produced by electro-erosion. Two modules of the light concentrator with different coatings (Aluminum and

2011 JINST 6 C11024

7. APPENDIX



Figure 1. Pictures of the position sensitive SiPM array. The figure on the left shows a view inside the detector. The SiPMs are read out from the back by four preamplifier boards. The temperature is stabilized by water- and Peltier-cooling. The light guide matrix on top of the SiPMs enlarges the detection area of the module. On the right hand side the detector is closed.

Chromium) were produced and tested. Figure 1 shows a picture of the light concentrator mounted on top of the SiPM matrix.

2.2 Prototype detector

The prototype of a position sensitive photo-detector consists of 64 SiPMs (Hamamatsu MPPC S10931-100P) with $3 \times 3 \text{ mm}^2$ active area and $100 \times 100 \mu\text{m}^2$ pixel size, arranged in a 8×8 array. The SiPM array is combined with a light concentrator on top. Each photo-sensor is read out separately. An individual bias supplier for each SiPM ensures that the gains of the sensors can be adjusted to be the same. The four preamplifier boards, developed at SMI, consist of 16 preamplifiers each and provide sufficient signal amplification with a gain of around 5 and reasonably fast shaping time ($\sim 2 \text{ ns}$). A picture of the prototype detector is shown in figure 1.

3 Efficiency measurements and simulations

3.1 Measurements of the light concentrator efficiency

In order to estimate the collection efficiency of the light concentrator, the SiPM array, with the light concentrator on top, is scanned in two dimensions with a blue laser (407 nm). The beam spot of about 1 mm diameter is moved in steps of $500 \mu\text{m}$ and the average output pulse height is recorded with an oscilloscope. The expected incident angle is $\theta = 0 \pm 4^\circ$. The measurements are done inside a dark box. Since it is known that the key parameters of SiPMs show a strong temperature dependence [3, 4], the whole setup is kept stable at 15°C , using water- and Peltier-cooling.

The detection efficiency of a single funnel can be written as $\epsilon_{\text{detect}} = \epsilon_{\text{col}} \times \epsilon_{\text{PDE}}$, where $\epsilon_{\text{col}} = n_d/N_{\text{phot}}$ is the collection efficiency of the light concentrator, with n_d being the number of photons reaching the exit aperture and N_{phot} being the total number of photons hitting the entrance aperture, and ϵ_{PDE} is the photon detection efficiency of the photo-sensor.

7.4 Time resolution below 100ps for the SciTil detector of PANDA employing SiPM

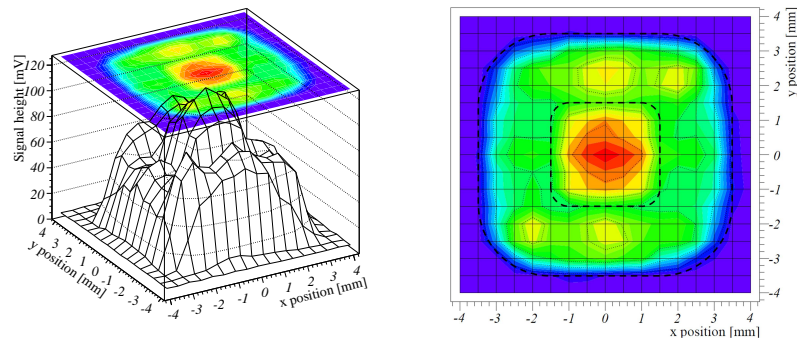


Figure 2. The plots show the results from a scan of one cell of the SiPM array with a laser spot of about 1 mm diameter in steps of $500\ \mu\text{m}$ in 3D- (left) and top-view (right). The chromium-plated light concentrator is used. The dimensions of the entrance- and exit aperture are indicated in the right plot.

Figure 2 shows a measurement done for one cell (one funnel plus SiPM) of the array, using the Chromium-plated light concentrator. One can identify the edges of the entrance and exit aperture at $x = y = \pm 3.5\ \text{mm}$ and $x = y = \pm 1.5\ \text{mm}$, respectively, and the SiPM centered at $x = y = 0$. The use of the light concentrator clearly helps to increase the detection area of the module. The partly inhomogeneous surface and xy-asymmetry of the light concentrator is supposed to originate from a non-uniform coating quality. The fact that the profiles of other cells reveal very similar features strengthens this suspicion. Besides, there are less efficient areas at $\pm 1.5\ \text{mm}$. This becomes more obvious when looking at figure 3. The plots show the profiles of a scan for the same cell in x- and y-direction in steps of $250\ \mu\text{m}$, comparing the Chromium- and Aluminum-plated light concentrator. The less efficient bands at a position of $\pm 1.5\ \text{mm}$ are likely due to defects, oxidation or bad coating at the edges of the funnel or due to none perfect matching between light guide and SiPM, but could also be a feature of the photo-sensor. This needs further investigation. Nevertheless, the fact that the Aluminum coated light concentrator shows a symmetric behavior in x- and y-direction confirms the previous assumption of a non-uniform coating quality in case of the Chromium-plated light guides. Other cells have been tested and provided comparable results.

From the measurements we find an average light collection efficiency of $\epsilon_{\text{col}} = 57\%$ for the Chromium-plated light concentrator, which shows that it is working quite efficiently. In order to compare with simulation, the data from the above measurements are normalized to the maximum signal height, so that the photon detection efficiency ϵ_{PDE} , which is not considered in the simulation, is canceled out.

3.2 Simulations of the light concentrator efficiency

A series of Monte Carlo simulations using a self-developed code was carried out in order to evaluate the collection efficiency ϵ_{col} of the light concentrator [5]. Assuming a reflection coefficient of 0.55

2011 JINST 6 C11024

7. APPENDIX

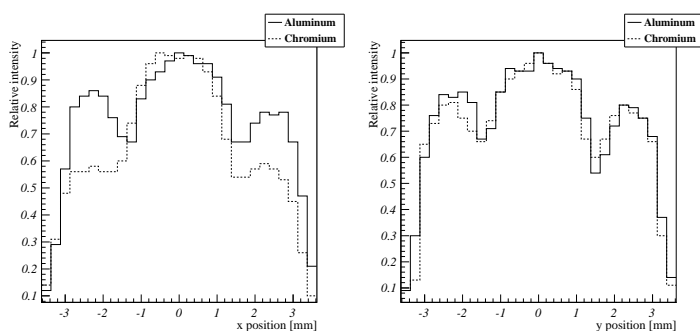


Figure 3. The plots show a comparison between the Aluminum- and Chromium-plated light guide. One cell is scanned in x-direction (left) at fixed y-position ($y = 0$) and in y-direction (right) at fixed x-position ($x = 0$). On average, the Aluminum-plated light concentrator performs better than the Chromium-plated one.

(Chromium at 400 nm [6]) and a reasonable surface smoothness, the simulations show an average light collection efficiency of around 52% at $\theta = 0^\circ$, where θ is the angle relative to the aperture normal, which is in very good agreement with the measured value of 57%.

4 Conclusions and outlook

A prototype of a position sensitive photo-detector with SiPM readout has been built and tested. Measurements were done in our laser laboratory and recently also at the T9 test beam at CERN in Geneva, Switzerland. The data recorded in ten days beam time are currently under investigation. It was shown that the light concentrator clearly increases the acceptance of the module and that the efficiency measurements are in good agreement with the simulations. The Aluminum-plated light guide is the preferred solution for future measurements. Further laser tests with different incident angles and smaller laser spots in the range of the MPPC pixel size and below are planned. In a next step it's also foreseen to use existing ASIC chips for the SiPM readout.

Acknowledgments

This work is partly supported by the EU Project HadronPhysics 2 (project 227431).

References

- [1] B. Seitz et al., *Development of DIRC counters for the PANDA experiment at FAIR*, *Nucl. Instrum. Meth. A* **628** (2011) 304.
- [2] A. Lehmann et al., *Systematic studies of micro-channel plate PMTs*, *Nucl. Instrum. Meth. A* **639** (2011) 144.
- [3] G.S.M. Ahmed et al., *Studies of GM-APD (SiPM) properties*, 2009 *JINST* **4** P09004.

7.4 Time resolution below 100ps for the SciTil detector of PANDA employing SiPM

- [4] G.S.M. Ahmed et al., *Silicon photomultiplier timing performance study*, *Nucl. Instrum. Meth. A* **652** (2011) 528.
- [5] G.S.M. Ahmed et al., *Application of Geiger-mode photo-sensors in Cherenkov detectors*, *Nucl. Instrum. Meth. A* **639** (2011) 107.
- [6] Refractive Index Database, <http://refractiveindex.info/>.

2011 JINST 6 C11024

7. APPENDIX

7.5 Efficiency and uniformity measurement of a light concentrator in combination with an SiPM array

Reprinted, with permission, from M. Rihl, L. Gruber, J. Marton, K. Suzuki, A. Hirtl. Reference:

Nuclear Instruments and Methods in Physics Research A 732 (2013) 419–422



Contents lists available at [ScienceDirect](#)

Nuclear Instruments and Methods in Physics Research A

journal homepage: www.elsevier.com/locate/nima



Efficiency and uniformity measurements of a light concentrator in combination with a SiPM array 

Mariana Rihl^{a,b,*}, Stefan Enrico Brunner^{a,c}, Lukas Gruber^{a,c}, Johann Marton^a, Ken Suzuki^a

^a Stefan Meyer Institute for Subatomic Physics, Austrian Academy of Sciences, Boltzmannngasse 3, 1090 Vienna, Austria
^b University of Vienna, Faculty of Physics, Boltzmannngasse 5, 1090 Vienna, Austria
^c Vienna University of Technology, Faculty of Physics, Karlsplatz 13, 1040 Vienna, Austria

<p>ARTICLE INFO</p> <hr/> <p>Available online 7 June 2013</p> <p>Keywords: Silicon photomultipliers SiPM Light concentrator Cherenkov detector Position sensitive photon detector</p>	<p>ABSTRACT</p> <hr/> <p>A position sensitive Cherenkov detector was built, consisting of 64 SiPMs with an active area of $3 \times 3 \text{ mm}^2$ and a pixel size of $100 \times 100 \mu\text{m}^2$. The sensitive area is increased by a light concentrator which consists of 64 pyramid-shaped funnels. These funnels have an entrance area of $7 \times 7 \text{ mm}^2$ and an exit area of $3 \times 3 \text{ mm}^2$, guaranteeing a sufficient position resolution e.g. for the barrel DIRC detector of the PANDA experiment at FAIR. The efficiency and uniformity of the light concentrator in combination with the SiPM array was tested by scanning the array in two dimensions, using a pulsed light beam. Results of these tests and comparison with simulations are given here.</p> <p style="text-align: right;">© 2013 Elsevier B.V. All rights reserved.</p>
---	---

1. Introduction

Silicon Photomultipliers (SiPMs) are multi-pixel APDs operated in Geiger mode. This solid-state photon detection technology provides good single photon detection capability and high photon detection efficiency. Further features are their compact size, insensitivity to magnetic fields and cost efficiency, which make them suitable for many research fields that require photon detection, such as particle physics, nuclear physics or medical imaging.

A position sensitive Cherenkov detector was built, consisting of an array of 8×8 SiPMs (Hamamatsu S10931-100P) with an active area of $3 \times 3 \text{ mm}^2$ each and a pixel size of $100 \times 100 \mu\text{m}^2$. The signals are amplified with four 16 channel amplifiers that were built in-house and are based on Photonique amplifiers. In addition, a suitable light concentrator consisting of 64 pyramid-shaped funnels was developed. With an entrance surface of $7 \times 7 \text{ mm}^2$ and an exit surface of $3 \times 3 \text{ mm}^2$, this light concentrator, which is made out of brass and coated with aluminium, increases the detection area of the module, while providing sufficient position resolution, e.g. for the barrel DIRC detector [1] at the PANDA experiment at the FAIR facility in Darmstadt [2]. Increasing the detection area of the detector by this method gives several advantages. One essential advantage is that the signal-to-noise ratio improves by increasing the sensitive area using light focusing and keeping the dark count rate constant [3]. Another benefit is

that the number of read-out channels can be kept low, thus the module can be built very compactly.

In previous work, simulations for the collection efficiency were performed [4] as well as a scan with a laser beam to measure the collection efficiency of the module. However, the beam spot diameter was as large as 1 mm and the step size was $250 \mu\text{m}$ [5]. These two parameters have been improved significantly in the new tests, providing a more detailed picture of the characteristics of the SiPMs and the light concentrator. Also, a scan with a finite incident angle was performed. The new data allows to further optimise the light guide.

2. Test setup

To test the position sensitive photon detector, the complete setup was put inside a dark box. The test setup consists of the detector module, a light source and two stepping motors which move the beam spot across the area of the scanned SiPMs.

The Hamamatsu 10931 $3 \times 3 \text{ mm}^2$ SiPMs with a pixel size of $100 \times 100 \mu\text{m}^2$ were chosen because they have the highest photon detection efficiency and an adequate dynamic range. The 10931 sensor series has the photon detection maximum at $\lambda = 440 \text{ nm}$. For the scan, a light source with a wavelength near that maximum looked reasonable and an LED with a wavelength range of $465 \text{ nm} < \lambda < 475 \text{ nm}$ was used.

The light source was set to emit pulses instead of a continuous wave in order not to saturate the sensor. The pulse rate of the LED was about 900 kHz with a pulse width of about 6.5 ns.

To reduce the beam spot diameter from $1.3 \pm 0.1 \text{ mm}$ at the LED exit to $108 \pm 4 \mu\text{m}$ at the SiPM surface, an optical setup, including three biconvex lenses and a $10 \mu\text{m}$ pinhole were included into the test

* Corresponding author at: Stefan Meyer Institute for Subatomic Physics, Austrian Academy of Sciences, Boltzmannngasse 3, 1090 Vienna, Austria.
Tel.: +43 6507885300.
E-mail address: mariana.rihl@assoc.oew.ac.at (M. Rihl).

7.5 Efficiency and uniformity measurement of a light concentrator in combination with an SiPM array

420

M. Rihl et al. / Nuclear Instruments and Methods in Physics Research A 732 (2013) 419–422

setup. This optical apparatus, which is presented in Fig. 1 was moved by the two stepping motors, which changed the beam spot position on the detector and the array by steps of $100\ \mu\text{m}$. This guaranteed that each pixel of the SiPM was triggered by the light beam.

During the tests, the coordinate convention was defined as follows: the x - and z -axis build a plane parallel to the detector surface and the y -axis is parallel to the beam direction. Fig. 2 shows a schematic of the optical setup and its mounting on the stepping motors. Furthermore, it gives an overview of the chosen coordinate convention. Due to the fact that the motors are high precision tools and that the weight had to be completely poised in order to keep the precision of the motors at its high level, some measures had to be taken. The beam spot could be moved in an x - and z -direction. In order to reduce the wiggling of the motor tips, cage plates were mounted to serve as stabilisers. The optical apparatus is fixed via fixation cage plates on the x -axis motor tip, the beam direction is parallel to the y -axis of this setup.

Fig. 3 shows the opto-motoric setup together with the detector module inside the dark box.

3. Scanned channels and scanning mode

Due to timing restraints not all 64 sensors could be scanned. Thus, three adjacent SiPMs were chosen randomly for the test. These sensors are referred to as F2, F3 and F4. Their position on the detector module surface can be seen in Fig. 4.

The sensors were scanned in three different ways. In the first two setups, all three sensors were scanned at once, with and without light concentrator. In order to test the behaviour of the collection efficiency in dependence of the incident beam angle, each sensor was scanned separately with light concentrator and an incident beam angle of about 15° .

4. Data acquisition

For the data acquisition, a LeCroy 735Zi WavePro digital oscilloscope was used. Three channels were used to acquire the signal, while the fourth one was used as trigger input.

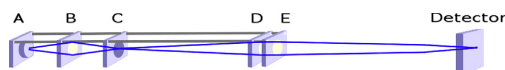


Fig. 1. Schematic of optomechanical items and laser beam. A: LED beam exit. B: biconvex lens with $f = 30\ \text{mm}$. C: $10\ \mu\text{m}$ pinhole, serves as point-like light source. D: collimating biconvex lens with $f = 100\ \text{mm}$. E: focusing biconvex lens with $f = 200\ \text{mm}$.

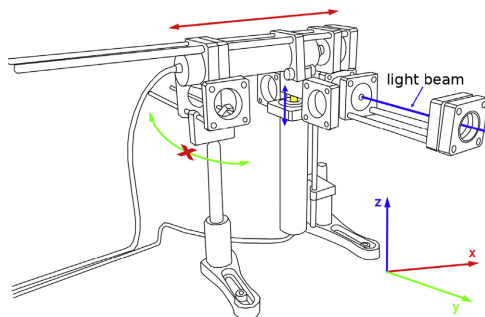


Fig. 2. Schematic of motor and optical setup, the coordinates x , y and z of movements are defined.

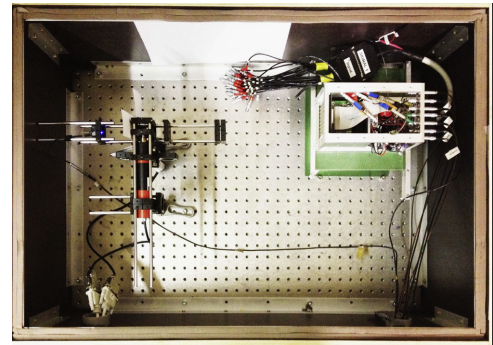


Fig. 3. Test setup inside dark box. On the left side of the box the optical and motor setup is mounted. On the right side of the box sits the detector prototype.

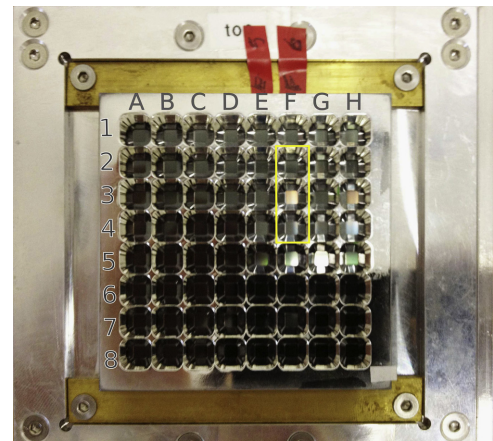


Fig. 4. Detector module with light concentrator. The scanned sensors are highlighted by the rectangular frame.

The scope of the experiment was to extract the pulse height from the signal of the respective SiPM. The amplitude of the signal was measured by acquiring the minimum of each waveform during the acquisition window of $200\ \text{ns}$. To achieve good statistics, 1000 samples were taken per position of the photon source for each of the three channels respectively. The oscilloscope calculated the mean and standard deviation of 1000 samples of the amplitude. The acquired data for each channel was background corrected and then added up. The data is referred to as $\langle a \rangle_{LC}$ and $\langle a \rangle_{noLC}$ for the mean amplitude with and without light concentrator respectively.

These two data values (per channel) were saved into a text file, together with information about the coordinates of the beam position.

Taking into account the number of data points that need to be acquired during the scans, it is obvious that an automation routine is beneficial. Such a routine was created with LabVIEW and regulates the beam spot movement by the motors as well as the data acquisition by the oscilloscope and the saving of the data.

Fig. 5 shows a snapshot of the data acquisition with the oscilloscope.

7. APPENDIX

5. Results

5.1. Qualitative analysis

The data acquired during the scans was transformed into two dimensional histograms, using routines based on C++ and ROOT. Fig. 6 shows the two dimensional histograms from a top view. It is possible to clearly distinguish between the original sensitive area and the enhanced sensitive area when the light concentrator is applied. Also, the reduced collection efficiency due to an incident beam angle is evident in Fig. 6(c).

As can be seen in Fig. 6, it can be distinguished between active areas and the areas where no photons get detected. One reason for the inactive area is the finite rim which separates the funnels from each other. At these areas, photons get reflected. Another reason is that the sensors were not soldered in perfect alignment, resulting in an offset between the exit area of the light concentrator and the active area of the SiPMs. Fig. 7 shows a comparison between the two dimensional histograms and microscope photos of the respective channels, illustrating the offset of the sensors in relation to the light concentrator.

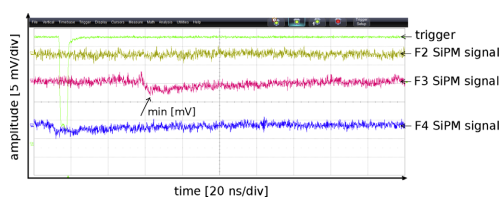


Fig. 5. Data acquisition with trigger and SiPM signals. Due to the beam diameter of about 108 μm (FWHM), only one SiPM sends a signal at a time, represented here by sensor F3.

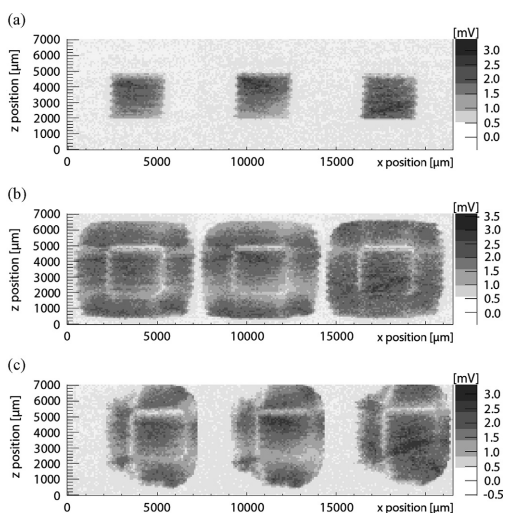


Fig. 6. Two-dimensional histogram of the scan data for the three sensors (a) without LC, (b) with LC and (c) with LC and an incident beam angle of about 15°. The colour scheme gives the mean intensity of signal height of the SiPMs in mV.

5.2. Collection efficiency

The collection efficiency of the light concentrator can be calculated by comparing the data from the scans with light concentrator to the scans without the light concentrator. The collection efficiency ϵ_{col} of one funnel of the light concentrator is defined by

$$\epsilon_{col} = \frac{n_d}{\alpha \cdot n_{d0}} \quad (1)$$

with n_d being the number of photons detected with light concentrator, n_{d0} the number of detected photons without light concentrator and $\alpha = (\frac{2}{3})^2 \cdot 0.93$ an area factor [5]. The 0.93 in the area factor α is the geometric fill factor and puts into account the fact that the edges are rounded.

The area factor α represents the enlargement of the detection area of a SiPM and is in this specific case $A_{entrance}/A_{exit}$, where $A_{entrance}$ and A_{exit} represent the entrance and exit area respectively. The collection efficiency ϵ_{col} was calculated, using the following equation for a certain funnel:

$$\epsilon_{col} = \frac{\sum \langle a \rangle_{LC}}{\sum \langle a \rangle_{noLC} \cdot \alpha} \quad (2)$$

Table 1 shows the results for the collection efficiency for each sensor with incident beam angles of 0° and 15° respectively. The mean collection efficiency is also given.

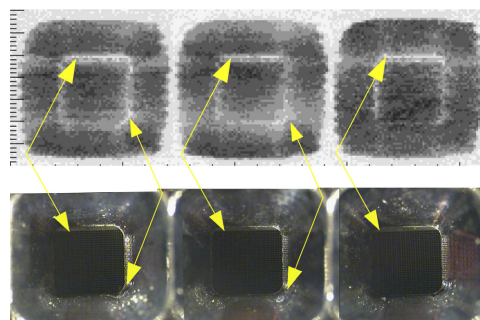


Fig. 7. Histogram of mean intensity and photo of the sensors with the light concentrator on top. The arrows indicate areas where no photons get detected as a result of imperfections of the alignment of the sensor array and the light concentrator.

Table 1

Collection efficiencies for the evaluated three channels at two different photon incident angles. Standard deviations of the collection efficiencies are also shown, indicating the fluctuations of the collection efficiency funnel by funnel.

Channel	Angle (°)	Collection efficiency, ϵ_{col} (%)
F2	0	88.6
F3	0	83.4
F4	0	86.0
Mean	0	86.0 ($\sigma = 2.6$)
F2	15	56.8
F3	15	55.4
F4	15	58.4
Mean	15	56.7 ($\sigma = 1.5$)

7.5 Efficiency and uniformity measurement of a light concentrator in combination with an SiPM array

422

M. Rihl et al. / Nuclear Instruments and Methods in Physics Research A 732 (2013) 419–422

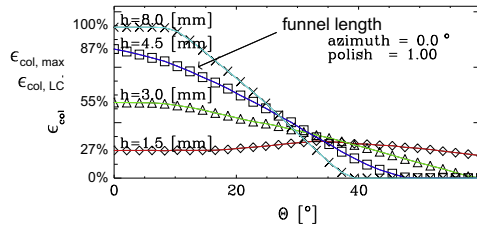


Fig. 8. Simulation of the collection efficiency in dependence of the incident beam angle and different funnel lengths [4].

5.3. Comparison to simulations

Comparing the measured mean values with simulations of the collection efficiency of the light concentrator shows that the results are in good agreement with the simulations. The simulated collection efficiency for a light concentrator with a funnel length of 4.5 mm and an incident beam angle perpendicular to the detector surface is about 86%. The mean of the measured collection efficiency for the light concentrator with an incident beam angle of 0° is also about 86%. Applying an incident beam angle of 15° results in a mean collection efficiency of about 57%, compared to the simulation value of 61%. Fig. 8 shows the results of the simulation for the light concentrator, which was done previously by the authors [4]. The figure displays the collection efficiency for different funnel lengths. The simulated collection efficiencies are given in dependence of the incident beam angle.

6. Conclusion and outlook

A prototype of a position sensitive SiPM array with a light concentrator was tested in order to evaluate the collection efficiency by scanning with a narrowly-focused LED light. The scans were performed with a light source of a beam spot diameter of $108 \pm 4 \mu\text{m}$ and a stepping size of $100 \mu\text{m}$. These parameters have been improved significantly to earlier tests, giving a more detailed picture of the collection efficiency and uniformity. In addition, the performance of the light concentrator collection efficiency was tested for two different incident light beam angles, 0° and 15° . The simulation agrees well with the data and can be used to further optimise the geometry of the light concentrator.

Ideas to optimise the detector include better alignment of the sensors to the concentrator or a slightly narrower exit area in order to remove the gaps in-between and to develop a different kind of light concentrator with plexiglas cones instead of a metal grid.

References

- [1] B. Seitz, et al., Nuclear Instruments and Methods in Physics Research Section A 628 (2011) 304.
- [2] W.F. Henning, Journal of Physics G: Nuclear and Particle Physics 34 (2007) 551.
- [3] S. Korpar, et al., Nuclear Instruments and Methods in Physics Research Section A 610 (2009) 427.
- [4] G. Ahmed, et al., Nuclear Instruments and Methods in Physics Research Section A 639 (2011) 107.
- [5] L. Gruber, et al., Journal of Instrumentation 6 (2011) C11024.

7.6 Oversaturation behaviour of SiPM at high photon exposure

Reprinted, with permission, from L. Gruber, J. Marton, K. Suzuki. Reference: (54).

Author's personal copy

Nuclear Instruments and Methods in Physics Research A 737 (2014) 11–18



Contents lists available at ScienceDirect

Nuclear Instruments and Methods in
Physics Research A

journal homepage: www.elsevier.com/locate/nima



Over saturation behavior of SiPMs at high photon exposure



L. Gruber*, S.E. Brunner, J. Marton, K. Suzuki

Stefan Meyer Institute for Subatomic Physics, Austrian Academy of Sciences, Vienna, Austria

ARTICLE INFO

Article history:

Received 23 July 2013

Received in revised form

2 October 2013

Accepted 1 November 2013

Available online 14 November 2013

Keywords:

Semiconductor photo detector

Silicon Photomultiplier (SiPM)

Multi Pixel Photon Counter (MPPC)

Dynamic range

ABSTRACT

Several types of Silicon Photomultipliers were exposed to short pulsed laser light (~ 30 ps FWHM) with its intensity varying from single photon to well above the number of microcells of the device. We observed a significant deviation of the output of SiPMs from the expected behavior although such response curve is considered to be rather trivial. We also noticed that the output exceeds the maximum expected pulse height, which should be defined as the total number of pixels times the single photon pulse height. At the highest light intensity (~ 500 times the number of pixels) that we tested, the signal output reached up to twice the maximum theoretical pulse height, and still did not fully saturate.

© 2013 Elsevier B.V. All rights reserved.

1. Introduction

The Silicon Photomultiplier (SiPM) is a semiconductor photo detector which consists of multiple pixels (typically a few 100) of Avalanche Photodiodes working in Geiger-mode. Because of its characteristics such as compact size, low cost, insensitivity to magnetic fields, high photon detection efficiency (PDE) and high gain, the SiPM can be used in many different fields ranging from astrophysics, particle physics to medical imaging, as an alternative to vacuum Photomultiplier Tubes.

Due to its design, the SiPM dynamic range should be limited to an order of the total number of pixels. This effect is reflected in a saturation behavior of the SiPM response. The relation between the number of incident photons on the detector surface (N_{photon}) and the number of fired pixels (N_{fired}) can be described by the following model:

$$N_{\text{fired}} = N_{\text{total}} \times \left[1 - \exp\left(-\frac{N_{\text{photon}} \times \text{PDE}}{N_{\text{total}}}\right) \right] \quad (1)$$

with N_{total} , the total number of pixels of the SiPM. With increasing N_{photon} , the SiPM response curve, i.e. the relation between light input and SiPM output (N_{fired}), deviates from linearity, dependent on the PDE, and saturates at $N_{\text{fired}} = N_{\text{total}}$. Eq. (1) is valid for an ideal photosensor and an infinitely short light pulse. In a real SiPM, however, the response to incident light is influenced by several effects, such as after-pulsing, cross-talk, dark-noise and the pixel recovery. Therefore, the SiPM output is expected to deviate from the response curve as given by Eq. (1).

As presented in the following sections, we came across to observe a deviation between the SiPM output and the expected response, which cannot be explained only by the above effects. We measured the response curve for various SiPMs, all with 1 mm^2 sensitive area but different number of pixels and from different vendors. The models tested are the Hamamatsu MPPC S10362-11-100U with 100 pixels and S10362-11-050U with 400 pixels, the SSPM-0611B1MM-T018 from Photonique¹ with 556 pixels and a Zecotek MAPD-1 with 560 pixels. The main parameters of all tested devices are summarized in Table 1.

2. Setup and method

To measure the response curve, the SiPMs were exposed to short light pulses with intensities ranging from single photon up to several ten thousand. The measurement setup is shown schematically in Fig. 1. All tests were done at room temperature (~ 25 °C). As light source we used a pulsed laser with 32 ps pulse width (FWHM) from Advanced Laser Diode Systems. The emission wavelength of the laser head (PL040) is $\lambda = 404$ nm. The repetition frequency was set to a level of 20 kHz, to have a time interval between two laser pulses well above the SiPM cell recovery time. After passing a variable optical attenuator, the laser pulses were split using a beam splitter with a splitting ratio of 45:55 (45% reflectivity, 55% transmission). One path of the beam is targeted at a Hamamatsu S5971 PIN photodiode for monitoring the light intensity. The current of the PIN photodiode was measured using a Keithley 6517 electrometer. After passing another variable optical

* Corresponding author.

E-mail address: lukas.gruber@oeaw.ac.at (L. Gruber).

¹ Photonique SA has suspended its operations. Product information can be found here: <http://www.photonique.ch/LEGACY>.

7.6 Oversaturation behaviour of SiPM at high photon exposure

Author's personal copy

12

L. Gruber et al. / Nuclear Instruments and Methods in Physics Research A 737 (2014) 11–18

Table 1

Main SiPM parameters. The breakdown voltage, V_{bd} , has been measured. The operating voltage V_{bias} is typically set ~ 1 V above V_{bd} . The exact values and the corresponding gain are given. Other parameters are taken from the data sheets [1–3]. The PDE given by Hamamatsu includes effects from cross-talk and after-pulsing. There are several other measurements of the PDE available, but the results are also known to strongly depend on the operating conditions, e.g. over-voltage and temperature, and the measurement procedure. Therefore, we refer to the values given by the companies.

Parameter	Hamamatsu MPPC		Photonique SSPM	Zecotek MAPD
	S10362-11-100U	S10362-11-050U	0611B1MM-T018	MAPD-1
Active area (mm ²)	1 × 1	1 × 1	1 × 1	1 × 1
Number of pixels	100	400	556	560
Pixel size (μm ²)	100 × 100	50 × 50	–	–
Fill factor (%)	78.5	61.5	> 70	–
PDE (% @ 400 nm)	72	47	18	15
Capacitance (pF)	35	35	40	75.6
Breakdown voltage (V)	69.45	68.65	27.80	34.00
Operating voltage	69.95	69.85	29.00	34.70
V_{bias} (V)				
Gain @ V_{bias}	1.1×10^6	6.6×10^5	5.4×10^5	5.9×10^5

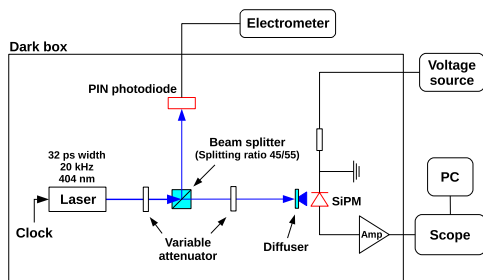


Fig. 1. Schematic of the measurement setup.

attenuator, the second beam was directed to a diffuser in order to homogeneously distribute the light on the SiPM active area. The second attenuator in between beam splitter and SiPM is needed to deal with the different sensitivities of the SiPM and the photodiode.

The SiPM signal was amplified by using a Photonique AMP-0611 preamplifier [2]. The DC voltage supply was set to 5 V. The linearity of the preamplifier was confirmed by measuring the preamplifier response to defined input pulses. Within the whole input range we tested, a linear behavior of both, the output pulse height as well as the output charge, was found. The measurement resulted in a gain of about 23. The operating voltage of the sensor, V_{bias} , was typically set to $V_{over} \sim 1$ V above the breakdown voltage, V_{bd} , which had been determined in a separate measurement. The values are given in Table 1. The corresponding gain of the SiPM, G , can be estimated by $G = C_{pix} \cdot V_{over} / q_e = C_{pix} \cdot (V_{bias} - V_{bd}) / q_e$, with C_{pix} being the pixel capacitance and q_e the elementary charge. The operating voltages given in Table 1 were selected in order to operate the SiPMs at low to moderate gain and therefore low noise (dark-noise, after-pulsing, cross-talk).

The SiPM response, i.e. the number of fired pixels, N_{fired} , was determined by measuring the average output pulse height with the LeCroy WavePro 735Zi digital oscilloscope. In order to estimate N_{fired} from the measured pulse height, the output signal of a single fired pixel must be determined. This is done at low light intensity

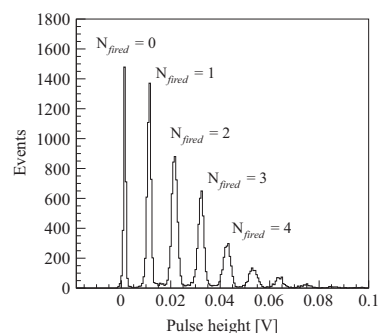


Fig. 2. Single photon spectrum of the Hamamatsu MPPC with 100 pixels operated at $V_{over} = 1$ V. The peaks correspond to a certain number of fired pixels.

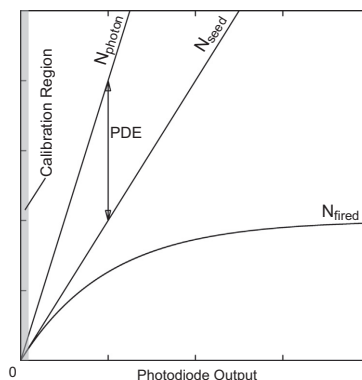


Fig. 3. Schematic of the calibration method.

by filling the pulse height values into a histogram, as shown in Fig. 2. Each peak corresponds to a certain number of fired pixels (N_{fired}). By fitting the spectrum and extracting the distance between adjacent peaks, the pulse height corresponding to a single fired pixel can be determined several times.

The PIN photodiode was calibrated at very low light intensities ($N_{fired} < 10$, in case of Hamamatsu 100U, $N_{fired} < 20$, for the others), where one can expect a linear behavior of the response, due to the homogeneous distribution of input photons on the sensor surface. The calibration procedure is illustrated schematically in Fig. 3. For interpretation of the data, we introduce the average number of “seeds”, N_{seed} , which is the average number of photons arriving at the sensitive area of the SiPM, that could trigger an avalanche unless the cells had been fired already. The number of fired pixels, N_{fired} , is the main observable of the measurement. N_{fired} can be determined by measuring the signal pulse height, as described before. In the calibration region $N_{seed} = N_{fired}$, thus N_{seed} and the linear relation between the photodiode output current and the number of “seeds” can be determined and in the following extrapolated to higher light intensities. The relation between N_{seed} and the number of incident photons, N_{photon} , is given by $N_{photon} = N_{seed} / PDE$. In order to avoid the use of a PDE, which depends on the temperature, the operation voltage and the way it is measured, we plot N_{fired} as a function of N_{seed} and compare

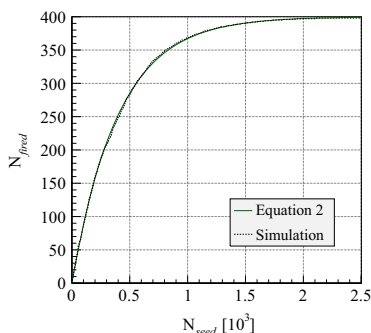


Fig. 4. Comparison between simulated and modeled response of an SiPM with $N_{total} = 400$.

different types of SiPMs. This is a more “natural” representation, because only measured quantities are involved and therefore the actual PDE of the sensor is included a priori. The expectation curve then appears as the following equation:

$$N_{fired} = N_{total} \times \left[1 - \exp\left(-\frac{N_{seed}}{N_{total}}\right) \right] \quad (2)$$

As mentioned before, we are determining N_{fired} by measuring the signal pulse height rather than the output charge. The idea behind is to minimize the influence of delayed correlated noise, like after-pulsing and cross-talk related to this after-pulsing, as well as the influence from dark-noise. In course of the measurements we also monitored the integrated charge and checked that there is no apparent change in the signal shape for all light intensities that were tested. Since we are operating the SiPM at low gain and therefore low noise, we realized that the measured SiPM response is hardly affected by the method used to determine N_{fired} (pulse height or charge measurement). The impact of the diverse noise effects on the measurement results is estimated in the following.

Dark- : The pulse height measurement is not influenced by noise dark-noise, unless the dark-counts occur within the rise time of the signal, which is about 2–3 ns. Since the dark-count rate is typically below 1 MHz for a 1 mm² SiPM, the probability for a dark-count to occur within this time interval is in the order of a few per mill and therefore the impact on the measurement is negligible.

After- : The measured output pulse height could be affected by after-pulses that happen within a very short time interval after the initial breakdown, within the signal rise time, however, the influence is small due to the finite recovery time of the pixels (~200 ns till full recovery for the Hamamatsu 100U, ~50 ns for the Hamamatsu 050U [4,5]) and a certain after-pulse probability. Taking the recovery process into account, an after-pulse happening 2–3 ns after the initial avalanche in a microcell may give rise to an additional output of ~5–15% of the single photon signal, depending on the pixel size. Assuming additionally an after-pulse probability of 10% for the MPPCs with 100 μm² and 50 μm² pixel size [6], the total output signal of the SiPM might be overestimated finally by ~1–2% due to fast after-pulsing.

Cross- : The cross-talk probability is known to be ~5% at the talk: operating conditions we are using [6]. The impact of

cross-talk related to fast after-pulsing is negligible because of the relatively small effect of after-pulsing itself. In fact, the measurement is mainly influenced by almost instantaneous cross-talk following the initial photon input (laser pulse). However, this effect is suppressed especially at high light intensities (in the non-linear range) because the pixel occupancy is already nearly 100%. In this range most of the measurements were performed. In the calibration region the effect is also small. The SiPM response (N_{fired}) might be overestimated by ~5% in the linear region due to cross-talk and thus also N_{seed} , since we use $N_{seed} = N_{fired}$ to determine the number of “seeds”. Another uncertainty in the photon count (N_{seed}) comes from statistical fluctuations in the number of photons detected.

Because of the above considerations, the uncertainty of the SiPM output (N_{fired}) due to after-pulsing, cross-talk and dark-noise is < 2% for most light intensities that were used in the measurements, i.e. beyond the linear region of the response. In this regime, the response is mainly influenced by after-pulsing. For low light intensities, also cross-talk starts to play a role and N_{fired} and N_{seed} , respectively, may be overestimated by ~5%. There should be no impact of the recovery process on the measured SiPM response, since the incident light pulse duration is rather short (~30 ps) compared to the pixel recovery time (few 10 ns). Therefore, one can use Eqs. (1) and (2), respectively, to describe the measured response curves.

For verification of the model equation, we performed a Monte Carlo simulation including a geometrical consideration and obtained a response curve. The result is shown in Fig. 4 together with the curve expected from the model, as given by Eq. (2). The two curves are found essentially identical, indicating that the approximation of the SiPM response using the model equation is reasonable.

3. Results

Fig. 5 shows the measured response curves, N_{fired} as a function of N_{seed} , for the Hamamatsu MPPC with 100 pixels and 400 pixels, as well as for the Photonique SSPPM with 556 pixels and Zecotek MAPD with 560 pixels. N_{fired} is the direct observable of our setup, while N_{seed} is determined via measuring the PIN photodiode output current as described in Section 2. However, N_{fired} and N_{seed} are both derived from the measurement, and therefore both variables include the actual PDE of the respective SiPM. In Fig. 5 the same data is presented always with wide range (left) and narrow range (right) of input photons. A spline curve is added to guide the trend of the response curve. The curve expected from the model as in Eq. (2) is also drawn in the figure for comparison. The expected outputs approach exponentially the maxima, N_{total} , which are indicated by the horizontal dotted lines.

For all sensors we tested, the data agree well with the expected response curve at low photon intensity, however, soon start to diverge. It is clearly visible that the pulse height exceeds the maximum expected value. One notices also that the effect of this over saturation behavior varies among the SiPMs tested here. The maximum output we obtained from Hamamatsu 100U (100 pixels) and Hamamatsu 050U (400 pixels) amounts roughly 200 p.e. (photoelectrons) equivalent and 800 p.e. equivalent, respectively, which would be the expected output for a sensor having twice the number of pixels. On the other hand, the Zecotek device with $N_{total} = 560$ seems less affected and the maximum measured output is ~650 p.e. equivalent, that amounts ~15% larger output

7.6 Oversaturation behaviour of SiPM at high photon exposure

Author's personal copy

14

L. Gruber et al. / Nuclear Instruments and Methods in Physics Research A 737 (2014) 11–18

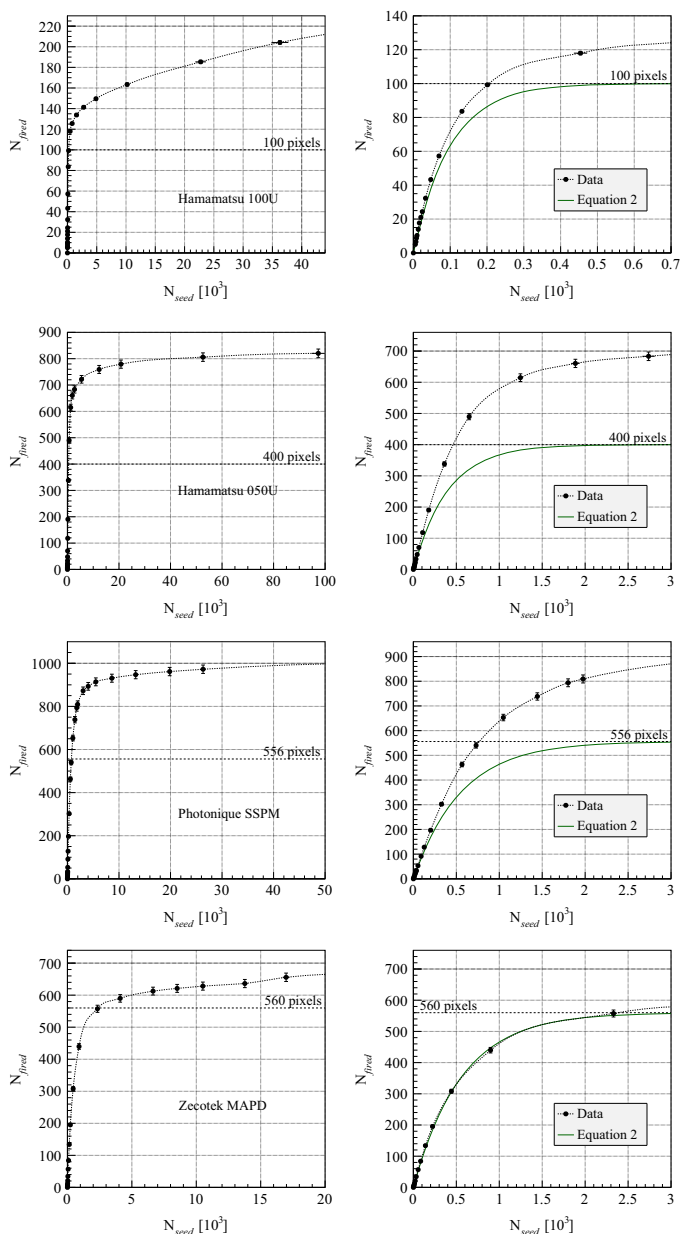


Fig. 5. Response curves of Hamamatsu MPPC with 100 pixels operated at $V_{over} = 0.5$ V, Hamamatsu MPPC with 400 pixels operated at $V_{over} = 1.2$ V, Photonique SSPM with 556 pixels operated at $V_{over} = 1.2$ V and Zecotek MAPD-1 with 560 pixels operated at $V_{over} = 0.7$ V (top to bottom) for high light intensities (left) and low to medium light intensities (right). The data points are compared with the result of a model calculation given by Eq. (2). The expected values of saturation are indicated by the horizontal dashed lines.

than expected. It is also to be noted that within the maximum light intensity (~ 100 k “seeds”), we see no clear sign of full saturation of the device, especially in the case of the Hamamatsu 100U.

Looking at the response curves of the MPPC with 400 pixels and the SSPM with 556 pixels, one can observe an additional enhancement of the dynamic range compared to the model calculation.

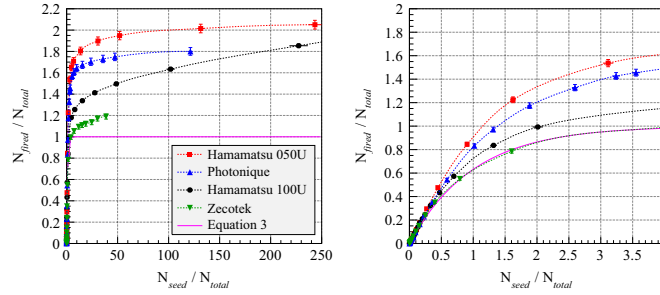


Fig. 6. Response curves of various SiPMs, normalized to the total number of pixels of each device, N_{total} , for high (left) and low to medium light intensities (right).

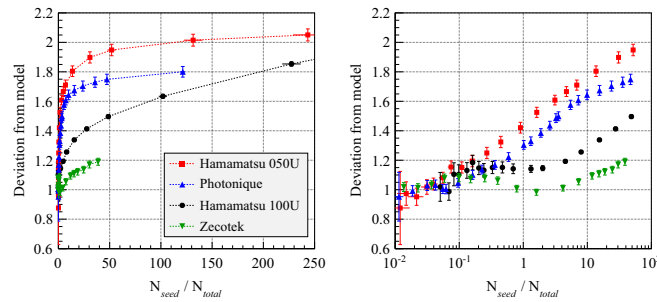


Fig. 7. Deviation of the response curves of various SiPMs from the model curve given by Eq. (3). The results are normalized to the total number of pixels of each device, N_{total} . The deviation is defined as the ratio between measured and calculated values.

For better comparison, the SiPM response curves are normalized to the total number of pixels corresponding to the respective device. Then the expectation curve appears as the following equation:

$$\frac{N_{fired}}{N_{total}} = 1 - \exp\left(-\frac{N_{seed}}{N_{total}}\right) \quad (3)$$

In this representation the response curve is universal to all types of SiPMs. The data from all four SiPMs as well as the universal response function (Eq. (3)) are overlaid and compared in Fig. 6. The plot shows clearly that the degree of the over saturation differs from one SiPM model to the other (Fig. 6, left). Within the plotted range, the largest effect is seen in Hamamatsu 050U, followed by Photonique, Hamamatsu 100U and Zecotek. At very high light intensities ($N_{seed}/N_{total} > 400$), the output of the Hamamatsu 100U even exceeds the one measured for the Hamamatsu 050U device (Fig. 5, left). At low light input, the SiPM response is linear and following the model curve, with increasing light intensity the data start to diverge from the expected behavior. The Zecotek sensor appears to be the only device following the expected function at light inputs up to $N_{seed}/N_{total} = 4$ (Fig. 6, right).

In order to emphasize the degree of deviation from the theoretical function, we normalized Fig. 6 using the function given by Eq. (3). The results are shown in Fig. 7. At low light intensity ($N_{seed}/N_{total} < 0.3$), where actually the sensors are commonly used, the deviations are very small and all SiPM respond in a similar manner (Fig. 7, right). In this region it seems that the deviation from the theoretical function increases monotonically for all SiPMs. However, for higher light input we notice two qualitatively different tendencies of deviation. Around $N_{seed}/N_{total} \sim 0.5$ the deviation starts to decrease and tends to return to the expected

value for Hamamatsu 100U and Zecotek sensors, before increasing again. For the other two SiPMs the deviation increases monotonically. It is also to be noted that even the two Hamamatsu MPPCs, which are supposed to have a comparable response, show a different behavior.

In a last step, we determined the over-voltage dependency of the SiPM response, as shown in Fig. 8 for the Hamamatsu 100U. At low light intensities ($N_{seed}/N_{total} < 0.3$) all curves are following the model given by Eq. (3) (Fig. 8, right). Increasing the light intensity the response curves deviate from the model calculation. Moreover, the deviation is strongly correlated with the applied over-voltage, especially for very high light intensities (Fig. 8 left).

4. Discussion

In Section 3, the raw data of the measurements (N_{fired} and N_{seed}) are used to describe the SiPM response curves. By using the PDE of the respective device, we can obtain an alternative representation of the response curves, i.e. we can plot N_{fired} as a function of N_{photon} , the number of incident photons. As illustrated in Fig. 3, the relation between N_{seed} and N_{photon} is given by $N_{photon} = N_{seed}/PDE$.

The PDE values for the Hamamatsu MPPCs (72% for 100U, 47% for 050U at 400 nm) were taken from the data sheet [1]. As here the PDEs are evaluated by a current measurement, which cannot distinguish after-pulsing and cross-talk effects, the values are overestimated. These two effects would amount in an overestimation of $\sim 20\%$ and $\sim 10\%$ of the PDE [7], respectively. For the Photonique SSPM and Zecotek MAPD, PDE values of 18% [2] and 15% [3] for a wavelength of 400 nm were found. There are several other measurements of the PDE available, but the results are also

7.6 Oversaturation behaviour of SiPM at high photon exposure

Author's personal copy

16

L. Gruber et al. / Nuclear Instruments and Methods in Physics Research A 737 (2014) 11–18

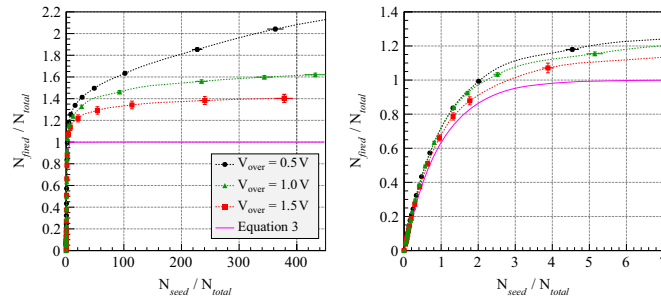


Fig. 8. Over-voltage dependency of the response curve for Hamamatsu 100U. The data are compared with the model calculation given by Eq. (3). The results are normalized to the total number of pixels of the device, N_{total} .

known to depend on the operating conditions, e.g. over-voltage and temperature. Therefore, in order to handle this problem the best, we refer to the PDE values provided by the company and, in case of the Hamamatsu MPPCs, we take those values as an upper boundary of an uncertainty band going down to a $\sim 30\%$ smaller value. It is important to stress, that the choice of the PDE value does not affect the measurement result, the PDE is only needed to evaluate N_{photon} , N_{fired} and N_{seed} include the actual PDE already, because they are measured quantities.

Fig. 9 shows the response curves represented as N_{fired} as a function of N_{photon} , for all tested SiPMs. The same data is again presented always with wide range (left) and narrow range (right) of input photons. A spline curve is added to guide the trend of the response curve. The curve expected from the model as in Eq. (1) is also drawn in the figure for comparison. The expected maxima, N_{total} , are indicated by the horizontal dotted lines. For the plots, N_{photon} is calculated by using a certain PDE value. In case of the Hamamatsu SiPMs the data are plotted for two different values of the PDE and the model is calculated within a PDE range, as described above. The slopes of the response and model curves change accordingly. However, the maximum measured output (N_{fired}) is unaffected by the choice of the PDE value (Fig. 9, left).

The response curves of all four SiPMs are again normalized to the total number of pixels corresponding to the respective device and are overlaid in Fig. 10. The response curves are crossing (Fig. 10, right) because of the different PDE values utilized to evaluate N_{photon} on one hand, and the varying strength of the over saturation effect on the other hand. At low number of induced photons, the SiPM response is still linear and the slope of the curve is mainly determined by the PDE used. With increasing light intensity the data start to diverge from the expected behavior (depending on the strength of the effect) and the curves cross.

Up to now, no convincing explanation for this over saturation and enhanced dynamic range could be found. Other groups report a similar observation. In Ref. [8], a SiPM response exceeding the total number of pixels at high operating voltage is reported. In this case, however, the number of fired pixels is estimated by integrating the signal using a charge ADC and the result could be explained by the correlated noise (after-pulsing, cross-talk and dark-noise). As discussed, in our case the influence of delayed correlated noise is small, as we are operating the SiPMs at low gain and evaluate the number of pixels from the signal pulse height and not from the collected charge. Cross-talk that occurs almost instantaneously to the initial laser pulse is suppressed for most of the measurements due to high pixel occupancy at high light intensities. Very fast after-pulses occurring within the signal rise time of $\sim 2\text{--}3\text{ ns}$, may lead to an overestimation of the SiPM

output (N_{fired}) by $\sim 1\text{--}2\%$, and thus cannot explain the large over-saturation we observed. Also the over-voltage dependency of the SiPM response (Fig. 8) shows that the measurement is hardly affected by correlated noise: If the measured response was influenced by any of these effects, the over saturation effect would be stronger at higher over-voltage, since the probabilities for after-pulsing, cross-talk as well as for dark-noise would increase. As one can see from Fig. 8, this is not the case.

As described in Ref. [9], the SiPM output is strongly depending on the pulse width of the light pulses used to illuminate the sensor. When the pulse width is comparable to or exceeds the pixel recovery time, an enhancement of the dynamic range and an output beyond the total number of pixels can be observed. Since we are using a pulse width of 32 ps (FWHM), we are not influenced by the recovery process.

To exclude effects from electronics, in particular a non-linear behavior of the preamplifier at large input signals, the linearity of the preamplifier was confirmed in a measurement, which resulted in a mean gain of 23 ± 0.8 for the whole input range we tested. It is also to be noted that, if an input signal to the preamplifier exceeded the linear region, a pulse height measurement would underestimate the actual signal because of the saturation of the preamplifier output, which means that one would even underestimate the real over saturation. Eventually, the over saturation behavior was observed when the SiPM signal was not amplified but directly fed into the oscilloscope.

One possible explanation could be that a very high number of input photons per pixel may trigger several avalanches simultaneously, giving rise to a slightly higher output signal compared to the single photon signal. However, the fact that even the two MPPCs do not show the same behavior is in contrast to this assumption and indicates a more complex effect behind.

Another possible reason for the observed effect might be related to the region in-between the microcells. The trenches separating the individual pixels are coated with a thin reflective layer of aluminum and are supposed to be insensitive to incoming light. However, at very high light exposure, some photons may pass the layer, resulting in an additional signal. In order to explain the observed over saturation solely by this effect, one has to assume a gain of at least 10^3 for these inactive regions, which is questionable because of the low field there. However, such an effect could explain the discrepancy in the behavior of the two MPPCs. The Hamamatsu 050U has a lower fill factor, i.e. a larger inactive area, than the Hamamatsu 100U.

In general one should note that SiPMs are typically not operated in the regime of very high light exposure since the output linearity is lost, but are preferably used to measure low

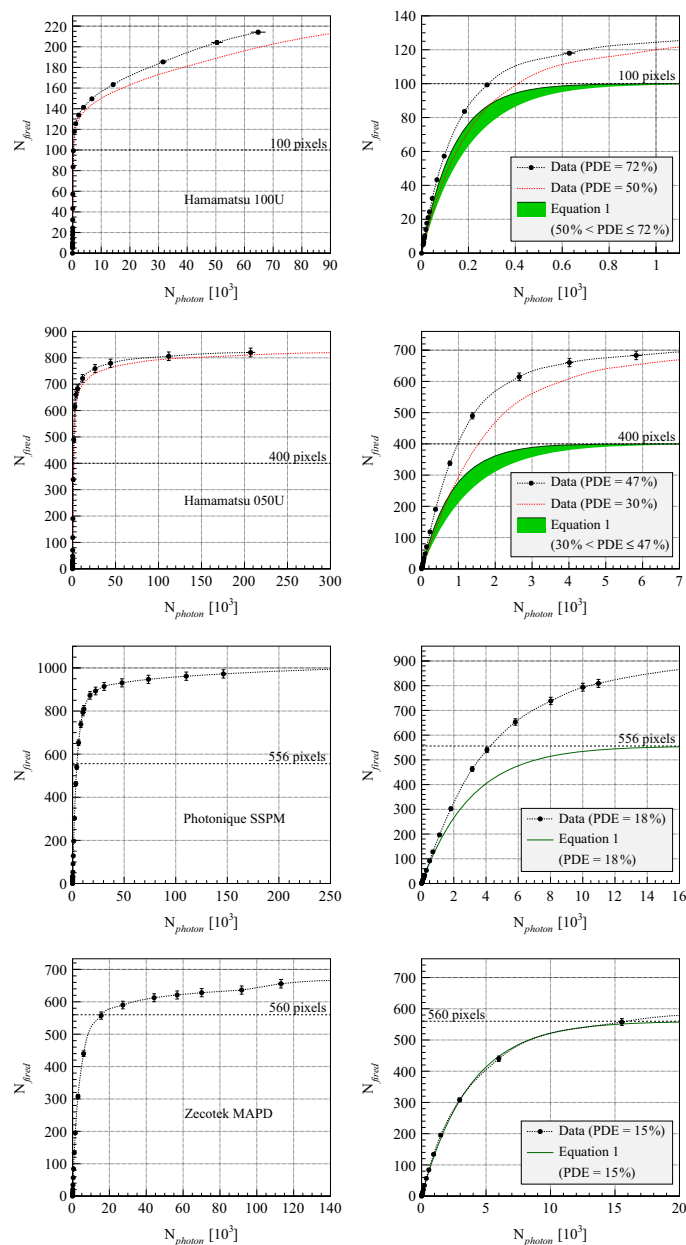


Fig. 9. Alternative representation of response curves (N_{fired} as a function of N_{photon}) for Hamamatsu MPPC with 100 pixels, Hamamatsu MPPC with 400 pixels, Photonique SSPM with 556 pixels and Zecotek MAPD-1 with 560 pixels (top to bottom) for high light intensities (left) and low to medium light intensities (right). The PDE values used to evaluate N_{photon} are indicated in the plots. The data points are compared with the result of a model calculation given by Eq. (1). The expected values of saturation are indicated by the horizontal dashed lines.

7.6 Oversaturation behaviour of SiPM at high photon exposure

Author's personal copy

18

L. Gruber et al. / Nuclear Instruments and Methods in Physics Research A 737 (2014) 11–18

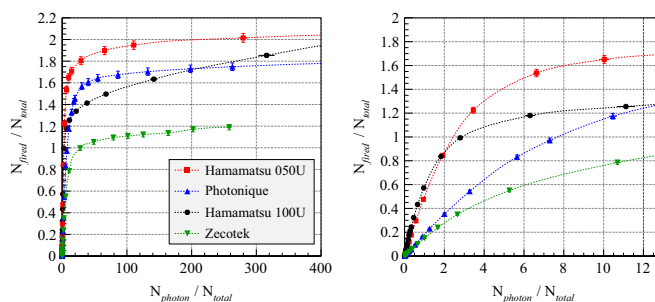


Fig. 10. Response curves, represented as $N_{\text{fired}}/N_{\text{total}}$ as a function of $N_{\text{photon}}/N_{\text{total}}$, for various SiPMs, normalized to the total number of pixels of each device, N_{total} , for high (left) and low to medium light intensities (right).

amounts of light, in the linear, dynamic range, where measurement and model agree well. Therefore, most cases of application would not be affected by our observation. Nevertheless, understanding this behavior is going to advance the overall understanding of this still relatively new device, and may open a new application, e.g. it may allow to use SiPMs for a wide range of light intensities, using calibration curves, of course with the drawback of decreasing accuracy for increasing intensity.

5. Conclusion

Our results show the SiPM signal response for a wide range of light intensity. For low light levels, the dynamic range of the photons follow the expected behavior as given by the model equation and simulation. With increasing light intensities the signal response starts to diverge from the predicted values and exceeds the expected maximum by a factor between 1 and 2. Furthermore, at light intensities reaching 500 times the number of pixels, still no full saturation was observed. This behavior was found for all tested devices but varies in magnitude. It suggests that the current understanding of SiPMs, i.e. each pixel acts as a

digital device giving 0 or 1 output regardless of the number of induced photons onto the pixel, might be rather naive and we have to improve our understanding of the device.

Acknowledgments

This work is partly supported by the EU Projects HadronPhysics2 (project 227431) and HadronPhysics3 (project 283286).

References

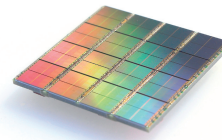
- [1] Hamamatsu Photonics K.K., <http://www.hamamatsu.com/jp/en/product/catalogory/3100/4004/4113/index.html>.
- [2] Photonique SA, (<http://www.photonique.ch/LEGACY>).
- [3] Zecotek Photonics Inc., Zecotek Brochure, 2008.
- [4] Opto-Semiconductor Handbook, Hamamatsu Photonics K.K., (http://www.hamamatsu.com/jp/en/hamamatsu/overview/bsd/solid_state_division/related_documents.html).
- [5] H. Oide, et al., PoS(PD07) 008, 2007.
- [6] P. Eckert, et al., Nucl. Instrum. Methods A 620 (2010) 217.
- [7] Hamamatsu Photonics K.K., Private communication, 2013.
- [8] P. Eckert, et al., J. Instrum. 7 (2012) P08011.
- [9] S. Uozumi, PoS(PD07)022, 2007.

7. APPENDIX

7.7 Leaflet Philips DPC

Accessed and downloaded July 2014, from <http://www.research.philips.com/initiatives/digitalphotoncounting/news/downloads/leaflet-digital-silicon-photomultiplier.pdf>.

Digital Silicon Photomultiplier



Application benefits

- Sensitivity
 - Low dark count level
- Speed
 - Excellent timing resolution
- Robustness
 - Against electromagnetic interference
 - Low sensitivity to temperature variations
- Dark count reduction due to the possibility of disabling individual cells

For system manufacturers

- Integrated electronics simplifies system integration (fully digital interface)
- Lower system cost
- Low power consumption
- Scalability of the detector area
- Customized detector and modular design

Partnership

As one of the underlying principles behind its policy of open innovation, Philips welcomes development partners with application expertise to fully exploit the market potential of its new digital silicon photomultiplier technology.

How it works

Working principle of a digital silicon photomultiplier

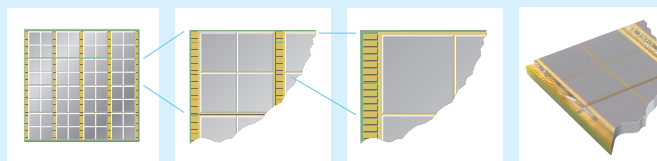


Figure 1a: One array comprises 16 dies (8x8 pixels)

Figure 1b: One die comprises 4 pixels

Figure 1c: One pixel

Figure 1d: Photo of a die

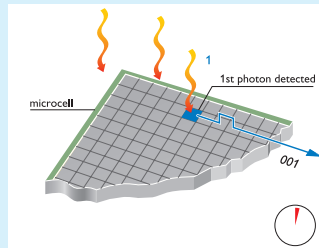


Figure 2: First photon hits the sensor, integrated photon counter increases to 001 and integrated timer measures arrival time of first photon per die.

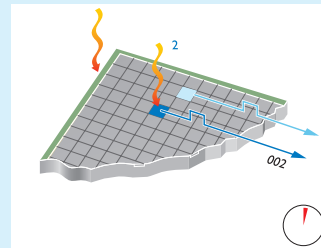


Figure 3: Second photon hits the sensor, the integrated photon counter increases to 002.

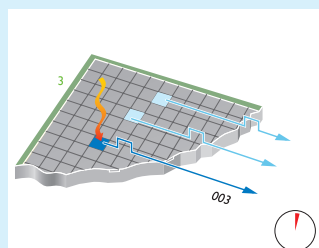


Figure 4: The chip has measured the 3 photons that have hit the sensor during the desired length of the detection process.

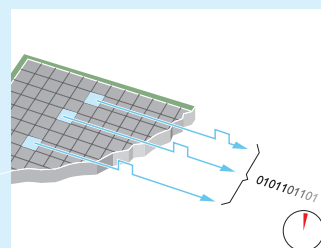


Figure 5: At the end of the detection process, the values of the integrated photon counter and timer can be read out via a digital interface.

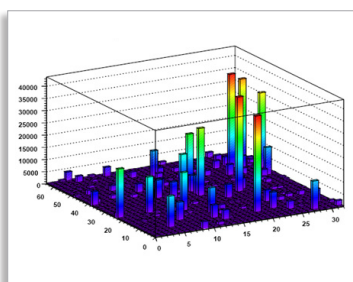
Digital Silicon Photomultiplier

Preliminary Short Data Sheet

DPC6400-22-44 / DPC3200-22-44



DPC Array



Dark count rate map: Option to physically disable arbitrary, user-selectable cells on the sensor.

Key Features

- 8 × 8 pixel array
- Single photon counting capability
- Integrated Time-to-Digital converters
- First photon trigger (configurable; up to 4th photon trigger)
- Excellent timing resolution
- Fully digital interface
- Four side tileable
- Configurable validation network for effective dark-count suppression
- Low disturbance by external magnetic fields

Specifications

PHYSICAL CHARACTERISTICS	DPC6400-22-44	DPC3200-22-44
OUTER DIMENSIONS	32.6 × 32.6 mm ²	32.6 × 32.6 mm ²
PIXEL PITCH (H × V)	4.0 mm × 4.0 mm	4.0 mm × 4.0 mm
PIXEL ACTIVE AREA	3.9 × 3.2 mm ²	3.9 × 3.2 mm ²
NUMBER OF CELLS PER PIXEL	6396	3200
CELL SIZE	59.4 × 32 μm ²	59.4 × 64 μm ²
SPECTRAL RESPONSE RANGE	380 nm – 700 nm	380 nm – 700 nm
PEAK SENSITIVITY WAVELENGTH (λ _p)	420 nm	420 nm
PHOTON DETECTION EFFICIENCY (PDE) @ λ _p (PIXEL LEVEL)	30 %	40 %
PIXEL FILL FACTOR (ALREADY INCLUDED IN PDE)	54 %	74 %
TILE FILL FACTOR	75%	75%
DARK COUNT RATE (95% CELLS ACTIVE)	< 5 MHz / pixel at room temperature	< 7 MHz / pixel at room temperature
OPERATIONAL BIAS VOLTAGE	27 +/- 0.5 V	27 +/- 0.5 V
TEMPERATURE DEPENDENCE OF PDE	-0.33%/°C in the range of 15°C - 25°C	-0.33%/°C in the range of 15°C - 25°C
INTRINSIC TIMING RESOLUTION*	44 ps	44 ps

Environmental Parameters

PARAMETER	DPC6400-22-44	DPC3200-22-44
STORAGE TEMPERATURE	0°C to +70°C	0°C to +70°C
OPERATING TEMPERATURE	0°C to +20°C	0°C to +20°C

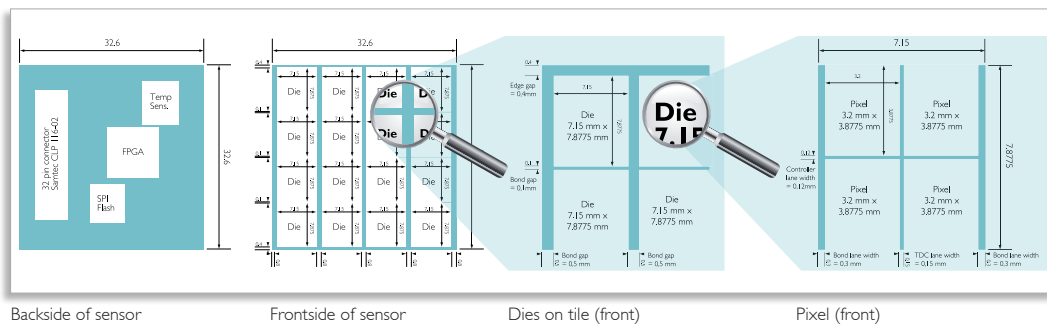
*Measured with pico second laser pulse with approx. 1000 photons.
Please note: All data is preliminary and subject to change without prior notice!

7. APPENDIX

Digital Silicon Photomultiplier

Preliminary Short Data Sheet

Dimensions



Backside of sensor

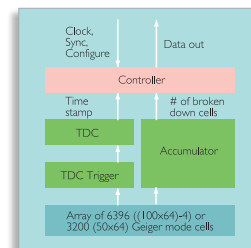
Frontside of sensor

Dies on tile (front)

Pixel (front)

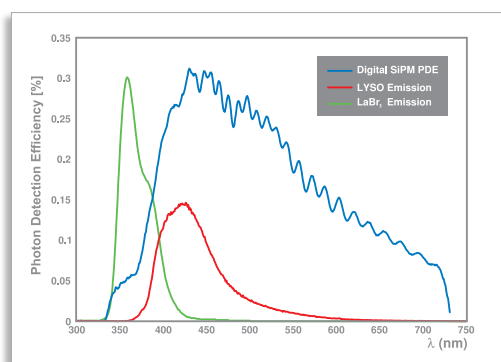
Description of Operation

The DPC6400-22-44 and the DPC3200-22-44 (tile) consist of 8 x 8 pixels arranged on 4 x 4 chips (dies). Each chip contains 2 x 2 pixels. Each pixel has access to two logic blocks to record the energy and the timestamp of a hit. The determination of the hit energy is done by recording the number of detected photons, i.e. broken-down cells, by means of an accumulator. The timestamp is generated by a combination of a 'fine' counter (time-to-digital converter, TDC) and a coarse counter (synchronous to the system clock). The SPI flash memory contains all die related information needed for calibration/correction of the photon count and timestamp. The tile FPGA controls/programs all individual dies, collects all the events for each die and performs post-processing to generate a full timestamp and photon count value for each event.

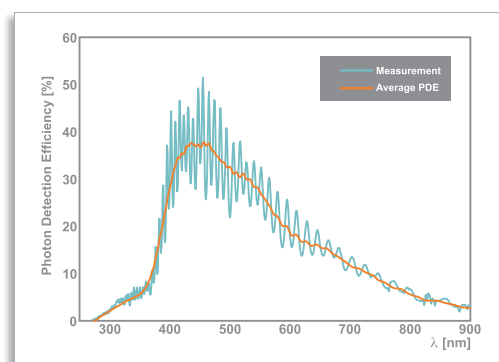


Single pixel block diagram

Performance Characteristics



Typical photon detection efficiency of DPC6400-22-44



Typical photon detection efficiency of DPC3200-22-44

Please note: All data is preliminary and subject to change without prior notice!



Contact

For further information, please contact:
 Philips Digital Photon Counting
 Pauwelsstraße 17
 52074 Aachen, Germany
 Phone: +49 241 969 79130
 Fax: +49 241 969 79191
 E-mail: digitalphotoncounting@philips.com
 www.philips.com/digitalphotoncounting

May 2012

7.8 Datasheet Saint Gobain optical grease BC-630

Accessed and downloaded June 2014, from <http://www.crystals.saint-gobain.com/uploadedFiles/SG-Crystals/Documents/Organic%20Product%20Accessories%20Data%20Sheet.pdf>.

Detector Assembly Materials

Saint-Gobain Crystals can provide you with various detector assembly materials. For more detailed specifications on BC-600, BC-620 and BC-622A, individual data sheets are available.

BC-600 Optical Cement –

BC-600 optical cement is a clear epoxy, which sets at room temperature and has a refractive index close to that of SGC plastic scintillators. It is therefore ideal for optically cementing plastic scintillators to light pipes or optical windows. It is not recommended for coupling scintillators to photomultiplier tubes. For that application, we recommend BC-634A or BC-630.

BC-620 Reflector Paint for Plastic Scintillators –

BC-620 is a highly efficient reflector employing a special grade of titanium dioxide in a water soluble binder. It is applied directly onto plastic scintillators, acrylic light guides, glass and metals. It is not intended for direct contact with liquid scintillators. It is a diffuse reflector and, therefore, should not be applied to sheets of scintillator or light guide material where the length is much longer than the thickness.

BC-620 can be removed with warm water.

BC-620 Consists of	%
Anatase Titanium Dioxide	40
Acrylic Emulsion Resin	24
Water	32
Glycol Coalescent	2.8
Surfactants & Thickeners	1.2

BC-622A Reflector Paint for Liquid Scintillator Tanks –

BC-622A reflector paint is intended for use with liquid scintillators. It is particularly useful in large steel or aluminum tanks, which require application of the paint at the research site. It is a diffuse reflector and, therefore, should not be used on the major surfaces of long, narrow tanks (total internal reflector and employed in these).

Can be removed from metal by submersing in Methol alcohol.

BC-630 Silicone Optical Grease –

BC-630 is a clear, colorless, silicone, optical coupling compound that features excellent light transmission and low evaporation and bleed at 25°C. It has a specific gravity of 1.06, an Index of Refraction of 1.465 and has a very flat transmission of approximately 95% for wavelengths between 280nm and 700nm. There is a sharp fall off below 280nm. Transmission at 270 and below is about zero. We supply this single component formulation in 60ml and 500ml jars.

Assembly Materials Available –

- Optical Cement
- Reflector Paint for Plastic Scintillators
- Reflector Paint for Liquid Scintillator Tanks
- Silicone Optical Grease
- Optical Interface Pads
- Black Wrapping Tape
- Plastic Masking Paper
- PTFE Reflector Tape



Pictured are a variety of BC-634A sizes

7. APPENDIX

Scintillation Products



USA

Saint-Gobain Crystals
17900 Great Lakes Parkway
Hiram, OH 44234
Tel: (440) 834-5600
Fax: (440) 834-7680

Europe

Saint-Gobain Crystals
104 Route de Larchant
BP 521
77794 Nemours Cedex, France
Tel: 33 (1) 64 45 10 10
Fax: 33 (1) 64 45 10 01

P.O. Box 3093
3760 DB Soest
The Netherlands
Tel: 31 35 60 29 700
Fax: 31 35 60 29 214

Japan

Saint-Gobain KK, Crystals Division
3-7, Kojimachi, Chiyoda-ku,
Tokyo 102-0083 Japan
Tel: 81 (0) 3 3263 0559
Fax: 81 (0) 3 5212 2196

China

Saint-Gobain (China) Investment Co., Ltd.
15-01 CITIC Building
19 Jianguomenwai Ave.
Beijing 100004 China
Tel: 86 (0) 10 6513 0311
Fax: 86 (0) 10 6512 9843

India

Saint Gobain Crystals and Detectors Ltd.
India Delegation, Leela Business Park
Andheri Kurla Road
Mumbai 400059 India
Tel: 91 22 4021 2121
Fax: 91 22 4021 2102

www.detectors.saint-gobain.com

Detector Assembly Materials

BC-634A Optical Interface Pad –

BC-634A is a self-wetting, flexible pad just hard enough to resist tearing while handling.

It is formulated for use within the temperature range of -10 to +60°C, has an index of refraction of 1.42 and an internal transmission >98% around 400nm.

If you cannot maintain sufficient interface pressure, apply a thin film of coupling grease to both sides of the interface pad.

BC-637 High Temperature Optical Interface Pad –

BC-637 interface pads are placed between the plastic and photomultiplier tube. BC-637 is rated at 200°C.

BC-638 Black Wrapping Tape –

BC-638 is a black adhesive tape 2" (50.8mm) wide by .008" (0.2mm) thick. Wrapping a plastic scintillator in one layer will give you a light-tight seal. We provide BC-638 in 36 yard (32.9m) rolls.

BC-640 Plastic Masking Paper –

This material is an adhesive-backed masking paper routinely used for protecting the surfaces of plastic scintillator during handling or storage. We supply BC-640 in rolls 12" (30.5cm) wide by 300' (91.4m) long.

BC-642 PTFE Reflector Tape –

BC-642 is a .003" (0.08 mm) thick (normal) Teflon tape and is frequently used as a reflecting material for non-hygroscopic scintillators. Three layers give you optimum reflectivity. It comes in rolls 2" (50.8mm) wide by 540" (13.7m) long.

*Manufacturer reserves the right to alter specifications.
©2005-12 Saint-Gobain Ceramics & Plastics, Inc. All rights reserved.*

(06-12)

8

Glossary

APD...avalanche photodiode
ASIC...application-specific integrated circuit
BBO...barium borate
BGO...bismuth germanate
CCD...charge-coupled device
CDF...cumulated distribution function
CPS...counts per second
CTW...coincidence time window
DCR... darkcount rate
DCM...darkcount map
DPC...digital photon counter
FWHM...full width at half maximum
HEP...high energy physics
i.i.d....independent and identically distributed
LSO...lutetium silicon orthosilicate
LuAG..lutetium aluminum garnet
MCP...microchannel plate
MR...nuclear magnetic resonance
MTA...multi-timestamp-approach
NDF...number of degrees of freedom
PANDA...anti-proton annihilation at Darmstadt
PET...positron emission tomography
PDF...probability density function
PMT...photomultiplier tube
PWO...lead tungstate
QDC...charge-to-digital converter
RF...radio-frequency
SiPM...silicon photomultiplier
SHG...second harmonic generation
SMI...Stefan-Meyer-Institute

8. GLOSSARY

SNR...signal-to-noise ratio

SPAD...single photon avalanche diode

SPTR...single photon time resolution

TDC...time-to-digital converter

TOF...time-of-flight

UV...ultra violet

Bibliography

- [1] M. Conti *et al.*, “Focus on time-of-flight PET: the benefits of improved time resolution.” *Eur. J. Nucl. Med. Mol. Imaging* 38-6, pp. 1147–1157, 2011. 3, 6, 7, 12
- [2] T. F. Budinger, “Time-of-Flight Positron Emission Tomography: Status relative to Conventional PET.” *JNM* 24, p. 73, 1983. 3
- [3] J. Karp *et al.*, “Benefit of timeofflight in PET: experimental and clinical results.” *JNM* 49, pp. 462 - 470, 2008. 3
- [4] W. W. Moses, “Recent advances and future advances on timeofflight PET.” *NIM A*, 580, pp. 919 - 925, 2007. 3, 12, 53, 120, 122
- [5] K. Ziemons, “Photon detection in Medical Imaging.” CERN, Geneva, 2011. 3
- [6] T. Beyer *et al.*, “The future of hybrid imaging - part 3: PET/MR, smallanimal imaging and beyond.” *Insights Imaging* 2, pp. 235 - 246, 2011. 3
- [7] T. Beyer *et al.*, “The future of hybrid imaging - part 3: PET/MR, smallanimal imaging and beyond.” <http://www.hybrid-pet-mr.eu/>, Accessed July, 2014. 3
- [8] P. Fischer *et al.*, “Fast Self Triggered Multi Channel Readout ASIC for Time and Energy Measurement.” *IEEE TNS* 53-3, pp. 1153 - 1158, 2009. 3
- [9] P. Beltrame, “AXPET: Concept, proof of principle and first results with phantoms.” *IEEE NSS/MIC*, pp. 2754 - 2757, 2009. 3
- [10] P. Beltrame, “Construction and tests of demonstrator modules for a 3D axial PET system for brain or small animal imaging.” *NIM A* 636, pp. S226 - S230, 2010. 3
- [11] ENDO-TOFPET-US. Accessed, July 2014, <http://endotofpet-us.web.cern.ch/endotofpet-us/>, 2014. 3
- [12] M. Morrocchi *et al.*, “Development of a PET detector module with depth of interaction capability.” *Vienna Conference on Instrumentation*, 2013. 3
- [13] H. vanDam *et al.*, “Sub200 ps CRT in monolithic scintillator PET detectors using digital SiPM arrays and maximum likelihood interaction ime estimation.” *Phys. Med. Biol.* 58, pp. 3243 - 3257, 2012. 3, 68, 101, 103

BIBLIOGRAPHY

- [14] S. Gundacker *et al.*, “Time of flight positron emission tomography towards 100 ps resolution with L(Y)SO: an experimental and theoretical analysis.” JINST, p. P07014, 2013. 3, 91
- [15] D. Schaart *et al.*, “LaBr(3):Ce and SiPMs for time-of-flight PET: achieving 100 ps coincidence resolving time.” Phys. Med. Biol. 55-7, pp. N179-189, 2010. 3
- [16] S. Seifert *et al.*, “The lower bound on the timing resolution of scintillation detectors.” Phys. Med. Biol. 57, pp. 1797 - 1814, 2012. 3, 67, 68, 101, 103
- [17] J. Humm *et al.*, “From PET detectors to PET Scanners.” Eur. J. Nucl. Med. Mol. Imaging 30-11, 1574–1597, 2003. 4, 12
- [18] M. E. Phelps, “PET, Physics Instrumentation and Scanners.” Springer Science Business Media, LLC, 2006. 4
- [19] P. Nahin, “Oliver Heaviside: The Life, Work, and Times of an Electrical Genius of the Victorian Age.” IEEE press, New York, 1987. 4
- [20] J. V. Jelley, “Cerenkov radiation and its applications.” Brit. Jour. Appl. Phys. 6, pp. 227-232, 1955. 4, 5, 6, 57, 62, 71, 72
- [21] S. Derenzo *et al.*, “The quest for the ideal inorganic scintillator.” Nucl. Instrum. Methods Phys. Res. A 505, pp. 111-117, 2003. 6, 55, 75, 89
- [22] A. Vasil’ev, “Relaxation of hot electronic excitations in scintillators: account for scattering, track effects, complicated electronic structure.” Proceedings of the Fifth International Conference on Inorganic Scintillators and their applications, 2000. 6, 55
- [23] R. Williams *et al.*, “In the first instants ... ultrafast views of radiation effects.” Radiation Measurements 33, pp. 497 - 502, 2001. 6, 55
- [24] G. Kalicky *et al.*, “Status of the PANDA Barrel DIRC.” JINST 9, p. C05060, 2014. 7, 19, 20
- [25] C. Schwarz *et al.*, “The Barrel DIRC of PANDA.” JINST 7, p. C02008, 2012. 7, 19, 20
- [26] L. Gruber *et al.*, “Position sensitive SiPM detector for Cherenkov applications.” JINST 6, p. C11024, 2011. 7, 19, 20, 21, 148
- [27] M. Rihl *et al.*, “Efficiency and uniformity measurement of a light concentrator in combination with an SiPM array.” NIM A 732, pp. 419 - 422, 2013. 7, 19, 20, 21, 154
- [28] K. Goetzen *et al.*, “Proposal for a scintillation tile hodoscope for PANDA.” Private communication, <https://panda-wiki.gsi.de/pub/Tof/SciTil/scitil.pdf> (last visited July) 2014. 7, 19, 28
- [29] S. E. Brunner *et al.*, “Time resolution below 100 ps for the SciTil detector of PANDA employing SiPM.” JINST 9-03, p. C03010, <http://iopscience.iop.org/1748-0221/9/03/C03010>, 2014. 7, 19, 21, 22, 29, 137
- [30] P. Lecoq *et al.*, “Inorganic Scintillators for Detector Systems.” Springer-Verlag Berlin Heidelberg, 2006. 10, 12, 74

BIBLIOGRAPHY

- [31] P. A. Rodnyi, “Physical processes in inorganic scintillators.” CRC Press LLC, 1997. 10, 11
- [32] M. J. Berger *et al.*, “XCOM: Photon cross section database.” <http://physics.nist.gov/PhysRefData>, 2009. 11, 12
- [33] W. R. Leo, “Techniques for Nuclear and Particle Physics Experiments.” Berlin, Germany: Springer, 1994. 11, 57
- [34] S. E. Brunner *et al.*, “New methods for improvement of TOF-PET.” Master thesis, CERN and Vienna UT, 2009. 11, 55, 67, 69, 71, 73, 80
- [35] F. Powolny, “Characterization of time resolved photodetector systems for Positron Emission Tomography.” Ph.D. Thesis, Universite de Neuchatel, 2009. 12, 69, 71
- [36] A. A. Annenkov *et al.*, “Lead tungstate scintillation material.” Nucl. Instr. Meth. A 490, pp. 30–50, 2002. 12
- [37] E. Auffray *et al.*, “LuAG material for dual readout calorimetry at future high energy physics accelerators.” IEEE Nucl. Sci. Symp. Conf. Rec., pp. 2245-2249, 2009. 12, 59, 60, 61, 62, 63, 64, 120, 126
- [38] W. Chewpraditkul *et al.*, “Scintillation Properties of LuAG:Ce, YAG:Ce and LYSO:Ce Crystals for Gamma-Ray Detection.” IEEE Trans. Nucl. Sci. 56-6, pp.3800–3805, 2009. 12, 120
- [39] Koike *et al.*, “Next generation hypernuclear γ -ray spectrometer: Hyperball-J.” Proceedings of The IX International Conference on Hypernuclear and Strange Particle Physics, Mainz, pp. 25–28, Oct. 2006. 12
- [40] P. A. Williams *et al.*, “Optical, thermo-optic, electro-optic, and photoelastic properties of bismuth germanate $\text{Bi}_4\text{Ge}_3\text{O}_{12}$.” Appl. Opt. 35, pp. 3562–3569, 1996. 12, 72
- [41] N. Dinu *et al.*, “Development of the first prototypes of Silicon PhotoMultiplier (SiPM) at ITC-irst.” Nucl. Instr. Meth. A 572-1, pp.422 - 426, 2007. 13
- [42] D. Renker *et al.*, “Geiger-mode avalanche photodiodes, history, properties and problems.” Nucl. Instr. Meth. A 567, pp. 48–56, 2006. 13
- [43] R. H. Haitz, “Model for the Electrical Behavior of a Microplasma.” J. Appl. Phys 35, pp. 1370 - 1376, 1964. 13
- [44] R. J. McIntyre, “Theory of Microplasma Instability in Silicon.” J. Appl. Phys 31, pp. 983 - 995, 1961. 13
- [45] S. Cova *et al.*, “Avalanche photodiodes and quenching circuits for single-photon detection.” Appl. Opt 35-12, pp. 1956 - 1976, 1996. 13
- [46] T. Frach *et al.*, “The digital silicon photomultiplier Principle of operation and intrinsic detector performance.” IEEE Nucl. Sci. Symp. Conf. Rec., pp. 19591965, Oct. 2009., 2009. 14, 15

BIBLIOGRAPHY

- [47] L. H. C. Braga *et al.*, “Complete characterization of SPADnet-I a digital 816 SiPM array for PET applications.” IEEE Nuclear Science Symposium and Medical Imaging Conference (NSS/MIC), pp. 1 - 4, 2013. 14
- [48] B. Frisch *et al.*, “Combining endoscopic ultrasound with Time-Of-FlightPET: The EndoTOFPET-US Project.” NIM A 732, pp. 577 - 580, 2013. 14
- [49] R. Schulze, “PDPC-TEK User Manual.” Philips Digital Photon Counting, Koninklijke Philips Electronics 2013, Version 0.20, 2013. 15, 99, 100
- [50] A. Lehmann *et al.*, “Systematic studies of micro-channel plate PMTs.” NIM A 628 - 1, pp. 177 - 147, 2011. 20
- [51] R. Brun and F. Rademakers, “ROOT - An Object Oriented Data Analysis Framework.” NIM A 389, pp. 81 - 86, 1997. 27
- [52] N. Dinu *et al.*, “Temperature and bias voltage dependence of the MPPC detectors.” IEEE Nucl. Sci. Symp. Med. Imaging Conf. Rec, pp. 215-219, Oct. 2010. 28
- [53] G. Collazuol *et al.*, “Single photon timing resolution and detection efficiency of the IRST silicon photo-multipliers .” Nucl. Instr. Meth. A 581, pp. 461-464, 2007. 28
- [54] L. Gruber *et al.*, “Oversaturation behaviour of SiPM at high photon exposure.” NIM A 737, pp. 11 - 18, 2013. 31, 158
- [55] T. Frach, “Optimization of the digital Silicon Photomultiplier for Cherenkov light detection.” JINST 7-01, p. C01112, 2012. 32, 33, 51, 61, 62
- [56] Mirzoyan *et al.*, “Light emission in Si avalanches.” NIM A 610, pp. 98 - 100, 2009. 45
- [57] M. Conti, “State of the art and challenges of time-of-flight PET.” Physica Medica 25, 1-11, 2009. 53, 120
- [58] R. Dolenec *et al.*, “Time-of-flight measurements with Cherenkov photons produced by 511 keV photons in lead crystals.” IEEE Nuclear Science Symp. Conf. Rec., pp. 280–284, 2010. 55, 126
- [59] P. Lecoq *et al.*, “Factors Influencing Time Resolution of Scintillators and Ways to Improve them.” IEEE Trans. Nucl. Sci. 57-5, pp. 2411-2416, 2010. 55, 67, 75, 89
- [60] S. E. Brunner *et al.*, “New Approaches for Improvement of TOF-PET.” Nucl. Instrum. Methods Phys. Res. A 732, pp. 560-563, 2013. 55, 77, 78, 79, 85, 87, 88, 94, 95, 128
- [61] S. E. Brunner *et al.*, “Studies on the Cherenkov Effect for Improved Time Resolution of TOF-PET.” IEEE Trans. Nucl. Sci. 61-1, pp. 443-447, 2014. 55, 56, 57, 58, 88, 90, 91, 93, 105, 106, 107, 132
- [62] S. Gobain, “Detector Assembly Materials.” www.cystals.saint-gobain.com, accessed Apr. 2014. 56
- [63] M. J. Berger *et al.*, “Stopping-Power and Range Tables for Electrons, Protons, and Helium Ions.” National Institute of Standards and Technology webpage, <http://physics.nist.gov/PhysRefData/Star/Text/contents.html>, 2009. 57

BIBLIOGRAPHY

- [64] A. Thomson *et al.*, “X-Ray Data Booklet.” Lawrence Berkeley National Laboratory, 2001. 57
- [65] R. Mao *et al.*, “Emission Spectra of LSO and LYSO Crystals.” IEEE Trans. Nucl. Sci. 55-3, pp.1759–1766, 2008. 60
- [66] R. Mao *et al.*, “Optical and Scintillation Properties of Inorganic Scintillators in High Energy Physics.” IEEE Nuclear Science Symposium and Medical Imaging Conference (NSS/MIC), pp.2285–2291, 2007. 60, 61, 120
- [67] Schott AG. Jena, Germany, www.schott.com, accessed, May 2014. 61, 62, 64
- [68] J. Zhou *et al.*, “Immersion lithography with numerical apertures above 2.0 using high index optical materials.” Proc. SPIE 6520, Optical Microlithography XX, March 2007. 61, 63, 64
- [69] F. J. Lynch, “Improved Timing With NaI(Tl).” IEEE Transaction on Nuclear Science, vol. 13, page 140, 1966. 67, 71
- [70] R. F. Post and L. I. Schiff, “Statistical limitations on the resolving time of a scintillation counter.” Phys. Rev. 8, p. 1113, 2012. 67, 69
- [71] Y. Shao, “A new timing model for calculating the intrinsic timing resolution of a scintillator detector.” Phys. Med. Biol. 52 pp. 1103-1117, 2007. 67, 69, 75, 89
- [72] A. G. Wright *et al.*, “Exact expression for the variance of the photon emission process in scintillation counter.” Nuc. Inst. and Meth. in Ph. Research, vo. A564, page 184, 2006. 67, 71
- [73] L. G. Hyman, “Time resolution of photomultiplier systems.” Rev. Sci. Instr. 36, pp. 193 - 196, 1965. 67
- [74] C. H. Westscott *et al.*, “A study of expected loss rates in the counting of particles from pulsed sources.” Proc. Royal Soc. A 194, p. 508, 1948. 69
- [75] E. Jellison *et al.*, “Spectroscopic refractive indices of monoclinic single crystal and ceramic lutetium oxyorthosilicate from 200 to 850 nm.” J. Appl. Phys. 112, 063524, 2012. 72
- [76] Y. Kuwano *et al.*, “Crystal growth and properties of $(\text{Lu,Y})_3\text{Al}_5\text{O}_{12}$.” Journal of Crystal Growth 260, pp. 159–165, 2003. 72
- [77] W. W. Moses and D. S.E., “Prospects for Time-of-Flight PET using LSO Scintillator.” IEEE Trans. Nucl. Sci. 46-3, pp. 474-478, 1999. 75, 85, 86, 89
- [78] EPIC crystal. Shanghai, China, www.epic-crystal.com, accessed, August 2014. 75, 98, 108, 121
- [79] R. Wiener *et al.*, “Signal analysis for improved timing resolution with scintillation detectors for TOF PET imaging.” IEEE Nuclear Science Symposium and Medical Imaging Conference (NSS/MIC), pp.1191–1195, 2010. 77
- [80] W. J. Ashmanskas *et al.*, “Crystal growth and properties of $(\text{Lu,Y})_3\text{Al}_5$.” Journal of Crystal Growth 260, pp. 159–165, 2003. 77, 80
- [81] S. Korpar *et al.*, “Study of TOF PET using Cherenkov light.” Nucl. Instr. Meth. A 654, 532–538, 2011. 126

Stefan E. Brunner, M.Sc.

Address Antonsplatz 13/22
1100 Wien
Austria

Mail stefan.enrico.brunner@oeaw.ac.at

Date of Birth 5th of February, 1984

Citizenship Austrian

Education

2010 – today PhD student of technical physics at Vienna University of Technology, Austria,
Employed at the Stefan Meyer Institute for Subatomic Physics of the Austrian Academy
of Sciences

2009 – 2010 Master thesis at CERN (PH-dept.), Geneva, Switzerland, employed as technical
student
Thesis title: New methods for improvement of time of flight positron emission tomography

2008 Mobility semester (ERASMUS) at ETH Zürich, Switzerland

2003 – 2010 Master studies in technical physics at Vienna University of Technology (passed with
distinction)

Work Experience

2011 – today Board member of the Austrian Physical Society (ÖPG)
*Responsible for students issues, e.g., reviewer for the annual prize for the best graduation
thesis in physics*

2011 – today Safety officer at Stefan Meyer Institute (with certificate)
Responsible for laboratory safety

2010 Charity worker in public relations at the Austrian headquarters of the NGO Caritas,
Vienna, Austria
*Editor of press releases and project sheets and responsible for press releases on the Caritas
and Caritas related websites*

2007 Scientific employee at Austrian Institute of Technology (former Arsenal Research), Vienna, Austria
Simulations on wind loads for the new Vienna central station using finite element method

2007 Scientific trainee at Austrian Institute of Technology, Vienna, Austria
Training on CAD and the finite element method

Skills C++, Fortran, Geant4, LabView, Matlab, ROOT. Experience in particle detection with focus on scintillation and Cherenkov detectors for high energy physics and medical applications (TOF-PET), single photon detection with focus on analog and digital SiPM, signal processing (NIM, Camac, VME, offline waveform analysis) and particle beam measurements including project planning (beam times 2014 at COSY Forschungszentrum Jülich, 2012 at INFN Frascati, 2011 at PS, CERN and 2009 at SPS, CERN). Furthermore, experience in editorial work as author for publications and press releases.

Languages English, German (native)

Oral presentations

2014 Symposium on PET, Cracow, Poland (invited talk)
Status and prospects for fast Cherenkov emission for TOF-PET

2014 ICTR-PHE, Geneva, Switzerland (plenary talk)
Potential of detection of fast Cherenkov photons for improved time of flight positron emission tomography

2013 DIRC workshop on fast Cherenkov detectors, Rauischholzhausen, Germany
Comparative timing performance study of SiPMs for gamma detectors using hybrid Cherenkov-scintillation readout

2013 EANM annual congress, Lyon, France
Improving TOF-PET by studying scintillation photon propagation and the Cherenkov effect

2013 SCINT, Shanghai, China
Studies of the Cherenkov effect for improvements of TOF-PET and DOI determination

2012 Invited talk at Medical University of Vienna, Austria
The Cherenkov effect for improvement of TOF-PET

2011 MEDPHYS, Vienna, Austria
Improving TOF-PET using silicon photo multipliers

2009 Annual Meeting of the Austrian and Swiss Physical Societies
A novel time driven photo detector scheme for PET using SiPMs

Poster presentations

- 2013 VCI, Vienna Austria
New approaches for improvement of TOF-PET
- 2013 Annual Meeting of the Austrian and Swiss Physical Societies
Improving the time of flight method for positron emission tomography
- 2012 ICTR-PHE, Geneva, Switzerland
Improving time of flight PET using silicon photo multipliers

Research projects

- 2008 CERN, Geneva, Switzerland for the Ax-PET collaboration of ETH Zürich, Switzerland
Development of a test setup for radiation-damage-measurements of wavelength-shifters for Axial-PET
- 2007 Austrian Institute of Atomic and Subatomic Physics, Vienna, Austria
Dating of archaeological finds using thermoluminescence
- 2005 Medical University Vienna, Austria
Development of a automatic digitization routine for radiographs using commercial negative scanners

Publications (peer reviewed)

- [1] S. E. Brunner, L. Gruber, J. Marton, H. Orth, K. Suzuki, "Time resolution below 100 ps for the SciTil detector of PANDA employing SiPM", J. Instrum., Accepted for publication, 2013, arXiv:1312.4153.
- [2] S. E. Brunner, L. Gruber, J. Marton, K. Suzuki, A. Hirtl, "Studies on the Cherenkov Effect for Improved Time Resolution of TOF-PET", IEEE Trans. Nucl. Sci., Accepted for publication, 2013, DOI: 10.1109/TNS.2013.2281667, arXiv:1305.6257.
- [3] S. E. Brunner, L. Gruber, J. Marton, K. Suzuki, A. Hirtl, "New approaches for improvement of TOF-PET," Nucl. Instr. Meth. A, vol. 732, pp. 560–563, 2013, DOI: 10.1016/j.nima.2013.05.028, arXiv:1305.1560.
- [4] L. Gruber, S. E. Brunner, J. Marton, and K. Suzuki, "Over saturation behavior of SiPMs at high photon exposure," Nucl. Instr. Meth. A, vol. 737, pp. 11–18, 2013, DOI: 10.1016/j.nima.2013.11.013, arXiv:1304.2493.
- [5] M. Rihl, S. E. Brunner, L. Gruber, J. Marton, and K. Suzuki, "Efficiency and uniformity measurements of a light concentrator in combination with a SiPM array," Nucl. Instr. Meth. A, vol. 732, pp. 419–422, 2013, DOI: 10.1016/j.nima.2013.05.187.
- [6] S. E. Brunner, J. Marton, K. Suzuki, L. Gruber, A. Hirtl, M. Jankovec, P. Knoll, A. Gamal, "Improving Time-Of-Flight PET using silicon photomultipliers," Radiotherapy and Oncology, vol. 102, suppl. 1, pp. S137 – S138, 2012, DOI: 10.1016/S0167-8140(12)70228-1.
- [7] F. Powolny, E. Auffray, S. E. Brunner, M. Despeisse, E. Garutti, M. Goettlich, H. Hillemanns, P. Jarron, P. Lecoq, T. Meyer, F. Powolny, W. Shen, H.-C. Schultz-Coulon, M. C. S. Williams, "Time-Based Readout of a Silicon Photomultiplier (SiPM) for Time of Flight Positron Emission Tomography (TOF-PET)," IEEE Trans. Nucl. Sci., vol. 58, pp. 597 – 604, 2011, DOI: 10.1109/TNS.2011.2119493.

- [8] L. Gruber, G. S. M. Ahmed, S. E. Brunner, P. Bühler, J. Marton, and K. Suzuki, "Position sensitive SiPM detector for Cherenkov applications," *J. Instrum.*, vol. 6, no. 11, pp. C11024–C11024, 2011, DOI: 10.1088/1748-0221/6/11/C11024.
- [9] F. Powolny, E. Auffray, S. E. Brunner, E. Garutti, M. Goettlich, H. Hillemanns, P. Jarron, P. Lecoq, E. T. Meyer, H. C. Schultz-Coulon, W. Shen, and M. C. S. Williams, "A time driven readout scheme for PET and CT using APDs and SiPMs", *Nucl. Instr. Meth. A*, vol. 617, pp. 232–236, 2010.
- [10] P. Lecoq, E. Auffray, S. E. Brunner, H. Hillemanns, P. Jarron, A. Knapitsch, T. Meyer, and F. Powolny, "Factors Influencing Time Resolution of Scintillators and Ways to Improve Them," *IEEE Trans. Nucl. Sci.*, vol. 57, no. 5, pp. 2411–2416, 2010.
- [11] E. Auffray, D. Abler, S. E. Brunner, B. Frisch, A. Knapitsch, P. Lecoq, G. Mavromanolakis, O. Poppe, and A. Petrosyan, "LuAG material for dual readout calorimetry at future high energy physics accelerators," *IEEE Nucl. Sci. Symp. Conf. Rec. (NSS-MIC)*, pp. 2245–2249, Oct. 2009.
- [12] P. Lecoq, E. Auffray, S. E. Brunner, H. Hillemanns, P. Jarron, A. Knapitsch, T. Meyer, and F. Powolny, "Factors Influencing Time Resolution of Scintillators and Ways to Improve Them," *IEEE Nucl. Sci. Symp. Conf. Rec. (NSS/MIC)*, pp.1880–1885, Oct. 2009.
- [13] P. Jarron, E. Auffray, S. E. Brunner, M. Despeisse, E. Garutti, M. Goettlich, H. Hillemanns, P. Lecoq, T. Meyer, F. Powolny, W. Shen, H.-C. Schultz-Coulon, M. C. S. Williams, "Time based readout of a silicon photomultiplier (SiPM) for time of flight positron emission tomography (TOF-PET)," *Nucl. Sci. Symp. Conf. Rec. (NSS/MIC)*, pp. 1212–1219, Oct. 2009, DOI: 10.1109/NSSMIC.2009.5402391.